Light Alkane Reactivity on Pt(111) Investigated Using Effusive Molecular Beam Methods

Jason Keith Navin
Jonestown, Pennsylvania

B.S., Lebanon Valley College, 2008

A Dissertation presented to the Graduate Faculty
of the University of Virginia in Candidacy for the Degree of
Doctor of Philosophy

Department of Chemistry

University of Virginia
August, 2014

_____

_____

_____

_____

_____

Acknowledgements

First and foremost, I would like to thank Dr. Ian Harrison for allowing me to study in his group and thus, giving me the opportunity to study surface science. In addition, the conversations that Dr. Harrison and I had, not only helped my project but also broadened my overall view of science. I would also like to thank the Harrison research group for all of their support and help throughout my graduate career. In particular, I would like to thank Yifeng Song and Dr. Scott Donald, without whom, I would not have been able to complete many of the tasks that were set before me. Credit should be given to Scott, who conducted all of the MURT and PMMT modeling in this dissertation. If it were not for my close friends, I do not believe that I would have survived graduate school. In particular, I would like to thank Monica McEntee, Eun Yi, and Dr. Ana Stevanovic, for their friendship as well as their thought provoking scientific conversations with me. Along those lines, my family has also supported me with words of encouragement and I am extremely grateful for them. Lastly, I thank God for giving me the strength and the will to soldier on through graduate school.

Abstract

Dissociative sticking coefficients (DSCs) were measured for a wide range of normal alkanes on a Pt(111) metal surface using a heated effusive molecular beam technique. The effusive beam emits gas with a cosine angular distribution that allows measurement of angle-resolved DSCs (ar-DSCs), $S(\vartheta; T_g, T_s)$ where ϑ is the angle from the surface normal and the gas temperature (T_g) and surface temperature (T_s) are separately varied. Averaging measured thermal ar-DSCs, $S(\vartheta; T = T_g = T_s)$ over the cosine flux distribution appropriate to an ambient thermal gas, yields the thermal DSC, S(T), relevant to high pressure catalysis. DSCs along the direction of surface normal, $S_n(T_g, T_s)$, were measured for a number of alkanes under thermal $T = T_g = T_s$, and non-equilibrium, $T_g \neq T_s$, conditions.

A precursor-mediated microcanonical trapping (PMMT) model of gas-surface reactivity, employing RRKM rate constants, allowed for DSC prediction and evaluation of experimental values. A general version was utilized to handle statistical systems and several other versions of the PMMT model were implemented in order to account for dynamical effects as well as gas-surface energy transfer.

Measurements of angle-resolved DSCs provided both great insights into dynamics, as well as allowed for the measurement of S(T) DSCs. Angle-resolved DSCs were measured for CH_4, C_2H_6, and C_3H_8 at $T_g = T_s = 700$ K on Pt(111). The distributions were initially sharp for CH_4 and increased in broadness up to C_3H_8. Both CH_4 and C_2H_6 behave dynamically on Pt(111), however, C_3H_8 seems to be the point at which alkane systems begin to behave statistically. The angle-resolved distributions were integrated to yield the thermal DSCs at T = 700 K, S(T = 700 K). In addition, ar-DSCs were measured for methane on Pt(111) and K/Pt(111)

surfaces at T = 900 K and it was found that the angular distribution was sharper on the K/Pt(111) surface.

An Arrhenius analysis of $S_n(T)$ yielded activation energies, E_a, for dissociation of alkanes on Pt(111). Results showed that E_a scales with the van der Waals attractions between the impinging alkane and the metal surface which is approximated by the energies for molecular desorption, E_d, of intact alkanes from the surface. In addition , it is believed that the van der Waals attractions stabilize the products of alkane dissociative chemisorption thus reducing the activation barrier for chemisorption.

Non-equilibrium DSCs can provide insight into reactivity as well as gas-surface energy transfer between the impinging alkane and the metal surface. We find that gas-surface energy transfer increases with the size of the alkane. The tendency of the gas-surface energy transfer is to drive the molecular degrees of freedom towards thermalization to the temperature of the surface. In the case where there is little energy transfer, we find that increasing either T_s or T_g increases the DSCs and the effect of varying one temperature is greatest when the other temperature is relatively low. Conversely, when there is high gas-surface energy transfer, the effect of varying T_g on DSCs is muted and in the limiting case, DSCs become solely dependent on T_s, such that ambient gas dosing experiments at any T_s become equivalent to thermal DSCs, $S(T = T_s)$.

Table of Contents

Section 1 - Introduction

1.1 Purpose

Catalytic activation of small alkanes is essential to many industrial processes ranging from hydrogen production and alcohol formation to providing feedstock for larger reaction products. The vast majority of these reactions occur over transition metal catalysts at high temperature and pressure. Although the end products of these reactions are known, there remains little direct characterization of the individual catalytic steps between the starting reactants and final products. The rate-limiting step in steam reforming of methane, which produces the industrial supply of hydrogen and synthesis gas, is believed to be the activated dissociative chemisorption of methane.[1] Consequently, we study this gas-surface reaction with the aspiration that a thorough understanding will help us to predict and design improved catalytic processes. To those ends, we measure dissociative sticking coefficients, a measure of the initial C-H bond cleavage, of light alkanes on Pt(111). In addition, we present a precursor-mediated microcanonical trapping model to both reproduce and predict our results. Through our work, we hope to provide not only experimental measurements but also a theoretical understanding of alkane reactivity as well.

1.2 Heterogeneous Catalysis

Homogeneous catalysis in which both the catalyst and reagents are in the same phase, such as acid or base catalyzed reactions, is commonplace in research but in industrial synthesis of chemicals, heterogeneous catalysis is typically preferred. Through heterogeneous catalysis, high turnover rates can be produced, but perhaps just as importantly, there is no step that requires separation of catalyst from products. One of the most important heterogeneous reactions, the

Haber-Bosch process, involves the conversion of hydrogen and nitrogen to ammonia over the surface of a potassium doped, iron nanocatalyst.[2] The process is still the main method for producing ammonia today.

$$N_2 + 3\,H_2 \rightarrow 2\,NH_3 \qquad \Delta_r H^0_{298.15\,K} = -92 \text{ kJ/mol}$$

Although the rate-limiting step of this reaction is believed to be the dissociation of nitrogen onto the surface, the majority of energy consumed in this reaction is actually derived from the high-energy cost of producing hydrogen via steam reforming.[3,4]

Steam reforming involves the reaction of water and an alkane, generally methane, over nickel nanocatalysts to produce both hydrogen gas and carbon monoxide.

$$CH_4 + H_2O \rightarrow CO + 3\,H_2 \qquad \Delta_r H^0_{298.15\,K} = 206 \text{ kJ/mol}$$

Approximately 47% of the world's hydrogen is produced via this reaction, with an additional 49% being derived from other fossil fuels and the remaining 4% being derived from the electrolysis of water.[5] More hydrogen can then be extracted by reacting the carbon monoxide with additional water in a process known as the water-gas shift reaction.

$$CO + H_2O \rightarrow H_2 + CO_2 \qquad \Delta_r H^0_{298.15\,K} = -41 \text{ kJ/mol}$$

The resulting hydrogen from both reactions serves many purposes. It can be used in hydrogen fuel cells as well as being the key reagent in hydrogenation reactions.

1.3 Platinum Catalysts

Platinum is a rare transition metal that is used industrially as a catalyst for synthesizing chemicals[6,7] and as the main catalyst in automobile catalytic convertors.[8,9] One of its most important uses is as a dehydrogenation/hydrogenation catalyst.[7] The direction of hydrogen addition or subtraction is based simply on the partial pressure of hydrogen in the catalytic cell;

that is to say, that high pressures of hydrogen result in hydrogenation of the compound and the reverse occurs if the hydrogen pressure is low. Perhaps the most important catalytic use of platinum involves the reforming of naphtha into smaller fragment hydrocarbons or different hydrocarbon forms and producing high-octane gasoline.[10]

1.4 Alkanes

Generally, hydrocarbons are derived from crude oil and natural gas and range in size from the very small, methane, to the extremely large, ($C_{60}H_xS_yN_z$). Hydrocarbons derived from crude oil are generally unsaturated and large. Approximately 30% of conventional crude oil is composed of linear and branched alkanes and the remaining 70% is composed of cycloalkanes, aromatic hydrocarbons, resins, and asphaltenes.[11] The smaller hydrocarbons are removed via distillation whereas the larger hydrocarbons are cracked into smaller components, and converted to other products or feedstock. However, those derived from natural gas are generally saturated and smaller. In a given sample of natural gas, approximately 85% is methane, 3-8% is ethane, 1-2% is propane, and < 2% is composed of butane, pentane, and hexane.[12] The majority of reactions involving alkanes are conducted in high temperature (~700 - 900 K) reactors at high pressure (~20 atm) using transition metal catalysts.[7] Through steam reforming and the water-gas shift reaction, alkanes can be converted to CO, CO_2, and hydrogen gas. This hydrogen can then be used to form larger alkanes through the Fischer-Tropsch process on a cobalt or iron catalyst or used in the catalytic hydrogenation of unsaturated compounds over a platinum catalyst.

$$(2n+1)\,H_2 + n\,CO \rightarrow C_nH_{(2n+2)} + n\,H_2O$$

$$C_mH_n + H_2 \rightleftarrows C_mH_{(n+2)}$$

Alkanes can also be dehydrogenated to form less saturated alkenes and alkynes. These molecules are then used as starting materials for alkylation, hydration, and halogenation reactions.

1.5 Dissociative Chemisorption of Alkanes

Dissociative chemisorption is the process of a molecule dissociating at a surface to form chemisorbed fragments. Dissociative chemisorption is typically discussed as occurring through two mechanisms depending on whether the energy barrier for dissociation is above (activated) or below (unactivated) the barrier for molecular desorption. In the former case, the reaction is consider "direct" in that it involves a short-lived gas-surface collision complex in which the dissociation process must compete with the more energetically favored desorption process. Experimentally, an increase in energy from either the gas or the surface results in a higher dissociation probability for activated dissociation. For unactivated dissociative chemisorption, an impinging molecule that does not directly dissociate or desorb may instead undergo gas-surface energy transfer with the surface which leads to trapping of the molecule into the physisorption well. In the limiting precursor-mediated thermalized trapping (PMTT) mechanism, the trapped molecule comes to thermal equilibrium with the surface and proceeds to react or desorb with thermal Arrhenius rate constants. Unlike the activated pathway, an increase in T_s or T_g actually lowers the probability that a molecule will chemisorb to the surface. In the case of alkanes on Pt(111), research has shown that the smaller alkanes undergo activated dissociative chemisorption. This is important because it is believed that the rate-limiting step of alkane reforming is the initial cleavage of the C-H bond of the alkane.

The probability that a given molecule will dissociate and yield chemisorbed fragments on the surface is the dissociative sticking coefficient (DSC). For the dissociative chemisorption of alkanes, the rate of carbon deposition, $d\theta_c/dt$, is found to vary as,

$$\frac{d\theta_c}{dt} = FS(1 - \frac{\theta_c}{\theta_{max}}) \qquad \text{Equation 1.1}$$

where S is the DSC, F is the flux of gas-surface collisions, θ_c is the carbon coverage in monolayers, and θ_{max} is the maximum surface coverage of carbon in monolayers. In the limit that there is no coverage dependence of the DSC, integration of the above equation over time yields the *initial* DSC defined as the number of successfully reacting molecules divided by the total molecular impingement. By measuring DSCs of ethylene on Pt(111), Cushing et al. showed that for reasonable carbon coverages of 0.1 ML to 0.4 ML, with respect to platinum, the DSC was coverage independent.[13] In addition, θ_{max} was found to be equal to 2.57 ML with respect to platinum at T_s = 800 K, where graphene can form, and the overall DSC obeyed Equation 1.1. There are a variety of experiments involving DSCs that can help elucidate reactivity of a given species on a surface. Measurements of equilibrium DSCs, in which the gas temperature (T_g) and surface temperature (T_s) are equal, allow for the calculation of activation energies associated with activated dissociation. Non-equilibrium DSCs, where, ($T_g \neq T_s$), reveal the extent of gas-surface energy transfer, which will enable us to understand how energy exchange between the impinging molecule and surface affects reactivity. Lastly, DSCs can be measured as a function of impingement angle, $S(\vartheta; T)$ and $S(\vartheta; E_t)$. Although such experiments cannot be conducted via ambient dosing, supersonic and effusive molecular beam techniques exist which allow such measurements.

1.6 Alkane Dissociative Sticking Coefficient Studies

1.6.1 Thermal Bulb

The thermal bulb technique is perhaps the simplest technique to measure DSCs. Gas is dosed into a vacuum chamber in a non-directional manner such that a random ambient gas impinges on the crystal and may react. After a period of time, the chamber is evacuated and the carbon deposition is measured. If the surface temperature is different than the chamber temperature, the chamber pressure must be sufficiently high (ca., 3 Torr) as to allow for a full thermalization of the gas above the crystal face over the distance of a few mean free collision path lengths. Because of this high-pressure requirement, gas impingement fluxes are high and only DSCs of a low value can be measured (DSC < 10^{-8}); because otherwise the dosing time becomes too short to practically manage, unless the gas is diluted with high concentrations of unreactive gas such as argon or nitrogen. This technique is good for measuring thermal DSCs, because it allows for a direct measurement without having to make assumptions other than full thermalization and an ability to characterize $P(T \neq T_{chamber})$ directly above the surface. However, DSC studies using the thermal bulb technique are not ubiquitous given the fact that the majority of DSCs for given molecular systems are generally high enough to make measurement difficult, although several techniques have been implemented to circumvent this issue. In the past, many thermal bulb experiments relied on massive quantities of pumping speed in order to achieve reasonable experimental results. Generally, an amount of gas was allowed into the chamber while the crystal was cold, the desired pressure was achieved and then the crystal was heated to the desired temperature. After the experiment was over, valves were opened to allow for the swift removal of gas. Early experiments of this nature were conducted for CH_4 on tungsten,[14,15] rhodium,[16-18] and platinum[19] as well as CH_4, C_2H_6, C_3H_8 and n-C_4H_{10} on nickel.[20,21] In all cases,

it was found that increasing either T_g or T_s, resulted in an increase in the DSC. Although the majority of studies involved gas at approximately 300 K, several techniques were developed in order to conduct DSC measurements using heated gas. A technique used by Brass et al. increased the gas temperature by preheating the gas in a valved section of a UHV chamber.[18] This valved section of chamber was submersed in a water bath and the temperature was set. Methane was then admitted into the valved section and allowed to thermalize. Once the methane had come to thermal equilibrium within the valved section of the chamber, the valve was opened and gas was allowed to strike the crystal. In addition, both Beebe et al.[20] and Sault et al.[21] performed experiments in which the pressure of methane was approximately 1 Torr. The authors' believed that the methane gas would come to equilibrium with the surface temperature at this high pressure because of the short mean free path of methane. However, work by Luntz and Winters showed that a higher pressure is required.[22]

Given a pressure constraint of $p \geq 3$ Torr to insure gas thermalization above the surface, it would be difficult to measure higher DSC values in thermal bulb experiments without having to do prohibitively (practically) short gas exposure times; however, one possible solution is to dilute the reactive gas with a non-reactive diluent such as argon. Luntz and Winters introduced this method to measure non-equilibrium and equilibrium DSCs for CH_4, CD_4, C_2H_6, and C_2D_6 on Pt(110).[22] The non-equilibrium measurements were performed at low pressure ($\sim 10^{-4}$ Torr) for all four species. High pressure, equilibrium measurements (7.8 Torr) were also carried out for CH_4 by backfilling the chamber with additional argon to achieve the desired pressure in order to achieve thermalization, ($T_g \approx T_s$). It was found that both CH_4 and C_2H_6 follow activated dissociation. Seets et al. conducted similar experiments for CH_4 and CD_4 on Ir(111).[23] However,

only low pressure (~10^{-4} Torr), non-equilibrium experiments were conducted, and it was found that CH_4 and CD_4 followed activated dissociation as well.

To circumvent the requirement for high pressures, Larsen and Chorkendorff measured equilibrium DSCs of CH_4 on Ni(100) by using a thermal finger situated in front of the crystal to control the impinging gas temperature.[24,25] By heating the thermal finger to the same temperature as the crystal, molecules striking the thermal finger were also thermalized towards the temperature of the crystal. With the boundary conditions of two surfaces at T_s, the intervening gas should eventually thermalize to T_s. The authors found that without the thermal finger, the chamber pressure had to be increased to 3 mbar in order to achieve full thermalization. However, the highest DSC recorded was less than $2*10^{-7}$. For higher DSCs, it is a question as to whether or not the experimental exposures would be too short in time to measure accurately.

1.6.2 Supersonic Molecular Beams

Although early experiments involving the laser pumping of vibrational excited states were conducted, which probed dynamics of CH_4 on rhodium using thermal bulb techniques, the total population of molecules transferred to an excited state by the laser was so small, that no discernible change in DSCs was measured.[16,17] In order to more efficiently probe dynamics, thermal bulb techniques were traded for supersonic molecular beams, which are now often used to study DSCs. In a supersonic molecular beam, high pressure gas exits through a small hole in a heated nozzle into high vacuum, differentially pumped regions separated by skimmers and small orifices, before reaching the UHV chamber. This results in a highly collimated beam of molecules. Because of the substantial pressure difference between the nozzle and the source high vacuum region, the gas undergoes a supersonic expansion. Collisional buffeting during the

supersonic expansion cools the relative translational motion amongst molecules in the beam and although the mean translational energy is $\approx 5/2\ k_b\ T_{Nozzle}$, the local translational temperature amongst the beam molecules drops to ca. 20 K. Because translational to rotational energy transfer is highly efficient, the supersonic expansion also cools the beam molecules rotational temperature to ca. 20 K. Translational to vibrational energy transfer is far less efficient, particularly for small molecules with high frequency modes. Consequently, vibrations are not cooled in a supersonic expansion for methane, but for alkanes of increasing size, there will be increasing vibrational cooling in supersonic exposures. The translational energy of molecules in a supersonic molecular beam can be described as relatively narrow and can be tuned by varying the nozzle temperature or seeding in inert carrier gases of different mass. Ultimately, the supersonic molecular beam is a well-collimated beam with a narrow translational energy distribution whose translational temperature, relative to the mean stream velocity of the beam molecules, is typically ca. 20 K.

The general technique for using supersonic beams to measure DSCs is named the King and Wells method.[26] Although different adaptations of this method exist, the general method will be repeated here. The molecular beam first enters the chamber and strikes a chemically inert "beam flag" which blocks the beam from striking the crystal face and a background pressure increase in the chamber is measured. The flag is then removed and the beam strikes the crystal face and a drop in pressure is measured. The ratio of the pressure drop upon lifting the beam flag, due to the pumping effect of the crystal surface, to the initial pressure increase, due to allowing the beam to strike the beam flag, gives the DSC directly. A graphical representation of the King and Wells method is shown in Figure 1.1. Only relatively high DSCs ($> 10^{-2}$) can be measured with this technique because pressure changes are difficult to measure to better than

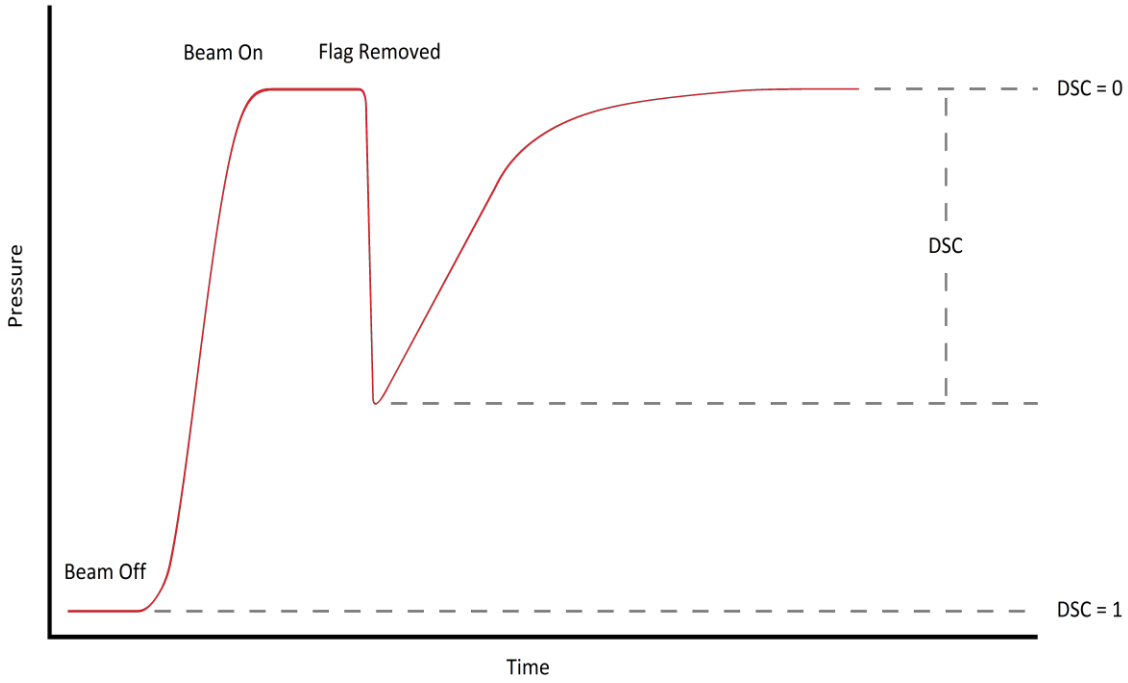

Figure 1.1: Graphical representation of the King and Wells method for measuring dissociative sticking coefficients. Gas is first sent into the chamber through the supersonic molecular beam nozzle and strikes a beam flag causing the chamber pressure to increase. The flag is then removed and the beam strikes the crystal surface and gas is pumped as it reacts. As the surface is covered, the pumping speed of the crystal decreases and the pressure rises. The dissociative sticking coefficient (DSC) is related to the drop in pressure after the beam strikes the crystal.

one percent precision. Supersonic molecular beams have been used to study a variety of reactive systems, but the remainder of this section will focus on their use in probing alkane reactivity on metal surfaces.

Varying the nozzle temperature, backing pressure, and composition of diluent gases of the supersonic molecular beam yields different translational energies; when coupled to surface temperature dependence, it is possible to elucidate the reactivity of alkanes on metal surfaces with regards to most degrees of freedom other than rotations. Many studies have been performed in which DSCs were measured as a function of beam translational energies. DSC studies for light alkanes on metal surfaces using supersonic molecular beams have been conducted on platinum,[27-35] nickel,[33-45] iridium,[46-50] and many others. A complication can be that when tuning the beam translational energy, by varying the nozzle temperature, the rotational and vibrational energy content of the molecule is also varied. In general, it has been found that light alkanes follow activated pathways for dissociation, though there are exceptions. For instance, alkanes reacting on Ir(110) at low translational energies, follow an unactivated mechanism, such that there is no barrier to reaction that rises above the energy of the separated reagents. Using supersonic molecular beams, Luntz and Bethune found that the DSC for methane on Pt(111) obeys normal energy scaling,[27]

$$S(E) = S(E_n) \qquad \text{Equation 1.2}$$

where,

$$E_n = E_t \cos^2 \vartheta \qquad \text{Equation 1.3}$$

where E_n is the translation energy normal to the surface, E_t is the total translational energy, and ϑ is the angle from surface normal. $S(E_n)$ typically increases roughly exponentially with E_n. By

varying the incident beam angle, Weaver et al. revealed that C_2H_6, C_3H_8, n-C_4H_{10}, i-C_4H_{10}, and neopentane also obey normal energy scaling on Pt(111).[32]

Since translational energy, and in particular normal translational energy, plays such a prominent role in dissociation, it is a question as to how vibrational energy affects reactivity. The next challenge then, has been to understand what role vibrational energy plays in the dissociation of alkanes. Early work by Luntz and Bethune on CH_4 on Pt(111) compared $S(E_n)$ measured at two different nozzle temperatures (T_N = 300 K and 680 K), where E_t was varied by changing the seed gas mixture alone. They concluded that vibrational energy promoted reactivity with about the same efficiency as normal translational energy.[27]

The vibrational state-resolved energy dependence of DSCs can be probed by coupling laser pumping with supersonic beams. All of the catalytic work has been performed for CH_4 and its deuterated derivatives, however, state dilution and IVR with laser pumping would likely make this technique impractical for larger alkanes. Vibrational state-resolved DSCs have been measured for methane on nickel[33-35,38-45] and platinum[33-35] surfaces. By pumping different vibrational modes and then measuring the change in DSCs, it is possible to understand how vibration affects reactivity. By comparing the difference in the energy required to achieve a certain DSC from vibration and translation, an efficacy for vibrational energy to promote dissociation relative to normal translational energy can be established. For example, if an additional 40 kJ of translational energy or 50 kJ of vibrational energy is required in order to achieve a certain DSC from a given experimental set of conditions, then vibration is only 80% as efficacious as translation and so has a vibrational efficacy equal to 0.8, denoted $\eta_{vib} = 0.8$. Studies have shown that different vibrational modes have different vibrational efficacies. These quantum state-resolved experiments mainly were conducted with molecules no larger than CH_4.

This is because of spectral dilution of oscillator strength across an increasing number of vibrational states, coupled to the diminishment of the thermal population in any particular mode, as well as the onset of intramolecular vibrational redistribution (IVR) in larger molecules. Conversely, IVR does not occur for small molecules with stiff vibrational modes, like methane, because the rovibrational density of states is sufficiently low (<< 10 states/cm^{-1}) and so there is no mixing between vibrational modes.[51]

1.6.3 Effusive Molecular Beams

Like supersonic molecular beams, effusive molecular beams emit a directed flux of gas molecules. However, there are significant differences between the two. Effusive beams operate on the principles of molecular flow in which molecule-wall collisions occur much more frequently then molecule-molecule collisions. Gas at low pressure, in molecular flow, is introduced into the cavity behind a beam orifice, and allowed to effuse into the vacuum chamber. There is no supersonic expansion for the effusive molecular beam, which leads to a well characterized beam where the vibrational, rotational, and translational temperatures of the molecule are equal to the nozzle temperature, ($T_v = T_r = T_t = T_g$). In addition, effusive molecular beams, with a sufficiently thin orifice wall, emit a cosine angular flux distribution that helps facilitate angle-resolved measurements of thermal gas reactivity. The projection of flux onto a two-dimensional plane from a random gas distribution in three-dimensional space results in a cosine angular dependence. If the orifice is not sufficiently thin, then gas-surface collisions on the edge of the orifice will direct the gas flow down the center of the beam, and the doser will deviate substantially from pure cosine behavior.

Although effusive beams are not a new technology and have widespread use, such beams have not been used to measure DSCs outside of UVA. Our group has measured and published DSCs for CH_4, C_2H_6, and C_3H_8 on Pt(111) using this technique.[13,52-58] Non-equilibrium, $S_n(T_g = T_s)$, equilibrium, $S_n(T_g = T_s = T)$, and angle-resolved, $S(\vartheta; T)$ DSCs have all been measured.

1.7 Theoretical Analysis

1.7.1 One-dimensional Tunneling of Hydrogen in C-H Bond Cleavage

A hydrogen tunneling model for methane dissociative chemisorption was first introduced by H. F. Winters.[14] He studied CH_4, CH_3D, CH_2D_2,CHD_3, and CD_4 dissociation on tungsten and found that the decrease in reactivity from CH_4 to CD_4 could be rationalized using this model which assumed that the reaction rate was based solely on a hydrogen atom tunneling through the reaction barrier for C-H bond scission. Rettner et al. also proposed a tunneling model which has different barrier heights than the model of Winters.[59] Lee and co-workers studied CH_4 and CD_4 on Ni(111) and hypothesized that the barrier for dissociation followed a mechanism in which the impinging methane must distort in order to bring the carbon atom close enough to react with the surface, in addition to tunneling.[36,37] Their argument was that tunneling alone cannot explain the reactivity increase with vibrational energy. A more complete analysis of CH_4 and CD_4 on Pt(111) was conducted by Luntz and Bethune in which the authors varied E_n, E_v, and T_s.[27] The authors found that the tunneling models cannot explain the translational and vibrational activation nor T_s dependence. In addition, the distortion model of Lee cannot explain the T_s dependence of the DSC.

Luntz summarized several key facts. Dissociative chemisorption is enhanced by normal translational energy but not motion parallel to the surface. Dissociation is also enhanced by vibrational degrees of freedom, however, it is not as efficacious as normal translational energy. In addition, dissociation is strongly affected by surface energy in the form of collective surface vibrations known as phonons. Lastly, none of the aforementioned models can simultaneously handle E_n, E_v, and T_s dependence of the DSCs.

1.7.2 Thermally Assisted Tunneling (TAT) Model

Harris et al. developed a variation of the one-dimensional tunneling model which included a surface temperature dependence.[60] In this model, the tunneling barrier is coupled to the surface thermal motion and tunneling occurs on initial impact. Although the general trend of T_s and E_t are properly reproduced, the model is far from quantitatively accurate. In fact, it appears that the authors' predictions for most of the dissociative sticking coefficients are orders of magnitude different than the experimental values.

1.7.3 Statistical and Microcanonical Modeling

Ukraintsev and Harrison developed a statistical model incorporating Rice-Ramsperger-Kassel-Marcus (RRKM) rate constants to model their methane associative desorption; the model was demonstrated to be clearly superior to the thermally assisted tunneling model.[61] Shortly thereafter, Newell and co-workers studied CH_4 and C_2H_6 on Pt(111) using supersonic beams and found a great enhancement of DSCs with increasing vibrational energy.[29] They modeled their results based on the assumption that molecules required a minimum vibrational energy content to successfully react. Valden et al. studied CH_4 on Pt(111) and Pd(110) using supersonic beams

and fit the results using both a one-dimensional tunneling model as well as the statistical model of Harrison and achieved good results with both models.[30] The statistical physisorbed complex (PC) microcanonical unimolecular rate theory (MURT), or PC-MURT, model was enhanced by adding a gas-surface energy transfer parameter that accounts for energy transfer between the impinging molecule and the surface.[62] The model which handles energy transfer is referred to the master equation (ME) or ME-MURT. The MURT models have had success in modeling many systems such as CH_4/Pt(111),[52,54,55] CH_4/Ir(111),[63] C_2H_6/Pt(111),[53-55] C_3H_8/Pt(111),[54,55] and CH_4/Ru(0001).[64] However, in the case of quantum state-resolved DSC measurements, the PC-MURT does not achieve the desired quantitative agreement with experiment.[65,66] Because the PC-MURT is a statistical model, and quantum resolved experiments show that methane activation is not statistical at the level of individual quantum states, the PC-MURT fails to quantitatively reproduce quantum state-resolved experiments. In order to account for this discrepancy, Donald and Harrison added a vibrational efficacy parameter to the PC-MURT model to account for dynamical biases away from statistical behavior in a state averaged manner; the model is called the dynamically biased, (d-), precursor mediated microcanonical trapping (PMMT) model.[67] The vibrational efficacy parameter, η_v, is a mean value typically derived from averaging over the thermally populated vibrational modes relevant to an experiment's reactivity. This d-PMMT model, with transition state vibrational frequencies provided by density functional theory (DFT) calculations and tunneling reaction pathways included, has successfully handled such systems as CH_4/Pt(111),[56,57,67] C_2H_6/Pt(111),[58] and H_2/Cu(111).[68]

References

(1) Wei, J. M.; Iglesia, E. Structural and Mechanistic Requirements for Methane Activation and Chemical Conversion on Supported Iridium Clusters. *Angew. Chem.* **2004**, *43*, 3685.

(2) Ertl, G. Reactions at Surfaces: From Atoms to Complexity (Nobel Lecture). *Angew. Chem. Int. Ed.* **2008**, *47*, 3524.

(3) Ertl, G. Primary Steps in Catalytic Synthesis of Ammonia. *J. Vac. Sci. Technol., A* **1983**, *1*, 1247.

(4) Ertl, G.; Weiss, M.; Lee, S. B. Reprint of: The Role of Potassium in the Catalytic Synthesis of Ammonia. *Chem. Phys. Lett.* **2013**, *589*, 18.

(5) Stiegel, G. J.; Ramezan, M. Hydrogen from Coal Gasification: An Economical Pathway to a Sustainable Energy Future. *Int. J. Coal. Geol.* **2006**, *65*, 173.

(6) Speight, J. G. *Chemistry and Technology of Petroleum (3rd Edition)*; CRC Press: New York, NY, USA, 1999.

(7) Rase, H. F. *Handbook of Commercial Catalysts : Heterogeneous Catalysts*; CRC Press: Boca Raton :, 2000.

(8) Ozkan, U. *Design of Heterogeneous Catalysts New Approaches Based on Synthesis, Characterization and Modeling*; Wiley-VCH, 2009; Vol. Weinheim :.

(9) Lloyd, L. *Handbook of Industrial Catalysts*; Springer: New York, 2007; Vol. New York.

(10) Rahimpour, M. R.; Jafari, M.; Iranshahi, D. Progress in Catalytic Naphtha Reforming Process: A Review. *Appl. Energ.* **2013**, *109*, 79.

(11) Speight, J. G. *The Chemistry and Technology of Petroleum*; 4th ed. ed.; CRC Press/Taylor & Francis: Boca Raton :, 2007.

(12) Kidney, A. J.; Parrish, W. R. In *Fundamentals of Natural Gas Processing*; CRC Press: 2006.

(13) Cushing, G. W.; Navin, J. K.; Valadez, L.; Johanek, V.; Harrison, I. An Effusive Molecular Beam Technique for Studies of Polyatomic Gas-Surface Reactivity and Energy Transfer. *Rev. Sci. Instrum.* **2011**, *82*, 11.

(14) Winters, H. F. The Activated, Dissociative Chemisorption of Methane on Tungsten. *J. Chem. Phys.* **1975**, *62*, 2454.

(15) Winters, H. F. The Kinetic Isotope Effect in the Dissociative Chemisorption of Methane. *J. Chem. Phys.* **1976**, *64*, 3495.

(16) Brass, S. G.; Reed, D. A.; Ehrlich, G. Vibrational Excitation and Surface Reactivity: An Examination of n_3 and $2n_3$ Modes of CH_4. *J. Chem. Phys.* **1979**, *70*, 5244.

(17) Yates, J. T.; Zinck, J. J.; Sheard, S.; Weinberg, W. H. Search for Vibrational Activation in the Chemisorption of Methane. *J. Chem. Phys.* **1979**, *70*, 2266.

(18) Brass, S. G.; Ehrlich, G. Internal Molecular Motions and Activated Chemisorption: CH_4 on Rhodium. *J. Chem. Phys.* **1987**, *87*, 4285.

(19) Weinberg, W. H.; Sun, Y.-K. Quantification of Primary Versus Secondary C-H Bond Cleavage in Alkane Activation: Propane on Pt. *Science* **1991**, *253*, 542.

(20) Beebe, T. P.; Goodman, D. W.; Kay, B. D.; Yates, J. T. Kinetics of the Activated Dissociative Adsorption of Methane on the Low Index Planes of Nickel Single Crystal Surfaces. *J. Chem. Phys.* **1987**, *87*, 2305.

(21) Sault, A. G.; Goodman, D. W. Dissociative Adsorption of Alkanes on Ni(100): Comparison with Molecular Beam Results. *J. Chem. Phys.* **1988**, *88*, 7232.

(22) Luntz, A. C.; Winters, H. F. Dissociation of Methane and Ethane on Pt(110): Evidence for a Direct Mechanism Under Thermal Conditions. *J. Chem. Phys.* **1994**, *101*, 10980.

(23) Seets, D. C.; Reeves, C. T.; Ferguson, B. A.; Wheeler, M. C.; Mullins, C. B. Dissociative Chemisorption of Methane on Ir(111): Evidence for Direct and Trapping-Mediated Mechanisms. *J. Chem. Phys.* **1997**, *107*, 10229.

(24) Nielsen, B. O.; Luntz, A. C.; Holmblad, P. M.; Chorkendorff, I. Activated Dissociative Chemisorption of Methane on Ni(100): A Direct Mechanism Under Thermal Conditions? *Catal. Lett.* **1995**, *32*, 15.

(25) Larsen, J. H.; Chorkendorff, I. From Fundamental Studies of Reactivity on Single Crystals to the Design of Catalysts. *Surf. Sci. Rep.* **1999**, *35*, 165.

(26) King, D. A.; Wells, M. G. Reaction Mechanism in Chemisorption Kinetics: Nitrogen on the {100} Plane of Tungsten. *Proc. R. Soc. London Ser. A-Math. Phys. Eng. Sci.* **1974**, *339*, 245.

(27) Luntz, A. C.; Bethune, D. S. Activation of Methane Dissociation on a Pt(111) Surface. *J. Chem. Phys.* **1989**, *90*, 1274.

(28) Schoofs, G. R.; Arumainayagam, C. R.; Mcmaster, M. C.; Madix, R. J. Dissociative Chemisorption of Methane on Pt(111). *Surf. Sci.* **1989**, *215*, 1.

(29) Newell, H. E.; Oakes, D. J.; Rutten, F. J. M.; McCoustra, M. R. S.; Chesters, M. A. Impact-Induced Dissociation of Methane and Ethane on Pt(111) and $Pt_{0.25}Rh_{0.75}$(111). *Faraday Discuss.* **1996**, *105*, 193.

(30) Valden, M.; Pere, J.; Hirsimaki, M.; Suhonen, S.; Pessa, M. Activated Adsorption of Methane on Clean and Oxygen-Modified Pt{111} and Pd{110}. *Surf. Sci.* **1997**, *377*, 605.

(31) Higgins, J.; Conjusteau, A.; Scoles, G.; Bernasek, S. L. State Selective Vibrational ($2n_3$) Activation of the Chemisorption of Methane on Pt (111). *J. Chem. Phys.* **2001**, *114*, 5277.

(32) Weaver, J. F.; Krzyzowski, M. A.; Madix, R. J. Direct Dissociative Chemisorption of Alkanes on Pt(111): Influence of Molecular Complexity. *J. Chem. Phys.* **2000**, *112*, 396.

(33) Bisson, R.; Sacchi, M.; Dang, T. T.; Yoder, B.; Maroni, P.; Beck, R. D. State-Resolved Reactivity of $CH_4(2\nu_3)$ on Pt(111) and Ni(111): Effects of Barrier Height and Transition State Location. *J. Phys. Chem. A* **2007**, *111*, 12679.

(34) Juurlink, L. B. F.; Killelea, D. R.; Utz, A. L. State-Resolved Probes of Methane Dissociation Dynamics. *Prog. Surf. Sci.* **2009**, *84*, 69.

(35) Utz, A. L. Mode Selective Chemistry at Surfaces. *Curr. Opin. Solid State Mater. Sci.* **2009**, *13*, 4.

(36) Lee, M. B.; Yang, Q. Y.; Tang, S. L.; Ceyer, S. T. Activated Dissociative Chemisorption of CH_4 on Ni(111): Observation of a Methyl Radical and Implication for the Pressure Gap in Catalysis. *J. Chem. Phys.* **1986**, *85*, 1693.

(37) Lee, M. B.; Yang, Q. Y.; Ceyer, S. T. Dynamics of the Activated Dissociative Chemisorption of CH_4 and Implication for the Pressure Gap in Catalysis: A Molecular Beam-High Resolution Electron Energy Loss Study. *J. Chem. Phys.* **1987**, *87*, 2724.

(38) Beck, R. D.; Maroni, P.; Papageorgopoulos, D. C.; Dang, T. T.; Schmid, M. P.; Rizzo, T. R. Vibrational Mode-Specific Reaction of Methane on a Nickel Surface. *Science* **2003**, *302*, 98.

(39) Juurlink, L. B. F.; McCabe, P. R.; Smith, R. R.; DiCologero, C. L.; Utz, A. L. Eigenstate-Resolved Studies of Gas-Surface Reactivity: CH_4 (n_3)Dissociation on Ni(100). *Phys. Rev. Lett.* **1999**, *83*, 868.

(40) Juurlink, L. B. F.; Smith, R. R.; Killelea, D. R.; Utz, A. L. Comparative Study of C-H Stretch and Bend Vibrations in Methane Activation on Ni(100) and Ni(111). *Phys. Rev. Lett.* **2005**, *94*, 4.

(41) Killelea, D. R.; Campbell, V. L.; Shuman, N. S.; Smith, R. R.; Utz, A. L. Surface Temperature Dependence of Methane Activation on Ni(111). *J. Phys. Chem. C* **2009**, *113*, 20618.

(42) Killelea, D. R.; Campbell, V. L.; Shuman, N. S.; Utz, A. L. Bond-Selective Control of a Heterogeneously Catalyzed Reaction. *Science* **2008**, *319*, 790.

(43) Maroni, P.; Papageorgopoulos, D. C.; Sacchi, M.; Dang, T. T.; Beck, R. D.; Rizzo, T. R. State-Resolved Gas-Surface Reactivity of Methane in the Symmetric C-H Stretch Vibration on Ni(100). *Phys. Rev. Lett.* **2005**, *94*, 4.

(44) Schmid, M. P.; Maroni, P.; Beck, R. D.; Rizzo, T. R. Surface Reactivity of Highly Vibrationally Excited Molecules Prepared by Pulsed Laser Excitation: CH_4 ($2\nu_3$) on Ni(100). *J. Chem. Phys.* **2002**, *117*, 8603.

(45) Smith, R. R.; Killelea, D. R.; DelSesto, D. F.; Utz, A. L. Preference for Vibrational over Translational Energy in a Gas-Surface Reaction. *Science* **2004**, *304*, 992.

(46) Kelly, D.; Weinberg, W. H. Trapping-Mediated Dissociative Chemisorption of C_3H_8 and C_3D_8 on Ir(110). *J. Chem. Phys.* **1996**, *105*, 271.

(47) Kelly, D.; Weinberg, W. H. Trapping-Mediated Dissociative Chemisorption of Propane on Ir(110). *J. Vac. Sci. Technol., A* **1996**, *14*, 1588.

(48) Kelly, D.; Weinberg, W. H. Direct Dissociative Chemisorption of Methane, Ethane, Propane, and Cyclopropane on Ir(110). *J. Vac. Sci. Technol., A* **1997**, *15*, 1663.

(49) Seets, D. C.; Wheeler, M. C.; Mullins, C. B. Trapping-Mediated and Direct Dissociative Chemisorption of Methane on Ir(110): A Comparison of Molecular Beam and Bulb Experiments. *J. Chem. Phys.* **1997**, *107*, 3986.

(50) Hamza, A. V.; Steinruck, H. P.; Madix, R. J. The Dynamics of the Dissociative Adsorption of Alkanes on Ir(110). *J. Chem. Phys.* **1987**, *86*, 6506.

(51) Stewart, G. M.; McDonald, J. D. Intramolecular Vibrational Relaxation from C–H Stretch Fundamentals. *J. Chem. Phys.* **1983**, *78*, 3907.

(52) DeWitt, K. M.; Valadez, L.; Abbott, H. L.; Kolasinski, K. W.; Harrison, I. Using Effusive Molecular Beams and Microcanonical Unimolecular Rate Theory to Characterize CH_4 Dissociation on Pt(111). *J. Phys. Chem. B* **2006**, *110*, 6705.

(53) DeWitt, K. M.; Valadez, L.; Abbott, H. L.; Kolasinski, K. W.; Harrison, I. Effusive Molecular Beam Study of C_2H_6 Dissociation on Pt(111). *J. Phys. Chem. B* **2006**, *110*, 6714.

(54) Cushing, G. W.; Navin, J. K.; Donald, S. B.; Valadez, L.; Johanek, V.; Harrison, I. C-H Bond Activation of Light Alkanes on Pt(111): Dissociative Sticking Coefficients, Evans-Polanyi Relation, and Gas-Surface Energy Transfer. *J. Phys. Chem. C* **2010**, *114*, 17222.

(55) Cushing, G. W.; Navin, J. K.; Donald, S. B.; Valadez, L.; Johánek, V.; Harrison, I. Addition/Correction to: C-H Bond Activation of Light Alkanes on Pt(111): Dissociative Sticking Coefficients, Evans-Polanyi Relation, and Gas-Surface Energy Transfer (vol 114, pg 17222, 2010). *J. Phys. Chem. C* **2010**, *114*, 22790.

(56) Navin, J. K.; Donald, S. B.; Tinney, D. G.; Cushing, G. W.; Harrison, I. Communication: Angle-Resolved Thermal Dissociative Sticking of CH_4 on Pt(111): Further Indication that Rotation is a Spectator to the Gas-Surface Reaction Dynamics. *J. Chem. Phys.* **2012**, *136*, 4.

(57) Donald, S. B.; Navin, J. K.; Harrison, I. Methane Dissociative Chemisorption and Detailed Balance on Pt(111): Dynamical Constraints and the Modest Influence of Tunneling. *J. Chem. Phys.* **2013**, *139*.

(58) Navin, J. K.; Donald, S. B.; Harrison, I. Angle-Resolved Thermal Dissociative Sticking of Light Alkanes on Pt(111): Transitioning from Dynamical to Statistical Behavior. *J. Phys. Chem. C* **2014**, *Currently under review*.

(59) Rettner, C. T.; Pfnur, H. E.; Auerbach, D. J. Dissociative Chemisorption of CH_4 on W(110): Dramatic Activation by Initial Kinetic Energy. *Phys. Rev. Lett.* **1985**, *54*, 2716.

(60) Harris, J.; Simon, J.; Luntz, A. C.; Mullins, C. B.; Rettner, C. T. Thermally Assisted Tunneling: CH_4 Dissociation on Pt(111). *Phys. Rev. Lett.* **1991**, *67*, 652.

(61) Ukraintsev, V. A.; Harrison, I. A Statistical Model for Activated Dissociative Adsorption: Application to Methane Dissociation on Pt(111). *J. Chem. Phys.* **1994**, *101*, 1564.

(62) Bukoski, A.; Blumling, D.; Harrison, I. Microcanonical Unimolecular Rate Theory at Surfaces. I. Dissociative Chemisorption of Methane on Pt(111). *J. Chem. Phys.* **2003**, *118*, 843.

(63) Abbott, H. L.; Harrison, I. Dissociative Chemisorption and Energy Transfer for Methane on Ir(111). *J. Phys. Chem. B* **2005**, *109*, 10371.

(64) Abbott, H. L.; Harrison, I. Methane Dissociative Chemisorption on Ru(0001) and Comparison to Metal Nanocatalysts. *J. Catal.* **2008**, *254*, 27.

(65) Abbott, H. L.; Bukoski, A.; Kavulak, D. F.; Harrison, I. Dissociative Chemisorption of Methane on Ni(100): Threshold Energy from $CH_4(2\nu_3)$ Eigenstate-Resolved Sticking Measurements. *J. Chem. Phys.* **2003**, *119*, 6407.

(66) Abbott, H. L.; Bukoski, A.; Harrison, I. Microcanonical Unimolecular Rate Theory at Surfaces. II. Vibrational State Resolved Dissociative Chemisorption of Methane on Ni(100). *J. Chem. Phys.* **2004**, *121*, 3792.

(67) Donald, S. B.; Harrison, I. Dynamically Biased RRKM Model of Activated Gas-Surface Reactivity: Vibrational Efficacy and Rotation as a Spectator in the Dissociative Chemisorption of CH_4 on Pt(111). *PCCP* **2012**, *14*, 1784.

(68) Donald, S. B.; Harrison, I. Rice–Ramsperger–Kassel–Marcus Simulation of Hydrogen Dissociation on Cu(111): Addressing Dynamical Biases, Surface Temperature, and Tunneling. *J. Phys. Chem. C* **2013**, *118*, 320.

Section 2 - Experimental Setup

2.1 Chamber Design

2.1.1 Main Chamber

The ultra-high vacuum (UHV) chamber is constructed of electro-polished 316 stainless steel. It is pumped by a TMH-261 Pfeiffer turbo-molecular pump (TMP) with a nominal pumping speed of 210 L/s as well as a Physical Electronics ion pump with a nominal pumping speed of 210 L/s. In addition, a titanium sublimation pump (TSP) situated within the double-ended ion pump can also pump the chamber. Both the TMP and ion/TSP combination pumps are separated from the chamber by UHV valves from VAT. The chamber pressure is measured using a 370 Stabil-Ion, Bayard-Alpert gauge and controller from Granville-Phillips that are designed for vacuum metrology. The gauge and controller are factory calibrated to one another with a claimed accuracy for N_2 of $\pm$4%.[1] The full measureable pressure range of the gauge and controller is $2*10^{-11}$ Torr to $1*10^{-4}$ Torr. Higher pressures can also be measured using two model 615 capacitance manometers from MKS Instruments. Separately, the manometers can measure absolute pressures from 10^{-4} Torr to 1 Torr and from 10^{-1} Torr to 1000 Torr, giving a combined range of 10^{-4} Torr to 1000 Torr. The capacitance manometer accuracy for N_2 is $\pm$0.25% of measured value.[2] The base pressure of the UHV chamber is ~ $1*10^{-10}$ Torr.

Schematic representations of the chamber are shown in both Figure 2.1 and Figure 2.2. The chamber is equipped with a variety of analytic devices. For Auger electron spectroscopy, the chamber is outfitted with a PHI model 15-255 GAR double-pass cylindrical mirror analyzer with internal electron gun. In addition, the chamber is equipped with a 40-548 x-ray source (Physical Electronics) controlled by a 50-096 x-ray source control/supply (Physical Electronics) for use in x-ray photoelectron spectroscopy (XPS). For simple mass spectroscopic analysis of research gases and helium leak checking, the chamber is outfitted with a model RGA 200,

residual gas analyzer (RGA) from Stanford Research Systems that is capable of mass detection over a 1-200 amu range. For higher sensitivity mass spectrometry, the chamber is outfitted with a differentially pumped quadrupole mass spectrometer (QMS) from Extrel Mass Spectrometers that has a mass range of 1-500 amu. The Extrel QMS is generally used for temperature programmed desorption (TPD).

The crystal is placed at the end of a 4-axis manipulator built by McAllister Technical Services and is capable of movement along the x, y, and z axes as well as rotation around the z-axis perpendicular to the x-y plane parallel to the mounting port. Gaseous reagents enter the chamber through either a heated effusive molecular beam doser for directed gas experiments, through a calibrated leak for ambient gas dosing, or through a variable leak valve for gas analysis, O_2 cleaning, or dosing for temperature programmed desorption (TPD). The chamber is also outfitted with a 04-161 ion gun (Physical Electronics), controlled by a 32-165 ion gun power supply (RBD Instruments) used for argon ion sputtering. Additionally, an infrared heat lamp is installed on the chamber and is used to help facilitate outgassing and baking of the chamber.

A schematic side view of the chamber is shown in Figure 2.1 wherein the x-y plane of the chamber is parallel with the ground and the z-axis points up. The central axes of the crystal manipulator, heated effusive molecular beam doser, TMP, and QMS all lie within the same x-y plane. Three windows and the capacitance manometers lie in the same x-y plane but are offset by 45 degrees from the previously mentioned components. The TMP, RGA, 4.5" window, crystal manipulator, and ion pump all lie within the same y-z plane. The ion pump, ion gun, effusive beam doser, electron analyzer, x-ray source, QMS, and ion gauge all lie in the same x-z plane. The variable leak valve is situated at the top of the chamber near the x-ray source and crystal manipulator, and the heat lamp enters the lower half of the chamber directly beneath the crystal manipulator.

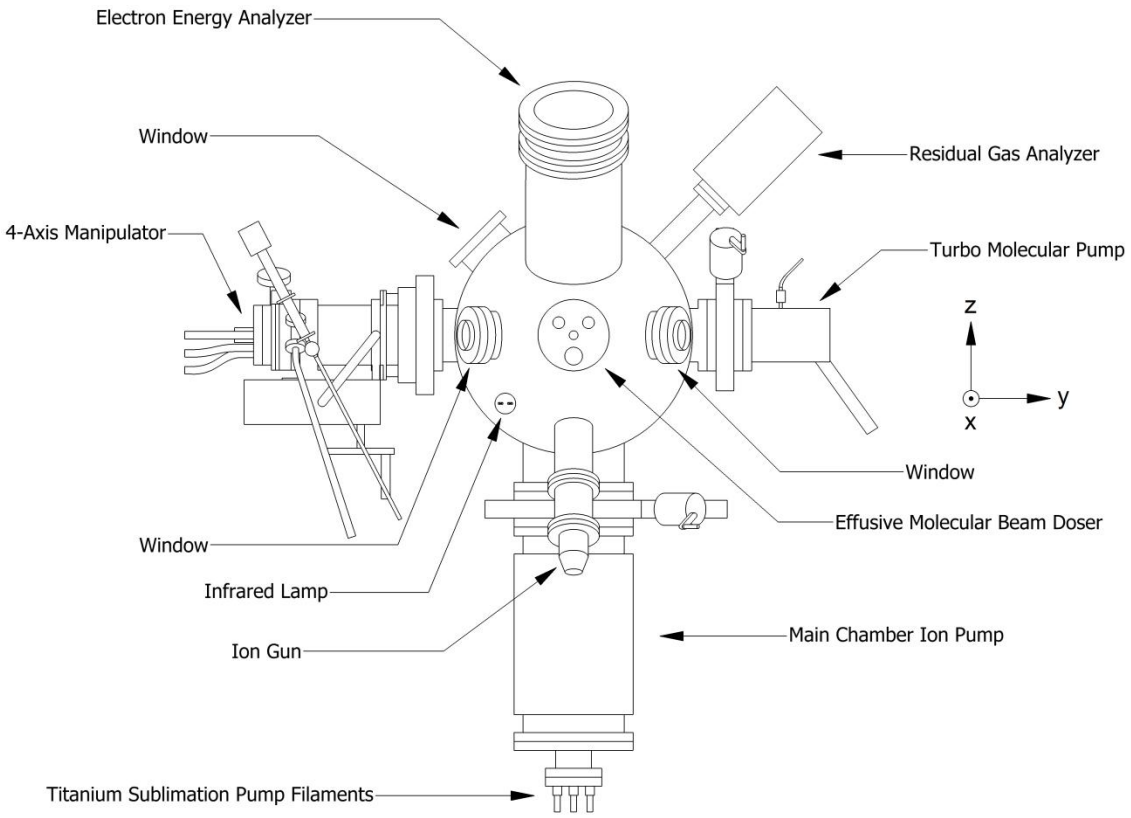

Figure 2.1: Schematic representation of UHV Chamber (Front).

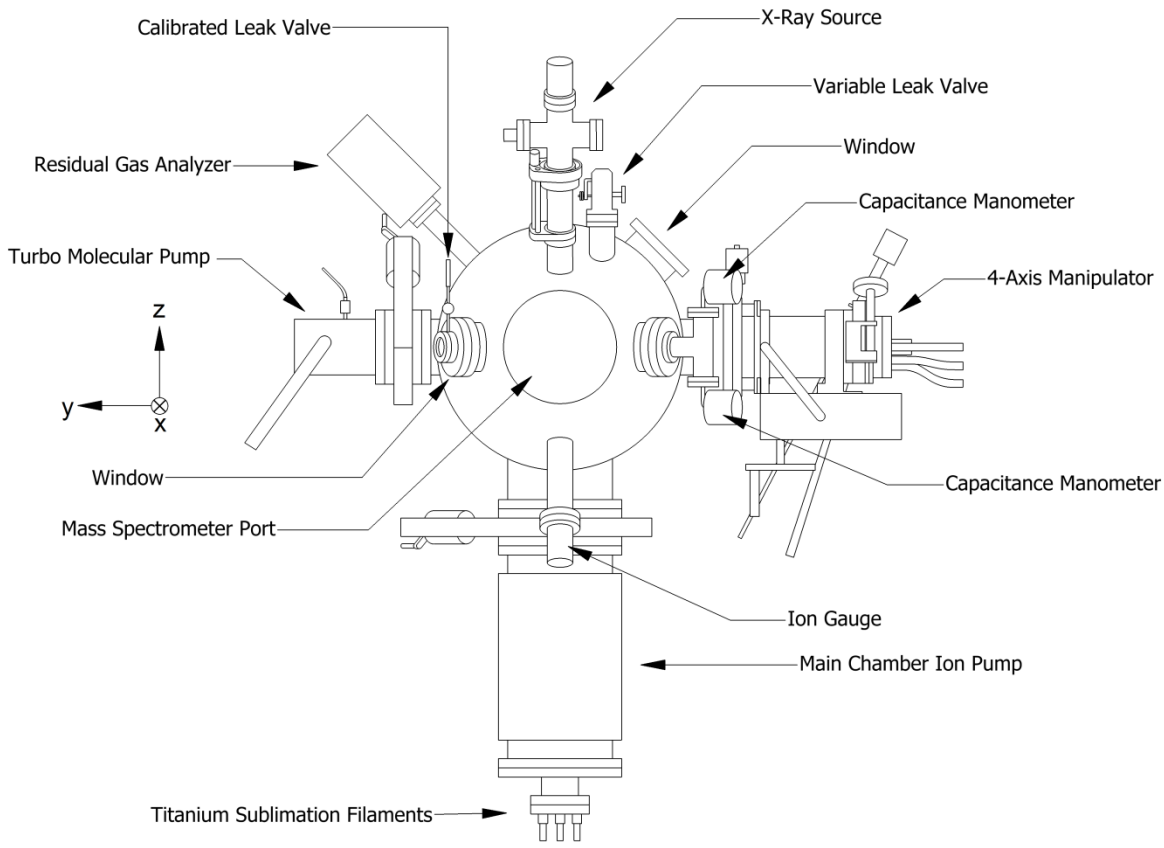

Figure 2.2: Schematic representation of UHV Chamber (Back).

2.1.2 Mass Spectrometer Chamber

A simplified schematic of the mass spectrometer chamber is shown in Figure 2.3. The mass spectrometer chamber is separated from the main chamber by two stainless steel cones with 1/8" diameter holes drilled in each section that limit throughput to 1 L/s per hole. The differentially pumped region between these two cones is pumped by a Physical Electronics ion pump situated directly above the chamber and has a nominal pumping speed of 20 L/s. The portion of the chamber that houses the mass spectrometer is pumped by a model 200L, Gamma Vacuum ion pump with a nominal pumping speed of 200 L/s. Overall, the partial pressure of the mass spectrometer region is approximately 4000 times less than the main chamber. As with the main chamber, the mass spectrometer chamber has TSP filaments located within the main ion pump. Additionally, the differential pumping region also has a port that enters in from the side and has electrical feedthroughs that connect to electrically floating aperture plates of the differential pumping walls and connect to the mass spectrometer ionizer controller. The floating aperture plates can be biased to help guide ions created external to the mass spectrometer (e.g., by laser photoionization) to the mass filter. The rear port is the mounting flange for the QMS and is outfitted with a 1.33" window that sights through the central axis of the spectrometer.

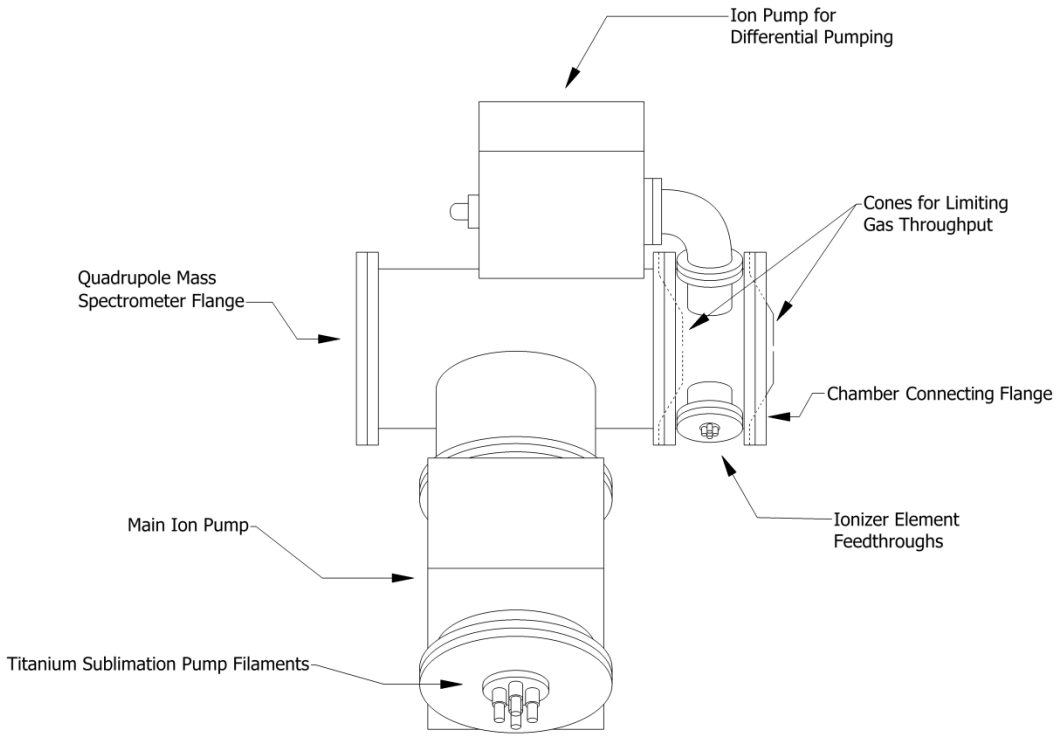

Figure 2.3: Schematic representation of mass spectrometry chamber (Topside).

2.2 Manipulator and Crystal Mount Design

2.2.1 Manipulator

The crystal is supported on a custom-built mount attached to a 4-axis manipulator capable of x, y, z, and angular rotation around the z-axis as depicted in Figure 2.4. The rotary flange is a McAllister Technical Services model DPRF 450. An Oxford Instruments Ultrastat, liquid He or N_2 flow, cryostat goes through the center of the outer most flange, which is outfitted with five electrical feedthroughs arranged in a half-moon shaped pattern around the central cryostat port. Two of the feedthroughs are used for heating the crystal, two are for monitoring the crystal temperature as well as monitoring temperatures along the mount, and the last is for monitoring the cryostat temperature. Temperatures are measured using Type K alumel/chromel thermocouples mounted on the backside of the crystal and along the central manipulator axis near the cryostat.

A twice differentially pumped, angular motion feedthrough (DPRF 450) allows for angular manipulation about the central z-axis. This rotation is achieved by turning a screw-drive handle mounted on the flange, which is meshed with a flange with gear teeth. Because traditional copper gaskets are immobile, the internal UHV chamber volume is separated from atmosphere by a series of three Viton o-rings. The two regions between the gaskets are differentially pumped to maintain UHV conditions in the main chamber. The outer region is pumped by a mechanical pump that also backs the main chamber TMP. The inner region is pumped by a Physical Electronics ion pump with a nominal pumping speed of 2 L/s. The DPRF 450 is connected to a bellows that rests on a block of aluminum. The block is connected to a gear drive, which meshes with the handle underneath the manipulator. This allows for the

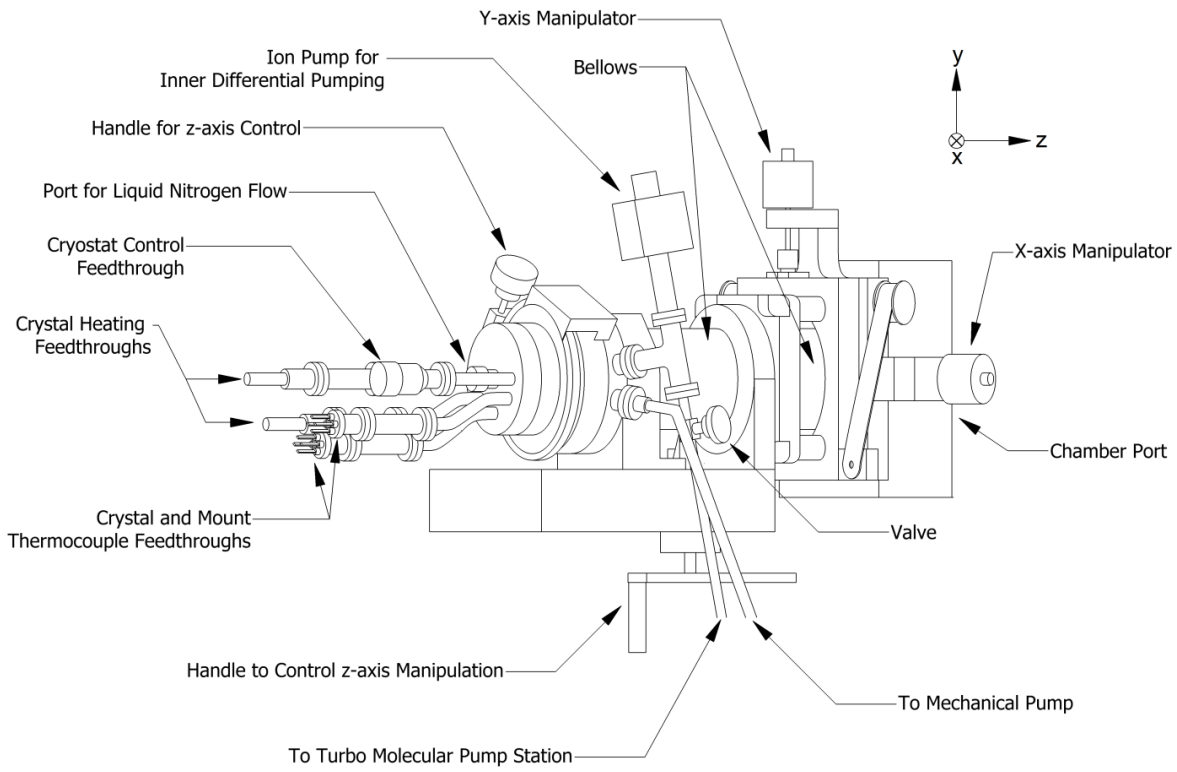

Figure 2.4: Schematic representation of 4-axis manipulator.

crystal to be moved in and out of the chamber along the z-axis. The bellows connects to another set of bellows and an x-y manipulator stage. The two sets of bellows allow flexibility when moving the crystal mount in the x, y, and z dimensions. One hand dial, situated directly above the manipulator z-axis, allows for y-axis manipulation. The second hand dial, situated 90 degrees away from the first hand dial, allows for x-axis manipulation. Lastly, there is a flange which is directly mounted to the UHV chamber.

2.2.2 Crystal Mount

The bulk of the crystal mount is constructed of oxygen-free, high conductivity copper (OFHC). Several other UHV compatible materials are also used in its construction. The mounted platinum single crystal was obtained from Surface Preparation Laboratory, Zaandam/Netherlands, with a base purity of 99.999% and was cut to within 0.1 degrees of the (111) facet. A schematic of the crystal mount is shown in Figure 2.5. The main block of copper is attached to the manipulator and cryostat via a large diameter copper rod at the base. There are four rectangular copper support structures situated at the four top corners of the main structure. These support structures are offset from the main structure via sapphire pieces and are held in place using four stainless steel screws that are isolated from the support structures by means of Macor washers from McAllister Technical Services.

Two tungsten rods run between each pair of copper support structures and run parallel to the manipulator z-axis. The rods are positioned in grooves on the crystal that were cut using stainless steel, diamond-coated cutting tools. The rods are spot welded to the crystal for both support and resistive heating. Voltage is supplied to the crystal through two copper rods that run from the manipulator to the support structure pairs. A stainless steel support structure is placed at the base of the main copper block which, holds the main thermocouple leads originating from the manipulator. Alumina sleeves are used to electrically isolate the thermocouple leads from

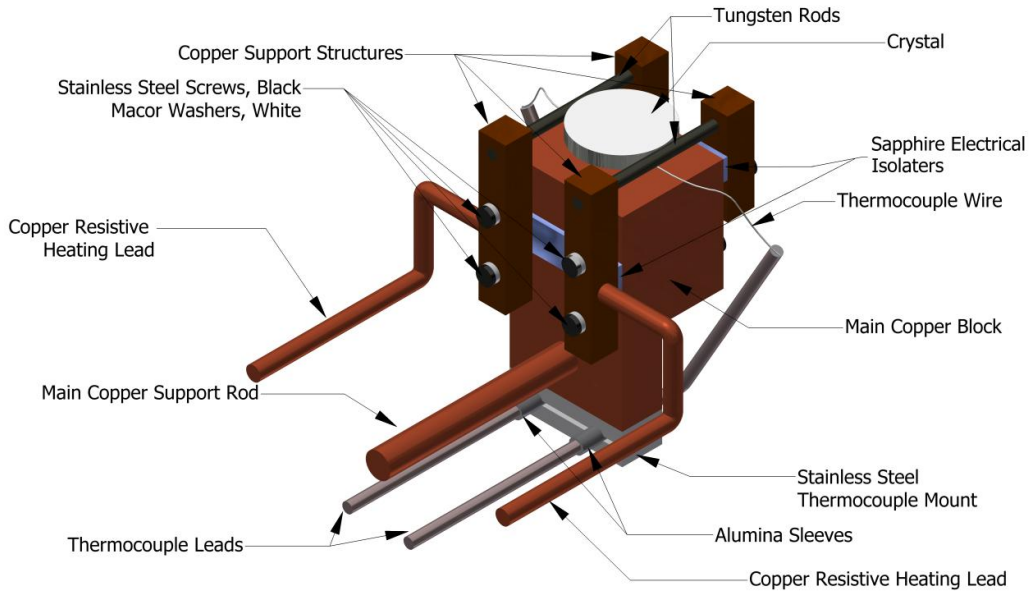

(a)

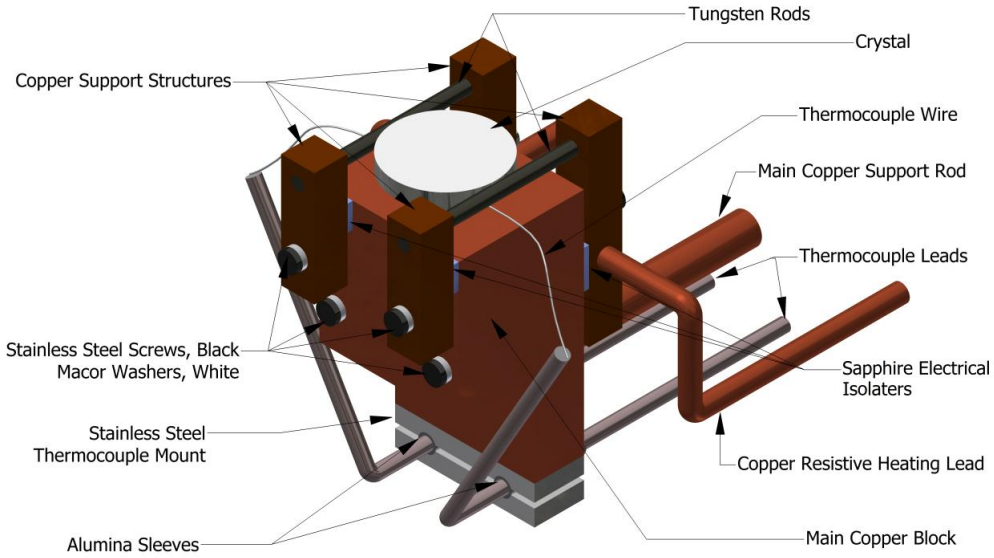

(b)

Figure 2.5: Schematic representation of crystal mount from the viewpoint of the manipulator (a), and the back of the mount (b).

the steel structure. The thermocouple leads run from under the mount and bend up and out to the sides; from here, one thin thermocouple wire is spot welded to each thermocouple lead and both wires are then spot-welded together on the underside of the crystal.

2.3 Crystal Temperature Control

The crystal heating is controlled by a 906S Eurotherm temperature controller, which receives power from a XFR 12-100 DC power supply from Xantrex. An Oxford Ultrastat system composed of the cryostat, cryogen transfer arm, and an Oxford ITC 503 temperature controller is used to maintain the temperature of the mount and the crystal. Using liquid nitrogen as a cooling agent, the crystal temperature can be varied from 100 K to 1200 K using this setup.

2.4 Effusive Molecular Beam Doser

The previous doser design incorporated an alumina paste that contained a binding agent (K_2SiO_3) used to hold the paste onto the doser. However, this doser design was found to emit potassium, via decomposition of the K_2SiO_3, and subsequently deposited potassium onto the crystal surface at gas temperatures of 900 K and above. Therefore, the entire design of the doser was revamped. In addition, the flange assembly and heating system was also reconfigured for increased performance. The UHV flange, which supports the effusive molecular beam doser, is custom-built by MDC and is shown schematically in Figure 2.6. The flange is 4.5" in diameter and is constructed of 304 stainless steel. There is a 0.250" in diameter, 304 stainless steel tube that runs down the central axis of the flange face. Both ends are outfitted with a 1/4" VCR gland and a male 1/4" VCR nut. Above the central tube lie two OFHC electrical feedthroughs for resistive filament heating. In addition, a 1.33" mini-conflat flange allows for the addition of a

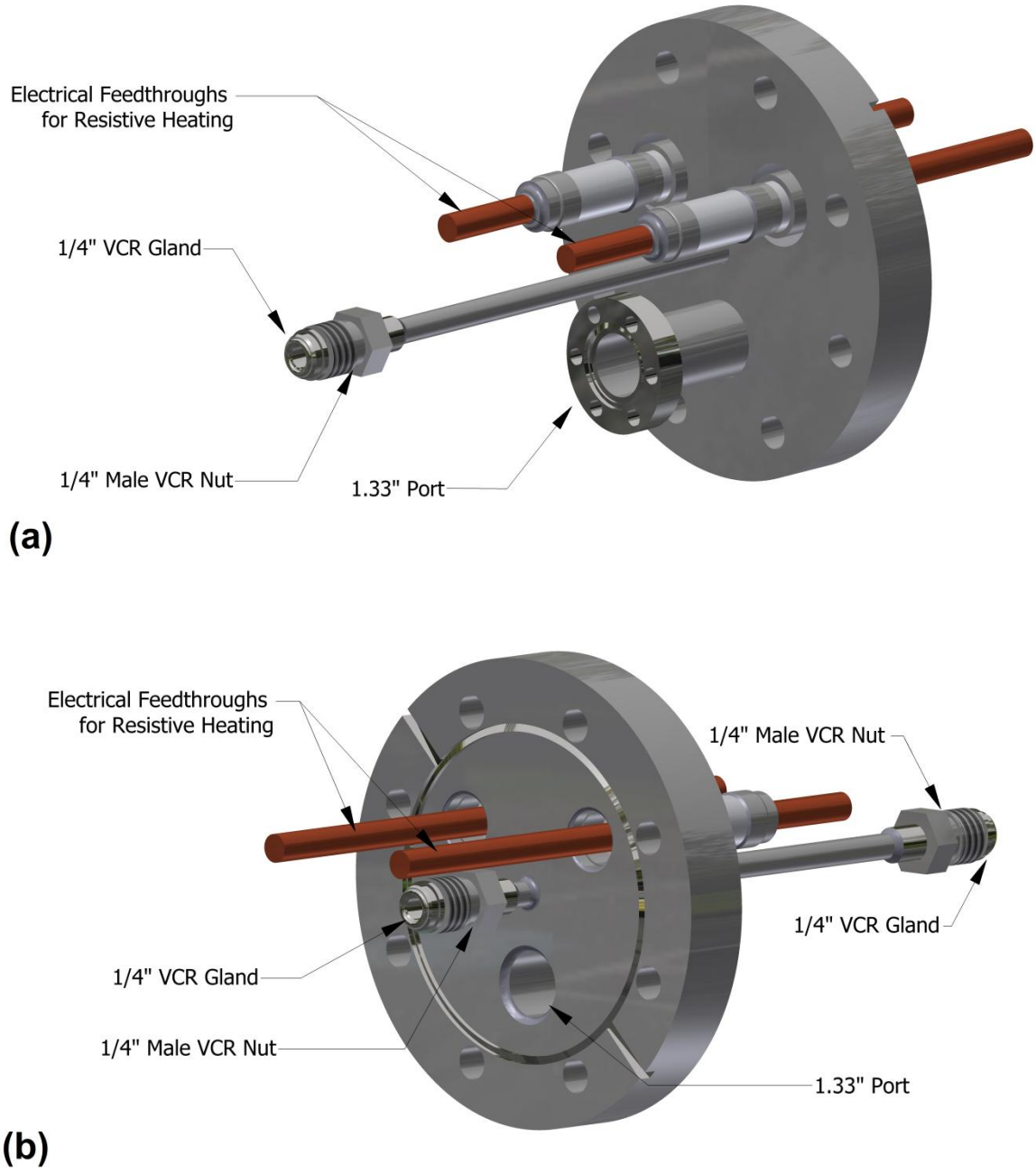

Figure 2.6: Schematic representation of effusive beam flange from the atmosphere side (a), and the UHV side (b).

thermocouple electrical feedthrough in order to monitor doser temperature.

The actual doser design has been updated entirely. It is composed of three layers in total: the stainless steel nozzle, an inner ceramic sleeve, and an outer ceramic sleeve. A schematic of the doser is shown in Figure 2.7. The central nozzle is composed of a 304 stainless steel tube with a nominal diameter of 0.250" and an overall length of 8". The welded nozzle tip terminates with a 0.250" diameter, 0.003" thick, stainless steel disk that has a 0.5 mm laser drilled hole through the center. The back of the nozzle terminates with a 1/4" VCR gland and a female 1/4" VCR nut. This nozzle is covered by two pieces of Aremcolox 502-1400 FF machined alumina from Aremco. The inner piece, which touches the stainless steel tube, is a threaded alumina tube with a nominal I.D. and O.D. of 0.26" and 0.50" respectively, and an overall length of 6.00". Approximately 5" of the tube is right-hand threaded with 1/2"-20 UNF-2A threads that allow the filament to be hidden from the front of the doser. The threaded grooves of the alumina tube are wrapped with 0.25 mm diameter tungsten wire (99.95% purity, Goodfellow) for resistive heating. The outer piece of alumina has a nominal I.D. and O.D. of 0.555" and 0.610" respectively, with a total length of 6.00". The purpose of this outer alumina piece is twofold; one is that it reradiates heat back to the doser, and two, it blocks the line of sight of the filament towards the metal sample surface. The doser is connected to the UHV flange via the 1/4" female VCR cap using a 316 stainless steel gasket. The tungsten wires are spot-welded to the OFHC electrical feedthroughs on the vacuum flange. Alumel/chromel thermocouples are spot welded to the front of the stainless steel nozzle and along the nozzle base for temperature measurement. The filament is heated using a TE10A power thyristor from Eurotherm, which is controlled by a 2416 Eurotherm temperature controller. This setup is capable of sending 120 VAC at 15 amperes to the filament and is capable of raising the temperature of the doser to 1000 K at 45% power.

Figure 2.7: Schematic representation of the effusive molecular beam nozzle. From top to bottom: nozzle, with inner alumina tube, with tungsten filament, with outer alumina tube.

Inset: Close-up view of doser front face.

After outgassing the newly designed doser at a gas temperature of 1100 K for several days, it was confirmed by Auger electron spectroscopy that this effusive molecular beam doser design was free of potassium and did not deposit any measurable quantity of potassium onto the crystal surface up to gas temperatures of 1100 K. In addition, the chamber pressure was ~1 $*10^{-10}$ Torr up to gas temperatures of 800 K and did not exceed 2.5 * 10^{-10} Torr at a gas temperature of 1000 K.

2.5 Manifold Design

Reagent gases are stored on the gas manifold that is connected to the chamber. A schematic representation of the manifold is shown in Figure 2.8. The entire manifold is attached to an aluminum mounting plate for support. A series of stainless steel gas cylinders are connected to the central tubing of the manifold, and each cylinder is separated from the manifold by two valves in series; this allows for better pressure control of the gases. The manifold is outfitted with two 275 Convectron, Pirani vacuum gauges (Granville-Phillips) and one 122B capacitance manometer (MKS Instruments) for pressure measurement during experiments and other procedures. The Convectrons can measure relative pressures from $1*10^{-4}$ Torr to 1000 Torr, because Pirani vacuum gauge measurements are gas dependent. The capacitance manometer can measure absolute pressures from $1*10^{-4}$ Torr to 1 Torr. The base of the manifold is connected to a TSU 065D pumping station (Pfeiffer) that is used to keep a high quality vacuum in the manifold. Although manifold pressures less than 10^{-4} Torr cannot be measured directly, by opening the manifold to the chamber and then measuring the pressure change in the chamber, it is possible to indirectly measure the manifold pressure. Using this method, the manifold base pressure was determined to be less than $1*10^{-7}$ Torr because the pressure

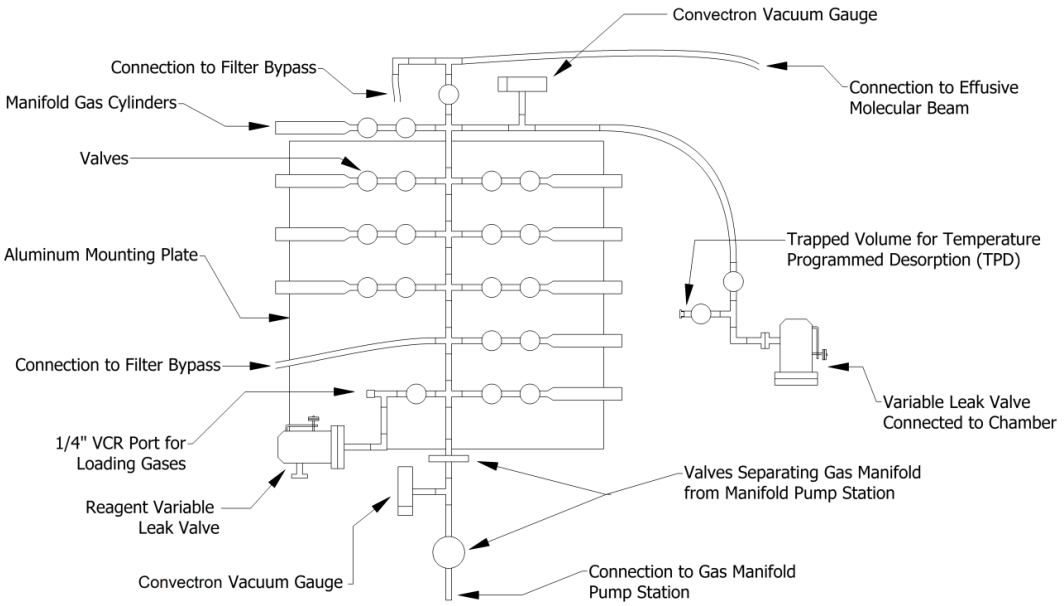

(a)

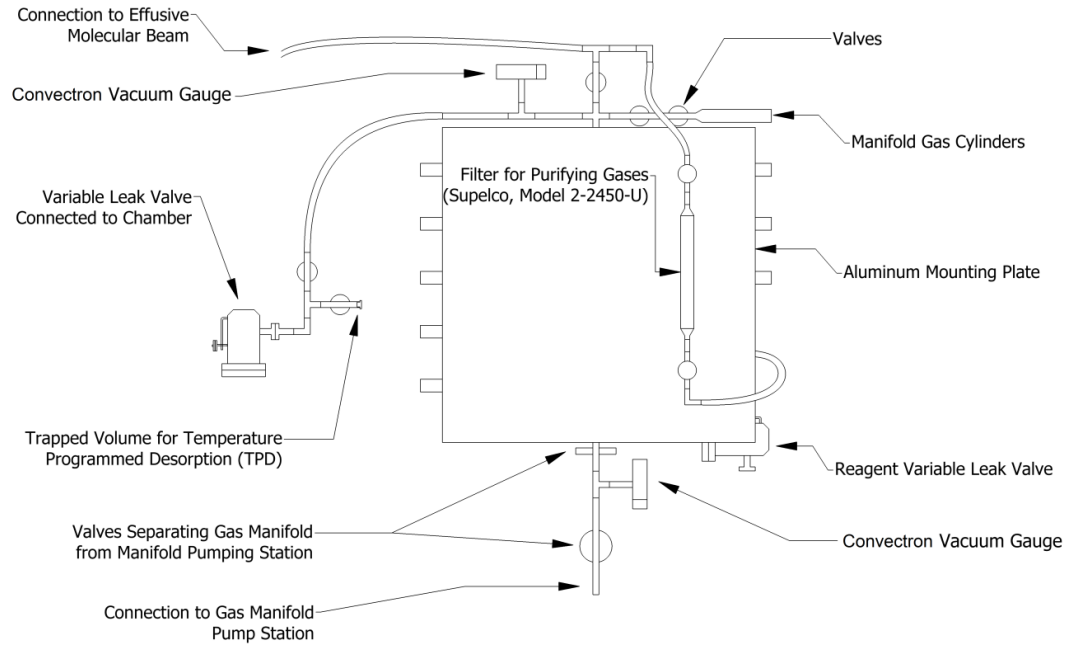

(b)

Figure 2.8: Schematic representation of gas manifold front (a) and back (b).

change in the chamber is less than $1*10^{-12}$ Torr. There are two valves situated at the base of the manifold that allow for isolation of the manifold from the pumping station. In addition, the manifold has two variable leak valves connected to it. One variable leak valve separates the manifold from the chamber and allows for the dosing of gas into the chamber; the other valve controls reagent gas flow from a gas cylinder into the manifold. A gas-filtering bypass was added to the manifold incorporating a 2-2450-U gas filter (Supelco), separated from the manifold by a series of valves, that allows for the purification of non-reactive gases such as methane, nitrogen, and argon and is shown in Figure 2.8(b). The filter is capable of removing O_2, H_2O, CO_2, CO, NH_3, alcohols, alkanes larger than CH_4, alkenes, amines, aromatics, diethylether, halogens, and sulfur compounds by means of a highly reactive mixture of powdered transition metal oxides of copper, nickel, manganese, cobalt, and aluminum.[3,4] Further modification of the gas manifold includes an additional bypass section. A schematic representation of the bypass is shown in Figure 2.9. This bypass is designed to limit the flux of gases from the doser into the chamber. The bypass reduces the total throughput into the chamber by a factor of 60.

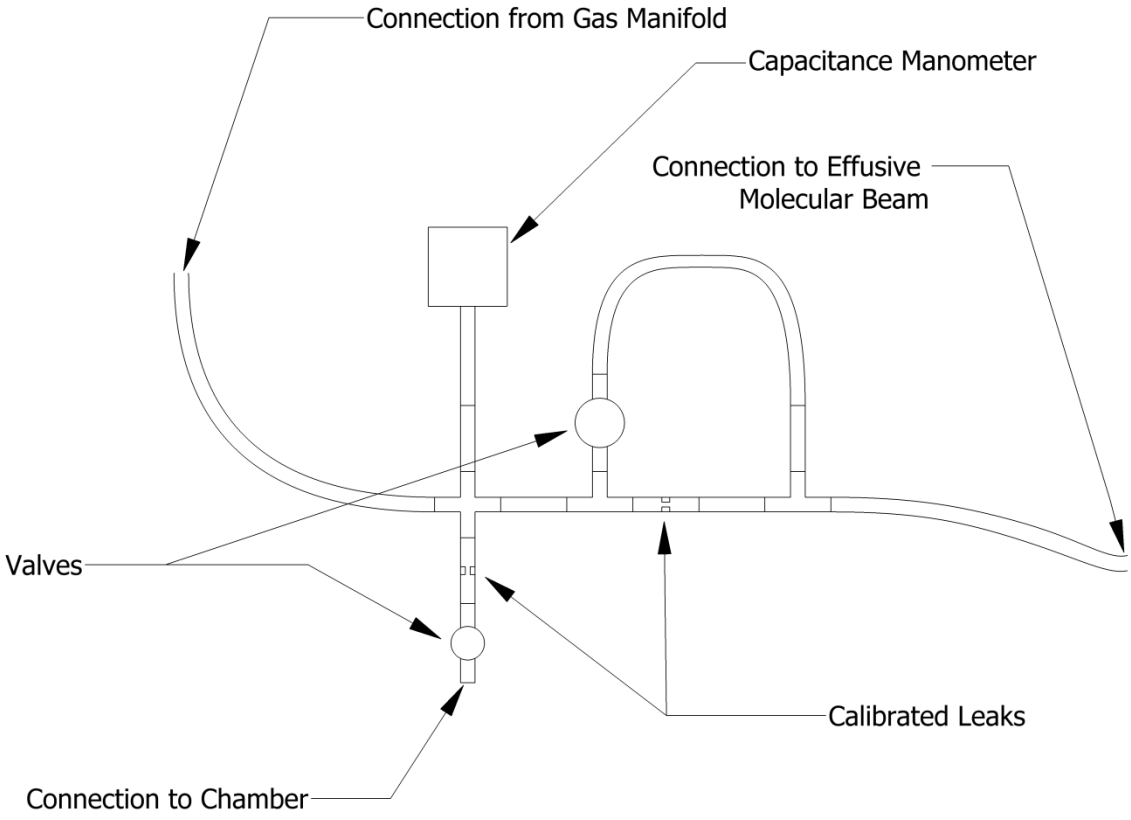

Figure 2.9: Schematic representation of gas manifold doser bypass.

2.6 Auger Electron Spectroscopy

When alkanes dissociate onto metal surfaces at temperatures above 400 K, the remaining hydrogen desorbs and only alkyl fragments and/or carbon remain. The total adsorbed carbon is proportional to the number of successfully reacting molecules, assuming negligible alkane recombinative desorption. This assumption is appropriate given the fact that hydrogen recombinative desorption is ultrafast at surface temperatures above 400 K which severely limits alkane recombinative desorption. In addition, for Pt(111), carbon does not diffuse into the bulk until ~1100 K at a bulk concentration of 0.9 atomic percent.[5] Auger electron spectroscopy (AES) allows us to measure the platinum and carbon composition of the surface and thus deduce the total number of molecules that have dissociated. The principle behind the Auger process is relatively straightforward and involves the interaction of an electron beam with the core electrons of an element. The Auger process is depicted in Figure 2.10. The Auger process is a three-body process involving electron ejection, relaxation, and a secondary ejection.

An electron with high kinetic energy (1500 eV to 4000 eV) collides with a core electron of an atom which, when ejected from the atom leaves a vacancy in the orbital. In order to maintain stability in the atom, an electron of higher energy relaxes in order to fill the vacancy. The energy from this exchange must be conserved and can be imparted to an electron of higher level, which is ejected from the atom. This second ejected electron is an Auger electron, the kinetic energy of which is directly proportional to the energy difference between the initial and final state of the relaxed electron minus the ionization energy of the ejected Auger electron. Because of this, the Auger electron is characteristic of the element, although there can be overlap of Auger electron energies of different elements if the energy gaps and ionization energies are similar.

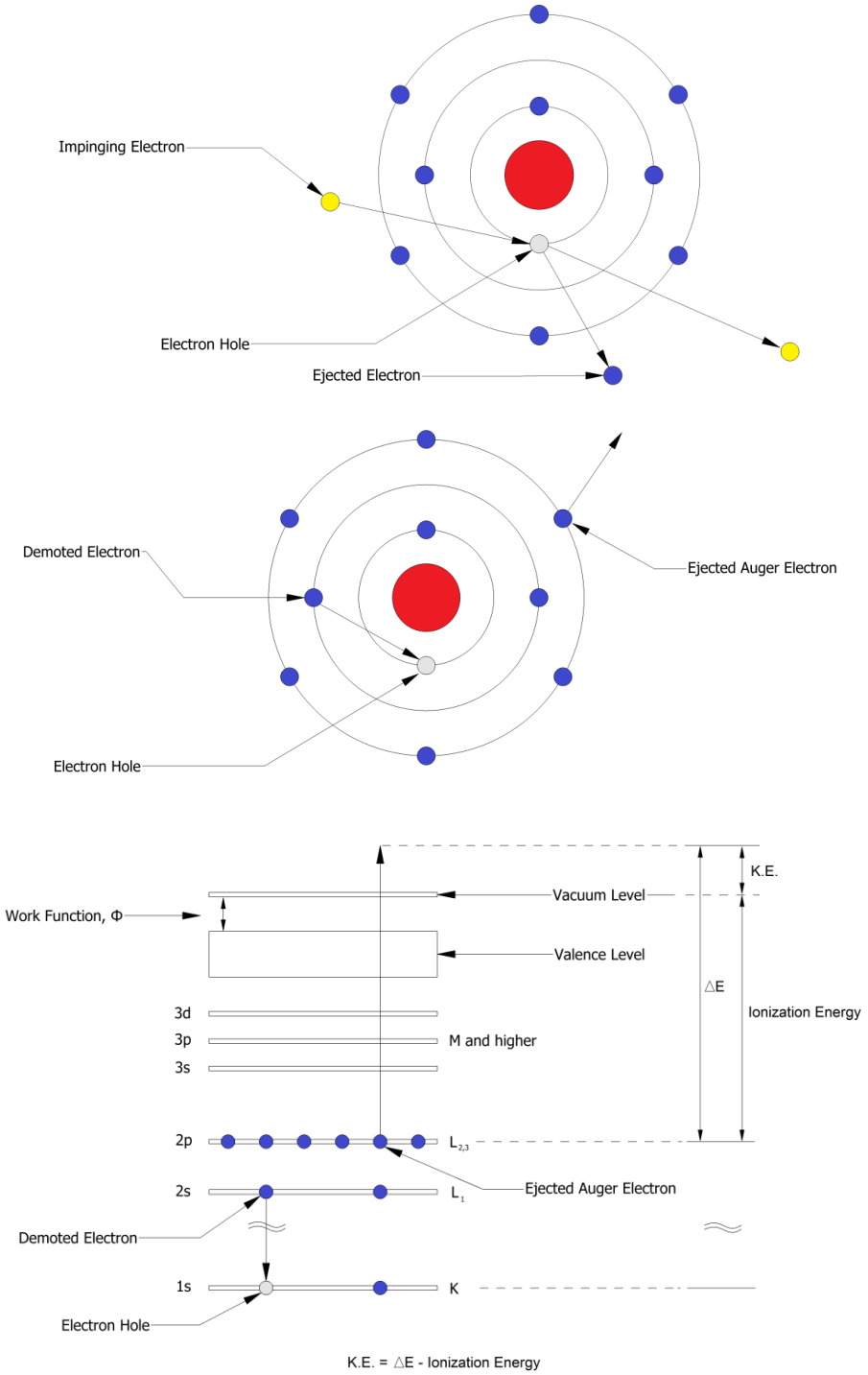

Figure 2.10: Schematic representation of the initial electron collision (top), Auger electron emission (middle), and the electron energy diagram (bottom). An electron strikes an electron in a core orbital and ejects it from the atom. An electron of higher energy then decays to fill the vacancy. The energy from the decaying electron is then imparted onto another electron which is then ejected. The final ejected electron is the Auger electron the energy of which is characteristic of the element.

References

(1) Granville-Phillips *Granville-Phillips® Series 370 Stabil-Ion® Vacuum Gauge and Controller Advanced Vacuum Measurement Solutions*, 2013.

(2) MKS_Instruments_Inc. *MKS Baratron® Types 615A/616A/617A High Accuracy Sensor Heads, Manual*, 2009.

(3) Sigma-Aldrich Bulletin 918 - Selecting Purifiers for Gas Chromatography. **2000**.

(4) Sigma-Aldrich Supelpure®-O Oxygen/Moisture Trap, Safety Data Sheet. **2014**.

(5) Hamilton, J. C.; Blakely, J. M. Carbon Layer Formation on Pt (111) Surface as a Function of Temperature. *J. Vac. Sci. Technol.* **1978**, *15*, 559.

Section 3 - Effusive Molecular Beam Experiments

3.1 Overview

Surface reactions involving alkanes involve a multitude of steps; however, the rate-limiting step for steam reforming on catalytic transition metal surfaces is believed to be the initial dissociative chemisorption of the alkane.[1] Although this may not necessarily be the rate-limiting step for other catalytic processes, alkane dissociative chemisorption is still important, since an alkane must be first chemisorbed in order to undergo any further reaction. When an alkane is dissociated onto a metal surface, the C-H bond is initially cleaved, leaving a chemisorbed alkyl fragment and hydrogen adatom. Upon further heating, the alkyl fragment fully decomposes to form carbon and desorbing hydrogen. The reaction schematically is,

$$C_nH_{2n+2,g} \xrightarrow{S*F} (C_nH_{2n+1})_c + H_c \xrightarrow{\Delta} nC + (n+1)H_{2,g}$$

where the initial dissociative sticking coefficient (DSC), *S*, is the probability that a given gas-surface collision will result in a chemisorbed alkane and, *F* is the flux, defined as the rate at which molecules strike the surface per unit area, per unit time. Therefore the quantity *S***F* is the total rate of dissociative chemisorption which, is directly proportional to the rate of carbon deposition. Consequently, the DSC can be determined with knowledge of the fluence, the time integrated flux, and the total carbon coverage. The fluence is determined by knowledge of the background pressure or in the case of a directed gas, the specifications of the molecular beam. The carbon coverage is determined by Auger electron spectroscopy (AES).

3.2 Conceptual

3.2.1 Effusive Beam Flux

Gas flux is defined as the rate at which molecules strike a unit area per unit time. If we consider the simple case, where a random distribution of background gas strikes a surface, then standard gas kinetics theory shows that the flux follows the functional form,

$$F_{bkg} = \frac{p}{\sqrt{2\pi m k_b T_c}} \qquad \text{Equation 3.1}$$

where, F_{bkg} is the background gas flux, p is the chamber pressure, m is the mass of the gas molecule, k_b is Boltzmann's constant, and T_c is the chamber temperature and the assumed gas temperature, T_g, such that $T_g = T_c$. In the case of directed flux from an effusive source, the functional form is more complicated.

An effusive molecular beam works on the principles of effusion, which involves the escaping of gas through a small orifice. Gas can only undergo effusion when in molecular flow, where the mean free path is substantially larger than the dimensions of the orifice. In this flow regime, the effusing molecules strike the walls of the container far more often than they do each other. Thus, gas molecules are not forced through the orifice by intermolecular collisions, but are instead emitted with a well-defined distribution that is independent of pressure. Gas effusing through an orifice has a cosine-like distribution that follows the functional form,[2]

$$\frac{dN}{dt} = \int \frac{d^2N}{d\Omega dt} d\Omega = \frac{p_n A_n}{\sqrt{2\pi m k_B T_n}} \int \frac{j(\vartheta)}{\pi} d\Omega \qquad \text{Equation 3.2}$$

where T_n is the nozzle temperature, $d\Omega$ is an increment of solid angle, $j(\vartheta)$ is the flux angular function, which is equal to $\cos(\vartheta)$ for an infinitely thin orifice, A_n, is the area of the orifice, and p_n, is the pressure behind the orifice.

Integration over the forward hemisphere of solid angle yields the total rate of effusion,

$$\frac{dN}{dt} = \frac{p_n A_n}{\sqrt{2\pi m k_B T_n}} \int \frac{j(\vartheta)}{\pi} d\Omega = \frac{p_n A_n W}{\sqrt{2\pi m k_B T_n}} \qquad \text{Equation 3.3}$$

where *W* is the transmission coefficient which is dependent on the geometry of the orifice.

Although the flux varies nominally as cos(ϑ) in solid angle, when projected onto a two-dimensional surface, such as a crystal, the flux distribution becomes sharper. Assuming that a surface is a perpendicular distance, *d*, from the effusive beam orifice, and *x* is the distance from beam centerline, then we can calculate the projection of the directed beam flux, F_{dir}, onto a flat surface. By transforming Equation 3.2 using the fact that $d\Omega = dA \cos(\vartheta) / r^2$, where dA is an increment of area on the sample surface, $r = d/\cos(\vartheta)$, and $\vartheta = \tan^{-1}(x/d)$, then the beam flux takes on the form,

$$F_{dir} = \frac{d^2N}{dAdt} = \frac{d^2N}{d\Omega dt}\frac{d\Omega}{dA} = \frac{p_n A_n}{\sqrt{2\pi m k_B T_n}}\frac{j(\vartheta)}{\pi}\frac{cos^3(\vartheta)}{d^2} = \frac{dN}{dt}\frac{j(\vartheta)}{W\pi}\frac{cos^3(\vartheta)}{d^2} \qquad \text{Equation 3.4}$$

For our doser, $j(\vartheta)$ is approximately equal to cos(ϑ), so the projection of effusive beam flux varies angularly as a function of $\cos^4(\vartheta)$ and decreases as a function of $1/d^2$.

Under experimental conditions, the effusive beam flux is directed at a crystal surface and allowed to react. However, the majority of the gas does not react and is deflected away from the crystal, contributing to the background flux. In order to minimize F_{bkg}, the effusive beam experiments are conducted while under continuous pumping conditions. Under these conditions, the gas throughput entering the system through the effusive molecular beam comes to equilibrium with the gas being removed from the system by the TMP. Mathematically the throughput balance is expressed as,

$$C_c p = \frac{d(pV)}{dt} = k_B T_c \frac{dN}{dt} \qquad \text{Equation 3.5}$$

where C_c is the pumping speed of the TMP, which is the effective pumping speed of the chamber, and it is assumed that the gas from the doser is rapidly equilibrated to the chamber temperature, T_c. Solving for p and inserting into Equation 3.1 yields,

$$F_{bkg} = \frac{p}{\sqrt{2\pi m k_b T_c}} = \frac{1}{C_c}\sqrt{\frac{k_B T_c}{2\pi m}}\,\frac{dN}{dt} \qquad \text{Equation 3.6}$$

Substituting Equation 3.3 for dN/dt, and solving for p_n, yields the following relationship between the chamber pressure and the nozzle pressure,

$$p_n = \frac{p C_c \sqrt{2\pi m k_B T_n}}{k_B T_c W\, A_n} \qquad \text{Equation 3.7}$$

If the pumping speed and chamber pressure are known, p_n can easily be calculated and so, can ensure that molecular flow conditions apply. In turn, by using Equation 3.4, the directed beam flux across the sample surface can be calculated. In practice, a working curve is generated that relates the chamber pressure, p, to the pressure in the gas manifold, p_m, which is slightly higher that p_n. The chamber pressure is measured using a hot filament, Bayard-Alpert gauge; during experiments, the gauge must be turned off in order to prevent the decomposition of alkanes on the filament. However, this does not impact experiments because the chamber pressure is back calculated from the manifold pressure where, $p = p(p_m)$. With knowledge of the pumping speed, it is possible to determine the ratio of directed to background flux. For a typical dosing distance of 12.7 mm, the ratio of directed flux to background flux for methane is approximately 3 to 1 normal to the surface.

3.2.2 Dissociative Sticking Coefficients

The rate of carbon deposition, $d^2N_c/dA\,dt$, from the dissociative chemisorption of alkanes, is a function of the sticking coefficient, S, and the flux, $d^2N/dA\,dt$, of gas-surface collisions and can be written as,

$$\frac{d^2N_c}{dA\,dt} = \frac{d^2N}{dA\,dt}S * n \qquad \text{Equation 3.8}$$

where both the carbon deposition rate, and the flux are written in terms of molecules per unit area per unit time, and n is the number of carbon atoms in the chemisorbed alkane. By multiplying and dividing by the atom areal density of Pt(111) [$1.50 * 10^{15}$/cm^2], σ, on the left hand side and rewriting the flux as F, we can rearrange Equation 3.8 into terms of coverage with respect to platinum monolayers,

$$\sigma * \frac{d\theta_c}{dt} = F * S * n \qquad \text{Equation 3.9}$$

Integrating the above equation with respect to carbon coverage and time, yields the deposited carbon coverage as a function of total time and flux,

$$\int_0^{\theta_c} d\theta_c = \int_0^t \frac{F*S*n}{\sigma}\, dt \qquad \text{Equation 3.10}$$

$$\theta_c = \frac{F*S*n*t}{\sigma} \qquad \text{Equation 3.11}$$

where, F/σ is the flux of gas-surface collisions per unit time in units of platinum monolayers, t is the total time, and θ_c is the carbon coverage in platinum monolayers. Equation 3.11 assumes that the DSC is independent of carbon coverage which is true for low carbon coverage.

During an effusive molecular beam experiment, carbon coverage is contributed from both the background and the directed fluxes. In order to determine the DSC, one must consider

that the total carbon coverage is the summation of both the background and directed contributions such that,

$$\theta_c = \theta_{c,dir} + \theta_{c,bkg} \quad \text{Equation 3.12}$$

Substitution of Equation 3.11 into Equation 3.12 yields the total carbon coverage as a function of the respective DSCs and fluxes,

$$\theta_c = \frac{S_{dir}*F_{dir}*n*t}{\sigma} + \frac{S_{bkg}*F_{bkg}*n*t}{\sigma} \quad \text{Equation 3.13}$$

which, can then be solved for S_{dir},

$$S_{dir} = \frac{1}{R}\left(\frac{\sigma\,\theta_c}{F_{bkg}} - S_{bkg}\right) \quad \text{Equation 3.14}$$

where,

$$R = \frac{F_{dir}}{F_{bkg}} \approx \frac{C_c\sqrt{2m}\,cos^3(\vartheta)\,j(\vartheta)}{W\sqrt{\pi k_B T_c}\,d^2} \quad \text{Equation 3.15}$$

S_{bkg} is independently determined by measuring the DSC of background dosed ambient temperature gas and using the following equation derived from Equation 3.11,

$$S_{bkg} = \frac{\sigma\,\theta_c}{F_{bkg}\,n\,t} \quad \text{Equation 3.16}$$

where the background flux, F_{bkg}, is calculated using Equation 3.1.

3.3 Auger Analysis

Post-dosed carbon was measured using Auger electron spectroscopy (AES). The measurements were taken over the range of 200 eV to 300 eV where both the platinum and carbon Auger peaks reside, in order to determine the total carbon coverage on the surface. Figure 3.1 shows a full Auger spectrum of a clean Pt(111) crystal and Figure 3.2 shows a representative AES spectrum for carbon deposition on Pt(111). Before experiments, crystal cleanliness was checked using AES, and it was found that the surface was free of measureable quantities of Ca, S, K, O, C, and Si. For a given experiment, the total fluence of each gas dose was limited such that the total carbon coverage was in the range of 0.05 ML to 0.4 ML (with respect to platinum). Lower coverage could result in artificially large DSC values due to highly reactive defect sites. Conversely, higher coverage could result in artificially small DSC values due to increased site blocking. Although carbon can diffuse into the platinum bulk, it has been shown that carbon diffusion does not occur below 1100 K.[3] In addition, carbon deposition from methane and ethylene dissociative chemisorption was found to be linear with respect to total fluence over the 0.03 ML to 0.4 ML range on Pt(111).[4] Therefore, subsurface carbon does not impact the measured dissociative sticking coefficients. The program, CasaXPS, was used to fit and integrate the undifferentiated spectra and the carbon coverage was determined by taking the ratios of the integrated intensities of the Pt_{237} and C_{272} Auger peaks. This fitting method yielded better results than a comparison of the differentiated spectra. However, a total of four Auger peaks were used for quantification, in order to make the fitting more accurate. The Auger peaks Pt_{219}, Pt_{237}, Pt_{248}, and C_{272} were fit with 30% Lorentzian/70% Gaussian peak shapes using a Marquardt non-linear least squares fitting routine. Shirley background subtraction was used over the 205 eV to 280 eV region. Table 3.1 contains a list of constraints used in the analysis.

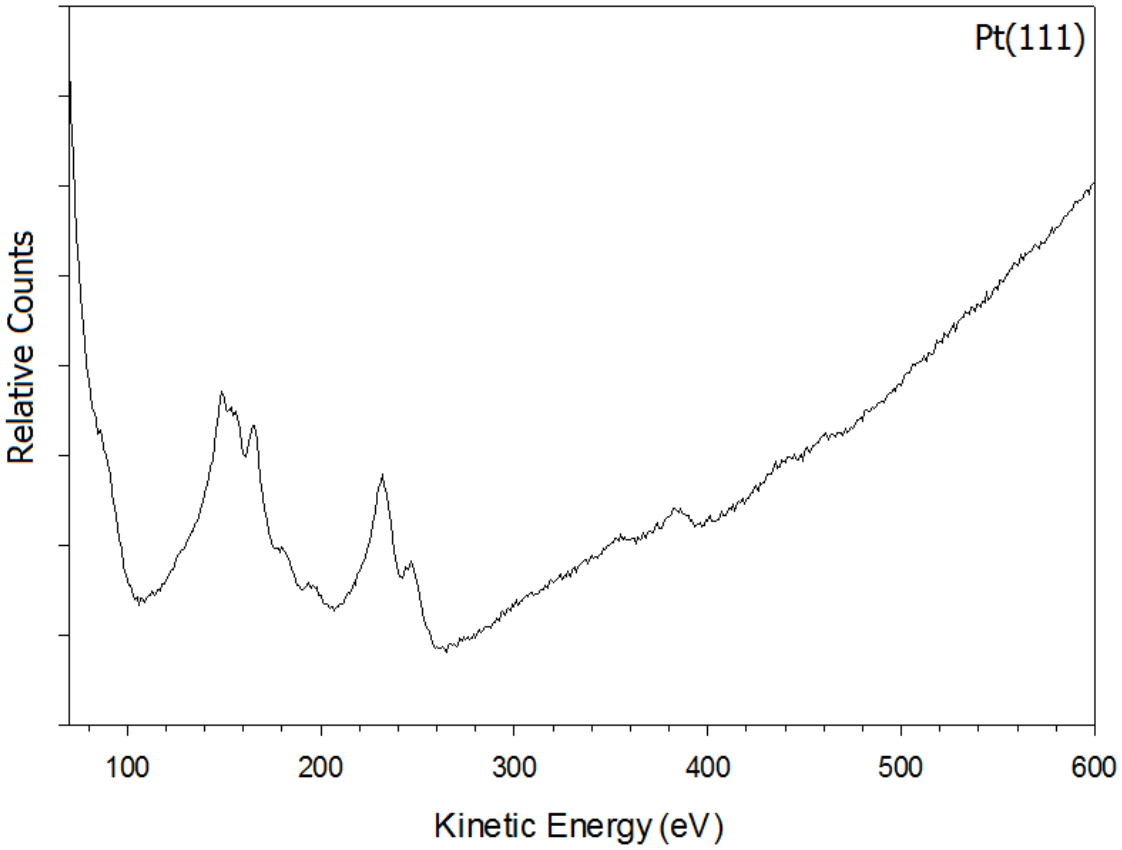

Figure 3.1: Representative Auger spectrum of a clean Pt(111) crystal acquired using a 15-255 GAR double-pass CMA. Auger peaks at 150, 158, 167, 182, 195, 237, 248, 357, 385, 440 , and 462 eV are characteristic of platinum.

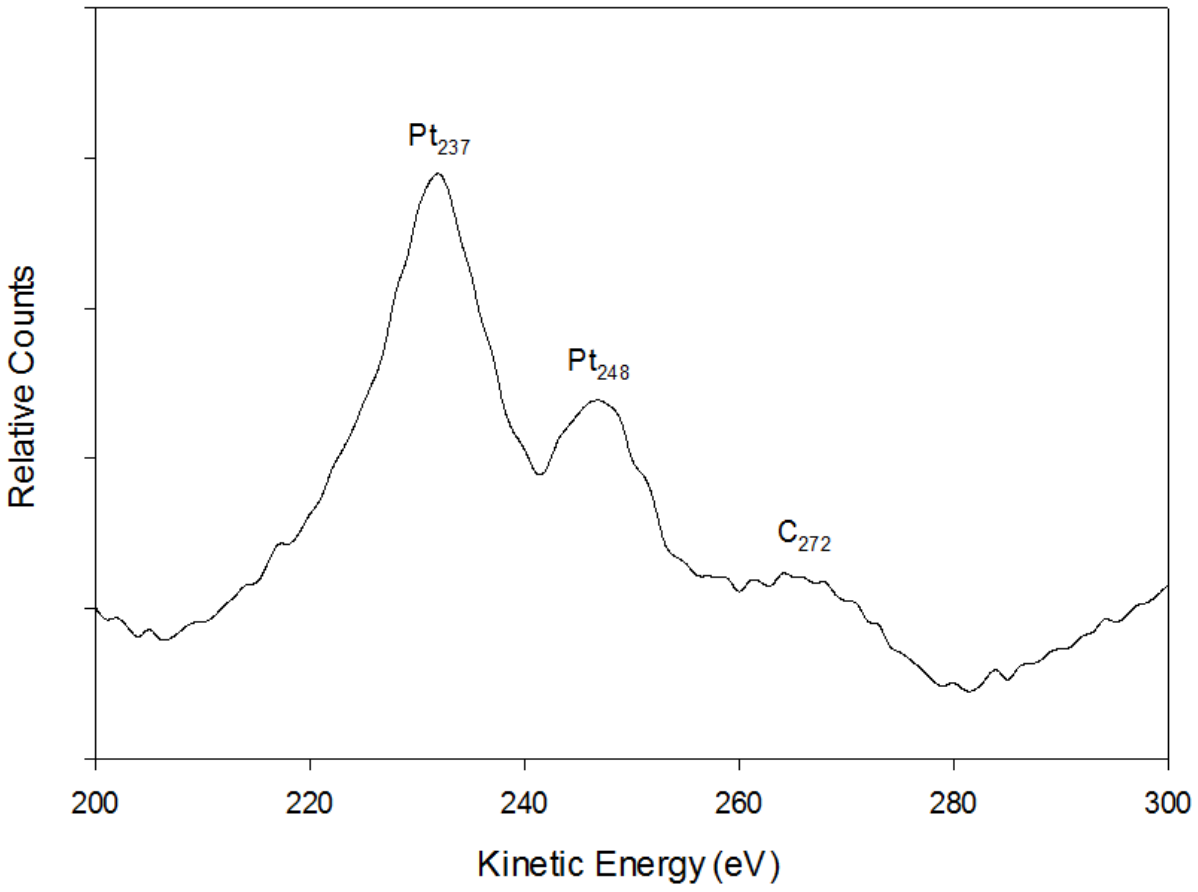

Figure 3.2: Representative Auger spectrum of carbon deposited on a Pt(111) crystal acquired using a 15-255 GAR double-pass CMA. The spectrum shows the peaks that are used to determine carbon coverage on Pt(111). Here, the coverage of carbon is approximately 0.25 ML with respect to platinum.

The Pt_{219} peak is not a true Auger peak and was included in order to better fit the Pt_{237} Auger peak.

Auger Peak	Position Constrained	FWHM (eV)	Integrated Peak Area Ratios to Pt_{237}
Pt_{219}	Yes	11.7	0.15
Pt_{237}	Yes	12.5	1.00
Pt_{248}	Yes	11.2	0.48
C_{272}	No	15	-----

Table 3.1: Constraints used for AES analysis.

After the integrated values were collected, the carbon coverage in platinum surface monolayers was calculated using the following equation,

$$\theta_c = 0.61 \frac{Int(C_{272})}{Int(Pt_{237})} \qquad \text{Equation 3.17}$$

Determination of the various fitting parameters are described in a previous work.[4]

3.4 Experimental Methods

3.4.1 General Procedure for DSC Measurements

When performing a DSC measurement, there are several steps that are common for all measurements. Before an experiment is conducted, the main chamber ion pump and the mass spectrometer ion pumps are turned off and closed approximately five minutes or more before the start of an experiment. This eliminates any possibility of residual pumping and limits the formation of highly reactive species. The ion gauge and all extraneous filaments or voltage sources are also turned off to avoid any spurious formation of reactive species. All DSC measurements are conducted under constant flow conditions wherein gas flows into the main chamber and exits through the turbo molecular pump throughout the experiment. Constant flow

conditions allow for ease of pressure control as well maintaining low concentrations of background contaminants. After all filaments (excepting the doser) are turned off and all ion pumps are turned off or separated from the chamber, the crystal is heated to the desired temperature and is oriented either towards the doser (directed dosing) or straight up (ambient dosing) and the reagent gas is loaded into the manifold. The dosing valve is then opened allowing gas to flow into the chamber at the same time that the measurement is started. After a certain fluence is achieved, the manifold is opened to the manifold pumping station, and the gas is pumped out. When the pressure in the manifold is relatively low, the dosing valve is closed and the crystal is cooled. Afterwards, the ion gauge and the Auger electron spectrometer are both turned on, while the crystal is positioned away from both of them. The desired values are set on the spectrometer and then the crystal is positioned in front of the electron beam and the carbon coverage is measured. Once the measurement is over, the Auger electron spectrometer is turned off and the ion pumps are restarted. During experiments, the manifold pressure and the dosing time are recorded using a custom-built program designed using the LabView software suite. In addition, the pressure in the manifold was kept in the molecular flow regime and the pressure was varied over the range of $1*10^{-3}$ to $2*10^{-2}$ Torr depending on the reactivity of the gas. Lastly, the total dosing time was kept above 300 seconds in order to minimize the error from starting or stopping gas flow.

3.4.2 Ambient Gas Dosing DSC Measurements

Ambient DSC measurements are the simplest form of DSC measurements. Basically, gas is admitted into the chamber through a calibrated leak that controls the total gas flux entering the chamber and is positioned such that there is no direct line of sight to the crystal. This port allows the gas to enter the chamber in a random, non-directed distribution. During the experiment, the crystal is positioned such that the crystal face points directly up in the chamber to ensure that no directed gas flux strikes the crystal. The procedure from section 3.4.1 is then applied.

3.4.3 Directed Gas Dosing DSC Measurements

For directed DSC measurements, gas is admitted into the chamber through the doser and directed at the center of the crystal face. The pressure behind the nozzle orifice remains low enough such that gas within the doser is in the molecular flow regime; this avoids a supersonic expansion and the associated alteration of the molecular energy distributions away from thermal ones. The procedure in section 3.4.1 is then followed with one exception; the crystal face is immediately moved away from the doser after the experiment is completed.

3.4.4 Angle-Resolved DSC Measurements

Angle-resolved DSC measurements follow the same procedure as directed gas dosing DSC measurements with a slight variation. Initially, the effusive beam centerline was found by dosing gas onto the surface and measuring the carbon profile across the surface using AES. The center of this carbon profile is the centerline of the beam flux. For the actual angle-resolved DSC measurements, the position of the effusive beam centerline on the crystal is first noted before the experiment begins. When the dosing is complete, the carbon coverage is measured at

several locations across the crystal face and is recorded with respect to the initial effusive beam centerline position. By measuring carbon coverage in this manner, the carbon profile over the crystal is mapped. The angle of impingement is calculated from the doser to crystal distance, *d*, and the distance from beam centerline, *x*. For subsequent experiments, the crystal is repositioned so that the centerline of the beam is located at a different position on the crystal face. By keeping a record of the effusive beam centerline, it is then possible to extend the angular measurement to a relatively high angle. The crystal is 10 mm in diameter, so when dosing at the center of the crystal, the carbon profile can be measured from -5 mm to +5 mm from the beam centerline. Alternatively, if the beam is centered on the edge of the crystal face, it is possible to scan from 0 mm to 10 mm from the beam centerline. The electron beam is ~0.2 mm in diameter which is focused enough to provide an accurate carbon profile.[5]

References

(1) Wei, J. M.; Iglesia, E. Structural and Mechanistic Requirements for Methane Activation and Chemical Conversion on Supported Iridium Clusters. *Angew. Chem.* **2004**, *43*, 3685.

(2) Pauly, H. *Atomic and Molecular Beam Methods*; Oxford University Press, New York, 1988; Vol. 1.

(3) Hamilton, J. C.; Blakely, J. M. Carbon Layer Formation on Pt (111) Surface as a Function of Temperature. *J. Vac. Sci. Technol.* **1978**, *15*, 559.

(4) Cushing, G. W.; Navin, J. K.; Valadez, L.; Johanek, V.; Harrison, I. An Effusive Molecular Beam Technique for Studies of Polyatomic Gas-Surface Reactivity and Energy Transfer. *Rev. Sci. Instrum.* **2011**, *82*, 11.

(5) Physical.Electronics Instruction Manual for Cylindrical Auger Electron Optics and Precision Electron Energy Analyzers. **1982**.

Section 4 - Theoretical Modeling

4.1 Introduction

The dissociative chemisorption of alkanes is an activated process in which an alkane molecule incident on a surface dissociates and forms a chemisorbed alkyl fragment and a hydrogen adatom. A schematic representation of alkane dissociative chemisorption is shown in Figure 4.1. An alkane molecule strikes the surface and forms a transient gas-surface collision complex as it interacts with a few local surface atoms, and if enough energy is available, dissociates onto the surface. If there is a deficiency in energy, then the impinging molecule is deflected back into the gas phase or is transiently molecularly adsorbed and then thermally desorbed at typical working temperatures of 300 K and higher. The reaction scheme of alkane dissociative chemisorption is described as,

$$C_nH_{2n+2,g} \longrightarrow C_nH_{2n+1,c} + H_c$$

The energy requirements for dissociation can be met with either molecular energy, surface energy, or some combination of the two. The impinging molecule has energy available in various degrees of freedom: translation, vibration, and rotation. The surface has its own energy pool based on vibrational motion of its atoms. In an idealized system that reacts statistically, energy in each degree of freedom is exchangeable and equally efficacious in helping to surmount the energetic barrier to dissociative chemisorption. However, for many energy-related small molecules, such as H_2, CO_2, and CH_4, the precise dynamics of their encounters with catalytic surfaces are important in the determination of reaction rates, and for these dynamical systems, not all degrees of freedom are equally efficacious in promoting dissociation.

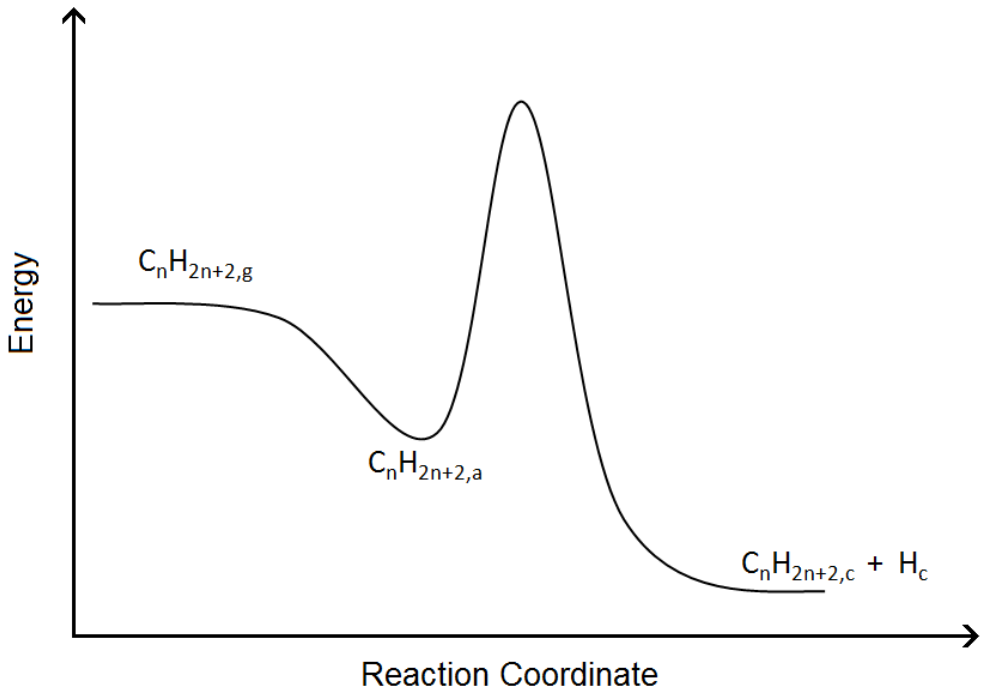

Figure 4.1: Schematic representation of the reactive potential for alkane dissociative chemisorption, where *g*, *a*, and *c* indicate a gas phase molecule, a molecularly adsorbed molecule, and chemisorbed species respectively.

4.2 Dynamics

4.2.1 Translation

Alkane dissociative chemisorption can be strongly activated by translational energy. On flat, close-packed metal single crystals, only the normal component of translational energy affects reactivity. This was initially confirmed for the methane/Pt(111) system and then extended to a range of other alkanes.[1,2] Measurements of dissociative sticking coefficients (DSC) of alkanes on flat metal surfaces confirmed that DSCs scale with the normal component of translation, such that,

$$S(E) = S(E_n) \qquad \text{Equation 4.1}$$

where,

$$E_n = E_t \cos^2\theta \qquad \text{Equation 4.2}$$

This is referred to as normal energy scaling of the DSC. On more stepped surfaces, such as (211) or (533), normal energy scaling may not hold. However, there are no experimental results to confirm that normal energy scaling is obeyed on these surfaces.

If one considers the potential energy of a molecule approaching a surface initially separated by an infinite distance, the potential energy decreases as the molecule approaches the surface because the attractive potential dominates. At a certain point, the potential energy is at a minimum and then increases exponentially as the molecule gets closer to the surface because of Coulombic and Pauli repulsion of electrons. Figure 4.2 (a) shows a graphical representation of potential energy as a function of the distance between the molecule and the surface, *z*. Thus, in order to approach the surface and overcome the electronic repulsion to allow dissociation to occur, normal translational energy is required. On the other hand, the surface atoms are closely packed together in an even, repeating pattern with no defects, such that the electron density is

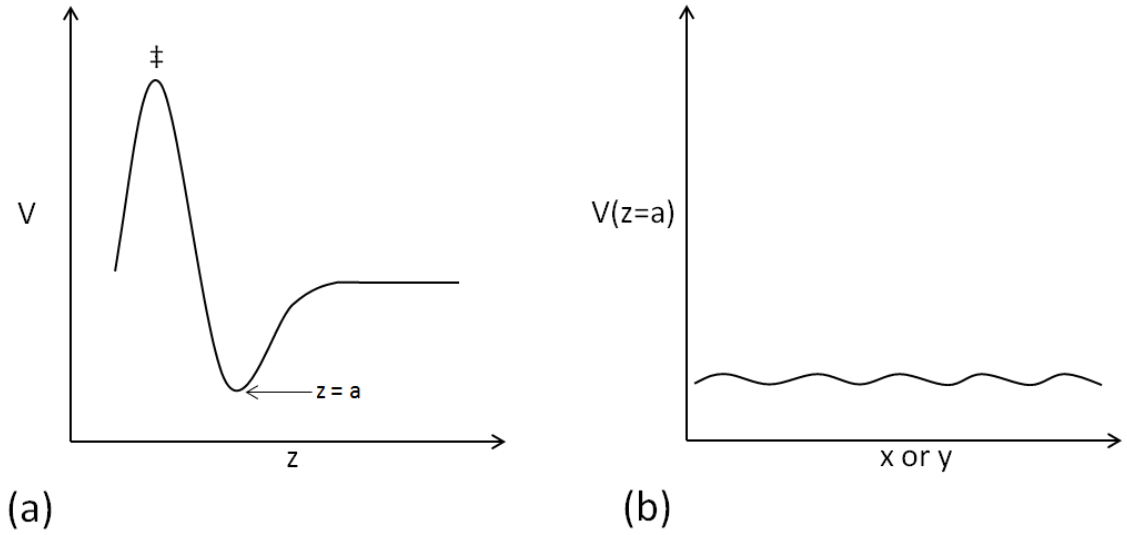

Figure 4.2: Potential energy as a function of the distance between the impinging molecule and the surface, *z* (a) and as a function of the *x* or *y* vector of the surface plane (b). The scales of both graphs are identical.

uniform and relatively invariant. Therefore, if *z* is held constant and the molecule is moved in the *x*-*y* plane of the surface, there is little change in the potential energy. Figure 4.2 (b) shows a graphic representation of the potential energy, with *z* fixed at the bottom of the physisorption well, as a function of position on the surface, in either the *x* or *y* dimensions on a flat, close-packed surface. It follows then that translational motion parallel to the surface should have little to no effect on reactivity because there is little to negligible corrugation of the potential parallel to the surface.

Although not discussed in this work, the electron density of fcc surfaces that are not smooth and relatively close-packed or flat, such as the (110) surface, varies more dramatically across the surface. Figure 4.3 shows models of the fcc surfaces (111), (100), and (110). The square fcc (100) surface is a slightly more open surface with a lower surface atom density than the hexagonal fcc (111) surface. Because of this, there is a greater oscillation of surface electron density for the (100) surface compared to the (111) surface. Holmblad et al. have shown that there is a deviation from normal energy scaling for the CH_4/Ni(100) system[3], where as CH_4/Ni(111) exhibits normal energy scaling.[4,5] In addition, CH_4 has been shown to be more reactive on Ni(111) than on Ni(100).[6] The fcc (110) surface has a missing row of atoms for every other row in one dimension. Therefore, it is likely that the translational energy parallel to the surface and across the rows would affect dissociation, since there is such a large corrugation in the electron density across the surface in that direction. Indeed, McMaster and Madix found normal energy scaling for CH_4/Pt(110) reactivity along the rows and closer to total energy scaling across the rows.[7]

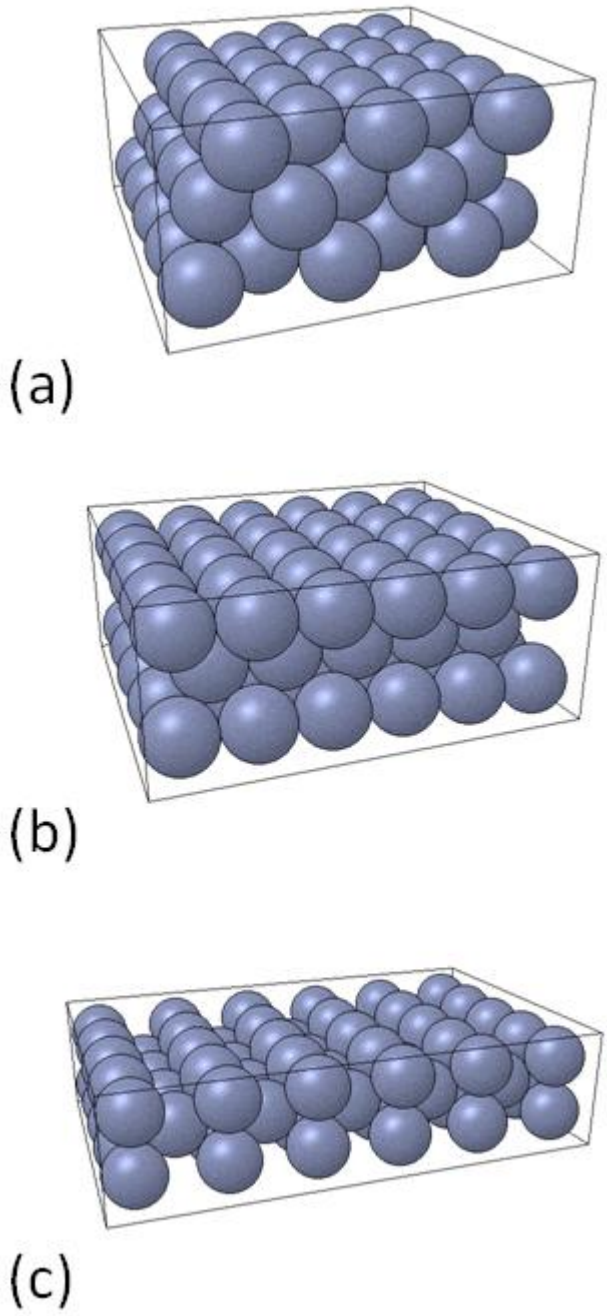

Figure 4.3: Volume filling models of fcc surfaces: hexagonal fcc (111) plane (a), square fcc (100) plane (b), and the fcc (110) plane (c).

4.2.2 Vibration

Non-linear, polyatomic molecules with N atoms have 3N-6 vibrational modes; for example, methane and ethane have 9 and 18 respectively. At low temperatures $T_g < 500$ K, the majority of these vibrational modes are in the ground state and so contribute little to reactivity. For example, the total amount of vibrational energy in methane is only 9.4 cm^{-1} at 300 K as calculated from the standard vibrational partition function. However, at higher temperatures the vibrational energy contribution becomes much greater and so, at 700 K, the vibrational energy of methane increases to ~450 cm^{-1}. For larger alkanes with more vibrational modes, the vibrational energy content is much larger; for propane, the vibrational energy is ~2900 cm^{-1} at 700 K compared to ~450 cm^{-1} for methane. In a purely statistical system then, there is a great deal of vibrational energy that can be accessed at reactive temperatures.

When an alkane dissociates onto a surface, the C-H bond cleaves before the C-C bond because the C-H bonds sterically hinder access of the surface to the C-C bonds. DFT studies have shown that the transition state for dissociation involves a weakening and elongation of the C-H bond and the formation of alkyl-metal and hydrogen-metal bonds.[8,9] DFT calculated transition state complexes for methane, ethane, and propane on Pt(111) calculated by Scott Donald are shown in Figure 4.4. For methane, which has no C-C bonds, vibrational modes corresponding to C-H stretching may affect bond dissociation because the C-H bond must be elongated in order to be cleaved. However, modes with pure C-H stretch should affect the reactivity more because these modes affect the length of the C-H bond the most. More complex alkanes, such as ethane and propane, have many more vibrational modes than methane. Some of these modes have C-C bond and C-H bond characteristics. Because the reaction coordinate is along the C-H bond, energy from vibrational modes that do not cause the C-H bond to elongate

should not affect reactivity as much.[10] Therefore, certain vibrational modes, such as those with pure C-H bond stretch characteristics, should be more efficient in C-H bond cleavage and thus promote dissociation more efficiently than those modes with C-C bond stretch character.

Although it seems reasonable that particular vibrational modes are more effective in promoting alkane dissociation, it is also important to understand whether vibrational energy promotes dissociation more so than either translation or rotation. Indeed, there have been a variety of supersonic molecular beam studies that have measured vibrational-state resolved efficacies to promoting methane dissociation on metal surfaces relative to the efficacy for normal translational energy.[5,6,11-19] Vibrational efficacies, η_v, are determined by first measuring the change in DSC value with changing normal translational energy. Next, the DSC dependence on vibrational energy is measured using laser pumped, vibrationally excited molecules. These experiments have shown that an increase in either translational or vibrational energy increases the rate of dissociation. In order to achieve a certain increase in the DSC, ΔDSC, there must be either an increase in the normal translational energy, ΔE_n, or an increase in the vibrational energy, ΔE_v. The ratio $\Delta E_v/\Delta E_n$ to yield the same ΔDSC is η_v. It has been determined that certain vibrational modes enhance dissociative chemisorption more efficaciously than other modes and in most cases, vibrational energy is less efficacious in promoting alkane dissociative chemisorption than normal translational energy such that, $\eta_v < 1$.

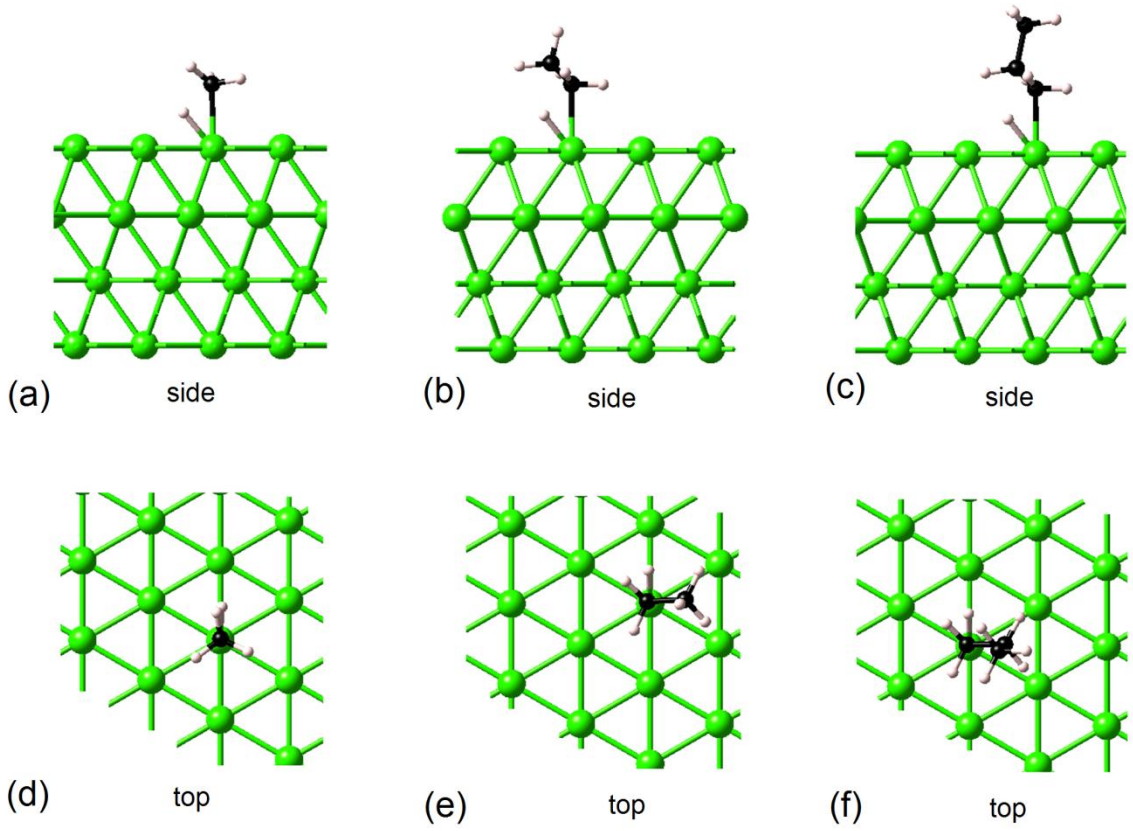

Figure 4.4: DFT transition state complexes for methane (a, d), ethane (b, e), and propane (c, f) dissociation on Pt(111) calculated by Scott Donald at the University of Virginia. The white, black, and green spheres correspond to hydrogen, carbon, and platinum atoms respectively.

4.2.3 Rotation

Although the total amount of rotational energy is similar to that of translational energy under thermal equilibrium conditions, the dynamical role of rotational energy is difficult to discern. Normal translational energy enables a molecule to overcome the potential energy barrier required to approach the surface so that the C-H bond can be broken; vibrational energy allows for the elongation and distortion of the C-H bond so that it can be cleaved. The role of rotation in alkane activation, however, is not as apparent. For rotational energy, if the j-state is significantly high, the molecule could theoretically dissociate from centripetal distortion which causes bond lengthening. However, reactions conducted at catalytic temperatures seldom achieve those states. Therefore, rotation must either have a more subtle effect or is a spectator altogether.

In order to determine the role of rotation, DSC studies would have to be performed with rotationally excited molecules or with rotational motion removed all together. Although exciting and substantially tuning only rotational energy, over a large range of J states, is not practical experimentally, because optical selection rules only allow $\Delta J = \pm 1$ for dipole transitions and $\Delta J = \pm 2$ for Raman transitions, it is possible to quench rotational energy. When DSC studies are conducted with supersonic molecular beams, there is a substantial amount of rotational cooling of the molecules within the supersonically expanding beam and the rotational temperature of these molecules is approximately 10 to 20 K and the rotational energy distribution is narrow. On the other hand, effusive molecular beams do not exhibit rotational cooling because there is no supersonic expansion and consequently, the energy is defined by a standard Maxwell-Boltzmann distribution. Therefore, the rotational energy content of molecules in an effusive beam is substantially larger than those in a supersonic beam. By comparing DSCs measured using

supersonic molecular beams to those measured using effusive molecular beams, across which, the rotational energy content varies widely, it has been shown that the DSCs are consistent with theoretical models in which rotation is a spectator.[20] In addition, Donald et al. has reproduced results for laser induced thermal reaction of CD_3 and D on Pt(111) to yield CD_4 using the d-PMMT model which holds rotation as a spectator degree of freedom.[21] As a result, it has been concluded that taking rotation as a spectator degree of freedom is a good approximation for the dissociation of methane on metal surfaces. If rotation fully participated in promoting reactivity, the DSCs measured with effusive molecular beams would be about an order of magnitude in variance with those measured with supersonic molecular beams for the CH_4/Pt(111) system according to PMMT models. However, it should be noted that for the H_2/Cu(111) system, increasing rotational energy from J = 0 initially inhibits reactivity; eventually, after about 15 kJ/mol of rotational energy, rotation begins to promote reactivity.[22] Therefore, rotational efficacies can vary from system to system.

4.2.4 Surface

The semi-infinite surface stores its energy in the form of lattice vibrations. The vibrational energy of the surface atoms directly involved in the transient gas-surface collision complexes can be imparted to the impinging alkane molecule by phonons, collective oscillations of surface vibrations. Although it is difficult to directly measure how well surface phonons couple with the vibrations of the impinging molecule or to the reaction coordinate, it is possible to determine how the surface energy affects reactivity by varying the surface temperature. DSC studies have shown that the surface energy contributes significantly to the rate of alkane

dissociative chemisorption because there is a large enhancement in dissociation when the surface temperature is increased.[1,4,21,23-29]

4.3 Precursor-Mediated Microcanonical Trapping (PMMT) Model

There are a variety of theoretical models that attempt to reproduce the results of alkane dissociative chemisorption studies. Dynamical models require accurate potential energy surfaces (PES) and high dimensional dynamical calculations. Recently, the PES accuracy seems to have improved[30] and high dimensional classical trajectory calculations are able to qualitatively reproduce many aspects of the reactivity,[8,31] though quantitative agreement is typically no better than 1-2 orders of magnitude in error. Typically, existing models do not have the ability to predict DSC values over a wide range of experiments or temperatures. A variety of different mechanistic assertions have led to statistical models,[25,32-38] tunneling models,[1,39,40] thermally assisted tunneling models,[41] and geometric distortion models.[4,27] Some of these models can qualitatively model translational and vibrational activation, while other models explain the surface temperature dependence. There are no dynamical models that can elucidate DSC dependencies on vibrational, rotational, translational, and surface energies simultaneously. Although most of these models can reproduce a small subset of experimentally determined DSCs, none of these models has the ability to reproduce experimental DSC values for a wide range of experiments. In addition, attempts have been made to calculate a full PES using DFT and molecular dynamics to calculate semi-quantitative DSCs, although only a limited subset of data can be reproduced.[10,31,42]

The precursor-mediated microcanonical trapping (PMMT) model was developed by the Harrison research group in order to handle the DSC dependence on all four exchangeable

energies. A full explanation of how the model calculates DSCs was published by other Harrison group members and can be found elsewhere.[20-22,36,37] However, a shortened version of the model will be stated here. The PMMT model is a mechanistically straightforward approach to dissociative chemisorption requiring a minimum of steps. A schematic of the PMMT model is shown in Figure 4.5.[21,23,24] An impinging molecule first strikes the surface and forms a precursor complex (PC) with the immediate surrounding surface atoms. The energy of the PC is microcanonically randomized by this initial collision through anharmonic coupling on the potential energy surface. The PC can then undergo secondary energy exchange with the surrounding bulk metal lattice. If the total energy of the PC, E^*, is higher than the barrier for dissociation, E_0, then the alkane can either dissociate or desorb with Rice-Ramsperger-Kassel-Marcus (RRKM) rate constants. For small molecules with high activation barriers, desorption lifetimes are ultrafast (< 1 ps) and PC-surrounding metal energy transfer is negligible. In such cases, the overall reaction scheme can be written as,

$$C_nH_{2n+2,g} \underset{k_D(E^*)}{\overset{F_0 f(E^*)}{\rightleftarrows}} C_nH_{2n+2,p} \xrightarrow{k_R(E^*)} C_nH_{2n+1,c} + H_c$$

where F_0 is the net molecular flux incident on the surface in monolayers per second, $f(E^*)$ is the probability distribution of forming a PC with an E* amount of exchangeable energy, and the rate constants for desorption and reaction are defined using RRKM rate constants of the form,

$$k_i(E^*) = \frac{W_i^{\ddagger}(E^* - E_{0,i})}{h\rho(E^*)} \qquad \text{Equation 4.3}$$

where $k_i(E^*)$ is the rate as a function of the active exchangeable energy, E^*, $W_i^{\ddagger}(E^*\text{-}E_{0,i})$ is the sum of states for transition state i, h is Planck's constant, and $\rho(E^*)$ is the density of states for the PC. The value i, denotes either the desorption (D) or reaction (R) channel and the threshold energies for desorption and reaction are $E_{0,D} = 0$ and $E_{0,R} = E_0$ respectively.

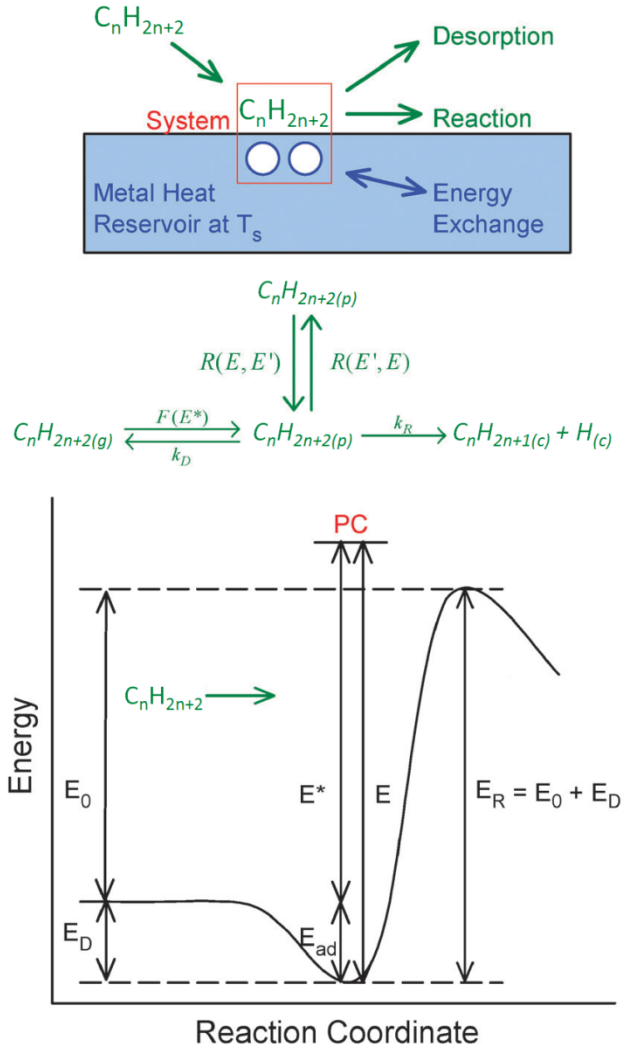

Figure 4.5: Schematic representation of dissociative chemisorption of alkanes with energies as defined by the PMMT model.[21,23,24] A molecule first strikes the surface and forms a precursor complex (PC) with the immediate surrounding surface atoms; the energy of the PC is microcanonically randomized by this initial collision. The PC can then undergo secondary energy exchange with the surrounding bulk metal lattice. If the total energy of the PC, E^*, is higher than the barrier for dissociation, E_0, then the alkane can either dissociate or desorb with Rice-Ramsperger-Kassel-Marcus (RRKM) rate constants.

The actual experimental dissociative sticking coefficient can be written as,

$$S = \int_0^\infty S(E^*) f(E^*) dE^* \qquad \text{Equation 4.4}$$

where S(E*) is the microcanonical DSC,

$$S(E^*) = \frac{k_R(E^*)}{k_R(E^*)+k_D(E^*)} = \frac{W_R^\ddagger(E^*-E_0)}{W_R^\ddagger(E^*-E_0)+W_D^\ddagger(E^*)} \qquad \text{Equation 4.5}$$

Therefore, the DSC is defined as the number of open channels to react $W_R^\ddagger(E^*\text{-}E_0)$, divided by the total number of channels, $W_R^\ddagger(E^*\text{-}E_0)/(W_R^\ddagger(E^*\text{-}E_0)+W_D^\ddagger(E^*))$.

For the statistical PMMT (s-PMMT) model, the exchangeable energy is determined by the summation of the total energy contributions of the surface energy, E_s, normal translational energy, E_n, vibrational energy, E_v, and rotational energy, E_r. All together, the exchangeable energy can be expressed as,

$$E^* = E_s + E_n + E_v + E_r \qquad \text{Equation 4.6}$$

The probability distribution, $f(E^*)$, is defined as,

$$f(E^*) = \int_0^{E^*} f_t(E_t) \int_0^{E^*-E_t} f_v(E_v) \times$$

$$\int_0^{E^*-E_v-E_t} f_r(E_r) f_s(E^* - E_t - E_v - E_r) dE_r dE_v dE_t \qquad \text{Equation 4.7}$$

Then, the dynamically biased PMMT (d-PMMT) model was introduced and, at that time, it was determined for the CH_4/Pt(111) system, that vibrational energy was not as efficacious as normal translational energy at promoting dissociation and rotation was a spectator. Therefore, the vibrational energy contribution is further multiplied by a vibrational efficacy term, η_v, which scales the vibrational energy contribution in dynamical systems and the contribution of rotational energy is discounted.

Hence, the exchangeable energy for the d-PMMT model is defined as,

$$E^* = E_n + \eta_v E_v + E_s \qquad \text{Equation 4.8}$$

where E_n is the normal translational energy and η_v is the vibrational efficacy. The probability distribution $f(E^*)$ is then redefined as,

$$f(E^*) = \int_0^{E^*} f_n(E_n) \int_0^{E^*-E_n} f_s(E_s) \times f_v(\eta_v{}^{-1}(E^* - E_n - E_s)) dE_s dE_n$$

$$\times f_v(\eta_v{}^{-1}(E^* - E_n - E_s)) dE_s dE_n \qquad \text{Equation 4.9}$$

Finally, a master equation (ME) version of the PMMT model was developed which explicitly accounts for gas-surface energy transfer. The master equation accounts for energy transfer between the PC and the surrounding bulk metal lattice and defines the time dependence of the PC energy distribution. The change in coverage of PCs at reactive energies, E^*, as a function of time is defined as,

$$\frac{d\theta_p(E,t)}{dt} = f(E,t) - \{k_R(E) + k_D(E) + \omega\}\theta_p(E,t)$$

$$+\omega \int_0^{\infty} P(E,E')\theta_p(E',t) dE' \qquad \text{Equation 4.10}$$

where E' is the initial energy of a PC with $E' < E$, ω is the total inelastic collision frequency, and $P(E, E')$ is the exponential down collision step size distribution,

$$P(E,E') = \frac{\rho(E)}{N(E')} e^{-(E'-E)/\alpha} \qquad \text{Equation 4.11}$$

where $\rho(E)$ is the density of states of PCs with energy E, $N(E')$ is a normalization constant, and α is the gas-surface energy transfer parameter. In the limit of the steady state approximation, where the gas-surface energy transfer comes to equilibrium, a formal solution for the master

equation would have the functional form,

$$S = \frac{1}{f_0}\frac{d\theta_c}{dt} = \int_0^\infty \frac{k_R(E)}{k_R(E)+k_D(E)+\omega} \times$$

$$\left(f(E) + \frac{\omega}{f_0}\int_0^\infty P(E',E)\theta_p^{ss}(E)dE'\right)dE \qquad \text{Equation 4.12}$$

where $\theta_p^{ss}(E)$ is the steady state coverage of PCs at energy E. Thus, PCs at E can either react, desorb, or exchange energy with the surface. The energy exchange with the surface can generate an additional coverage of PCs with energy E from coverages at energies E' that move to E.

When the PMMT model is used to calculate DSCs or other quantities, a total of four parameters are used: the barrier for dissociation, E_0, the number of surface atoms involved in the initial collision, or surface oscillators, s, the vibrational efficacy for promoting reactivity with respect to normal translation, η_v, and a gas-surface energy transfer parameter, α, which regulates the energy transferred to or from the PC to the rest of the bulk metal lattice per phonon collision. Several versions of the PMMT model have been implemented depending on the particular system under study. The purely statistical (s-) version of the PMMT model has the vibrational efficacy set to 1, rotation is held active, and there is no consideration of gas-surface energy transfer. However, measurements of DSCs of methane on Pt(111) have shown that rotational energy does not contribute to the dissociation of alkanes on Pt(111) and so is considered a spectator degree of freedom. [20] In addition, supersonic molecular beam experiments, in which the vibrational energy content was varied by varying the beam nozzle temperature[1,27,39,43,44] and various quantum state-resolved experiments[5,6,11-19] have determined that vibrational energy is not as efficacious as normal translational energy in promoting dissociation. Therefore, a dynamical version (d-) of the PMMT model was implemented where the vibrational efficacy has been set to 0.4, and rotational energy has been discounted. Although quantum-state resolved experiments show that the vibrational efficacy varies for different vibrational modes, we consider our

vibrational efficacy to be an average over the vibrational modes excited in the particular supersonic heated nozzle experiments we use to fix our model parameters. The master equation has also been implemented for both the statistical (ME s-) and dynamical (ME d-) PMMT models. For methane and ethane, the frequencies of the transition state complex have been set using density functional theory (DFT).

References

(1) Luntz, A. C.; Bethune, D. S. Activation of Methane Dissociation on a Pt(111) Surface. *J. Chem. Phys.* **1989**, *90*, 1274.

(2) Weaver, J. F.; Krzyzowski, M. A.; Madix, R. J. Direct Dissociative Chemisorption of Alkanes on Pt(111): Influence of Molecular Complexity. *J. Chem. Phys.* **2000**, *112*, 396.

(3) Holmblad, P. M.; Wambach, J.; Chorkendorff, I. Molecular-Beam Study of Dissociative Sticking of Methane on Ni(100). *J. Chem. Phys.* **1995**, *102*, 8255.

(4) Lee, M. B.; Yang, Q. Y.; Tang, S. L.; Ceyer, S. T. Activated Dissociative Chemisorption of CH_4 on Ni(111): Observation of a Methyl Radical and Implication for the Pressure Gap in Catalysis. *J. Chem. Phys.* **1986**, *85*, 1693.

(5) Bisson, R.; Sacchi, M.; Dang, T. T.; Yoder, B.; Maroni, P.; Beck, R. D. State-Resolved Reactivity of $CH_4(2\nu_3)$ on Pt(111) and Ni(111): Effects of Barrier Height and Transition State Location. *J. Phys. Chem. A* **2007**, *111*, 12679.

(6) Juurlink, L. B. F.; Smith, R. R.; Killelea, D. R.; Utz, A. L. Comparative Study of C-H Stretch and Bend Vibrations in Methane Activation on Ni(100) and Ni(111). *Phys. Rev. Lett.* **2005**, *94*, 4.

(7) McMaster, M. C.; Madix, R. J. Alkane Dissociation Dynamics on Pt(110)-(1x2). *J. Chem. Phys.* **1993**, *98*, 9963.

(8) Nave, S.; Jackson, B. Methane Dissociation on Ni(111) and Pt(111): Energetic and Dynamical Studies. *J. Chem. Phys.* **2009**, *130*, 054701.

(9) Nave, S.; Tiwari, A. K.; Jackson, B. Methane Dissociation and Adsorption on Ni(111), Pt(111), Ni(100), Pt(100), and Pt(110)-(1x2): Energetic Study. *J. Chem. Phys.* **2010**, *132*, 054705.

(10) Jiang, B.; Guo, H. Mode and Bond Selectivities in Methane Dissociative Chemisorption: Quasi-Classical Trajectory Studies on Twelve-Dimensional Potential Energy Surface. *J. Phys. Chem. C* **2013**, *117*, 16127.

(11) Juurlink, L. B. F.; Killelea, D. R.; Utz, A. L. State-Resolved Probes of Methane Dissociation Dynamics. *Prog. Surf. Sci.* **2009**, *84*, 69.

(12) Utz, A. L. Mode Selective Chemistry at Surfaces. *Curr. Opin. Solid State Mater. Sci.* **2009**, *13*, 4.

(13) Beck, R. D.; Maroni, P.; Papageorgopoulos, D. C.; Dang, T. T.; Schmid, M. P.; Rizzo, T. R. Vibrational Mode-Specific Reaction of Methane on a Nickel Surface. *Science* **2003**, *302*, 98.

(14) Juurlink, L. B. F.; McCabe, P. R.; Smith, R. R.; DiCologero, C. L.; Utz, A. L. Eigenstate-Resolved Studies of Gas-Surface Reactivity: CH_4 (n_3)Dissociation on Ni(100). *Phys. Rev. Lett.* **1999**, *83*, 868.

(15) Killelea, D. R.; Campbell, V. L.; Shuman, N. S.; Smith, R. R.; Utz, A. L. Surface Temperature Dependence of Methane Activation on Ni(111). *J. Phys. Chem. C* **2009**, *113*, 20618.

(16) Killelea, D. R.; Campbell, V. L.; Shuman, N. S.; Utz, A. L. Bond-Selective Control of a Heterogeneously Catalyzed Reaction. *Science* **2008**, *319*, 790.

(17) Maroni, P.; Papageorgopoulos, D. C.; Sacchi, M.; Dang, T. T.; Beck, R. D.; Rizzo, T. R. State-Resolved Gas-Surface Reactivity of Methane in the Symmetric C-H Stretch Vibration on Ni(100). *Phys. Rev. Lett.* **2005**, *94*, 4.

(18) Schmid, M. P.; Maroni, P.; Beck, R. D.; Rizzo, T. R. Surface Reactivity of Highly Vibrationally Excited Molecules Prepared by Pulsed Laser Excitation: CH_4 ($2\nu_3$) on Ni(100). *J. Chem. Phys.* **2002**, *117*, 8603.

(19) Smith, R. R.; Killelea, D. R.; DelSesto, D. F.; Utz, A. L. Preference for Vibrational over Translational Energy in a Gas-Surface Reaction. *Science* **2004**, *304*, 992.

(20) Donald, S. B.; Harrison, I. Dynamically Biased RRKM Model of Activated Gas-Surface Reactivity: Vibrational Efficacy and Rotation as a Spectator in the Dissociative Chemisorption of CH_4 on Pt(111). *PCCP* **2012**, *14*, 1784.

(21) Donald, S. B.; Navin, J. K.; Harrison, I. Methane Dissociative Chemisorption and Detailed Balance on Pt(111): Dynamical Constraints and the Modest Influence of Tunneling. *J. Chem. Phys.* **2013**, *139*.

(22) Donald, S. B.; Harrison, I. Rice–Ramsperger–Kassel–Marcus Simulation of Hydrogen Dissociation on Cu(111): Addressing Dynamical Biases, Surface Temperature, and Tunneling. *J. Phys. Chem. C* **2013**, *118*, 320.

(23) Cushing, G. W.; Navin, J. K.; Donald, S. B.; Valadez, L.; Johanek, V.; Harrison, I. C-H Bond Activation of Light Alkanes on Pt(111): Dissociative Sticking Coefficients, Evans-Polanyi Relation, and Gas-Surface Energy Transfer. *J. Phys. Chem. C* **2010**, *114*, 17222.

(24) Cushing, G. W.; Navin, J. K.; Donald, S. B.; Valadez, L.; Johánek, V.; Harrison, I. Addition/Correction to: C-H Bond Activation of Light Alkanes on Pt(111): Dissociative Sticking Coefficients, Evans-Polanyi Relation, and Gas-Surface Energy Transfer (vol 114, pg 17222, 2010). *J. Phys. Chem. C* **2010**, *114*, 22790.

(25) DeWitt, K. M.; Valadez, L.; Abbott, H. L.; Kolasinski, K. W.; Harrison, I. Using Effusive Molecular Beams and Microcanonical Unimolecular Rate Theory to Characterize CH_4 Dissociation on Pt(111). *J. Phys. Chem. B* **2006**, *110*, 6705.

(26) DeWitt, K. M.; Valadez, L.; Abbott, H. L.; Kolasinski, K. W.; Harrison, I. Effusive Molecular Beam Study of C_2H_6 Dissociation on Pt(111). *J. Phys. Chem. B* **2006**, *110*, 6714.

(27) Lee, M. B.; Yang, Q. Y.; Ceyer, S. T. Dynamics of the Activated Dissociative Chemisorption of CH_4 and Implication for the Pressure Gap in Catalysis: A Molecular Beam-High Resolution Electron Energy Loss Study. *J. Chem. Phys.* **1987**, *87*, 2724.

(28) Navin, J. K.; Donald, S. B.; Tinney, D. G.; Cushing, G. W.; Harrison, I. Communication: Angle-Resolved Thermal Dissociative Sticking of CH_4 on Pt(111): Further Indication that Rotation is a Spectator to the Gas-Surface Reaction Dynamics. *J. Chem. Phys.* **2012**, *136*, 4.

(29) Cushing, G. W.; Navin, J. K.; Valadez, L.; Johanek, V.; Harrison, I. An Effusive Molecular Beam Technique for Studies of Polyatomic Gas-Surface Reactivity and Energy Transfer. *Rev. Sci. Instrum.* **2011**, *82*, 11.

(30) Cramer, C. J.; Truhlar, D. G. Density Functional Theory for Transition Metals and Transition Metal Chemistry. *PCCP* **2009**, *11*, 10757.

(31) Jackson, B.; Nave, S. The Dissociative Chemisorption of Methane on Ni(111): The Effects of Molecular Vibration and Lattice Motion. *J. Chem. Phys.* **2013**, *138*, 11.

(32) Abbott, H. L.; Bukoski, A.; Harrison, I. Microcanonical Unimolecular Rate Theory at Surfaces. II. Vibrational State Resolved Dissociative Chemisorption of Methane on Ni(100). *J. Chem. Phys.* **2004**, *121*, 3792.

(33) Abbott, H. L.; Bukoski, A.; Kavulak, D. F.; Harrison, I. Dissociative Chemisorption of Methane on Ni(100): Threshold Energy from $CH_4(2\nu_3)$ Eigenstate-Resolved Sticking Measurements. *J. Chem. Phys.* **2003**, *119*, 6407.

(34) Abbott, H. L.; Harrison, I. Dissociative Chemisorption and Energy Transfer for Methane on Ir(111). *J. Phys. Chem. B* **2005**, *109*, 10371.

(35) Abbott, H. L.; Harrison, I. Methane Dissociative Chemisorption on Ru(0001) and Comparison to Metal Nanocatalysts. *J. Catal.* **2008**, *254*, 27.

(36) Bukoski, A.; Blumling, D.; Harrison, I. Microcanonical Unimolecular Rate Theory at Surfaces. I. Dissociative Chemisorption of Methane on Pt(111). *J. Chem. Phys.* **2003**, *118*, 843.

(37) Ukraintsev, V. A.; Harrison, I. A Statistical Model for Activated Dissociative Adsorption: Application to Methane Dissociation on Pt(111). *J. Chem. Phys.* **1994**, *101*, 1564.

(38) Valden, M.; Pere, J.; Hirsimaki, M.; Suhonen, S.; Pessa, M. Activated Adsorption of Methane on Clean and Oxygen-Modified Pt{111} and Pd{110}. *Surf. Sci.* **1997**, *377*, 605.

(39) Rettner, C. T.; Pfnur, H. E.; Auerbach, D. J. Dissociative Chemisorption of CH_4 on W(110): Dramatic Activation by Initial Kinetic Energy. *Phys. Rev. Lett.* **1985**, *54*, 2716.

(40) Winters, H. F. The Activated, Dissociative Chemisorption of Methane on Tungsten. *J. Chem. Phys.* **1975**, *62*, 2454.

(41) Harris, J.; Simon, J.; Luntz, A. C.; Mullins, C. B.; Rettner, C. T. Thermally Assisted Tunneling: CH_4 Dissociation on Pt(111). *Phys. Rev. Lett.* **1991**, *67*, 652.

(42) Shen, X. J.; Lozano, A.; Dong, W.; Busnengo, H. F.; Yan, X. H. Towards Bond Selective Chemistry from First Principles: Methane on Metal Surfaces. *Phys. Rev. Lett.* **2014**, *112*, 5.

(43) Verhoef, R. W.; Kelly, D.; Mullins, C. B.; Weinberg, W. H. Angular and Vibrational Effects in the Direct Dissociative Chemisorption of Deuterated Methane and Ethane on Ir(110). *Surf. Sci.* **1995**, *325*, 93.

(44) Newell, H. E.; Oakes, D. J.; Rutten, F. J. M.; McCoustra, M. R. S.; Chesters, M. A. Impact-Induced Dissociation of Methane and Ethane on Pt(111) and $Pt_{0.25}Rh_{0.75}(111)$. *Faraday Discuss.* **1996**, *105*, 193.

Section 5 - Experimental Results for Pt(111)

5.1 Methane

5.1.1 Ambient Gas Dosing DSC Measurements

Although ambient gas dosed DSC measurements, $S_{bkg}(T_g = 295\ K, T_s)$, of methane on Pt(111) were measured previously by Cushing et al.,[1,2] it was determined that the S_{bkg} asymptotically approached a limiting value of $1*10^{-7}$ with decreasing T_s. This is believed to have been the result of impurities present in the reagent methane used to conduct the DSC measurements. Therefore, additional ambient gas dosed DSCs were measured using purified methane. In order to further purify the methane gas, a filter was added to the gas manifold, which had the ability to remove a wide range of gases. The (Model 2-2450-U, Supelco) filter employed would essentially remove any impurity that was not hydrogen, methane, or a noble gas. The filter contains a combination of transition metal oxide powders of copper, nickel, manganese, cobalt, and aluminum which are highly reactive.[3] O_2 concentrations in the gas can be reduced to 2 ppb when the initial concentration is less than 10 ppm,[4] and it assumed that the same standard applies to more reactive impurities. Methane, in continuous flow through the filter, was used for DSC measurements.

The DSC is directly proportional to the amount of carbon remaining on the surface after reaction. Therefore, carbonaceous impurities with high DSC values, present in the reagent gas, would cause the total amount of deposited carbon to be higher than expected, and so the calculated DSC will be larger than expected. When no impurities are present in the reagent gas, then the measured DSC would be the true DSC. However, if the impurities contribute substantially to the total deposited carbon then the measured DSC is only an apparent DSC.

The apparent DSC, $S_{apparent}$, incorporates the carbon deposited by both the reagent as well as the impurities such that,

$$S_{apparent} = \frac{\theta_c}{F} = \frac{\sum_i S_i F_i n_i}{\sum_i F_i} \qquad \text{Equation 5.1}$$

where S_i is the DSC, F_i is the flux, and n_i is the number of carbon atoms in the dissociating molecule. By defining $F_i/\sum_i F_i$ as the percent concentration, C_i, then $S_{apparent}$ takes on the form,

$$S_{apparent} = S_{reagent} * C_{reagent} * n_{reagent}$$

$$+S_{impurity} * C_{impurity} * n_{impurity} \qquad \text{Equation 5.2}$$

Assuming the concentrations are held constant and $C_{reagent} >> C_{impurity}$, then $S_{impurity}$ would have to be large in order to affect $S_{apparent}$, therefore, it is assumed that $C_{reagent} = 1$ and $S_{impurity} = 1$. With these assumptions, $S_{apparent}$ is redefined as,

$$S_{apparent} = S_{reagent} + C_{impurity} * n_{impurity} \qquad \text{Equation 5.3}$$

for methane, since $n_{reagent} = 1$. If $C_{impurity} * n_{impurity}$ is set to a reasonable value of $1*10^{-7}$, then a plot of $S_{apparent}$ versus $S_{reagent}$ would look very similar to Figure 5.1. When $S_{reagent}$ is relatively large, the contribution of the impurities is negligible and when $S_{reagent} << C_{impurity}*n_{impurity}$, the curve approaches an asymptotic DSC value equal to $C_{impurity}*n_{impurity}$.

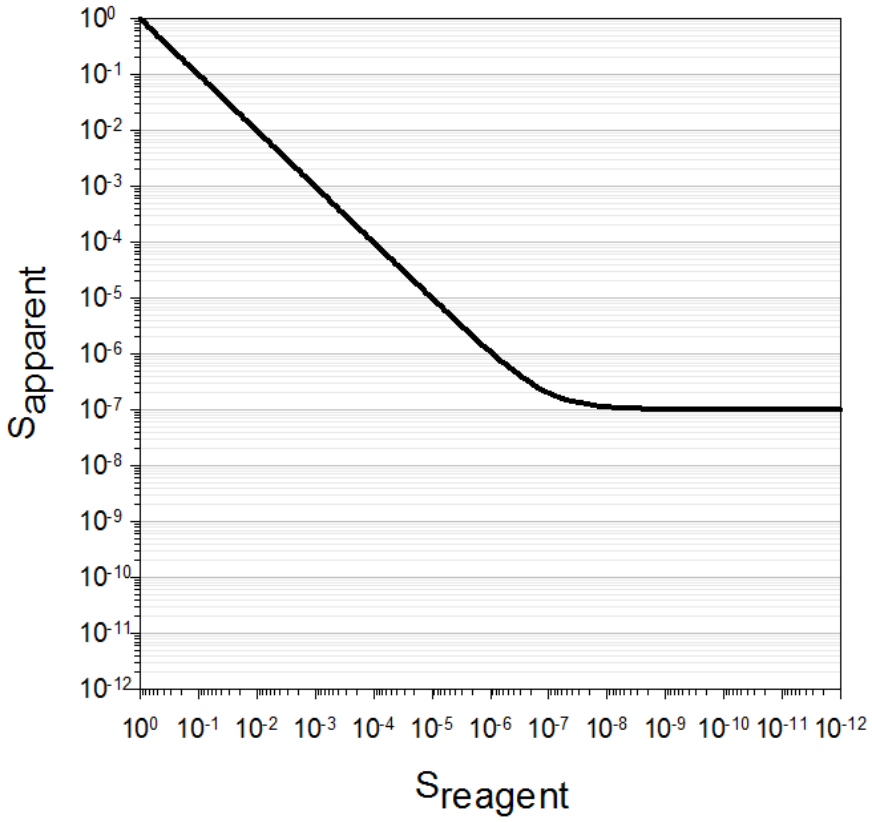

Figure 5.1: Theoretical plot of $S_{apparent}$ versus $S_{reagent}$ with $C_{impurity}$ * $n_{impurity}$ held constant at a value of $1*10^{-7}$. When $S_{reagent}$ is relatively large, the contribution of the impurities is negligible and when $S_{reagent} << C_{impurity}*n_{impurity}$, the curve approaches an asymptotic DSC value equal to $C_{impurity}*n_{impurity}$.

The current S_{bkg} and the S_{bkg} of Cushing et al. for methane on Pt(111) are shown in Figure 5.2. The current S_{bkg} were measured only for the surface temperature range of 600 K to 1000 K. At lower T_s, the DSC values are so low that the time constant for completion made the experiments not feasible to conduct (ca., days or longer). Although it would be possible to increase the pressure in the chamber, there is a limit to the highest pressure that can be used. Since the crystal is heated, the experiments must be conducted in the molecular flow regime where molecule-wall collisions dominate molecule-molecule collisions. If the experiments are not conducted in molecular flow, then the gas would be heated by convection, and thus the gas is no longer ambient gas with T_g = 295 K. The directed DSCs were limited to the surface temperature of 900 K and 1000 K because the effusive molecular beam must be operated in molecular flow as well. The experiments could be conducted, but the time required for experiment completion is extremely long (ca., days). The current S_{bkg} increase with increasing temperature as with the Cushing et al. data, because methane dissociative chemisorption on Pt(111) is an activated process. However, the current S_{bkg} do not approach an asymptotic value, and the ratio of the Cushing et al. data to the current S_{bkg} data increases substantially as T_s is decreased.[1,2] Since $S_{reagent}$ decreases as T_s decreases, the impurities become more apparent in the Cushing et al. data. Although S_{bkg} was not measured for T_s < 600 K, there is at least an order of magnitude difference between the S_{bkg} values currently measured and those of Cushing et al. at T_s = 600 K. Therefore, the impurity level was reduced by at least an order of magnitude to $1*10^{-8}$ and most likely is reduced to an even lower value given that the current S_{bkg} do not approach an asymptotic DSC value.

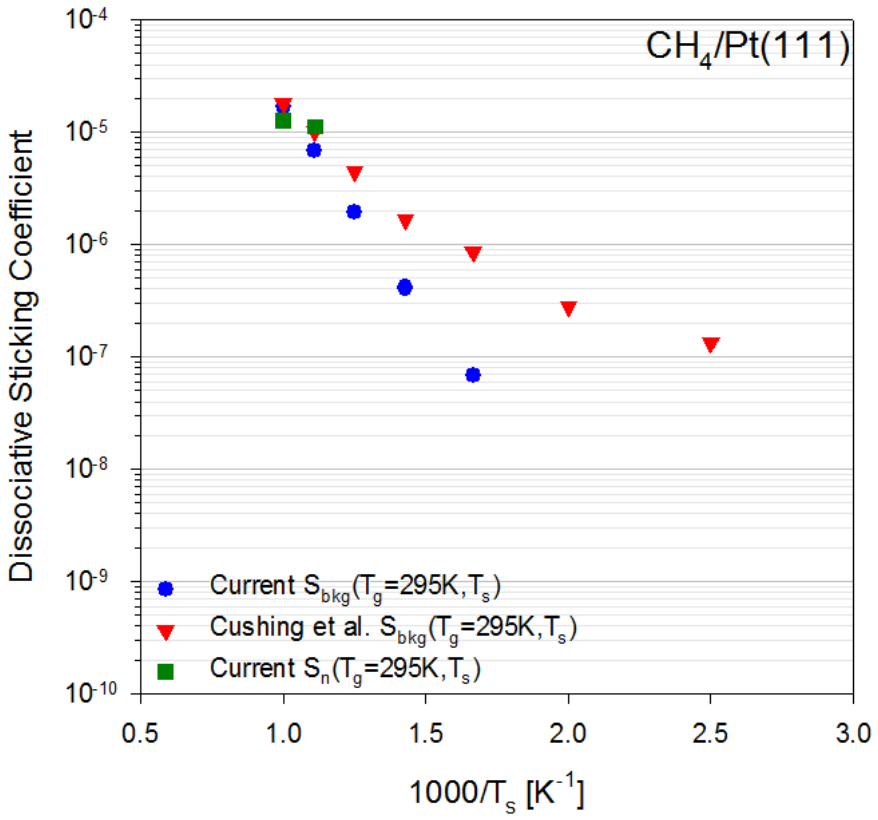

Figure 5.2: Plot of current S_{bkg}, Cushing et al. S_{bkg}, and current S_n for methane on Pt(111). The Cushing et al. S_{bkg} approach an asymptotic value of $1*10^{-7}$ whereas, the current S_{bkg} does not.

As seen from Figure 5.2, for the recently measured directed DSC values, $S_n(T_g, T_s)$, $S_n(T_g = 295\ K, T_s = 900\ K)$ has a value of $1.12*10^{-5}$, which is larger than the value for $S_{bkg}(T_g = 295\ K, T_s = 900\ K)$ of $6.77*10^{-6}$. This result is reasonable since the directed gas is more reactive than S_{bkg}. However, $S_n(T_g = 295\ K, T_s = 1000\ K)$ has a value of $1.26*10^{-5}$ which is less than the value for $S_{bkg}(T_g = 295\ K, T_s = 1000\ K)$ of $1.69*10^{-5}$. This result does not make physical sense because the directed gas should be more reactive than ambient gas. However, at high temperatures, the reactivity of the ambient and directed DSCs is quite similar. In addition, as discussed in section 3.2.2, the directed component of the DSC is actually calculated from the remainder of deposited carbon after the background contribution has been removed. Therefore, if S_{bkg} is slightly high, then the directed component appears less than the actual value. Thus the values are essentially equal.

5.1.2 Angle-Resolved DSC Measurements

Angle-resolved DSCs (ar-DSCs) were measured for methane on Pt(111) at $T_g = T_s = T = 700\ K$, $S(\vartheta; T = 700\ K)$, using two different effusive molecular beam doser designs. The measured DSCs provided a benchmark for testing the ability of the d-PMMT model to predict angular distributions. In addition, the thermal DSC of a gas in thermal equilibrium with the surface can be calculated by integrating the angular distribution,

$$S(T) = \int \frac{\cos\vartheta}{\pi} S(T;\vartheta) d\Omega \qquad \text{Equation 5.4}$$

The ar-DSC measurements were conducted by centering the effusive beam flux at different locations on the crystal and then measuring the post-dosed carbon by moving the crystal through the Auger electron beam and measuring the carbon profile across the surface. The angle of impingement is calculated based on the geometry of the doser and the centerline of the effusive

beam flux. The Auger electron beam width, using the PHI model 15-255 GAR double-pass cylindrical mirror analyzer with internal electron gun, is ~0.2 mm according to the manufacturer.[5]

S(ϑ; T = 700 K) values were calculated for each particular angle, and then all of the ar-DSCs were fit to the functional form,

$$S(\vartheta;T) = S_0 cos^n(\vartheta) \qquad \text{Equation 5.5}$$

where ϑ is the molecular angle of incidence away from the surface normal. Figure 5.3 shows S(ϑ; T = 700 K) for methane on Pt(111) for the two dosers as well as the d-PMMT model fit. Each data point is an average of multiple experiments, and error bars are indicative of an individual measurement. "Doser 1" corresponds to the original doser design from Cushing et al. that was found to emit potassium at $T_g \geq 900$ K, whereas "doser 2" corresponds to the current doser design (Section 2.4) and is the doser design used in all experiments throughout the remainder of the dissertation unless otherwise specified. The absolute intensity, as well as the degree of sharpness, for both distributions is approximately the same; Doser 1 has a distribution of the form, $8.2*10^{-5}\cos^{14.5}(\vartheta)$ and Doser 2 has a distribution of the form, $7.0*10^{-5}\cos^{11.1}(\vartheta)$. The average distribution of the two dosers is calculated to be $7.6*10^{-5}\cos^{12.8}(\vartheta)$ which, is quite similar to the d-PMMT model prediction of $5.0*10^{-5}\cos^{12.1}(\vartheta)$. Although the normal component of the experimentally derived fit is a factor of 1.5 times higher than the d-PMMT model prediction, the PMMT models, with parameters fixed by supersonic molecular beam experiments, slightly underestimate DSCs for most effusive molecular beam experiments. The d-PMMT model was used to reproduce the angle-resolved DSCs because supersonic molecular beam and effusive molecular beam results have confirmed that methane dissociative chemisorption on Pt(111) behaves dynamically,[6,7] and rotation is a spectator degree of freedom.[8-11] The angle-integrated

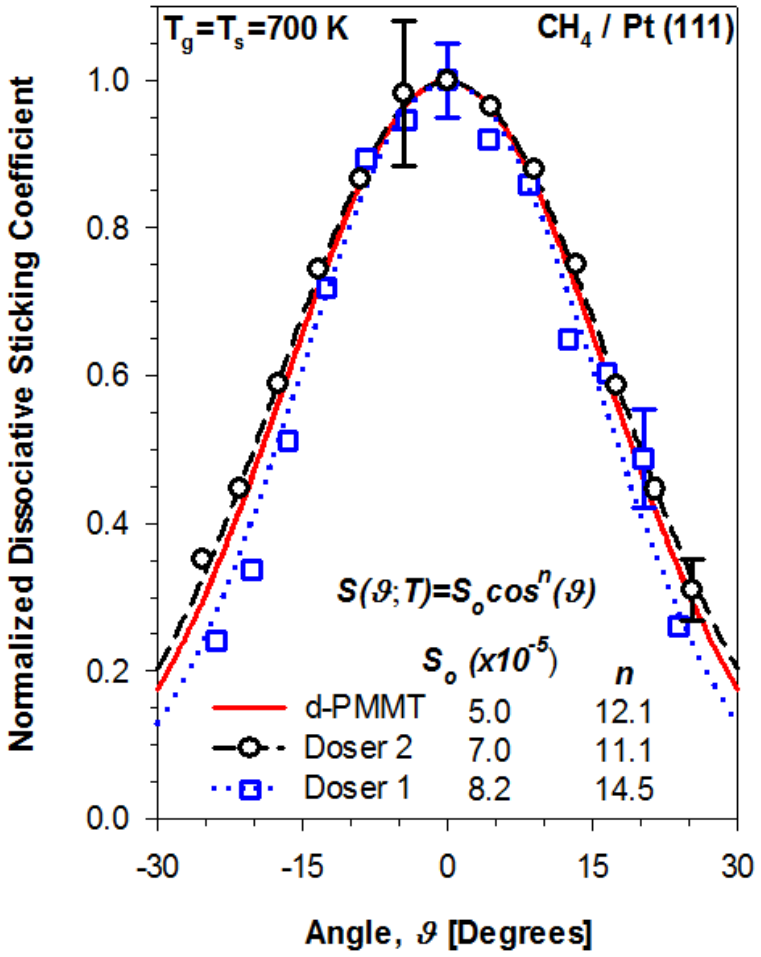

Figure 5.3: Angle-resolved DSCs measured at T = 700 K, S(ϑ; T = 700 K), for methane on Pt(111), using two different doser designs, compared to the d-PMMT model prediction. The error bars correspond to the relative error for an individual measurement.

value of the two DSC distributions yields a value for the thermal DSC of $9.94*10^{-6}$ and $1.07*10^{-5}$ for Doser 1 and Doser 2 respectively, with the average being ~$1.03*10^{-5}$.

5.1.3 Angle-Resolved DSC Measurements on K doped-Pt(111)

The "doser 2" design, mentioned in section 5.1.2, is the current effusive molecular beam doser design being implemented and is discussed in detail in section 2.4. A full explanation of "doser 1" is discussed elsewhere,[12] and will be repeated in short here. "Doser 1" was designed to have an alumina sleeve covering a stainless steel nozzle. To construct the doser, the alumina sleeve was first wrapped with a tungsten wire over the entire length of the sleeve. The wire wrapped sleeve was then dipped in an alumina slurry, consisting of Ceramabond 569 (Aremco) and 569-T solvent (Aremco), and allowed to dry. This process was repeated several times until the alumina tube was fully coated by a relatively thick layer of alumina slurry. The alumina slurry, however, contained another compound besides alumina powder and water. The slurry also contained the binding agent, potassium silicate (K_2SiO_3) which held the alumina oxide powder together. Although little to no research exists on the decomposition of K_2SiO_3, the K_2SiO_3 was found to decompose and emit potassium at gas temperatures of 900 K and higher. At a gas temperature of 900 K, enough potassium was emitted from the doser to be measurable by Auger analysis after 3 minutes of deposition with the sample surface held at T_s = 400 K. Although the gas temperature was 900 K, the filament temperature was most likely in excess of 1200 K. At T_g = 700 K, however, there was no measurable potassium coverage from doser 1, which is why the angular distributions of both dosers appear quite similar. The new doser, "doser 2," was constructed using high purity alumina and was initial outgassed at T_g = 1100 K for several days in order to remove any volatile impurities. The crystal was then placed in front

of the doser for 30 minutes at T_g = 1100 K and T_s = 400 K. Afterwards, Auger electron spectroscopy confirmed that no other elements were present in detectable amounts on the crystal surface. Therefore, doser 2 is free of potassium.

Initial measurements of S(ϑ; T = 900 K) of methane on Pt(111), using doser 1, yielded an angular distribution that was extremely sharp with a functional form of $1.8*10^{-3}\cos^{22.4}(\vartheta)$. However, this was difficult to rationalize with any physical argument. The surface contributes a great deal of energy to the dissociating molecule thus strongly affecting reactivity, and the surface energy is invariant to the angle of impingement. Therefore, an increase in surface temperature should cause the angular distribution to broaden, not to sharpen.
S(ϑ; T_g = 900 K, T_s = 700 K) was then measured so that a direct comparison could be made to S(ϑ; T = 700 K). Interestingly enough, the angular distribution could not be calculated properly because the peak intensity and integrated value of the platinum Auger peak at 248 eV was not in proper ratio to the platinum Auger peak at 237 eV. In addition, there was little or no change of the carbon peak at 272 eV. The ratios of the platinum Auger peaks should never change since the intensities and shape of Auger peaks are dependent on the element and not the bonding state. However, there was even more mystery surrounding the supposed carbon peak. By cross checking the measured Auger peaks with Auger spectra of other elements, it was determined that potassium was the only candidate that had Auger peaks that could affect both the platinum and carbon Auger peaks simultaneously. Two potassium Auger peaks exist at 252 eV and 276 eV, which match almost perfectly to the platinum 248 eV peak and the carbon 272 eV peak. Later, it was discovered that the alumina slurry contained the binding agent K_2SiO_3 which was determined to be the source of potassium. Therefore, S(ϑ; T = 900 K) was actually an angular distribution measured for a K/Pt(111) surface.

Although the steady-state coverage of potassium was initially unknown, it is possible to calculate the coverage, if the rate of deposition and rate of desorption are known. Alkali metals desorb from platinum at significantly high temperature, which is why potassium could not be detected when measuring S(ϑ; T = 900 K) but was detectable at lower surface temperatures. During an experiment, doser 1 emitted potassium at a constant rate while potassium was simultaneously desorbed from the surface. Therefore, the steady-state potassium coverage was small enough that it was difficult to discern using AES. In order to determine the deposition rate of potassium on the surface, potassium was dosed onto the surface at T_s = 400 K and T_s = 700 K. The lowest surface temperature (400 K) was chosen to inhibit CO and H_2 adsorption on the surface and T_s = 700 K was chosen as the higher temperature to determine if potassium remains on the surface in detectable amounts at an elevated surface temperature. At these temperatures, the desorption rate of potassium is negligible for low coverage, such that the deposition rate could be calculated.

The crystal was heated to the desired temperature and placed in front of doser 1 for a period of time and then an Auger analysis was conducted to determine the potassium coverage. The first derivative Auger spectra of the platinum peak at 252 eV was compared to the potassium/platinum peak at 272 eV and the potassium was calculated as the ratio between the two; the potassium calibration values were taken from Lehmann et al.[13] At T_s = 900 K, the surface temperature is high enough to allow for fast desorption of potassium. The TPD desorption kinetics for potassium on Pt(111) were determined using the analysis by Albano.[14] The desorption rate of alkali atoms leaving a metal surface is defined as,

$$-\frac{dN}{dt} = \nu_0 N e^{-E_D(N)/(RT)} \qquad \text{Equation 5.6}$$

where N is the number of adsorbed alkali atoms per unit area, v_0 is the pre-exponential factor, $E_D(N)$ is the activation energy for desorption, R is the ideal gas constant, and T is the surface temperature. Because the desorption rate of alkali atoms is strongly surface coverage dependent, the activation energy must be rewritten such that,

$$E_D(N) = E_D(\theta = 0) - E_R(\theta) \qquad \text{Equation 5.7}$$

where $E_D(\theta = 0)$ is the zero coverage desorption energy and $E_R(\theta)$ is the coverage dependent desorption energy. The author assumes that the surface alkali atoms can be treated as polarized dipoles such that, electrostatic repulsions of the atoms reduce the energy required for desorption. For brevity, after making assumptions about the electrostatics, the resulting functional form of $E_R(\theta)$ can be written as,

$$E_R(\theta) = \frac{9*P(\theta=0)^2\theta^{3/2}}{(1+9\alpha\theta^{3/2})^2} \qquad \text{Equation 5.8}$$

where $P(\theta = 0)$ is the dipole moment of an isolated adatom and α is the effective polarizability of the alkali-substrate complex. Thus, the full expression for alkali desorption can be written as,

$$-\frac{d\theta}{dt} = \nu_0\theta e^{((\frac{9*P(\theta=0)^2\theta^{3/2}}{(1+9\alpha\theta^{3/2})^2})-E_D(\theta=0))/(RT)} \qquad \text{Equation 5.9}$$

From Auger analysis, we determined that total deposition rate of potassium is $1.27*10^{15}$ atoms m^{-2} s^{-1}. Dividing by the areal density of platinum [$1.502*10^{19}$ atoms ML^{-1} m^{-2}] yields the deposition rate in terms of platinum monolayers,

$$\frac{d\theta_{dep}}{dt} = 8.453 * 10^{-5} ML\ s^{-1} \qquad \text{Equation 5.10}$$

Thus, the total time-dependent coverage is expressed as,

$$\frac{d\theta_{cov}}{dt} = \frac{d\theta_{dep}}{dt} + \frac{d\theta}{dt} =$$

$$8.453 * 10^{-5} - (\nu_0 \theta_{cov} e^{((\frac{9*P(\theta=0)^2(\theta_{cov})^{3/2}}{(1+9\alpha(\theta_{cov})^{3/2})^2}) - E_D(\theta=0))/(RT)}) \quad \text{Equation 5.11}$$

where θ_{cov} is the potassium coverage in terms of platinum monolayers. Although this equation cannot be solved exactly, the steady state coverage can be easily determined by setting $d\theta_{cov}/dt = 0$ and solving for N_{cov}. Using the values for the K/Pt(111) system: $P(\theta = 0)$ = 11.5 D, α = 17.2 Å^3, $E_D(\theta = 0)$ = 65 kcal/mol, and $\nu_0 = 10^{13}$s^{-1}, the steady state coverage was determined to be 0.025 ML with respect to platinum.

When the current effusive molecular beam doser was implemented, "doser 2," it was found that it did not emit potassium at gas temperatures up to 1100 K. S(ϑ; T = 900 K) was then measured so that it could be compared to the previous doser design. Figure 5.4 shows the ar-DSCs for S(ϑ; T = 900 K) for methane on Pt(111) (Doser 2) and for methane on K/Pt(111) (Doser 1). Each data point is an average of multiple experiments, and the error bars are indicative of an individual measurement. S(ϑ; T = 900 K) measured using doser 2, yielded a distribution of $1.6*10^{-3}\cos^{10.7}(\vartheta)$ which, is substantially broader than the distribution measured for doser 1. However, S_0 was quite similar for both distributions, therefore, S(T) was calculated for both doser designs so that a comparison could be made. Table 5.1 shows the calculated values for both dosers at T = 700 K and T = 900 K. From the table, it can be seen that the ratio of (S_{Doser2}(T = 900 K)/S_{Doser1}(T = 900 K)) is 1.70, whereas S_{Doser2}(T=700 K)/S_{Doser1}(T=700 K)) is equal to 1.08. In addition, S(ϑ = 0; T = 900 K) is very similar for both dosers. Therefore, it would seem that the potassium on the Pt(111) surface is affecting the angular variation of the DSCs more so than the DSC measured normal to the surface.

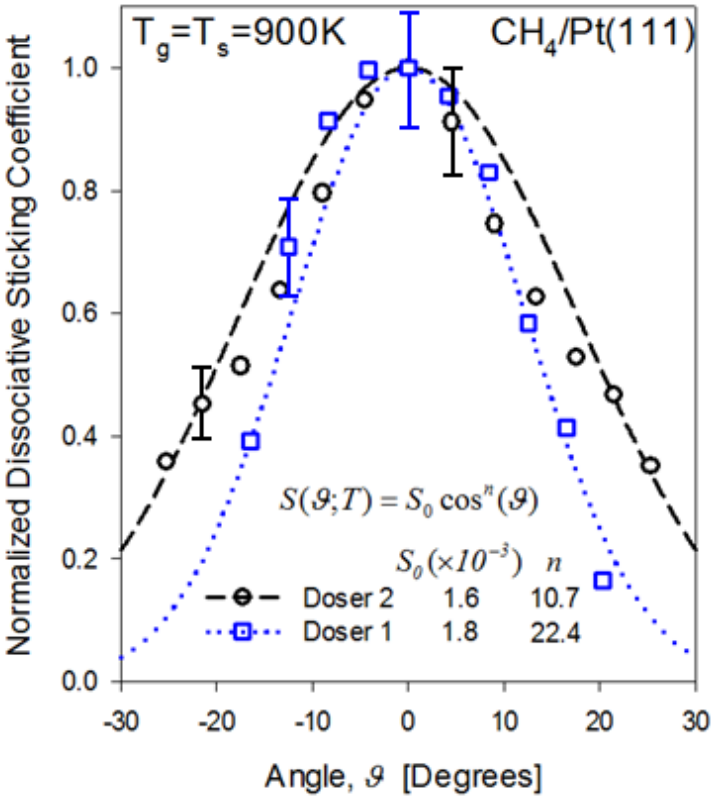

Figure 5.4: Angle-resolved DSCs measured at T = 900 K, S(ϑ; T = 900 K), for methane on Pt(111) (Doser 2) and K/Pt(111) (Doser 1). The error bars correspond to the relative error for an individual measurement.

Doser	S(ϑ; 700 K)	S(700 K)	S(ϑ; 900 K)	S(900 K)
Doser 1	$8.2 * 10^{-5} \cos^{14.5}$	$9.94 * 10^{-6}$	$1.8 * 10^{-3} \cos^{22.4}$	$1.48 * 10^{-4}$
Doser 2	$7.0 * 10^{-5} \cos^{11.1}$	$1.07 * 10^{-5}$	$1.6 * 10^{-3} \cos^{10.7}$	$2.52 * 10^{-4}$
Doser 2/Doser 1	----------	1.08	----------	1.70

Table 5.1: Measured S(ϑ; T) and calculated S(T) for doser 1 and doser 2 at T = 700 K and 900 K. All S(ϑ; T) and S(T) correspond to CH_4/Pt(111), expect for doser 1 at T = 900 K, which corresponds to CH_4/K/Pt(111).

Bengaard et al. has shown that for CH_4 dissociative chemisorption on Ni(100) and Ni(111), DSCs decrease as a function of potassium coverage.[15] His work was conducted via ambient gas dosing of 300 K methane and is therefore similar to our angle integrated DSC values. The authors' DSC values are for a nickel single crystal and the surface temperatures are T_s = 475 K and T_s = 500 K. The average value for the ratio $(S_0(\theta_{K,\ 0ML})/S_0(\theta_{K,\ 0.025ML}))$ for methane dissociative chemisorption on Ni(111) at T_s = 475 K and T_s = 500 K is 2.5. The angle-integrated, thermal DSC is defined as being equal to the DSC of a thermalized gas distribution impinging randomly on a surface. Therefore, it is possible to make some comparisons between the authors' data and our S(T) data. The ratio of $(S_{Doser2}(T = 900\ K)/S_{Doser1}(T = 900\ K))$ is 1.70 for Pt(111), whereas the ratio for Ni(111) is much larger at a value of 2.5. The ratios are most likely dissimilar because at lower surface temperatures, the surface contributes less energy to dissociation and so, dynamics play a more significant role such that potassium adsorption should affect the reactivity to a higher degree. Previous studies concerning the dissociation of H_2 and D_2 on potassium covered Pt(111) have shown that there is a drastic reduction in the DSC with increasing potassium coverage.[16,17] In fact, the DSC of H_2 on Pt(111) at T_s = 150 K is reduced

by a factor 5 with a only a small coverage of potassium (0.022 ML). H_2 dissociation has already been shown to behave extremely dynamically on Cu(111) and most likely behaves similarly for other surfaces.[18] According to Brown et al.,[17] potassium acts as a poison on the Pt(111) surface by reducing the surface work function. Because of the reduced surface work function, electron density from the surface can extend further from the surface thus, allowing for enhanced Pauli repulsion; molecules impinging on such a surface must overcome this barrier with normal translational energy. Therefore, there is an increase in the relative importance of normal translational energy for promoting reaction on the potassium doped surface. Molecules that strike this surface at high angles of incidence have a deficit in normal translational energy which results in a substantial decrease in the DSC. This is a possible explanation for why the angular dependence is so different between the CH_4/Pt(111) and CH_4/K/Pt(111) systems, while $S(\vartheta = 0; T = 900\ K)$ is basically the same.

5.1.4 Summary

Current ambient dosed DSCs were measured for methane on Pt(111) using reagent methane that was purified using an inline filter. The measured DSCs are lower than those measured by Cushing et al. and do not approach an asymptotic value over the temperature range that DSCs were measured. Angle resolved DSCs were measured for methane on Pt(111) at $T = 700\ K$ and $T = 900\ K$ as well as for methane co-dosed with potassium on Pt(111) at $T = 900\ K$ using two different effusive molecular beam doser designs. For the methane/Pt(111) system, it was found that $S(\vartheta; T = 700\ K)$ remained relatively constant for both doser designs and the average angular distribution had the functional form of $7.6*10^{-5}\cos^{12.8}(\vartheta)$. The d-PMMT model was used to predict the distribution with excellent results, and the thermal DSC,

S(T = 700 K), was calculated to be $1.03*10^{-5}$. For the methane/K/Pt(111) system, a calculated steady-state coverage of 0.025 ML of potassium was present on the surface and it was determined that the angular distribution at T = 900 K, S(ϑ; T = 900 K), was relatively sharp with a functional form of $1.8*10^{-3}\cos^{22.4}(\vartheta)$. After the doser design was completely redesigned, the newly measured S(ϑ; T = 900 K) was found to vary as $1.6*10^{-3}\cos^{10.7}(\vartheta)$. The ratio ($S_{Doser2}$(T = 900 K)/$S_{Doser1}$(T = 900 K)) was 1.70. The increased sharpness of the distribution as well as the decrease in the thermal DSC is believed to stem from the fact that potassium behaves as a poison on Pt(111) which enhances Pauli repulsion, causing normal translational energy to become more important in surmounting the barrier for reaction.

5.2 Angle-Resolved Dissociative Sticking Coefficients

5.2.1 Introduction

Angle-resolved DSCs (ar-DSCs), serve a dual purpose. By measuring ar-DSCs and integrating over the cosine angular distribution, appropriate to thermal equilibrium reactivity, it is possible to calculate the thermal DSC, which is relevant to catalysis where gas is dissociating on a surface in thermal equilibrium. In addition, ar-DSCs give the unique ability to resolve whether systems behave statistically, where all exchangeable energies from different degrees of freedom are equivalent, or dynamically, where not all energies may be exchangeable or equivalent.

As stated previously, the energy for surface reactions is derived from the translational, vibrational, and rotational energy of an impinging molecule, and the energy supplied by the surface. Translational energy is unique for alkane dissociative chemisorption on Pt(111), because only the normal component of translational energy affects DSCs. In addition, normal

translation is the only active degree of freedom that varies with the angle of incidence. Thus, as the angle of impingement changes from 0 degrees to 90 degrees, the amount of normal translational energy decreases while energy from the other degrees of freedom remain constant. Therefore, the relative sharpness of the ar-DSC distribution reveals the importance of normal translational energy in overcoming the barrier for dissociation. For an early barrier reaction which is strongly activated by normal translational energy, the distribution would be sharp because the relative importance of vibrational and rotational energy is diminished compared to normal translational energy. Dynamical constraints on exchangeable vibrational and rotational energy can also cause a sharpening of ar-DSC distributions. In addition, dynamical constraints also reduce the absolute magnitude of DSCs. Therefore, by coupling ar-DSCs with results from non-equilibrium DSC measurements, $S_n(T_g, T_s)$, and effective modeling, it is possible to resolve whether or not a system behaves statistically or dynamically.

5.2.2 Methane/Pt(111)

For the methane/Pt(111) system, $S(\vartheta; T = 700\ K)$, fit to the functional form of Equation 5.5, and was found to be relatively sharp with a distribution of $7.6*10^{-5}\cos^{12.8}(\vartheta)$. The angular distribution was reproduced well using the d-PMMT model with parameters fixed by supersonic molecular beam experiments from Luntz.[8,19,20] Figure 5.5 shows $S(\vartheta; T = 700\ K)$ for methane on Pt(111) for the two doser designs. "Doser 1" refers to the original doser design as discussed in sections 5.1.2 and 5.1.3 and "Doser 2 refers to the current doser design as discussed in section 2.4. "Doser 2" was used for all other experiments not concerning methane. Each data point in Figure 5.5 is an average of multiple experiments, and the error bars are indicative of an individual measurement. Both distributions are relatively similar which shows the effectiveness of our experimental method. Since methane behaves dynamically on Pt(111), it would follow

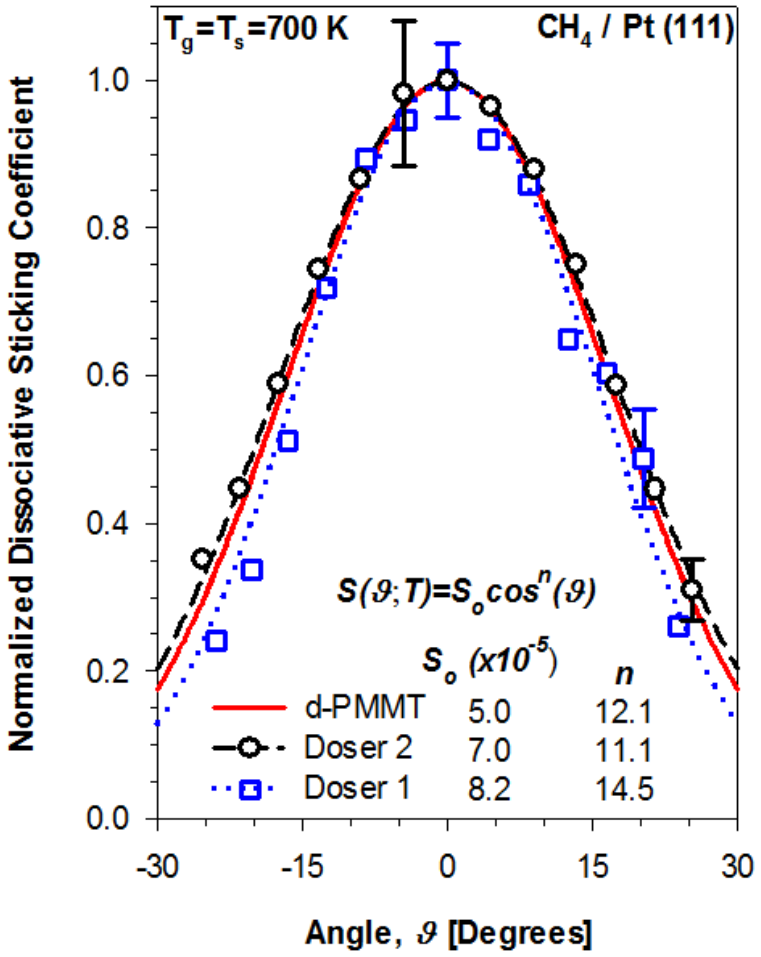

Figure 5.5: Angle-resolved DSCs measured at T = 700 K, S(ϑ; T = 700 K), for methane on Pt(111), using two different doser designs, compared to the d-PMMT model prediction. The error bars correspond to the relative error for an individual measurement.

that the dynamical restrictions on exchangeable energy enhances the importance of normal translational energy resulting in a sharp angular variation of the DSC. Studies have shown that vibrational energy is on average only 40% as efficacious as normal translational energy, and rotational energy is a spectator for promoting dissociation of methane on Pt(111).[6,8,21,22] Therefore, the d-PMMT model yields a sharply peaked S(ϑ; T = 700 K) because, with rotation held as a spectator degree of freedom and vibrational energy discounted by 60%, the relative importance of normal translational energy to surmount the activation barrier is enhanced. As the angle of incidence is varied from 0 degrees to 90 degrees, the amount of normal translational energy decreases drastically and since there is much less exchangeable vibrational energy and no exchangeable rotational energy, there is little energy available at high angle. The master equation PMMT models, that explicitly handle gas-surface energy transfer, were unnecessary to apply because the time constant for desorption (~100 fs) at energies sufficient to react is so short that there is no time for significant gas-surface energy transfer to occur.[23]

5.2.3 Ethane/Pt(111)

The S(ϑ; T = 700 K) distribution measured for ethane on Pt(111) is much broader than the methane/Pt(111) system and has a $\cos^{5.6}(\vartheta)$ component in its angular variation. Ethane has 9 additional vibrational modes compared to methane and so has a larger pool of exchangeable vibrational energy. Therefore, there is more energy available for dissociation at higher angle, and theory suggests that S(ϑ; T = 700 K) could be fit to the functional form,

$$S(\vartheta;T) = S_0 cos^n(\vartheta) + S_{90^\circ} \qquad \text{Equation 5.12}$$

where (S_0 + S_{90°) and S_{90° are the DSCs for molecules striking the surface at 0 and 90 degrees from the surface normal respectively. Physically, S_{90° is also the DSC of a molecule with no

normal translational energy impinging on the surface. Technically this parameter also exists for the methane/Pt(111) system, but because normal translational energy is so essential to the reactivity for this system, the angular distribution is very sharp and S_{90° is negligibly small. When fit to Equation 5.12, the ar-DSC distribution for ethane on Pt(111) can be expressed as $3.11*10^{-4}\cos^{5.6}(\vartheta) + 1.41*10^{-4}$. Figure 5.6 shows $S(\vartheta; T = 700\ K)$ for ethane on Pt(111) and the corresponding PMMT model predictions. Each data point in the figure is an average of multiple experiments, and the error bars are indicative of an individual measurement. For each model, both S_0 and S_{90° were fit using $S_n(T_g, T_s)$ data from Cushing et al.[2] The normal component of the ethane ar-DSC distribution, $(S_{90^\circ} + S_0)$, is significantly larger than that of methane; however, the distribution is much broader. Although there is a great deal of literature available about the dynamical nature of methane dissociative chemisorption on Pt(111), there is very little data for larger alkanes. Larger molecules in the gas phase tend to undergo intramolecular vibrational energy redistributions (IVR) at vibrational densities of state greater than 10 states/cm^{-1} such that, if a coherent vibrational superposition state is excited, that energy can then be redistributed to other vibrational modes.[24] Many of the vibrational eigenstates contain some component of C-C bond vibration as well as C-H bond vibration. Therefore, a C-H bond stretch excitation can dephase into many other vibrational modes. In addition, eigenstate-state resolved experiments are typically only feasible with supersonic molecular beams with extremely low vibrational and rotational temperatures such that the molecular population is not overly diffusely spread across many thermally populated states.

Because there is no definitive proof as to whether or not ethane or larger molecules behave dynamically, $S(\vartheta; T = 700\ K)$ for ethane on Pt(111) was predicted using several variations of the PMMT model: the statistical model, s-PMMT, the dynamical model, d-PMMT,

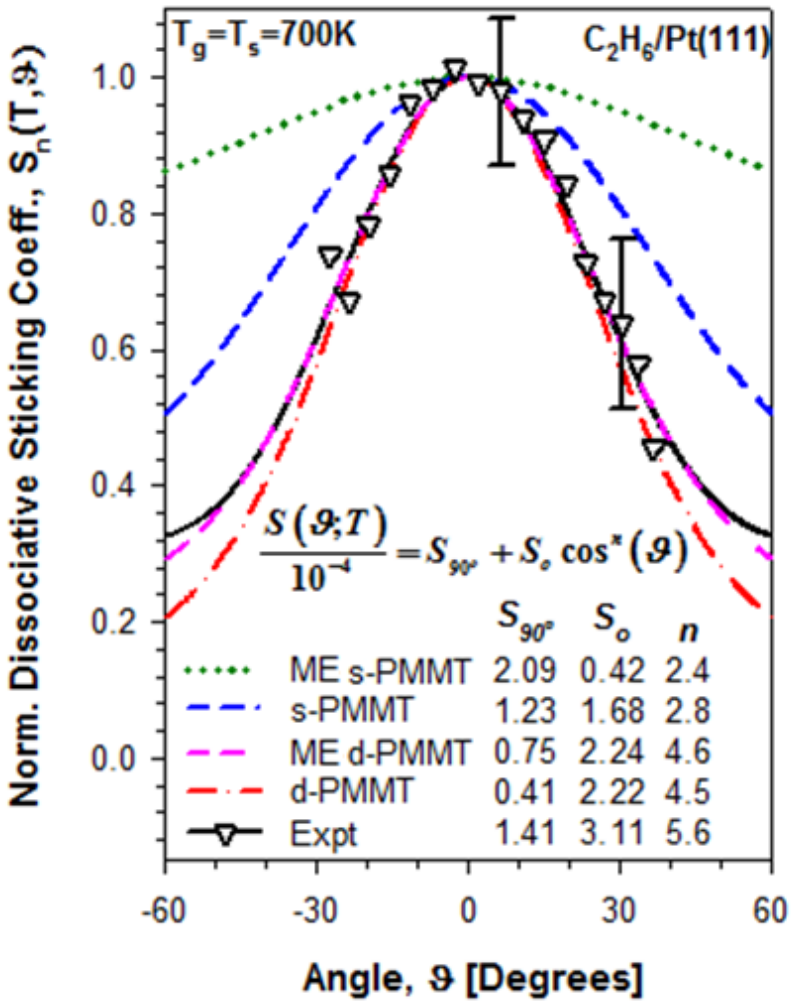

Figure 5.6: Angle-resolved DSCs measured at T = 700 K, S(ϑ; T = 700 K), for ethane on Pt(111) compared to the several PMMT model predictions. The error bars correspond to the relative error for an individual measurement.

a statistical master equation model, ME s-PMMT, and a dynamical master equation model, ME d-PMMT. Model parameters were fixed by fitting to the Cushing $S_n(T_g, T_s)$ data and then $S(\vartheta; T)$ distributions were predicted. Both of the statistical models overestimate the broadness of the angular distribution because a statistical model assumes that at sharper incidence angles, the vibrational and rotational energies compensate for the lack of normal translational energy. On the other hand, both dynamical models properly predict the sharpness of the distribution, but the dynamical master equation fits the data most accurately. The gas-surface energy transfer is enhanced for ethane because of the increase in the rovibrational density of states compared to methane; this increased density of states should enhance the PC density of states and allow better PC-phonon coupling. In addition, the ethane has a longer desorption lifetime at reactive energies (~2 ps) compared to methane,[1,2] such that there is more time to undergo gas-surface energy transfer.

5.2.4 Propane/Pt(111)

By far, propane exhibits the most statistical behavior of the three alkanes under study. $S(\vartheta; T = 700\ K)$ measured for propane on Pt(111), was fit to the same functional form as ethane; the expression for $S(\vartheta; T = 700\ K)$ is $7.8*10^{-4}\cos^{1.10}(\vartheta) + 5.3*10^{-4}$. Figure 5.7 shows $S(\vartheta; T = 700\ K)$ for propane on Pt(111) as well as PMMT model predictions. Each data point in the figure is an average of multiple experiments, and the error bars are for an individual measurement. Both S_{90° and S_0 were fit to the $S_n(T_g, T_s)$ Cushing et al. data for modeling purposes.[2] The angular distribution for propane on Pt(111) is significantly broader than the distributions of either methane or ethane and S_0 is also larger. The number of vibrational modes in propane is much larger than methane or ethane; the increased number of vibrational modes

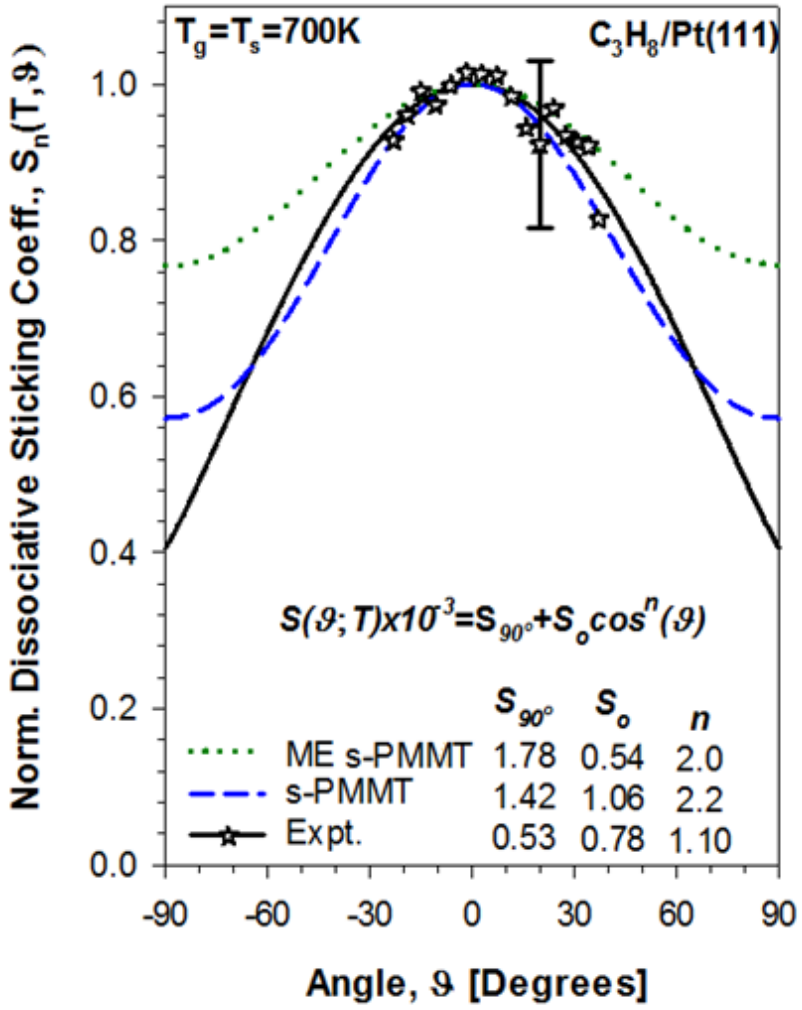

Figure 5.7: Angle-resolved DSCs measured at T = 700 K, S(ϑ; T = 700 K), for propane on Pt(111) compared to both statistical PMMT model predictions. The error bar corresponds to the relative error for an individual measurement.

leads to a larger amount of available exchangeable vibrational energy in propane compared to methane or ethane. Therefore, at higher incident angles, where there is a reduction in the normal translational energy, there is ample energy to react and so the ar-DSC distribution broadens. In addition, a previous effusive molecular beam study by Cushing et al. has shown that propane undergoes significant gas-surface energy transfer on Pt(111).[2] Because propane has more vibrational modes than either methane or ethane, the rovibrational density of states should also be greater, leading to a greater density of states in the propane PC; this should allow for better PC-phonon coupling. Additionally, the desorption lifetime at reactive energies is ~60 ps for propane, which is much longer than the desorption lifetime for ethane.[1,2] Overall then, propane should undergo more efficient gas-surface energy transfer compared to methane or ethane and so, because surface energy is independent of angle, the ar-DSC distribution should be relatively broad for propane.

$S(\vartheta; T = 700\ K)$ for propane was predicted using the standard statistical model (s-PMMT) as well as the statistical master equation model (ME s-PMMT). Both of the statistical models perform well in predicting the angular distribution, but it is difficult to verify which model is more accurate by analysis of the angular distribution alone. However, a purely statistical model was used in the past to reproduce $S_n(T_g, T_s)$ for propane on Pt(111) and the model was highly inaccurate.[2] Therefore, the ME s-PMMT model is the most accurate model for the propane/Pt(111) system.

5.2.5 Summary

Figure 5.8 shows a summary of $S(\vartheta; T = 700\ K)$ for methane, ethane, and propane on Pt(111); several conclusions can be drawn from the plot. First, DSCs increase with increasing alkane size; this is consistent with earlier $S_n(T_g, T_s)$ studies from the Harrison lab.[1,2,12,25] Second, the distributions become substantially broader as the alkane size is increased from methane to propane. At 700 K, the total amount of normal translation energy averaged over all angles of incidence is k_BT (~500 cm^{-1}) for all three alkanes, whereas the vibrational energy is ~450 cm^{-1}, ~1600 cm^{-1}, and ~2900 cm^{-1} for methane, ethane, and propane respectively. As the total amount of angle-invariant vibrational energy increases, the effect of normal translational energy is diminished, and so the distributions appear significantly broader for larger alkanes. Conversely, dynamical constraints on the exchangeable vibrational and rotational energy for methane and ethane limits the total contribution of rotational and vibrational energies to reactivity thus sharpening the ar-DSC distribution. Additionally, methane and ethane have relatively short desorption lifetimes and therefore gas-surface energy transfer has less impact on the ar-DSCs; whereas, propane undergoes significant gas-surface energy transfer and has no apparent dynamical constraints on exchangeable energy. Thus, at high incidence angle, where the system is starved for energy, the surface, vibrational, and rotational degrees of freedom can provide additional energy thus resulting in a broadening of the angular distribution. Third, although the general curvature of the angular distribution is accurately predicted by the PMMT models, the absolute magnitudes of the ar-DSCs do not lie exactly in line with the experimentally derived ar-DSCs. The reason for this behavior is that the parameters used in the PMMT models were calibrated against $S_n(T_g, T_s)$ values determined by Cushing et al.[1,2]

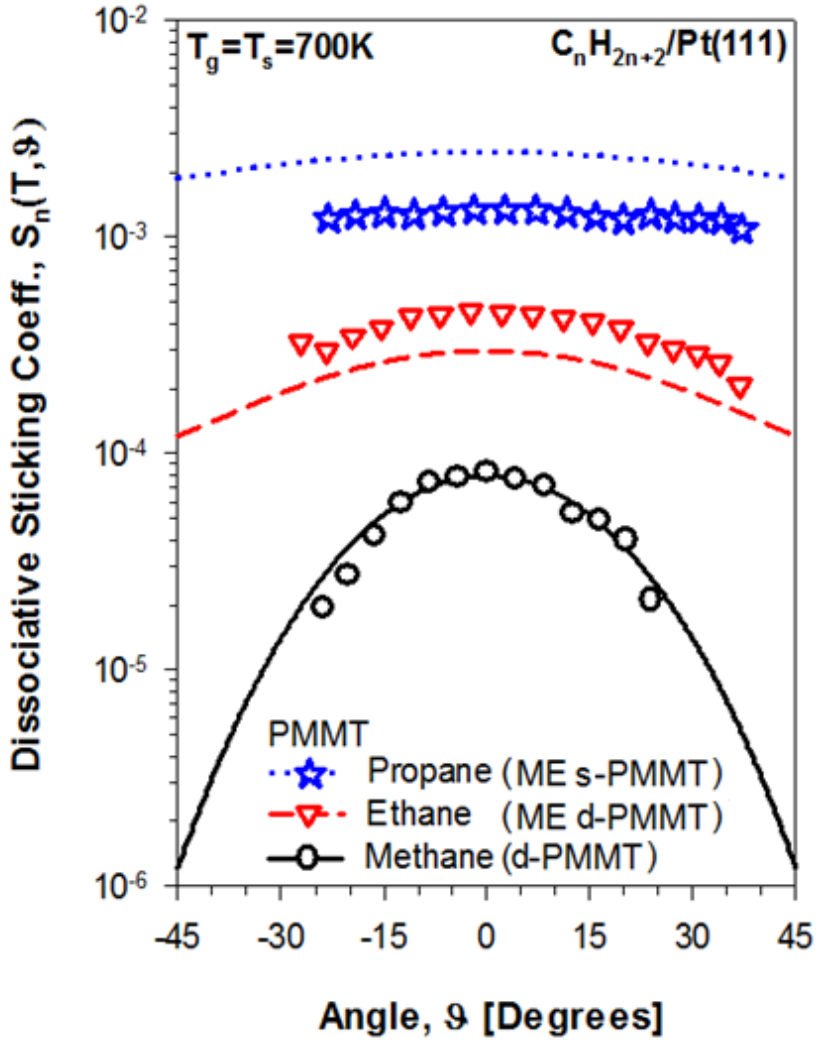

Figure 5.8: Angle-resolved DSCs measured at T = 700 K, S(ϑ; T = 700 K), for methane, ethane, and propane on Pt(111) compared to the PMMT models predictions that most accurately describe each set of data.

5.3 C_4-C_6 Linear Alkanes

5.3.1 Butane/Pt(111)

Ambient dosed $S_{bkg}(T_g = 295\ K, T_s)$ and directed $S_n(T_g, T_s)$ DSCs at gas temperatures of 300, 600, and 800 K were measured for butane on Pt(111) over a surface temperature range of 300 to 1000 K. DSC measurements at gas temperatures above 800 K were not conducted because of the possibility of thermal cracking.[26] A plot of $S_{bkg}(T_g = 295\ K, T_s)$ and $S_n(T_g, T_s)$ for butane on Pt(111) is shown in Figure 5.9. The general trend is that $S_n(T_g, T_s)$ increases with either increasing T_g or T_s. As is for the other alkanes, butane dissociative chemisorption on Pt(111) is an activated process. At surface temperatures less than 700 K, the ratio, $S_n(T_g = 800K, T_s) / S_n(T_g = 295\ K, T_s)$ increases with decreasing T_s, and is at a maximum at $T_s = 300$ K. However, at gas temperatures of 700 K and higher, the DSCs begin to collapse such that, $S_n(T_g = 800\ K, T_s) \approx S_n(T_g = 295\ K, T_s)$. At high surface temperatures, the surface can provide a great deal of energy for dissociation, such that the internal energy of the impinging molecule is inconsequential. At low surface temperatures, the exact opposite is true, because the internal energy of the impinging molecule is greater than that of the surface. Since the purity of the reagent butane is only 99.99%, we theorize that there are reactive impurities in the gas which limit the lowest possible DSC values to ~$1*10^{-5}$ and therefore, the DSCs approach an asymptotic value of $1*10^{-5}$ as seen in the Figure 5.9.

In order to determine the activation energy for the dissociative chemisorption of butane, $S_n(T)$ is fit to the Arrhenius functional form of,

$$S_n = S_0 e^{-E_a/(RT)} \qquad \text{Equation 5.13}$$

where S_n is the DSC measured along the surface normal, S_0 is the DSC at infinite temperature, E_a is the activation energy for dissociative chemisorption, R is the ideal gas constant, and T is the

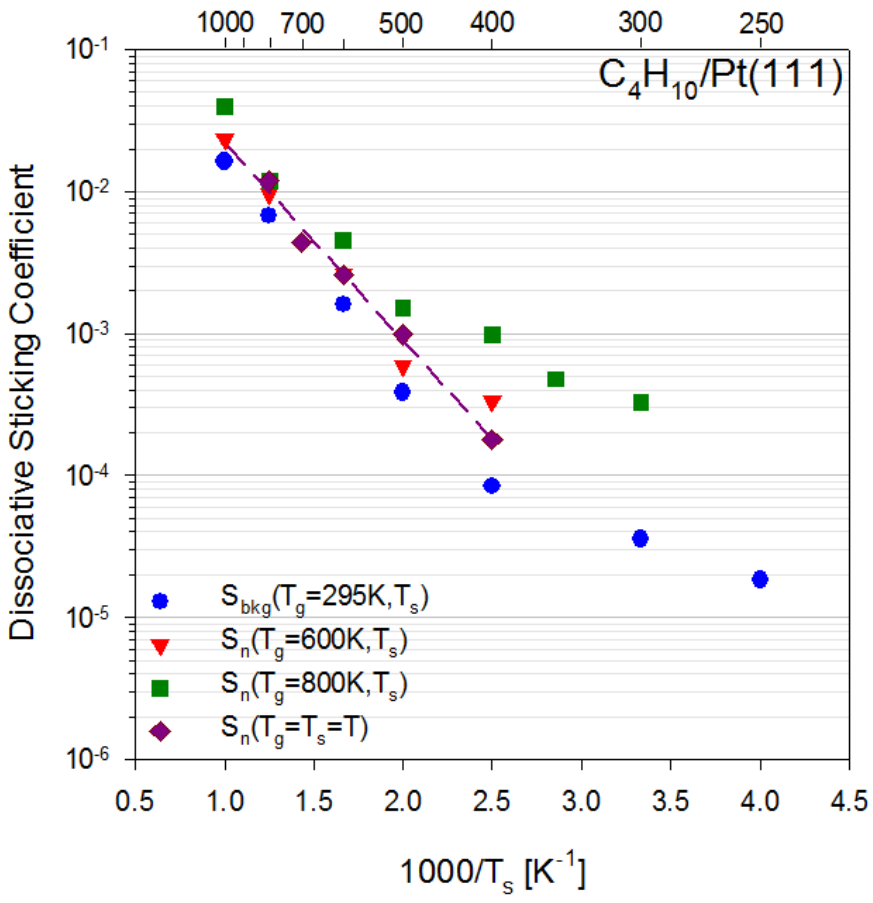

Figure 5.9: $S_{bkg}(T_g = 295$ K, $T_s)$ and $S_n(T_g, T_s)$ measured for butane on Pt(111). For $S_{bkg}(T_g = 295$ K, $T_s \leq 300$ K), the DSC values approach an asymptotic value of $1*10^{-5}$. The $S_n(T_g = T_s = T)$ line is calculated by fitting $S_n(T_g = T_s)$ to Equation 5.13.

temperature of the gas and surface at equilibrium, such that $T_g = T_s = T$. The Arrhenius analysis for $S_n(T)$, over the temperature range of 400 to 1000 K, yielded an activation energy of 26.6 kJ/mol and an S_0 of 0.54. $S_n(T = 300\ K)$ was not included in the analysis because the DSC value is near the asymptotic value. The activation energy for the dissociative chemisorption of butane is significantly less than that of methane, ethane, or propane on Pt(111). In addition, S_0 is also much larger than for any of the smaller alkanes.

5.3.2 Pentane/Pt(111)

The dissociative chemisorption of pentane on Pt(111) is very similar to that of butane on Pt(111). However, it was believed that increased gas-surface energy transfer for pentane would allow ambient gas dosed DSCs to become equivalent to thermal DSCs such that, $S_{bkg}(T_g = 295\ K, T_s) \approx S_n(T_g, T_s)$. In order to prove this hypothesis, $S_{bkg}(T_g = 295\ K, T_s)$ was measured for pentane on Pt(111) over the surface temperature range of 300 to 1000 K and then compared to directed $S_n(T_g = 600\ K, T_s)$ measured at surface temperatures of 400, 600, and 800 K. The goal was to investigate DSCs in three scenarios: $T_g > T_s$, $T_g = T_s$, and $T_g < T_s$. If $S_{bkg}(T_g = 295\ K, T_s) \approx S_n(T_g = 600\ K, T_s)$ in all three cases, it would be confirmed that the impinging gas does in fact thermalize to the surface temperature over the investigated temperature range. A gas temperature of 600 K was chosen for pentane because the variation of the DSC is maximized when comparing reactivity at different gas temperatures and studies have shown that pentane thermally cracks at gas temperatures above 600 K.[27,28] A plot of $S_{bkg}(T_g = 295\ K, T_s)$ and $S_n(T_g = 600\ K, T_s)$ for pentane dissociation on Pt(111) is shown in Figure 5.10. As shown in the plot, there is an increase in the DSC with increasing gas or surface temperature; therefore the dissociation is an activated process. By comparing the $T_g = 600$ K

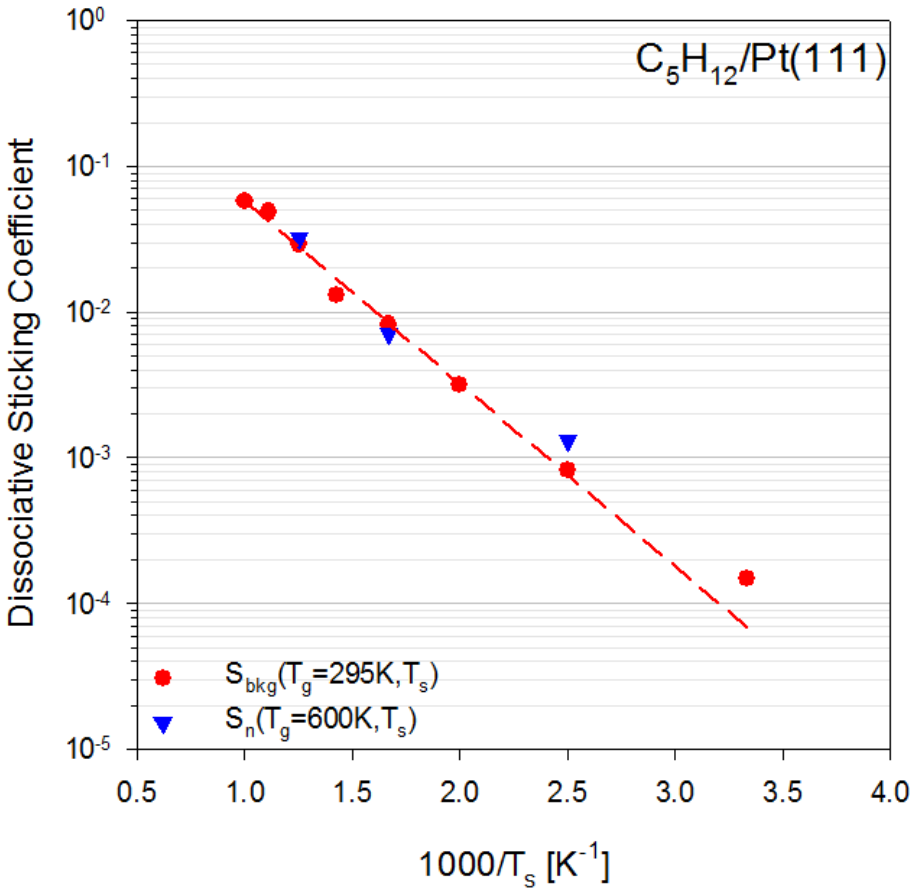

Figure 5.10: $S_{bkg}(T_g = 295\ K, T_s)$ and $S_n(T_g = 600\ K, T_s)$ measured for pentane on Pt(111). The $S_n(T_g = T_s = T)$ line is calculated by fitting $S_{bkg}(T_g = 295\ K, T_s)$ to Equation 5.13.

directed DSCs to the ambient dosed experiments it was determined that the gas is thermalized to the surface temperature. The ratio $S_{bkg}(T_g = 295\ K, T_s) / S_n(T_g = 600\ K, T_s)$ for the surface temperatures of 400, 600, and 800 K are 0.62, 1.16, and 0.91 respectively. Although the ratio for $T_s = 400$ K is slightly low, it should be noted that the direct to background flux of these experiments is 3:1 and the reactivity of the background flux is nominally the same as the direct flux. Therefore, background subtraction becomes increasingly difficult and errors can range up to $\pm$15%. Nonetheless, overall it appears that the gas is thermalizing to the surface temperature and it is safe to assume that $S_{bkg}(T_g = 295\ K, T_s) \approx S_n(T_g = 600\ K, T_s)$. An Arrhenius analysis of S_{bkg} over the temperature range of 400 to 1000 K yielded an activation energy of 24.0 kJ/mol and an S_0 of 1.02. The activation energy for dissociative chemisorption of pentane on Pt(111) is approximately 10% lower than for butane on Pt(111).

5.3.3 Hexane/Pt(111)

Analysis of ambient dosed and directed DSCs for the pentane/Pt(111) system revealed that the impinging gas thermalizes to the surface temperature such that, $S_{bkg} \approx S_n$. Therefore, DSCs measurements of hexane on Pt(111) were constrained to only S_{bkg} measurements over the surface temperature range of 400 to 1000 K. Figure 5.11 shows the results for $S_{bkg}(T_g = 295\ K, T_s)$ of hexane on Pt(111). The DSCs increase with increasing T_s, so the hexane/Pt(111) system follows an activated mechanism. An Arrhenius analysis of the measured DSCs yielded an activation energy for hexane dissociative chemisorption on Pt(111) of 18.2 kJ/mol and an S_0 of 1.04. The measured activation energy is approximately 24% less than that of pentane on Pt(111).

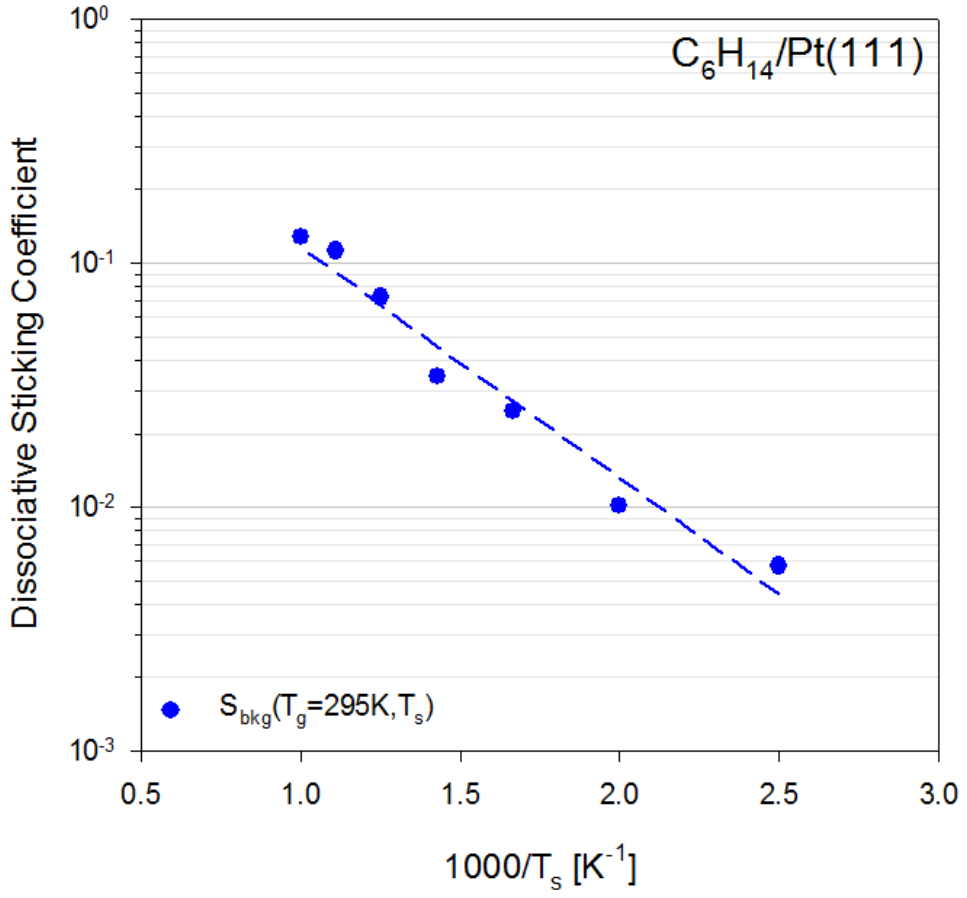

Figure 5.11: $S_{bkg}(T_g = 295\ K, T_s)$ measured for hexane on Pt(111). The $S_n(T_g = T_s = T)$ line is calculated by fitting $S_{bkg}(T_g = 295\ K, T_s)$ to Equation 5.13.

5.3.4 Summary

The DSCs of the linear alkanes, butane, pentane, and hexane on Pt(111), increase in value when either T_g or T_s is increased. Therefore, all three alkanes exhibit activated behavior on Pt(111). In the case of butane, variations in T_g or T_s resulted in a corresponding change in the DSC. Pentane exhibits the same T_s dependence as butane but does not share any similarity in T_g dependence; when T_g was changed for pentane, from T_g = 300 K to T_g = 600 K, there was no variation in the DSC. Therefore, impinging pentane molecules undergo sufficient gas-surface energy transfer such that $S_{bkg} \approx S_n$. For hexane, it was assumed that full thermalization occurs and therefore, the ambient dosed DSCs were equivalent to the fully thermalized DSCs. A plot of the equilibrium DSCs, $S_n(T)$, and $S_{bkg}(T_g = 295\ K, T_s)$ for the three alkanes is shown in Figure 5.12. An Arrhenius analysis of the thermal and ambient DSCs yielded activation energies for dissociative chemisorption as well as S_0. Table 5.2 shows the results of the Arrhenius analysis.

Alkane	**E_a (kJ/mol)**	**S_0**
Butane	26.6	0.54
Pentane	24.0	1.02
Hexane	18.2	1.04

Table 5.2: Activation energies for the dissociative chemisorption of selected alkanes on Pt(111), E_a, and S_0. E_a and S_0 are derived from Equation 5.13.

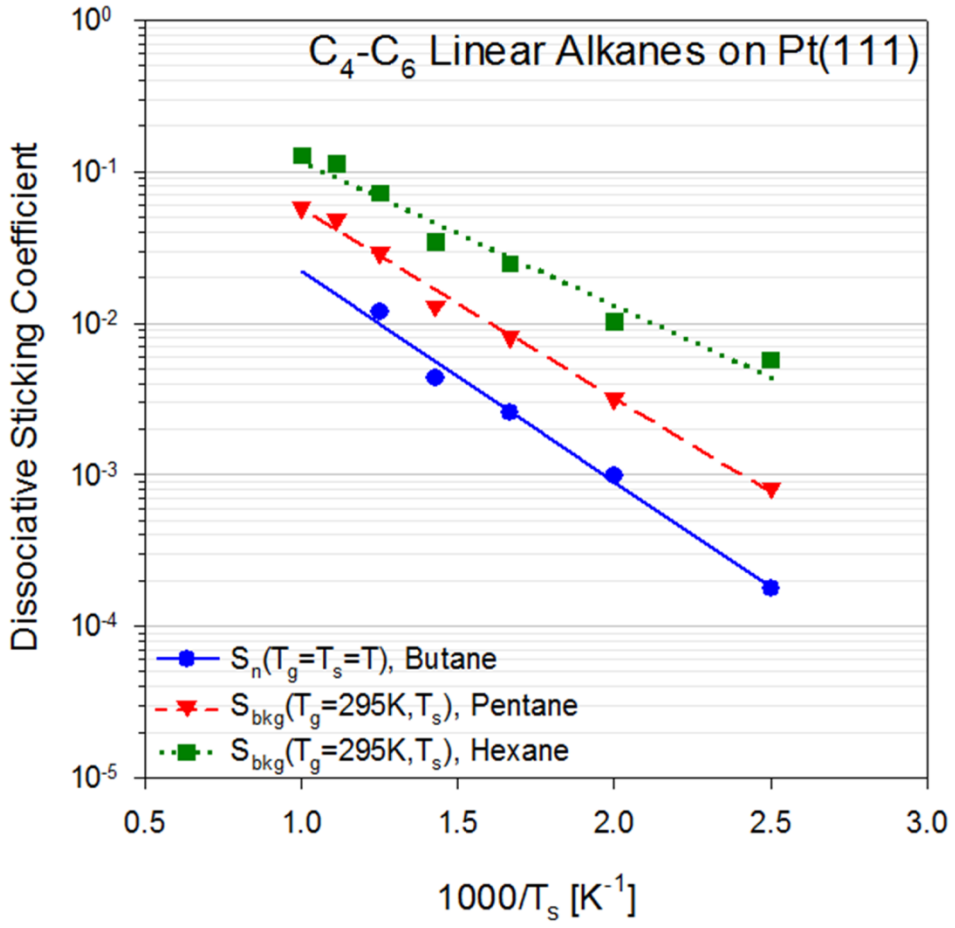

Figure 5.12: Plot of $S_n(T)$ for butane and $S_{bkg}(T_g = 295\ K, T_s)$ for pentane and hexane on Pt(111). For butane, the $S_n(T_g = T_s = T)$ line is calculated by fitting $S_n(T)$ to Equation 5.13. For pentane and hexane, the $S_n(T_g = T_s = T)$ line is calculated by fitting $S_{bkg}(T_g = 295\ K, T_s)$ to Equation 5.13.

References

(1) Cushing, G. W.; Navin, J. K.; Donald, S. B.; Valadez, L.; Johánek, V.; Harrison, I. Addition/Correction to: C-H Bond Activation of Light Alkanes on Pt(111): Dissociative Sticking Coefficients, Evans-Polanyi Relation, and Gas-Surface Energy Transfer (vol 114, pg 17222, 2010). *J. Phys. Chem. C* **2010**, *114*, 22790.

(2) Cushing, G. W.; Navin, J. K.; Donald, S. B.; Valadez, L.; Johanek, V.; Harrison, I. C-H Bond Activation of Light Alkanes on Pt(111): Dissociative Sticking Coefficients, Evans-Polanyi Relation, and Gas-Surface Energy Transfer. *J. Phys. Chem. C* **2010**, *114*, 17222.

(3) Sigma-Aldrich Supelpure®-O Oxygen/Moisture Trap, Safety Data Sheet. **2014**.

(4) Sigma-Aldrich Gas Chromatography Catalog. **2012**.

(5) Physical.Electronics Instruction Manual for Cylindrical Auger Electron Optics and Precision Electron Energy Analyzers. **1982**.

(6) Bisson, R.; Sacchi, M.; Dang, T. T.; Yoder, B.; Maroni, P.; Beck, R. D. State-Resolved Reactivity of $CH_4(2\nu_3)$ on Pt(111) and Ni(111): Effects of Barrier Height and Transition State Location. *J. Phys. Chem. A* **2007**, *111*, 12679.

(7) Juurlink, L. B. F.; Killelea, D. R.; Utz, A. L. State-Resolved Probes of Methane Dissociation Dynamics. *Prog. Surf. Sci.* **2009**, *84*, 69.

(8) Donald, S. B.; Navin, J. K.; Harrison, I. Methane Dissociative Chemisorption and Detailed Balance on Pt(111): Dynamical Constraints and the Modest Influence of Tunneling. *J. Chem. Phys.* **2013**, *139*.

(9) Navin, J. K.; Donald, S. B.; Tinney, D. G.; Cushing, G. W.; Harrison, I. Communication: Angle-Resolved Thermal Dissociative Sticking of CH_4 on Pt(111): Further Indication that Rotation is a Spectator to the Gas-Surface Reaction Dynamics. *J. Chem. Phys.* **2012**, *136*, 4.

(10) Navin, J. K.; Donald, S. B.; Harrison, I. Angle-Resolved Thermal Dissociative Sticking of Light Alkanes on Pt(111): Transitioning from Dynamical to Statistical Behavior. *J. Phys. Chem. C* **2014**, *Currently under review*.

(11) Juurlink, L. B. F.; Smith, R. R.; Utz, A. L. The Role of Rotational Excitation in the Activated Dissociative Chemisorption of Vibrationally Excited Methane on Ni(100). *Faraday Discuss.* **2000**, *117*, 147.

(12) Cushing, G. W.; Navin, J. K.; Valadez, L.; Johanek, V.; Harrison, I. An Effusive Molecular Beam Technique for Studies of Polyatomic Gas-Surface Reactivity and Energy Transfer. *Rev. Sci. Instrum.* **2011**, *82*, 11.

(13) Lehmann, J.; Roos, P.; Bertel, E. Incorporation of Alkali Metals on Pt(111). *Phys. Rev. B: Condens. Matter* **1996**, *54*, R2347.

(14) Albano, E. V. Thermal Desorption Mass Spectrometry of Alkali Metal Atoms from Transition Metal Surfaces. The Influence of Coadsorbed Oxygen. *J. Chem. Phys.* **1986**, *85*, 1044.

(15) Bengaard, H. S.; Alstrup, I.; Chorkendorff, I.; Ullmann, S.; Rostrup-Nielsen, J. R.; Norskov, J. K. Chemisorption of Methane on Ni(100) and Ni(111) Surfaces with Preadsorbed Potassium. *J. Catal.* **1999**, *187*, 238.

(16) Gebhard, S. C.; Koel, B. E. Influence of Potassium on the Adsorption of Hydrogen on Pt(111). *J. Phys. Chem.* **1992**, *96*, 7056.

(17) Brown, J. K.; Luntz, A. C.; Schultz, P. A. Long-Range Poisoning of D_2 Dissociative Chemisorption on Pt(111) by Coadsorbed K. *J. Chem. Phys.* **1991**, *95*, 3767.

(18) Donald, S. B.; Harrison, I. Rice–Ramsperger–Kassel–Marcus Simulation of Hydrogen Dissociation on Cu(111): Addressing Dynamical Biases, Surface Temperature, and Tunneling. *J. Phys. Chem. C* **2013**, *118*, 320.

(19) Harris, J.; Simon, J.; Luntz, A. C.; Mullins, C. B.; Rettner, C. T. Thermally Assisted Tunneling: CH_4 Dissociation on Pt(111). *Phys. Rev. Lett.* **1991**, *67*, 652.

(20) Luntz, A. C.; Bethune, D. S. Activation of Methane Dissociation on a Pt(111) Surface. *J. Chem. Phys.* **1989**, *90*, 1274.

(21) Utz, A. L. Mode Selective Chemistry at Surfaces. *Curr. Opin. Solid State Mater. Sci.* **2009**, *13*, 4.

(22) Higgins, J.; Conjusteau, A.; Scoles, G.; Bernasek, S. L. State Selective Vibrational ($2n_3$) Activation of the Chemisorption of Methane on Pt (111). *J. Chem. Phys.* **2001**, *114*, 5277.

(23) Bukoski, A.; Blumling, D.; Harrison, I. Microcanonical Unimolecular Rate Theory at Surfaces. I. Dissociative Chemisorption of Methane on Pt(111). *J. Chem. Phys.* **2003**, *118*, 843.

(24) Kim, H. L.; Kulp, T. J.; McDonald, J. D. Infrared Fluorescence Study on the Threshold of Intramolecular Vibrational State Mixing. *J. Chem. Phys.* **1987**, *87*, 4376.

(25) DeWitt, K. M.; Valadez, L.; Abbott, H. L.; Kolasinski, K. W.; Harrison, I. Effusive Molecular Beam Study of C_2H_6 Dissociation on Pt(111). *J. Phys. Chem. B* **2006**, *110*, 6714.

(26) Powers, D. R.; Corcoran, W. H. Pyrolysis of n-Butane-Explicit Effects of Primary and Secondary Butyl Radicals and of Secondary Reactions. *Ind. Eng. Chem. Fundam.* **1974**, *13*, 351.

(27) Frey, F.; Hepp, H. Thermal Decomposition of Simple Paraffins. *Ind. Eng. Chem.* **1933**, *25*, 441.

(28) Andersen, W. C.; Bruno, T. J. Rapid Screening of Fluids for Chemical Stability in Organic Rankine Cycle Applications. *Ind. Eng. Chem. Res.* **2005**, *44*, 5560.

Section 6 - Evans-Polanyi Correlation

6.1 Introduction

Initial C-H bond cleavage of an alkane on a metal surface is an important reaction, as it is believed to be a key and in some instances rate-limiting step in surface reactions, as in the steam reforming of alkanes.[1] For dissociative chemisorption of larger alkanes, it is believed that the C-H bond is cleaved before the C-C bond.[2-6] Since all alkanes undergo initial C-H bond cleavage, then logic would dictate that the activation energy for dissociative chemisorption, E_a, should be similar for all alkanes. Density functional theory (DFT) calculations predict that E_a should be 0.63 eV for methane[7] and 0.54 eV for ethane[8] on Pt(111), although the barriers are calculated to be identical on Pt(110) at 0.40 eV.[9] However, experimental results have shown that the activation energy changes substantially from methane to propane.[10] Therefore, there must be some effect that causes E_a to decrease as the alkane size is increased. It has been suggested that E_a scales with the weakest C-H bond in the molecule.[3,11] Bond dissociation energies (BDE) are a direct measurement of covalent bond strength, and the strongest alkyl C-H bonds exist on methane, which has a C-H BDE of D^o_{298K} = 439.3 kJ/mol.[12] In general, the lowest C-H BDE scales with the size of the alkane until an asymptotic BDE is achieved. For the series of alkanes, CH_4, C_2H_6, C_3H_8, and $(CH_3)_3CH$, the lowest BDEs (D^o_{298K}) are 439.3 kJ/mol, 420.5 kJ/mol**,** 410.5 kJ/mol, and 400.4 kJ/mol respectively.[12] Therefore, the series of alkanes can be listed in decreasing order of bond strength with, $CH_4 > C_2H_6 > C_3H_8 > (CH_3)_3CH$. After the ~5% drop between methane and ethane, the BDE changes half as quickly for the larger alkanes.

Effusive molecular beam studies of dissociative sticking coefficients (DSCs) have shown that the activation energy for alkane dissociative chemisorption on Pt(111) decreases substantially from methane to ethane and propane with respective activation energies of

58.0 kJ/mol, 42.7 kJ/mol, and 33.6 kJ/mol.[10,13] The activation energy drops by ~25% from methane to ethane and additional ~20% from ethane to propane. However, the BDE drops by only ~6.6% from methane to propane. It is difficult to believe that such a small change in the BDE would be responsible for such a drastic change in E_a, and therefore, some additional effect must be responsible for the drastic reduction in the DSCs. Additionally, an isotopically labeled supersonic molecular beam study reported that the activation energy for dissociative chemisorption of isobutane on Pt(110), via the 1°, 2°, and 3° C-H bonds, was found to vary by only 0.3 kJ/mol from a 1° C-H bond to a 3° C-H bond whereas the respective BDEs (D^o_{298K})[12] vary from 419.7 kJ/mol to 400.4 kJ/mol.[14] However, in the case of surface catalyzed C-X bond dissociation, where X is a halogen, the activation energy does strongly depend on the gas-phase BDE.[11] The BDE for a C-F bond is 513.8 kJ/mol and the BDE for a C-I bond is 253.1 kJ/mol,[12] and therefore, such a substantial difference in BDE should affect reactivity. Bond dissociation energies notwithstanding, the appreciable differences between the various alkanes are the mass, the total number of electrons, and the number of vibrational modes. The increased electron count in larger alkanes leads to increased polarizability, which can have some interesting ramifications.

6.2 Van der Waals Stabilization

Van der Waals (vdW) forces describe the attractions and repulsions of molecular dipoles. vdW forces can be comprised of three separate interactions between: two permanent dipoles (Keesom forces), a permanent dipole and an induced dipole (Debye forces), and two induced dipoles (London dispersion forces). These forces are much weaker than all other intermolecular forces and are the most dominant intermolecular forces exhibited by nonpolar molecules.

Although molecule-molecule van der Waals attractions are relatively weak, molecule-surface interactions are much stronger because the surface is composed of many more atoms than a single molecule. Figure 6.1 shows a schematic comparison between molecule-molecule vdW forces and molecule-surface vdW forces. In the case of alkanes, only the London dispersion forces dominate because only instantaneous dipoles can be formed. As electrons move throughout an atom or molecule, electron density becomes asymmetrical causing an instantaneous dipole to form. This instantaneous dipole then induces a dipole on a neighboring atom or molecule thus attracting the two particles together. Although the dipoles exist for only an instant, overall there is a net attraction between the particles, albeit a very weak one. The interaction between two neutral atoms or molecules is mathematically described by the Lennard-Jones potential model,

$$V = 4\varepsilon\left[\left(\frac{\sigma}{r}\right)^{12} - \left(\frac{\sigma}{r}\right)^{6}\right] \qquad \text{Equation 6.1}$$

where V is the intermolecular potential between two neutral particles, ε is the depth of the potential well, σ is the distance at which the potential between the two particles is at a minimum, and r is the distance between the two particles. The $(\sigma/r)^{12}$ term denotes the repulsive interaction and the $(\sigma/r)^{6}$ term is the attractive interaction. In order to accurately describe the interaction between a surface and a particle, Equation 6.1 must be integrated over a surface which yields,

$$V = \frac{3\sqrt{3}}{2}\varepsilon\left[\left(\frac{\sigma}{r}\right)^{9} - \left(\frac{\sigma}{r}\right)^{3}\right] \qquad \text{Equation 6.2}$$

where the $(\sigma/r)^{9}$ term denotes the repulsive interaction and $(\sigma/r)^{3}$ is the attractive interaction.[15] Thus the attractive molecule-surface interaction is much stronger than the molecule-molecule interaction. However, the Lennard-Jones potential model is simplistic and a more accurate

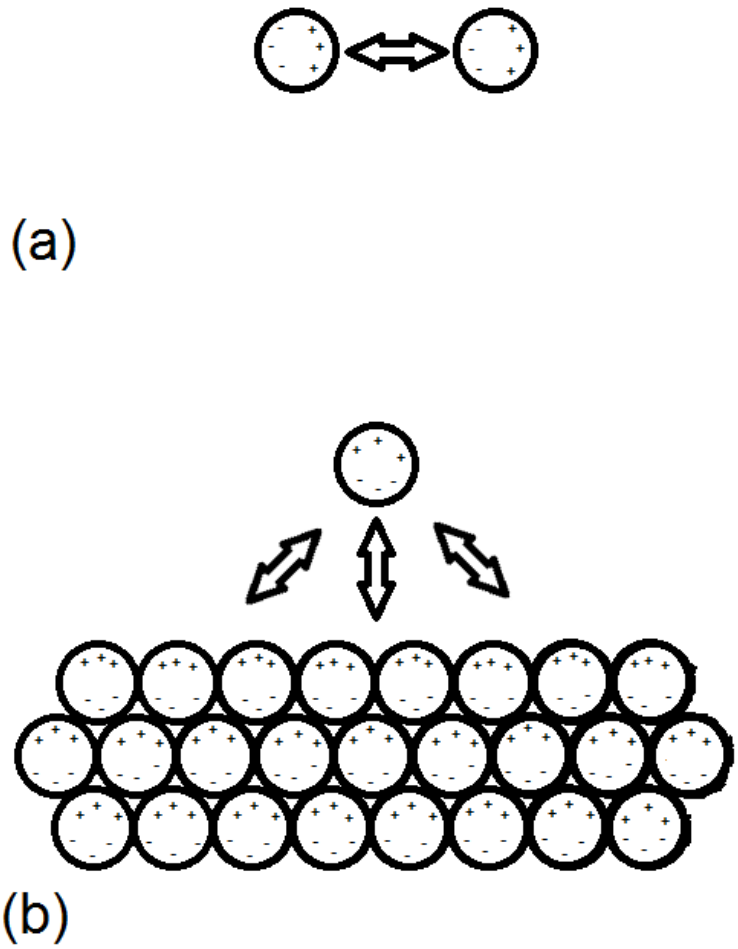

Figure 6.1: Schematic depiction of induced dipole-induced dipole van der Waals forces for a molecule-molecule interaction (a) and a molecule-surface interaction (b). Although a given molecule-surface atom interaction is as strong as a molecule-molecule interaction, the sheer number of surface atoms produces a very strong molecule-surface interaction overall.

mathematical description of the attractive interaction is,

$$V = -\frac{3}{2}\frac{I_1 I_2}{I_1+I_2}\frac{\alpha_1\alpha_2}{r^6} \qquad \text{Equation 6.3}$$

where I_i is the first ionization energy of the atom or molecule, α_i is the polarizability of the atom or molecule, and r is the distance between the two atoms or molecules. Equation 6.3 shows that the attractive forces fall off quickly as a function of $1/r^6$. As with the Lennard-Jones potential, the London dispersion forces for a surface-molecule interaction must be calculated as a total summation of all individual surface atom-molecule interactions. Integration of the interactions over the surface yields,[16]

$$V = -\frac{C}{Z^3} \qquad \text{Equation 6.4}$$

where C is the specific van der Waals parameter which depends on the type of surface (e.g. a metal surface, metal oxide surface, adsorbed organic layer, etc.) as well as the polarizabilty of the surface and molecule, and Z is the distance between the surface and molecule. Thus, for a surface comprised of many atoms, the London dispersion forces increase dramatically. Although London dispersion forces are generally discussed in the context of two separate bodies interacting, molecules can actually undergo intramolecular vdW attractions as well. Indeed, vdW forces are partly responsible the folding of large proteins.[17] In the context of gas-surface reactions, these intramolecular attractions stabilize the reactive transition state, and the chemisorbed fragment species.

The activated dissociative chemisorption of an alkane,

$$C_nH_{2n+2(g)} \xrightarrow{S*F} C_nH_{2n+1(c)} + H_{(c)}$$

involves an alkane striking the surface and if enough energy is available to overcome the barrier for dissociation, the alkane dissociates onto the surface leaving a chemisorbed alkyl fragment

and a hydrogen adatom. A schematic representation of activated alkane dissociative chemisorption is shown in Figure 6.2. If there is insufficient energy to overcome the barrier for dissociation, then the impinging molecule is deflected from the surface, and at reactive energies, the depth of the desorption well is irrelevant. As the size of the alkane is increased, there is also an increase in vdW forces between the molecule and the surface which then increases the depth of the physisorption well. The depth of the physisorption well can be determined experimentally via temperature programmed desorption (TPD). When a gas is dosed onto a surface at a temperature low enough to prevent desorption or dissociation, and then heated, the gas may desorb as intact molecules from the surface at a characteristic temperature. However, for large molecules that chemisorb via unactivated pathways, TPD measurements are extremely difficult as the molecule decomposes upon heating.[6] Studies have shown that for alkanes, and non-polar physisorbed molecules in general, the temperature required for molecular desorption increases substantially with molecular size,[6]; this is because the only attractive force between the non-polar molecule and the surface is vdW forces. After an alkane molecule successfully dissociates, it forms a chemisorbed alkyl fragment and a hydrogen adatom. Since the alkane fragments (C_nH_{2n+1}· + H·) still retain approximately the same number of electrons as the physisorbed alkane, then vdW forces should stabilize the chemisorbed products about as well as the physisorbed alkane and the transition state between them. Thus, increasing alkane size should increase the vdW forces and also increasingly stabilize the transition state and chemisorbed products.

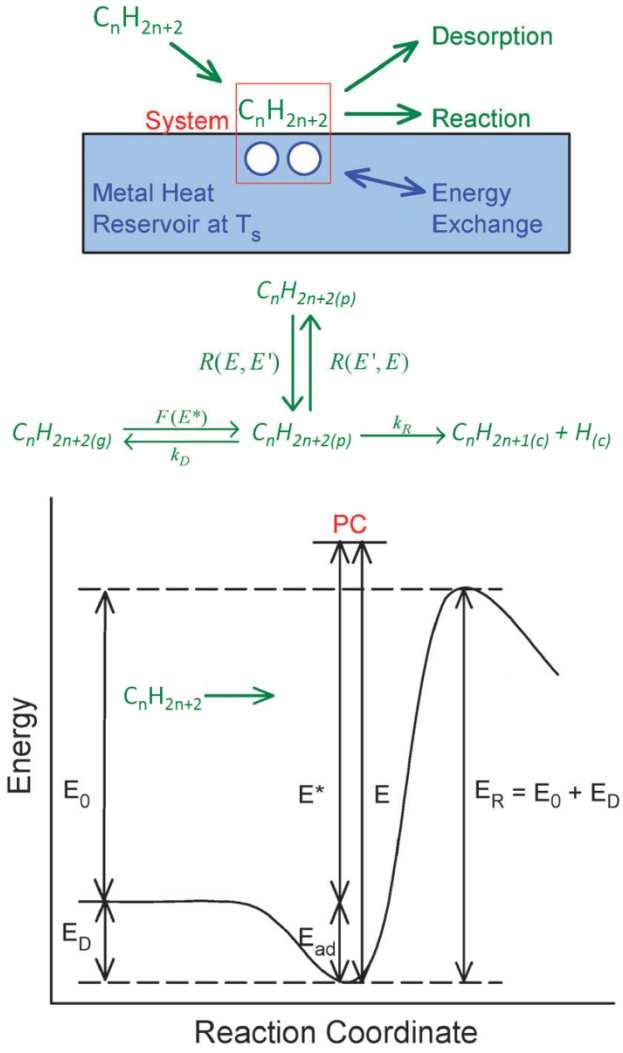

Figure 6.2: Potential energy surface for alkane dissociative chemisorption via the precursor mediated microcanonical trapping (PMMT) model.[10,13,29] A molecule first strikes the surface and forms a precursor complex (PC) with the immediate surrounding surface atoms; the energy of the PC is microcanonically randomized by this initial collision. The PC can then undergo secondary energy exchange with the surrounding bulk metal lattice. If the total energy of the PC, E^*, is higher than the barrier for dissociation, E_0, then the alkane can either dissociate or desorb with Rice-Ramsperger-Kassel-Marcus (RRKM) rate constants.

6.3 Evans-Polanyi Principle

The Evans-Polanyi principle[18,19] states that there is a linear relationship between the activation energy, E_a, for a family of reactions and the enthalpy of reaction, $\Delta_r H$, such that,

$$E_a = E_0 + \alpha\Delta(\Delta_r H) \qquad \text{Equation 6.5}$$

where E_0 is the activation energy of a reference reaction within the family and α is a value from 0 to 1, which characterizes the position of the transition state along the reaction coordinate. Assuming $\alpha \neq 0$, for a family of similar reactions, if the products are more stable then the product of the reference reaction, then the energy barrier for reaction is lowered. In addition, Hammond's postulate[18,20] states that two states which occur consecutively in a reaction and have roughly the same energy content, will only have a small reorganization of molecular structure. In other words, if the transition state is similar in structure to the products, as is the case for late barrier reactions, then changes in the enthalpy of the products affects the transition state strongly. For early barriers, where the transition state is similar to the reactants, changing the enthalpy of the products has little to no effect on the transition state. Therefore, the value α is related to whether or not the barrier for the reaction is early or late. Figure 6.3 shows theoretical potential energy curves depicting the Evans-Polanyi principle for a series of similar reactions. In general, for a given family of reactions, the activation energy is reduced by lowering the energy of the products because the zero of energy for the reactants is consistently defined with them at infinite separation at a temperature of 0 K. For a heterogeneous surface reaction, as in Figure 6.2, the transition state is a saddle point between the molecularly physisorbed molecule and the dissociated fragments. For alkane dissociative chemisorption, the alkane-surface vdW attractions increase with increasing alkane size which has a two-fold effect of increasing the depth of the molecular physisorption well as well as stabilizing the chemisorbed products.

Figure 6.4 shows potential energy curves with reduced reaction barriers for a series of dissociative chemisorption surface reactions. Although both the molecular physisorption well and the chemisorbed products are stabilized with increasing alkane size, only the stabilization of the chemisorbed products affects the transition state. Theoretically, with enough stabilizing energy, the reaction barrier can be reduced to an energy less than that of the gas phase reactants. At this point, the mechanism for dissociation is now unactivated. For an unactivated mechanism, a molecule with relatively low energy is initially trapped on the surface; the molecule is then thermalized to the surface temperature and reacts. This mechanistic pathway is available to the trapped molecule because the barrier for desorption is greater than that of reaction. However, if the impinging molecule has too much energy, then the molecule might be competitively deflected/desorbed from the surface before reaction can take place.

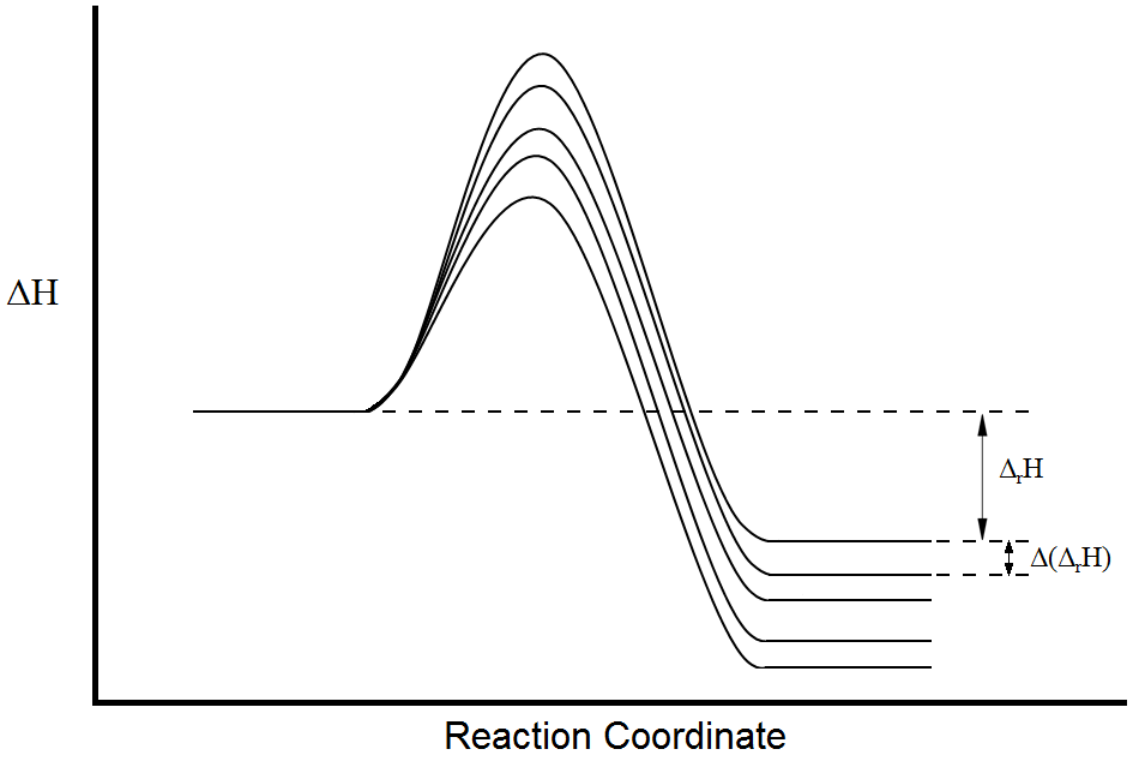

Figure 6.3: Potential energy curves depicting the change in enthalpy with a corresponding change in activation energy for a family of hypothetical reactions. As the products of reactions are increasingly stabilized, the activation barrier decreases.

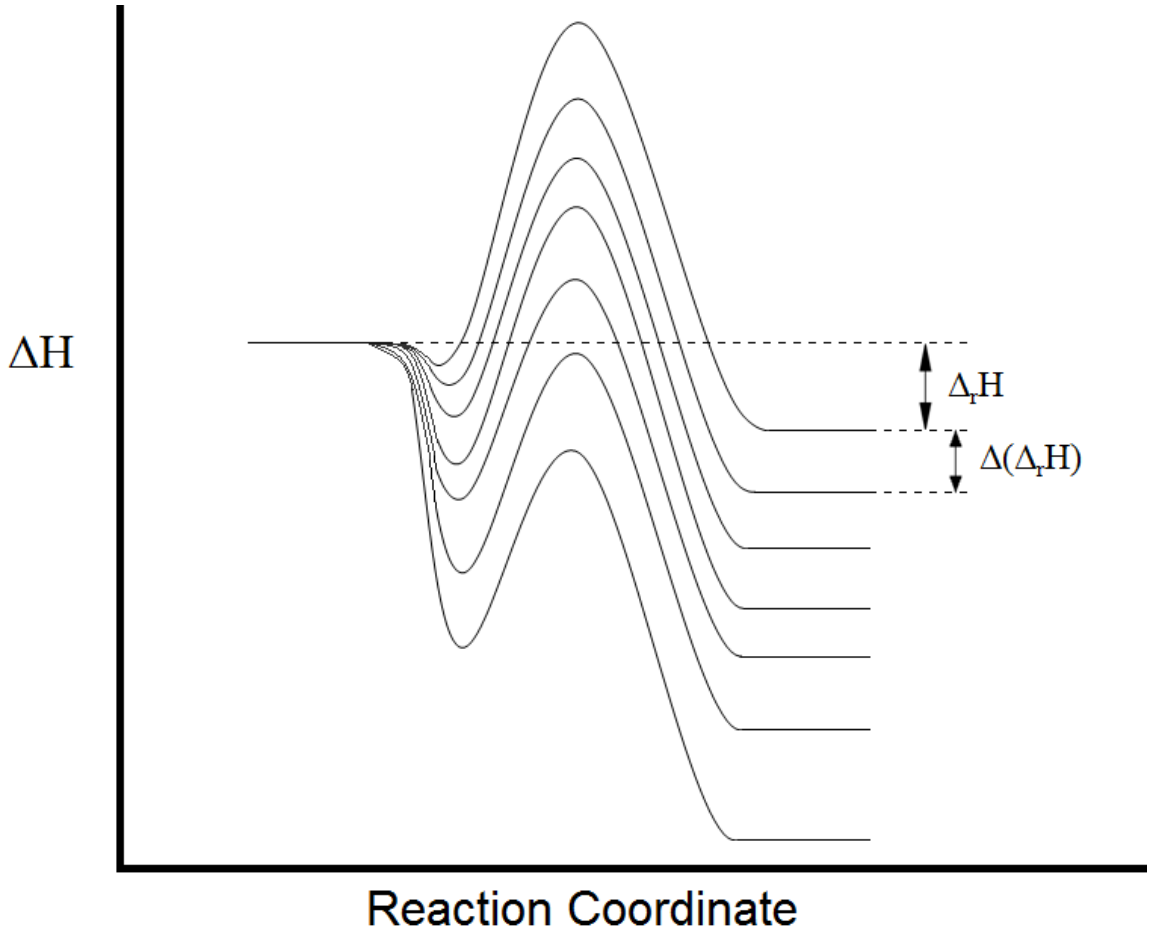

Figure 6.4: Potential energy curves which depict the change in enthalpy of the molecularly physisorbed reactants as well as the chemisorbed products with a corresponding change in activation energy for dissociative chemisorption.

6.4 Correlation

Although it is quite difficult to experimentally determine the vdW forces between the chemisorbed products of dissociative chemisorption and the surface, these forces can be approximated by the molecular desorption energy which is relatively easy to measure. By performing TPD measurements, it is possible to calculate the desorption energy required for a molecule to desorb from a surface, and increases in this desorption energy correspond to increases in the attractive vdW forces between the two. The activation energy for dissociative chemisorption is derived from effusive molecular beam measurements of DSCs over a broad temperature range. The activation energy for dissociative chemisorption, E_a,

$$E_a = -R \frac{d \ln S}{d\, {}^1/_T} \qquad \text{Equation 6.6}$$

can be extracted from Arrhenius plots, where *S* is the DSC, *R* is the ideal gas constant, and *T* is the thermal equilibrium temperature of the impinging gas and the surface. This Arrhenius analysis is possible when there is a linear correlation between *ln(S)* and *(1/T)*. The DSCs for activated dissociative chemisorption were well described by,

$$S = S_0 e^{-E_a/RT} \qquad \text{Equation 6.7}$$

Activation energies have previously been determined by Cushing et al. for methane, ethane, and propane on Pt(111).[10,13] Unpublished experimental results and calculations for isobutane, neopentane, octane, and nonane were also calculated by Cushing.[5] In this dissertation, DSCs were measured for dissociative chemisorption of butane, pentane, and hexane on Pt(111) and corresponding activation energies were calculated. Table 6.1 presents S_0 and the E_a for the various alkanes. Theoretically, S_0 must be less than or equal to 1, since the probability of reaction cannot exceed unity; however, because S_0 is calculated experimentally, several of the

gases listed in Table 6.1 have $S_0 > 1$. Nonetheless, for activated dissociative chemisorption with $S < \sim 10^{-2}$, the Arrhenius form is quite accurate.[21] Although E_a for nonane was determined using an Arrhenius analysis (Equation 6.6), an alternative precursor mediated thermal trapping[22] (PMTT) model was more appropriate to describe its unactivated dissociative sticking behavior over an extended temperature range.

Alkane	**S_0**	**E_a (kJ/mol)**
Methane	1.65	58.0
Ethane	0.53	42.5
Propane	0.82	33.6
Butane	0.54	26.6
Isobutane	0.37	28.9
Pentane	1.02	24.0
Neopentane	0.27	18.2
Hexane	1.04	18.8
Octane	0.85	8.4
Nonane	0.31	-4.3 (at 600 K)

Table 6.1: S_0 and E_a for alkane dissociative chemisorption on Pt(111).

Although the alkanes methane through octane exhibit activated behavior, nonane seems to be the tipping point at which linear alkane dissociative chemisorption begins to follow an unactivated mechanism. Figure 6.5 shows the thermal DSCs, S(T), calculated using the parameters in Table 6.1. For all alkanes besides nonane, the curves were calculated using Equation 6.7, since these alkanes follow activated processes. However, nonane was fit to a PMTT model because it follows an unactivated mechanism for dissociative chemisorption. For unactivated dissociative chemisorption, an incident molecule is first trapped on the surface in

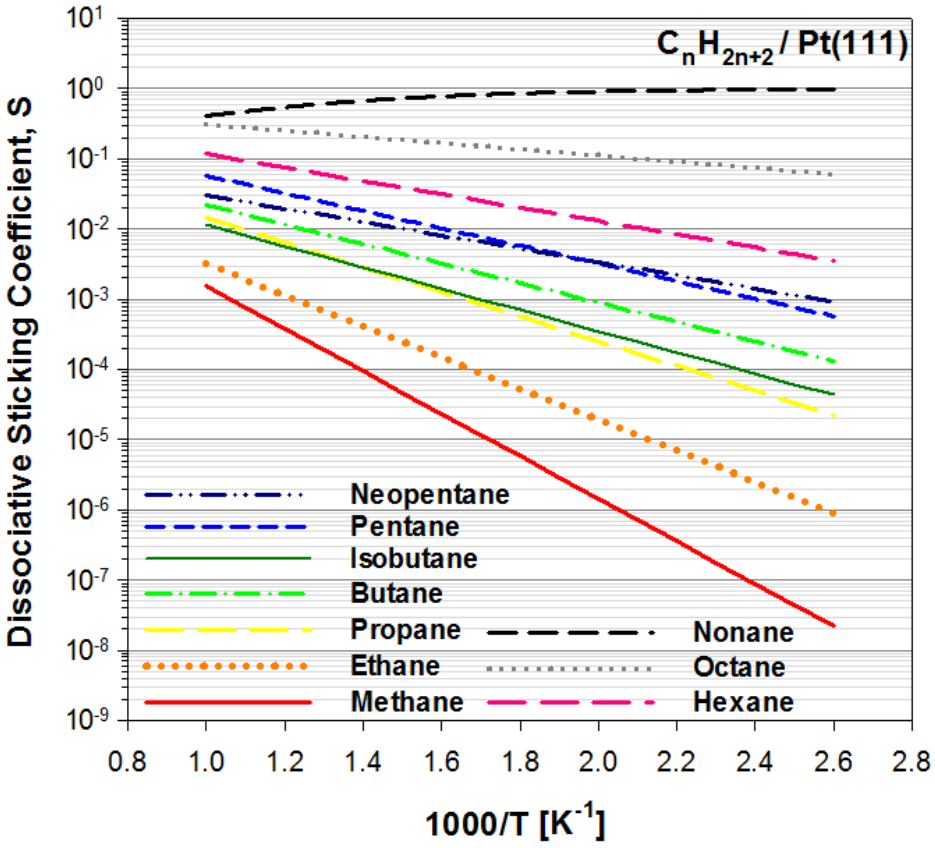

Figure 6.5: Thermal S(T) for alkane dissociative chemisorption on Pt(111). The DSCs for methane through octane were well described using Equation 6.7. Whereas, the DSCs for nonane were much better described by the PMTT model.

the physisorption well and is then thermalized to the surface temperature. The thermalized physisorbed molecule can then either dissociate or desorb from the surface. The reaction for unactivated dissociative chemisorption is written as,[23]

$$C_nH_{2n+2,g} \underset{k_D}{\overset{\zeta F}{\rightleftharpoons}} C_nH_{2n+2,p} \xrightarrow{k_R} C_nH_{2n+1,c} + H_c$$

where ζ is the probability that a molecule will trap on the surface, F is the flux of gas-surface collisions, and k_i are the Arrhenius thermal rate constants for desorption, D, and reaction, R. The DSC can then be derived from the above reaction scheme.[21] The coverage of physisorbed molecules, θ_p, is defined as,

$$\frac{d\theta_p}{dt} = \zeta F - (k_R + k_D)\theta_p \qquad \text{Equation 6.8}$$

Using the steady state approximation yields the steady state coverage of physisorbed molecules,

$$\theta_p^{ss} = \frac{\zeta F}{(k_R + k_D)} \qquad \text{Equation 6.9}$$

where θ_p^{ss} is the steady state coverage of physisorbed molecules. The reactive flux is then defined by,

$$\frac{d\theta_c}{dt} = k_R\, \theta_p^{ss} = \frac{\zeta k_R}{(k_R + k_D)} F = S * F \qquad \text{Equation 6.10}$$

Employing thermal rate constants, k_i, of the Arrhenius form,

$$k_i(T_s) = \nu_i e^{-E_{ai}/RT_s} \qquad \text{Equation 6.11}$$

where, ν_i are the pre-exponential factors, E_{ai} are the energies for the particular route, R is the ideal gas constant, and T_s is the temperature of the surface, the dissociative sticking coefficient, S, can then be written as,

$$S = \frac{\zeta k_R}{k_R + k_D} = \zeta\left(1 + \frac{k_D}{k_R}\right)^{-1} = \zeta\left(1 + \frac{\nu_D}{\nu_R} e^{-(E_{aD} - E_{aR})/RT_s}\right)^{-1} \quad \text{Equation 6.12}$$

E_{aR} and ν_R for nonane on Pt(111) were determined by assuming that ζ is equal to 1 and setting the values for ν_D and E_{aD} to 10^{19} s^{-1} and 117 kJ/mol respectively; the values for ν_D and E_{aD} were derived from TPD experiments conducted by Tait et al.[6] The activation energy for nonane that appears in Table 6.1 was evaluated at 600 K according to Equation 6.6 directly from the experimental data.

Molecular desorption energies of the various alkanes on Pt(111) were determined from the TPD experiments conducted by Tait et al.[6] The authors find that n-alkane molecular desorption energy is linearly related to the number of carbon atoms in the alkane by the equation,

$$E_d = E_0 + \Delta E * N \quad \text{Equation 6.13}$$

where E_0 and ΔE are fitting constants and N is the number of carbon atoms in the alkane. For the desorption of linear alkanes from Pt(111), E_0 = 2.67 kJ/mol and ΔE = 12.7 kJ/mol. For isobutane and neopentane, E_d was determined experimentally from TPD measurements conducted by Cushing et al.[5] Table 6.2 summarizes the desorption energies for the linear alkanes C_1-C_{10} and also for isobutane and neopentane on Pt(111).

Alkane	**E_d (kJ/mol)**	**Alkane**	**E_d (kJ/mol)**
Methane	15.4	Neopentane	53.2
Ethane	28.1	Hexane	78.9
Propane	40.8	Heptane	91.6
Butane	53.5	Octane	104.3
Isobutane	53.0	Nonane	117.0
Pentane	66.2	Decane	129.7

Table 6.2: Molecular desorption energies, E_d, for n-alkanes[6] on Pt(111) and isobutane[5] and neopentane[5] on Pt(111).

The Evans-Polanyi principle[18,19] relates reaction activation energies to enthalpic stabilization for a family of similar reactions. We find a correlation between the activation energy for alkane dissociative chemisorption to the molecular desorption energy of an alkane from the surface which presumably has the same origins. From Equation 6.5, the change in activation energy, ΔE_a, is defined as,

$$\Delta E_a = \alpha \Delta(\Delta_r H) \qquad \text{Equation 6.14}$$

We assume that the enthalpy of reaction, $\Delta_r H$, scales with the molecular desorption energy, E_d, from an initial enthalpy of reaction, $\Delta_r H_0$, such that,

$$\Delta H_r = \Delta_r H_0 - \beta\, E_d \qquad \text{Equation 6.15}$$

and it follows from equation 6.15 that,

$$\Delta(\Delta_r H) = -\beta\, E_d \qquad \text{Equation 6.16}$$

where, $0 \leq \beta \leq 1$ describes the likely stabilization of the chemisorbed products by vdW attractions and β may vary with the 1^o, 2^o, or 3^o nature of the C-H bond that is initially cleaved. Substitution of Equation 6.16 into Equation 6.14 yields,

$$\Delta E_a = -\alpha\, \beta\, E_d \qquad \text{Equation 6.17}$$

From Equation 6.17, the correlation between the activation energy and the molecular desorption energy is expressed as,

$$E_a = E_{a,0} - \gamma E_d \qquad \text{Equation 6.18}$$

where E_a is the activation energy for alkane dissociative chemisorption, $E_{a,0}$ is the y-intercept, E_d is the activation energy for molecular desorption, and $\gamma = \alpha\beta$, and likely has a value from 0 to 1, indicating the position along the reaction coordinate. The correlation between E_a and E_d is made by fitting the data in Table 6.1 and Table 6.2 to Equation 6.18. Figure 6.6 shows a plot of E_a for

alkane dissociative chemisorption versus E_d for alkane molecular desorption. From the figure, it can be seen that there are two anomalies: methane and neopentane. As shown in previous sections, methane behaves dynamically on Pt(111) and therefore, dynamical constraints on exchangeable energy increase the apparent activation energy. Neopentane has been shown to exhibit a much lower desorption energy than n-pentane on both Pt(111)[5] and Pd(111)[24]; this is perhaps due to the fact that neopentane is highly branched. Excluding methane and neopentane, the correlation yields a value of 52.2 kJ/mol for $E_{a,0}$ and a value of 0.45 for γ, which indicates that alkane dissociative chemisorption on Pt(111) has neither an early barrier nor a late barrier, but a combination of the two with respect to the full implementation of the vdW interactions. However, DFT calculated transition state geometries[25,26] and low vibrational efficacies[27] in d-PMMT modeling[28-31] and eigenstate resolved supersonic molecular beam experiments[32-34] indicate that alkane dissociative chemisorption on Pt(111) has an early barrier.

Figure 6.7 shows two-dimensional projections of three-dimensional potential energy surfaces depicting trajectories of reacting species of the type: $AB + M \rightarrow AM + B$. For an early barrier, as shown in Figure 6.7(a), translational energy increases reaction probabilities more so than vibrational energy because translational energy is required in order to approach the surface and react whereas vibrational energy does not contribute to this process. Conversely, for a late barrier, as shown in Figure 6.7(b), increases in vibrational energy affect reactivity a great deal more than translational energy because there is an increased importance on breaking bonds. An impinging molecule which has an excess of translational energy but is lacking sufficient vibrational energy, will merely be deflected from the surface in the case of a late barrier reaction. The vibrational efficacy for promoting a reaction is defined with respect to the normal translational energy, and is less than 1 for the dissociative chemisorption of alkanes on

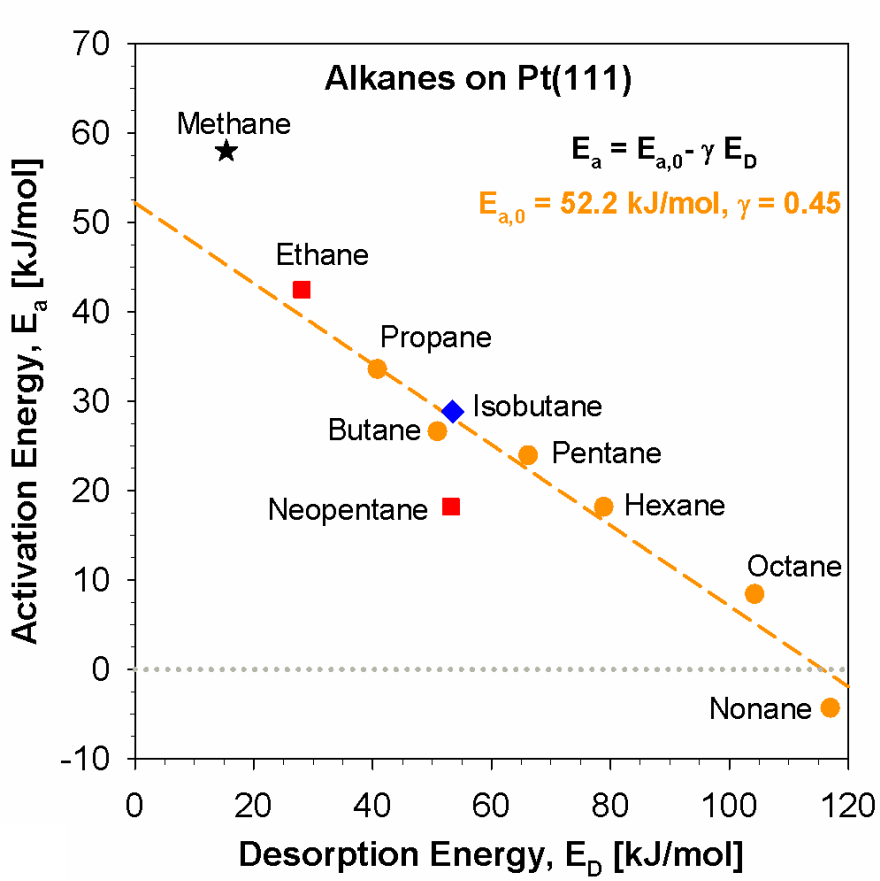

Figure 6.6: Evans-Polanyi correlation between the activation energy for alkane dissociative chemisorption, E_a, and the molecular desorption energy, E_d for a series of alkanes. Alkanes that have primary, secondary, and tertiary C-H bonds as the weakest C-H bond are indicated using squares, circles, and diamonds respectively. Fitting E_a and E_d for the alkanes (excluding methane and neopentane) to Equation 6.18 yielded 52.2 kJ/mol for $E_{a,0}$ and 0.45 for γ, which indicates that alkane dissociative chemisorption on Pt(111) has neither an early barrier nor a late barrier, but a combination of the two.

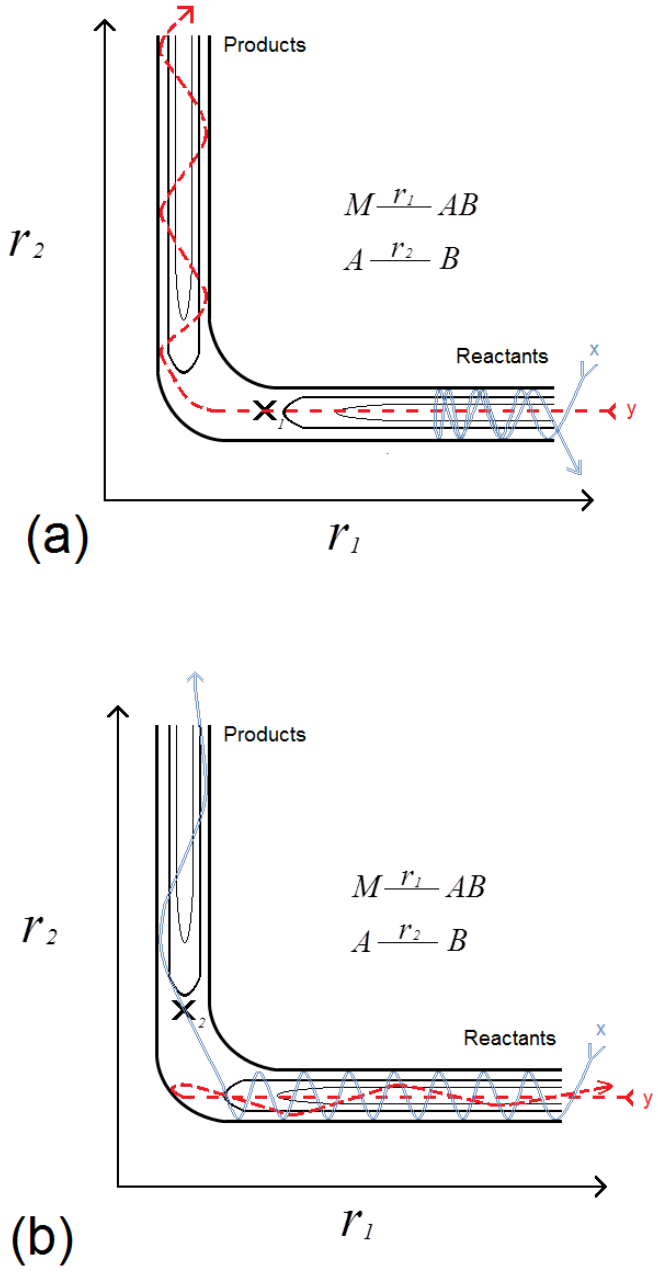

Figure 6.7: Potential energy surfaces for the reaction $AB + M \rightarrow AM + B$: r_1 is the distance between AB and M, and r_2 is the distance between A and B. The reaction trajectory *x* represents an AB molecule with an excess of vibrational energy and a deficit in translational energy and the reaction trajectory *y* represents an AB molecule with an excess of translational energy and a deficit in vibrational energy. Image (a) represents an early barrier reaction and image (b) represents a late barrier reaction.

Pt(111),[28,31-34] indicating that the barrier for dissociation is early. However, γ is calculated to be ~0.5; therefore, it would appear that, with respect to the full implementation of the vdW attraction, the barrier for alkane dissociation on Pt(111) is halfway between the reactants (gas phase alkane and surface at infinite separation) and the chemisorbed product limits.

Earlier, it was discussed that the decrease in activation energy for alkane dissociative chemisorption might scale with the weakest C-H bond in the alkane. For a given alkane, save methane, C-H bond cleavage can occur via primary (1°), secondary (2°), or tertiary (3°) C-H bonds. Table 6.3 lists bond dissociation energies (BDE) for 1°, 2°, and 3° C-H bond cleavage as well as the lowest BDE for a series of alkanes. C-H bonds on primary carbons are the most easily accessible for bond cleavage because of steric hindrance. Therefore if C-H bond cleavage occurs only at primary C-H bonds, then there is no correlation between the activation energy for dissociative chemisorption and the BDE. However, with the assumption that dissociative chemisorption occurs more readily at the C-H bond with the lowest BDE, there may be some correlation between E_a and the BDE.

A plot of the activation energy for dissociative chemisorption versus the lowest C-H BDE, is shown in Figure 6.8. As seen from the graph, there is a slight correlation between the activation energy and the lowest BDE for smaller alkanes such as methane, ethane, propane, and isobutane. However, this correlation does not hold well for alkanes the size of butane or larger. Therefore, the activation energy for dissociative chemisorption of linear alkanes on Pt(111) may scale with a combination of the weakest C-H bond strength and the desorption energy. It would be possible to determine the C-H bond cleavage selectivity by performing reflection absorption infrared spectroscopy (RAIRS) on dissociated fragments from effusive molecular beam experiments. This technique would determine which C-H bond on an alkane initially cleaves and in doing so, determine whether the activation energy for dissociative chemisorption scales solely with the molecular desorption energy or also with the weakest C-H bond.

Alkane	**1° C-H BDE[12] (kJ/mol)**	**2° C-H BDE[12] (kJ/mol)**	**3° C-H BDE[12] (kJ/mol)**	**Lowest C-H BDE (kJ/mol)**
Methane	--------	--------	--------	439.3
Ethane	420.5	--------	--------	420.5
Propane	422.2	410.5	--------	410.5
Butane	421.3	411.1	--------	411.1
Isobutane	419.7	--------	400.4	400.4
Pentane	419	415.1	--------	415.1
2-Methyl-butane	419	410	400.8	400.8
Neopentane	419.7	--------	--------	419.7
Hexane	419	410	--------	410
2-Methyl-pentane	419	410	396.2	396.2
2,3-Dimethyl-butane	419	410	399.2	399.2
Octane	419	410	--------	410
Nonane	419	410	--------	410

Table 6.3: C-H bond dissociation energies (BDE), D^{o}_{298K}, for select alkanes. BDEs decrease with increasing alkane size and eventually reach an asymptotic value.

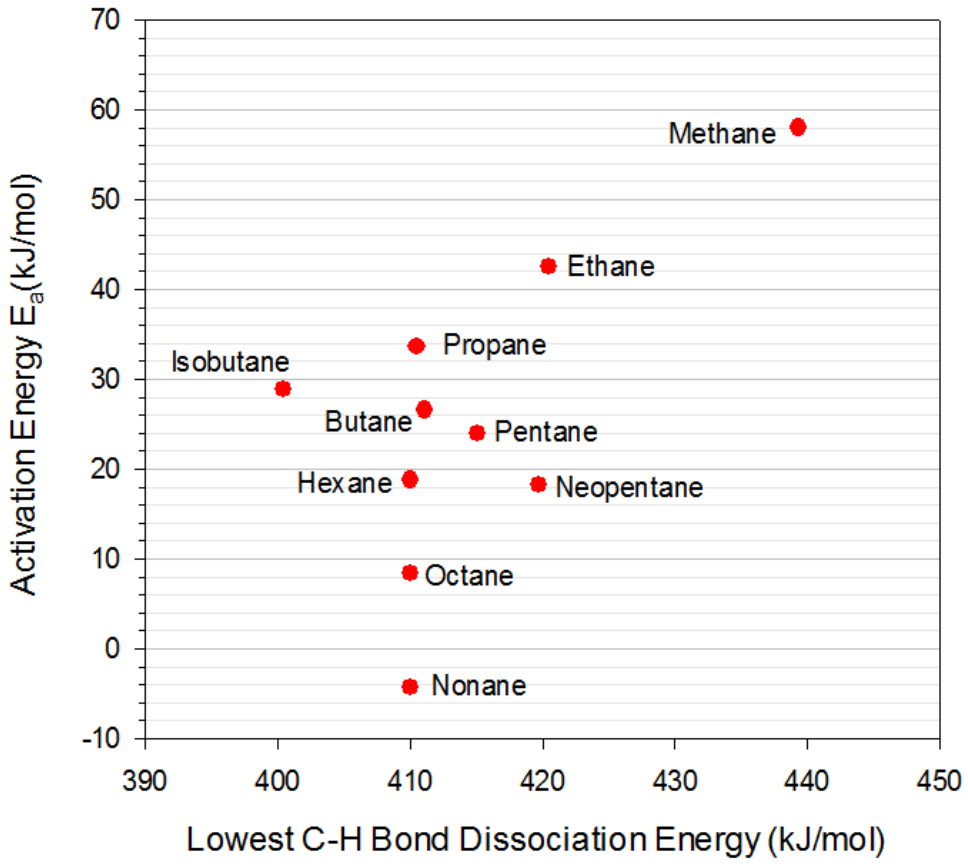

Figure 6.8: Correlation between the activation energy for alkane dissociative chemisorption, E_a,[5,10,13] and the lowest C-H bond dissociation energy[12] for the studied alkanes. There is a slight trend for methane, ethane, propane, and isobutane; however, this trend breaks down for larger alkanes.

6.5 Summary

The activation energy for alkane dissociative chemisorption on Pt(111) decreases with the size of the alkane from methane to nonane, becoming negative for nonane. This signifies that there is a shift from an activated mechanism to an unactivated mechanism for alkane dissociative chemisorption on Pt(111). In addition, there is a linear correlation between the activation energy for dissociative chemisorption and the molecular desorption energy. The molecular desorption energy is an estimate of the van der Waals (vdW) stabilization energy of the alkane on the surface because there are no formal chemical bonds to the surface. These vdW forces stabilize the dissociation transition state, the chemisorbed fragment products, as well as the molecularly adsorbed alkane. This stabilization lowers the activation energy for dissociative chemisorption and is in accord with the Evans-Polanyi principle. In addition, the correlation between the activation energy and the desorption energy, γ, has a value of ~0.5 which indicates that the transition state complex has neither reactant nor product character, but some combination of the two. Although it is reasonable to assume that the activation energy for dissociative chemisorption should scale with the weakest C-H bond in an alkane, this simple assumption yields the wrong limiting behavior as alkane size continues to increase.

References

(1) Wei, J. M.; Iglesia, E. Structural and Mechanistic Requirements for Methane Activation and Chemical Conversion on Supported Iridium Clusters. *Angew. Chem.* **2004**, *43*, 3685.

(2) Johnson, D. F.; Weinberg, W. H. Quantification of the Selective Activation of C-C Bonds in Short-chain Alkanes: Reactivity of Ethane, Propane, Isobutane, *n*-Butane and Neopentane on Ir(111). *J. Chem. Soc., Faraday Trans.* **1995**, *91*, 3695.

(3) Weinberg, W. H.; Sun, Y.-K. Quantification of Primary Versus Secondary C-H Bond Cleavage in Alkane Activation: Propane on Pt. *Science* **1991**, *253*, 542.

(4) Kelly, D.; Weinberg, W. H. Trapping-Mediated Dissociative Chemisorption of C_3H_8 and C_3D_8 on Ir(110). *J. Chem. Phys.* **1996**, *105*, 271.

(5) Cushing, G. W. "Hydrocarbon Reactivity on Pt(111): Dissociative Sticking Coefficients and Evans-Polanyi Relation", Ph.D. Thesis, University of Virginia, Charlottesville, VA, (2011).

(6) Tait, S. L.; Dohnalek, Z.; Campbell, C. T.; Kay, B. D. n-Alkanes on Pt(111) and on C(0001)/Pt(111): Chain Length Dependence of Kinetic Desorption Parameters. *J. Chem. Phys.* **2006**, *125*, 234308.

(7) Anghel, A. T.; Wales, D. J.; Jenkins, S. J.; King, D. A. Pathways for Dissociative Methane Chemisorption on Pt{110}-(1x2). *Phys. Rev. B: Condens. Matter* **2005**, *71*, 113410.

(8) Anghel, A. T.; Wales, D. J.; Jenkins, S. J.; King, D. A. Pathways for Dissociative Ethane Chemisorption on Pt{110} (1x2) Using Density Functional Theory. *Chem. Phys. Lett.* **2005**, *413*, 289.

(9) Chen, Y.; Vlachos, D. G. Hydrogenation of Ethylene and Dehydrogenation and Hydrogenolysis of Ethane on Pt(111) and Pt(211): A Density Functional Theory Study. *J. Phys. Chem. C* **2010**, *114*, 4973.

(10) Cushing, G. W.; Navin, J. K.; Donald, S. B.; Valadez, L.; Johanek, V.; Harrison, I. C-H Bond Activation of Light Alkanes on Pt(111): Dissociative Sticking Coefficients, Evans-Polanyi Relation, and Gas-Surface Energy Transfer. *J. Phys. Chem. C* **2010**, *114*, 17222.

(11) Ma, Z.; Zaera, F. Organic Chemistry on Solid Surfaces. *Surf. Sci. Rep.* **2006**, *61*, 229.

(12) Haynes, W. M. *CRC Handbook of Chemistry and Physics, 94th Edition*; Taylor & Francis Limited, 2013.

(13) Cushing, G. W.; Navin, J. K.; Donald, S. B.; Valadez, L.; Johánek, V.; Harrison, I. Addition/Correction to: C-H Bond Activation of Light Alkanes on Pt(111): Dissociative Sticking Coefficients, Evans-Polanyi Relation, and Gas-Surface Energy Transfer (vol 114, pg 17222, 2010). *J. Phys. Chem. C* **2010**, *114*, 22790.

(14) Weaver, J. F.; Carlsson, A. F.; Madix, R. J. The Adsorption and Reaction of Low Molecular Weight Alkanes on Metallic Single Crystal Surfaces. *Surf. Sci. Rep.* **2003**, *50*, 107.

(15) Abraham, F. F.; Singh, Y. Structure of a Hard-Sphere Fluid in Contact with a Soft Repulsive Wall. *J. Chem. Phys.* **1977**, *67*, 2384.

(16) Zaremba, E.; Kohn, W. Van der Waals Interaction Between an Atom and a Solid Surface. *Phys. Rev. B: Condens. Matter* **1976**, *13*, 2270.

(17) Berezovsky, I. N.; Trifonov, E. N. Van der Waals locks: Loop-n-Lock Structure of Globular Proteins. *J. Mol. Biol.* **2001**, *307*, 1419.

(18) Bruckner, R. *Advanced Organic Chemistry : Reaction Mechanisms*; Academic Press: Burlington, MA, USA, 2001.

(19) Temkin, O. N. *Homogeneous Catalysis with Metal Complexes : Kinetic Aspects and Mechanisms (2nd Edition)*; John Wiley & Sons: Hoboken, NJ, USA, 2012.

(20) Carey, F. A.; Sundberg, R. J. *Advanced Organic Chemistry, Part A: Structure and Mechanisms (4th Edition)*; Springer, 2000.

(21) Bukoski, A.; Blumling, D.; Harrison, I. Microcanonical Unimolecular Rate Theory at Surfaces. I. Dissociative Chemisorption of Methane on Pt(111). *J. Chem. Phys.* **2003**, *118*, 843.

(22) Jachimowski, T. A.; Hagedorn, C. J.; Weinberg, W. H. Direct and Trapping-Mediated Dissociative Chemisorption of Methane on Ir(111). *Surf. Sci.* **1997**, *393*, 126.

(23) Weinberg, W. H. In *Dynamics of Gas-Surface Interactions*; Rettner, C. T., Ashfold, M. N. R., Eds.; The Royal Society of Chemistry: Cambridge, 1991, p 171.

(24) Kao, C. L.; Madix, R. J. The Adsorption Dynamics of Molecular Methane, Propane, and Neopentane on Pd(111): Theory and Experiment. *J. Phys. Chem. B* **2002**, *106*, 8248.

(25) Nave, S.; Jackson, B. Methane Dissociation on Ni(111) and Pt(111): Energetic and Dynamical Studies. *J. Chem. Phys.* **2009**, *130*, 054701.

(26) Nave, S.; Tiwari, A. K.; Jackson, B. Methane Dissociation and Adsorption on Ni(111), Pt(111), Ni(100), Pt(100), and Pt(110)-(1x2): Energetic Study. *J. Chem. Phys.* **2010**, *132*, 054705.

(27) Polanyi, J. C. Some Concepts in Reaction Dynamics. *Acc. Chem. Res.* **1972**, *5*, 161.

(28) Donald, S. B.; Harrison, I. Dynamically Biased RRKM Model of Activated Gas-Surface Reactivity: Vibrational Efficacy and Rotation as a Spectator in the Dissociative Chemisorption of CH_4 on Pt(111). *PCCP* **2012**, *14*, 1784.

(29) Donald, S. B.; Navin, J. K.; Harrison, I. Methane Dissociative Chemisorption and Detailed Balance on Pt(111): Dynamical Constraints and the Modest Influence of Tunneling. *J. Chem. Phys.* **2013**, *139*.

(30) Navin, J. K.; Donald, S. B.; Harrison, I. Angle-Resolved Thermal Dissociative Sticking of Light Alkanes on Pt(111): Transitioning from Dynamical to Statistical Behavior. *J. Phys. Chem. C* **2014**, *Currently under review*.

(31) Navin, J. K.; Donald, S. B.; Tinney, D. G.; Cushing, G. W.; Harrison, I. Communication: Angle-Resolved Thermal Dissociative Sticking of CH_4 on Pt(111): Further Indication that Rotation is a Spectator to the Gas-Surface Reaction Dynamics. *J. Chem. Phys.* **2012**, *136*, 4.

(32) Bisson, R.; Sacchi, M.; Dang, T. T.; Yoder, B.; Maroni, P.; Beck, R. D. State-Resolved Reactivity of $CH_4(2\nu_3)$ on Pt(111) and Ni(111): Effects of Barrier Height and Transition State Location. *J. Phys. Chem. A* **2007**, *111*, 12679.

(33) Juurlink, L. B. F.; Killelea, D. R.; Utz, A. L. State-Resolved Probes of Methane Dissociation Dynamics. *Prog. Surf. Sci.* **2009**, *84*, 69.

(34) Higgins, J.; Conjusteau, A.; Scoles, G.; Bernasek, S. L. State Selective Vibrational ($2n_3$) Activation of the Chemisorption of Methane on Pt (111). *J. Chem. Phys.* **2001**, *114*, 5277.

Section 7 - Gas-Surface Energy Transfer Study

7.1 Introduction

In a gas-surface reaction, the energy required to surmount the activation barrier for reaction can come not only from the incident molecule but also from the surface. A molecule's energy depends on its translational, rotational, and vibrational motions. The surface's energy typically involved in gas-surface reactions is vibrational, although electronic excitations, such as electron/hole pair creation in metals, are also possible.[1,2] The vibrational frequencies of atoms in the metal bulk lattice are quite low and the periodic vibrational modes of the material are phonons. For platinum, the mean phonon frequency is 120 cm^{-1}.

Every atom in a molecule can move in the x, y, and z directions, therefore any given molecule has 3N degrees of freedom, where N is the number of atoms. For a non-linear, polyatomic molecule, the number of vibrational modes is determined simply by removing 3 degrees of freedom for molecular translation and 3 degrees of freedom for molecular rotation from the total degrees of freedom. Overall, a non-linear polyatomic molecule has 3N-6 vibrational modes. For a metallic single crystal, the total number of vibrational modes is also 3N-6, however, a single crystal has an astronomically large N therefore, there are approximately 3N vibrational modes. The majority of these vibrational modes have relatively low frequencies, since the metal lattice is comprised of heavy metal atoms. In the Debye model, periodic vibrational modes across the lattice are called phonons and they vary in frequency from a pure lattice displacement to the Debye frequency (the highest frequency of the $3N^{th}$ mode) which occurs at $k_B T_{Debye}/h$. The mean phonon frequency of the bulk material is 0.75 $k_B T_{Debye}/h$, given its quadratic density of states. For modeling purposes, we approximate the surface and bulk

atoms as Einstein oscillators all vibrating at the same frequency, the mean Debye frequency of the bulk material.

As discussed in section 4.3, our group models gas-surface reactivity using the precursor mediated microcanonical trapping (PMMT) model. A schematic of the PMMT model for alkane dissociative chemisorption is shown in Figure 7.1. Initially an alkane strikes the surface and interacts with a few local surface atoms forming a precursor complex (PC). The energy of the PC is microcanonically randomized by this initial collision. At reactive energies, E^*, which are at or above the threshold energy for reaction, E_0, the PCs may access the transition state region where strong anharmonic couplings are presumed to lead to efficient state-mixing and intramolecular vibrational energy redistribution (IVR). Subsequently, the PCs may competitively undergo "gas-surface" energy transfer with the surrounding bulk metal lattice, reaction (dissociative chemisorption), or molecular desorption from the surface. If the energy of the PC is lower than E_0, then anharmonic mode couplings are likely far weaker such that state-mixing and IVR will be relatively inefficient and the molecule is likely to scatter/desorb from the surface in a manner similar to that for a noble gas of comparable mass.[3] At reactive energies, the surrounding metal atoms can only effectively engage in energy transfer with the PC, if the PC desorption lifetime at reactive energies, τ_D, is substantially longer than the time constant for significant gas-surface (more precisely, PC to surroundings) vibrational energy transfer to occur. By definition, τ_D is the desorption lifetime for the PC to decompose back into surface atoms and a molecularly desorbing alkane. For modeling purposes, the PMMT model has 2 to 4 adjustable parameters depending on whether dynamical constraints and/or gas-surface energy transfer is considered. The variables are: the barrier for dissociation, E_0, the number of surface atoms involved in the initial collision or surface oscillators, s, the vibrational efficacy, η_v, for vibrational energy to promote reactivity relative to normal translational energy,

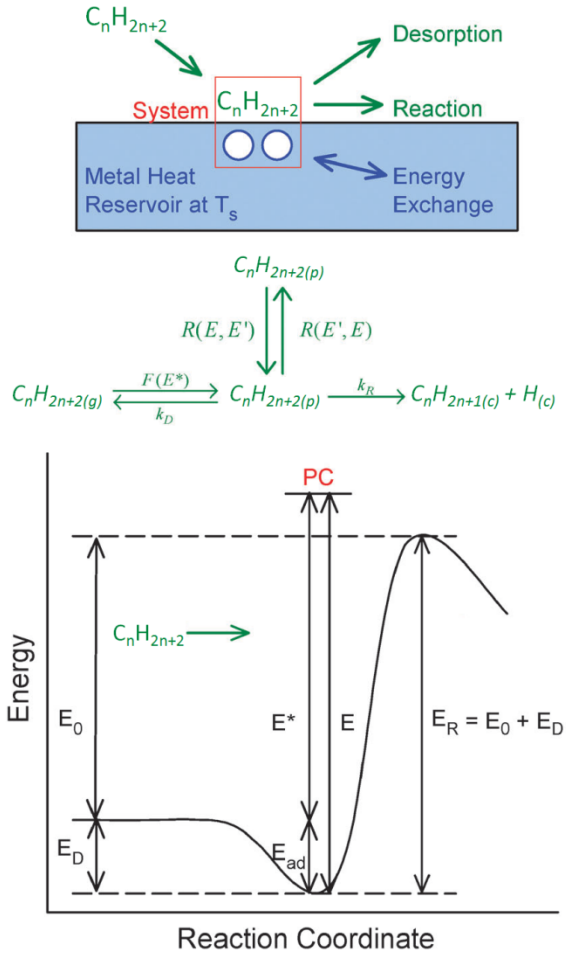

Figure 7.1: Schematic representation of dissociative chemisorption of alkanes with energies as defined by the PMMT model.[6,7] A molecule first strikes the surface and forms a precursor complex (PC) with the immediate surrounding surface atoms; the energy of the PC is microcanonically randomized by this initial collision. The PC can then undergo secondary energy exchange with the surrounding bulk metal lattice. If the total energy of the PC, E^*, is higher than the barrier for dissociation, E_0, then the alkane can either dissociate or desorb with Rice-Ramsperger-Kassel-Marcus (RRKM) rate constants.

and a gas-surface energy transfer parameter, α, which is the average energy transferred from the PC and to the bulk metal lattice per phonon collision that results in downwards energy transfer.[4-6]

7.2 Linear Alkane Results

In order to investigate the effects of gas-surface energy transfer on dissociative chemisorption, non-equilibrium dissociative sticking coefficients (DSC), in which the gas temperature, T_g, and the surface temperature, T_s, are not equal, $S_n(T_g \neq T_s)$, as well as quasi-equilibrium DSCs, $S_n(T_g = T_s = T)$, were measured for a series of alkanes on Pt(111) along the direction of the surface normal. In addition, non-directional, ambient dosed DSCs, $S_{bkg}(T_g = 295\ K, T_s)$ were measured for a number of alkanes as well. Cushing et al. has previously measured DSCs for methane, ethane, and propane on Pt(111),[7,8] and unpublished DSC measurements for the linear alkanes octane and nonane on Pt(111) have been made by Cushing as well.[9] Lastly, differential energy uptakes, d_j^* were calculated for methane, ethane, propane, and butane in order to discern the relative importance of gas and surface energy in promoting alkane dissociative chemisorption on Pt(111).

Precursor mediated microcanonical trapping (PMMT) models were used to analyze and reproduce DSCs. Four different PMMT models were considered, all of which treated molecular translational motion parallel to the surface as a spectator degree of freedom: a statistical model (s-PMMT) in which there were no dynamical constraints, a dynamical model (d-PMMT) in which rotation was taken as a spectator degree of freedom and a vibrational efficacy was introduced whose value was $\eta_v = 0.4$ for methane and ethane on Pt(111), a statistical master-equation model (ME s-PMMT) which accounts for gas-surface energy transfer, and a dynamical master-equation model (ME d-PMMT) which can account for both gas-surface energy transfer as well as dynamical constraints. The Cushing et al. data was fit using a less sophisticated PMMT

model called, at the time, a physisorbed complex, microcanonical unimolecular rate theory (PC-MURT) model. The only difference is that vibrational frequencies for the transition state are derived from generalized gradient approximation density functional theory (GGA-DFT) calculations in the PMMT models, whereas these frequencies were not available for the earlier PC-MURT modeling. Consequently, in the PC-MURT models, the transition state vibrational frequencies were taken to be the same as in the gas-phase molecule and the three rotations and the translation normal to the surface, which evolve into frustrated rotational and normal translational vibrations in the transition state, were assumed to have a common low vibrational frequency, ν_D, which was treated as an additional free parameter. The PC-MURT had 3 parameters, (E_0, s, ν_D) and the master equation version, ME-MURT, required an additional gas-surface energy transfer parameter, α. Dynamical models were never developed for the PC-MURT models because they would require too many parameters. PC-MURT and ME-MURT model calculations were conducted for methane, ethane, and propane dissociative chemisorption on Pt(111) by Cushing et al.[7,8,10] More recently, DFT derived transition state frequencies were calculated and PMMT models have been completed for methane[6,11-13] and ethane.[12] Although s-PMMT and ME s-PMMT modeling has been conducted for propane,[12] DFT derived transition state frequencies are not available yet. Therefore, full d-PMMT modeling has not yet been done for molecules larger than ethane. Such PMMT modeling would be of considerable interest for propane and butane because gas-surface energy transfer rates remain relatively slow compared to desorption rates at reactive energies for these molecules. However, for pentane, hexane, octane, and nonane on Pt(111), we practically observe that $S_n(T_g, T_s) = S_n(T_s) = S(T)$ - presumably because desorption lifetimes at reactive energies have become so long and gas-surface energy transfer rates are sufficiently rapid that thermalization is guaranteed.

Previous DSC studies using both supersonic and effusive molecular beams have shown that methane behaves dynamically on Pt(111).[6,11,14-26] In particular, measurements of eigenstate-resolved DSCs, using supersonic molecular beams, have shown that vibrational energy is not as efficacious in promoting methane dissociative chemisorption on Pt(111).[14-17,19,20,22,23] Methane does not undergo gas-surface energy transfer because the desorption lifetime of the methane PC on the Pt(111) surface is relatively short ~100 fs.[8] Bukoski[5] demonstrated that gas-surface energy transfer is negligible for methane reactivity on Pt(111), particularly for supersonic molecular beam reactivity. Modeling of effusive molecule beam experiments by Cushing et al. also showed negligible effect of gas-surface energy transfer on methane reactivity.[7,8] Methane in the gas-phase, does not exhibit IVR because there is a large energy difference between the vibrational modes and the density of states is too low[27] - this is an essential criteria if mode-selective gas-surface chemistry is to be easily interpreted.[27] Figure 7.2 shows $S_n(T_g, T_s)$ as well as $S_{bkg}(T_g = 300\ K, T_s)$ for methane on Pt(111) as well as various PC-MURT and PMMT model results. The PC-MURT model Figure 7.2(a) reproduces the data reasonable well with $E_0 = 48.2$ kJ/mol, $s = 4$, and $\nu_D = 315\ cm^{-1}$. The data was also reproduced equally well with the ME-MURT model using $\alpha = 50\ cm^{-1}$, as an additional fitting parameter in Figure 7.2(b). However, there is almost no difference between the PC-MURT and the ME-MURT modeling and so it seems that the inclusion of gas-surface energy transfer does not discernibly affect the model DSC results. By comparing the s-PMMT predictions with $E_0 = 47.3$ kJ/mol and $s = 3$ (Figure 7.2 (c)) to the d-PMMT predictions with $E_0 = 58.9$ kJ/mol, $s = 2$, and $\eta_v = 0.4$ (Figure 7.2 (d)), it is found that the statistical model over predicts the DSCs by almost an order of magnitude in some cases. The fact that dynamical constraints are required to reproduce the DSCs, shows that gas-surface energy transfer plays a negligible role in methane dissociative chemisorption on Pt(111) because the exchangeable energy of the impinging alkane affects reactivity to such a large degree.

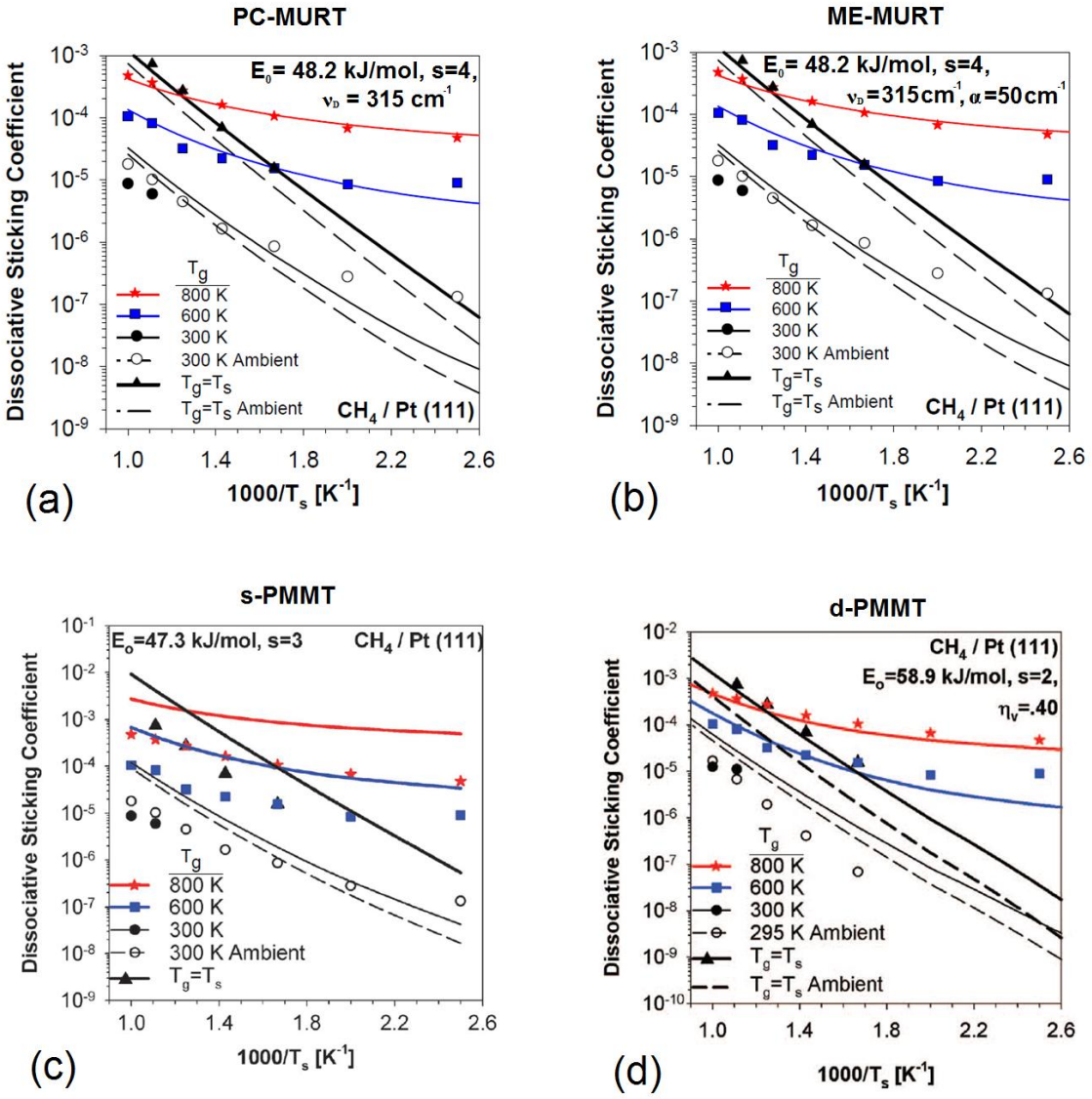

Figure 7.2: $S_n(T_g, T_s)$ and $S_{bkg}(T_g = 300\ K, T_s)$ shown with model predictions for methane on Pt(111): PC-MURT model predictions for Cushing et al. data (a), ME-MURT model predictions for Cushing et al. data (b), s-PMMT model predictions for Cushing et al. data (c), and d-PMMT model predictions for $S_n(T_g, T_s)$ from Cushing et al. data and Navin $S_{bkg}(T_g = 295\ K, T_s)$ (d). Handling gas-surface energy transfer explicitly does not seem to change the predictions. Additionally, dynamical constraints are required in order to properly reproduce the experimental results.

In the case of ethane dissociation on Pt(111), previous work by Cushing et al. has shown that gas-surface energy transfer affects DSCs slightly.[7,8] As is the case for methane, the calculated desorption lifetime of an ethane PC at reactive energies on Pt(111), is short at ~2 ps.[8] Therefore, it was assumed that the DSCs for ethane on Pt(111) could be reproduced using the PC-MURT model and that the ME-MURT model values would not differ much from the PC-MURT model. Figure 7.3 shows $S_n(T_g, T_s)$ and $S_{bkg}(T_g = 300\ K, T_s)$ for ethane on Pt(111) along with MURT model and PMMT model results. It can be seen that the PC-MURT model predictions with $E_0 = 34.4$ kJ/mol, $s = 4$, and $\nu_D = 145\ cm^{-1}$ correlate well with the experimental data. However, the PC-MURT model does not accurately reproduce $S_{bkg}(T_g = 300\ K, T_s)$. As the gas temperature increases, τ_D decreases sufficiently enough that gas-surface energy transfer can be discounted and so the PC-MURT can accurately describe ethane/Pt(111) DSCs at elevated gas temperatures with respect to the surface temperature. However, at hypothermal gas temperatures, τ_D is much longer, and so gas-surface energy transfer plays a greater role. Therefore, in order to accurately reproduce $S_{bkg}(T_g = 300\ K, T_s)$, the modeling must account for gas-surface energy transfer. And so, the ME-MURT model with $\alpha = 700\ cm^{-1}$ reproduces both $S_n(T_g, T_s)$ as well as $S_{bkg}(T_g = 300\ K, T_s)$. The value of α for ethane is much higher than the value for methane, $700\ cm^{-1}$ versus $50\ cm^{-1}$ respectively, which indicates that more energy is transferred per PC-phonon collision for ethane than for methane according to the MURT modeling. However, the model used by Cushing et al. cannot handle dynamical constraints, and angle-resolved DSC measurements, $S(\vartheta; T = 700\ K)$, of ethane on Pt(111) have confirmed that ethane behaves dynamically on Pt(111).[12] Therefore, the ethane/Pt(111) data was analyzed using the d-PMMT model with the parameter set $E_0 = 42.3$ kJ/mol, $s = 2$, and $\eta_v = 0.4$ and the DSCs

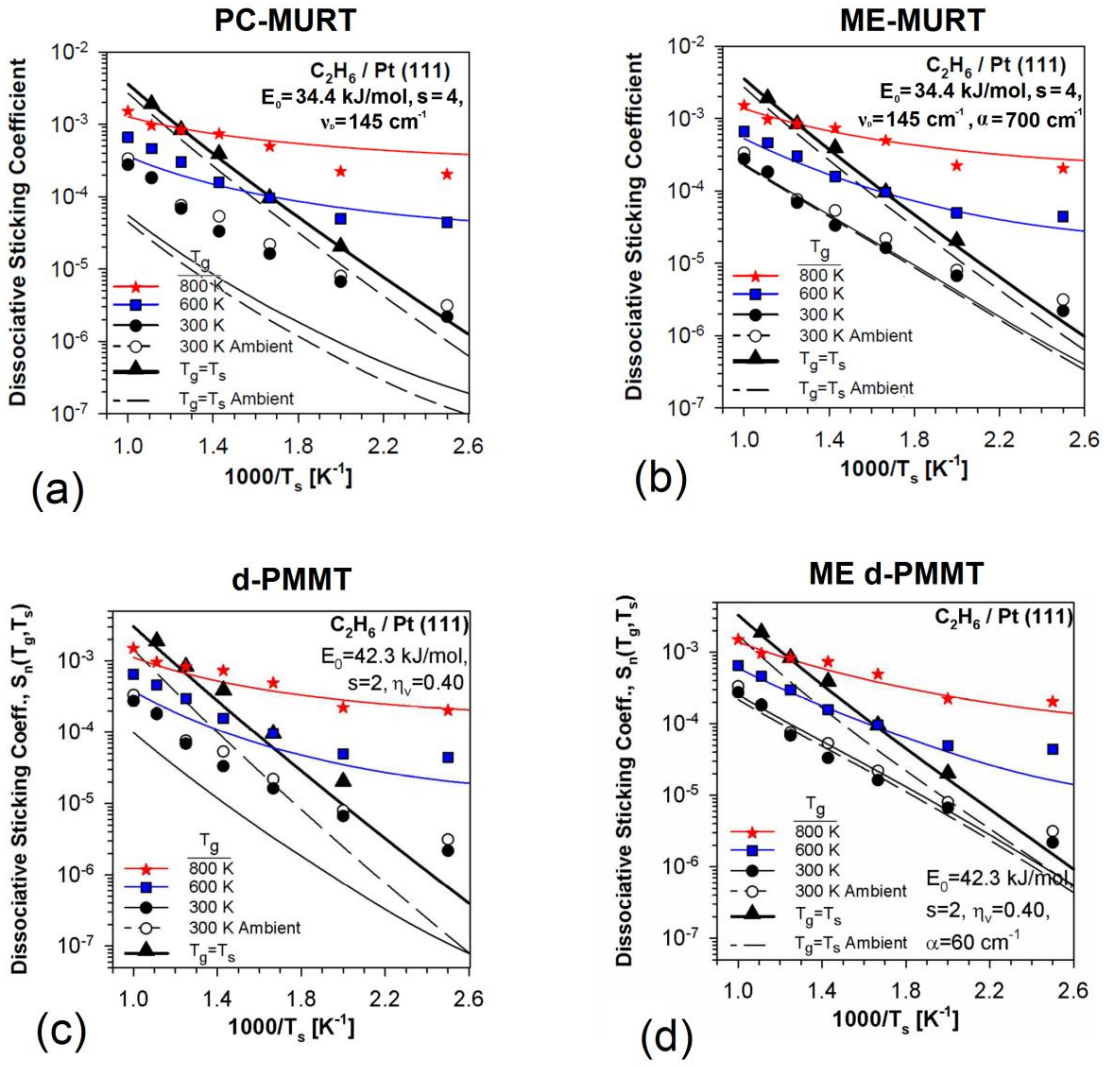

Figure 7.3: $S_n(T_g, T_s)$ and $S_{bkg}(T_g=300\ K, T_s)$ measured for ethane on Pt(111) from Cushing et al. data shown along with model predictions: PC-MURT model (a), ME-MURT model (b), d-PMMT model (c), ME d-PMMT model (d). Explicitly handling gas-surface energy transfer affects S_{bkg} more significantly than S_n, presumably because of increasing desorption lifetimes with decreasing T_g. Because ethane also behaves dynamically on Pt(111), both dynamical constraints as well as gas surface energy transfer must be accounted for.

were reproduced reasonably well. However, neither the d-PMMT model nor the PC-MURT model could accurately describe $S_{bkg}(T_g = 300\ K, T_s)$. Therefore, a new hybrid PMMT model was produced that could simultaneously handle both gas-surface energy transfer as well as dynamical biases (ME d-PMMT). The ME d-PMMT model with $\alpha = 60\ cm^{-1}$ is shown in Figure 7.3(d) and was required in order to accurately describe $S(\vartheta; T = 700\ K)$ for ethane on Pt(111)[12] and accurately reproduces $S_{bkg}(T_g = 300\ K, T_s)$. The α parameter for ethane is almost identical to the value for methane of $50\ cm^{-1}$. However, α is the mean energy transferred per phonon collision, not the total energy transferred. Because τ_D is much longer for ethane than for methane, the total energy exchanged between the PC and the surface is greater for ethane. Although the ME-MURT and ME d-PMMT models both reproduce $S_n(T_g, T_s)$ and $S_{bkg}(T_g = 300\ K, T_s)$ equally well, the ME d-PMMT model is the most physically accurate model and thus most accurately describes the reactivity of ethane on Pt(111).

Unlike methane and ethane, the calculated desorption lifetime at reactive energies for propane on Pt(111) is substantially longer at ~60 ps.[8] In addition, propane also contains many more vibrational modes, which increases the density of rovibrational states, thereby increasing the total density of states of the PC at reactive energies which, should allow for better phonon-PC coupling.[28,29] Therefore, it is more than likely that propane undergoes significant gas-surface energy transfer on Pt(111). For propane dissociation on Pt(111), $S_n(T_g, T_s)$ and $S_{bkg}(T_g = 300\ K, T_s)$ were measured by Cushing et al.[7,8] Figure 7.4 shows $S_n(T_g, T_s)$ and $S_{bkg}(T_g = 300\ K, T_s)$ for propane on Pt(111) as well as MURT model and PMMT model predictions. From the figure, it is quite apparent that neither the PC-MURT model with $E_0 = 21.2$ kJ/mol, $s = 4$, and $\nu_D = 70\ cm^{-1}$ nor the s-PMMT model with $E_0 = 23.6$ kJ/mol, $s = 2$ properly reproduces the $S_n(T_g \neq T_s)$ or S_{bkg}, although the equilibrium DSCs are reproduced well.

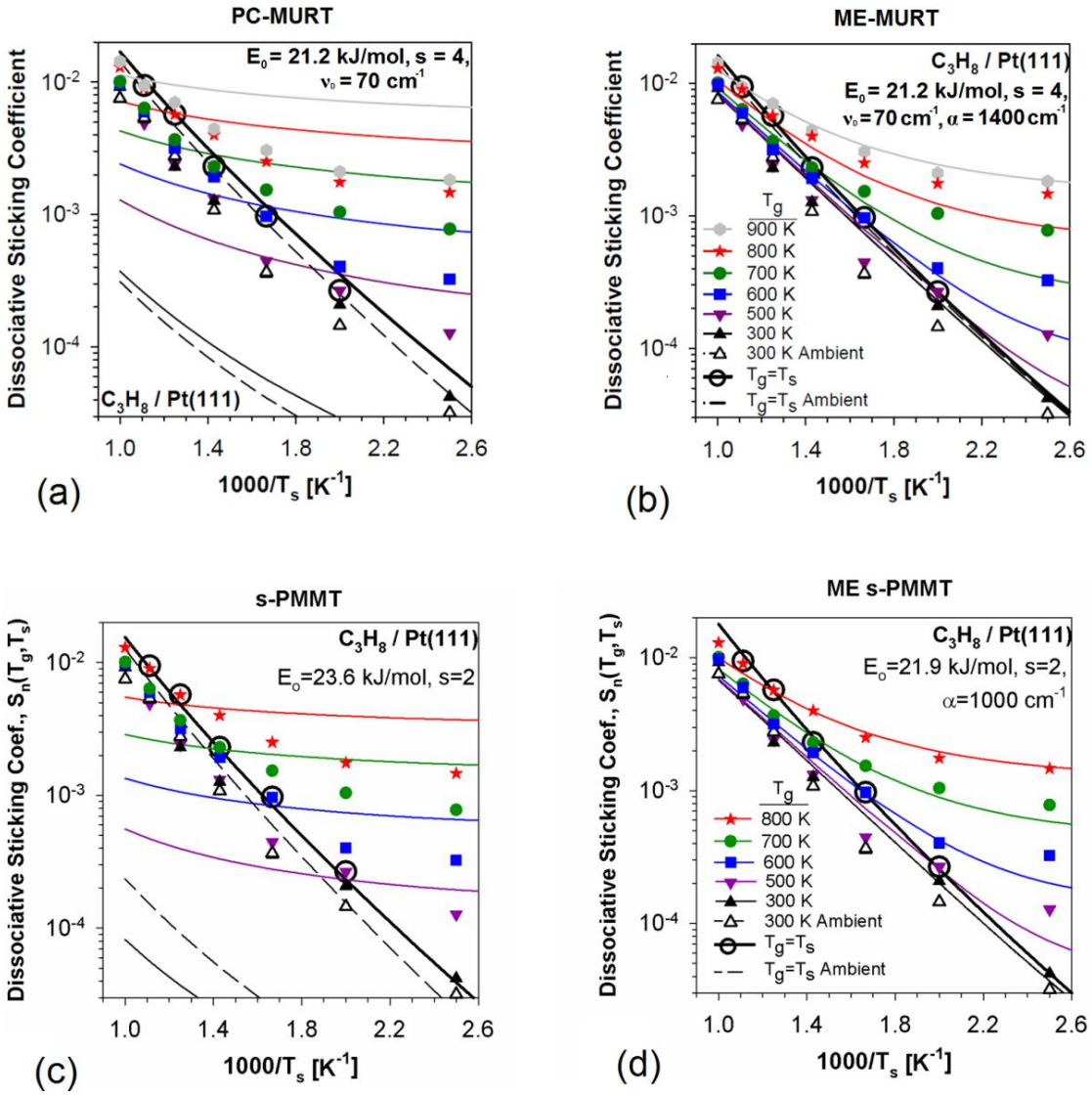

Figure 7.4: $S_n(T_g, T_s)$ and $S_{bkg}(T_g = 300\ K, T_s)$ for propane on Pt(111) from Cushing et al. data and model predictions: PC-MURT model (a), ME-MURT model (b), s-PMMT model (c), and ME s-PMMT model (d). If gas-surface energy transfer is not handled explicitly, then neither the MURT model nor the PMMT model can successfully reproduce $S_n(T_g, T_s)$. Because gas-surface energy transfer is so efficient for propane, the non-equilibrium DSCs collapse toward the equilibrium DSC values.

Thus, gas-surface energy transfer must be accounted for, and the ME-MURT model with $\alpha = 1400$ cm^{-1} as well as the ME s-PMMT model with $E_0 = 21.9$ kJ/mol and $\alpha = 1000$ cm^{-1} reproduce both $S_n(T_g, T_s)$ and $S_{bkg}(T_g = 300\text{ K}, T_s)$ reasonably well. However, the ME s-PMMT is a more accurate model of reactivity and so propane DSCs on Pt(111) are more accurately reproduced with this model as opposed to the ME-MURT model. It appears that the increased gas-surface energy transfer causes the non-equilibrium DSC measurements to tend toward the equilibrium DSC values. In addition, hyperthermal gas apparently thermalizes towards the surface temperature less efficiently than hypothermal gas because desorption lifetimes at reactive energies are shorter for more energetic gas. Although d-PMMT model calculations were not conducted for propane dissociation on Pt(111), angle-resolved DSCs measurements of propane on Pt(111), S(ϑ; T = 700 K), have shown that propane apparently behaves statistically on Pt(111),[12] and so, the ME s-PMMT model accurately describes propane reactivity on Pt(111).

Desorption lifetimes at reactive energies, τ_D , for molecules larger than propane were not calculated, but were instead extrapolated from τ_D calculated for methane, ethane, and propane in an exponential fashion.[7,8] The fit to methane, ethane, and propane yields,

$$\tau_D = 2.55 * 10^{-3} e^{3.32*N} \qquad \text{Equation 7.1}$$

where τ_D is the desorption lifetime at reactive energies in picoseconds and *N* is the number of carbons in the linear alkane. The desorption lifetime calculated from Equation 7.1 for butane on Pt(111) is ~1.5 ns which is substantially longer than propane on Pt(111). In addition, butane has many vibrational modes, and some are fairly low in frequency (< 500 cm^{-1}), therefore the density of rovibrational states should be very high and there should be relatively good overlap between the butane-PC and platinum phonon densities of states (including multi-quanta phonon states).[28,29] For butane dissociation on Pt(111), there are no PMMT model predictions because

the transition state complex parameters are not yet available from DFT calculations. Figure 7.5 shows $S_n(T_g, T_s)$ and $S_{bkg}(T_g = 295\ K, T_s)$ for butane on Pt(111). From the graph, it is apparent that both hyperthemal and hypothermal gas temperature, non-equilibrium DSCs are tending towards the equilibrium DSC values. As alkane size increases, the depth of the molecular physisorption well increases which causes τ_D to increase as well. Although no PMMT modeling was conducted for butane, α, the average energy transferred per phonon collision to or from the PC, increases as the alkane size increases. Because the average amount of energy transferred per phonon collision increases, and the total time the butane-PC remains intact on the surface increases, then the total amount of gas-surface energy transfer increases as well allowing both hyperthermal and hypothermal gas to equilibrate to the surface temperature.

For pentane dissociative chemisorption on Pt(111), no PMMT calculations were calculated because it was determined that the gas fully thermalized to the surface temperature. As previously shown, from methane to butane, increasingly efficient gas-surface energy transfer causes non-equilibrium DSCs to tend towards equilibrium DSC values. Therefore, at some point in the series of alkanes on Pt(111), the gas temperature should fully equilibrate to that of the surface temperature such that, $S_n(T_g, T_s) = S(T_s) = S(T)$. In order to test whether or not pentane fully thermalizes to the surface temperature, $S_n(T_g, T_s)$ were measured for three different scenarios: $T_g > T_s$, $T_g = T_s$, and $T_g < T_s$. If $S_n(T_g, T_s) \approx S_{bkg}(T_s)$ in all three cases, then pentane should undergo full thermalization to the surface temperature. As previously stated, pentane undergoes thermal cracking at gas temperature in excess of 600 K.[30,31] Therefore, DSC measurements were limited to $T_g \leq 600$ K. Figure 7.6 shows $S_n(T_g = 600\ K, T_s)$ and $S_{bkg}(T_g = 295\ K, T_s)$ for pentane on Pt(111). The ratio $S_{bkg}(T_g = 295\ K, T_s)/S_n(T_g = 600\ K, T_s)$ for $T_s = 400$ K, $T_s = 600$ K, and $T_s = 800$ K is shown in Table 7.1.

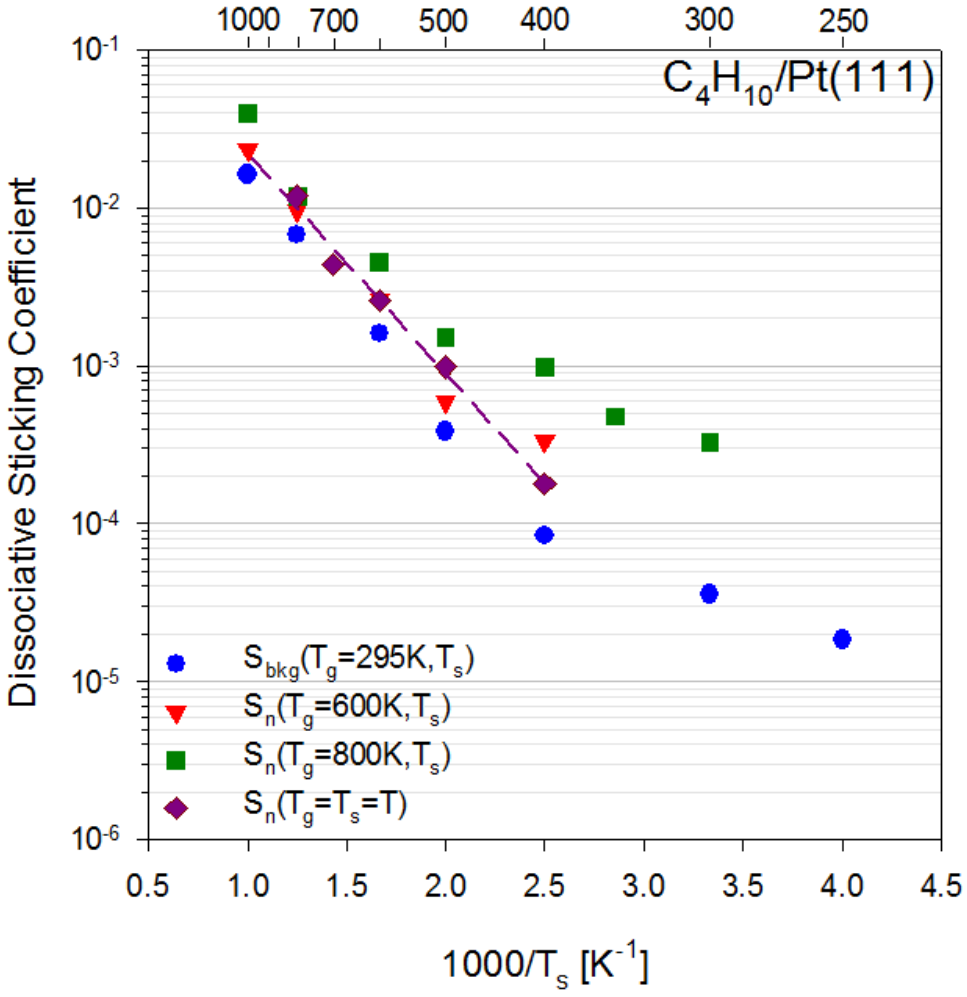

Figure 7.5: $S_n(T_g, T_s)$ and $S_{bkg}(T_g = 295\ K, T_s)$ shown for butane on Pt(111). Although no PMMT modeling was conducted for butane on Pt(111), increasingly efficient gas-surface energy transfer manifests as a collapse of the non-equilibrium DSCs toward the equilibrium DSC values.

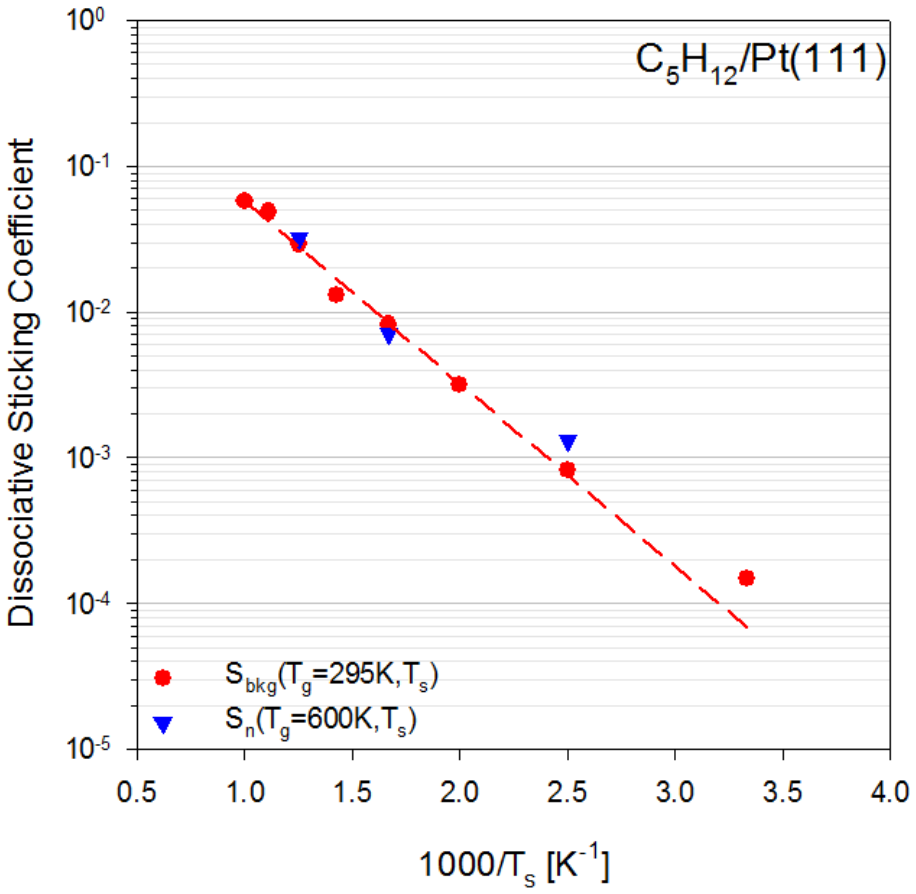

Figure 7.6: $S_n(T_g = 600\ K, T_s)$ and $S_{bkg}(T_g = 295\ K, T_s)$ for pentane on Pt(111). For pentane, gas-surface energy transfer is so efficient that $S_n(T_g, T_s) \approx S_{bkg}(T_s)$ and so, the temperature of the gas is apparently irrelevant for pentane reactivity on Pt(111).

T_s	$S_{bkg}(T_g = 295\ K, T_s) / S_n(T_g = 600\ K, T_s)$
400	0.62
600	1.16
800	0.91

Table 7.1: $S_{bkg}(T_g = 295\ K, T_s) / S_n(T_g = 600\ K, T_s)$ for butane on Pt(111), shown for various T_s.

In all three cases, $S_n(T_g = 600\ K, T_s) \approx S_{bkg}(T_g = 295\ K, T_s)$; although the value for $T_s = 400$ K is somewhat low, it should be noted that the direct to background flux of these experiments is 3:1 and the reactivity of the background flux is nominally the same as the directed flux. Therefore, background subtraction becomes increasingly difficult and errors can range up to $\pm$ 15%. Overall then, it seems that the impinging pentane molecules are initially trapped on the surface and thermalized to the surface temperature, independent of the initial gas temperature. Pentane has 9 more vibrational modes than butane and several of these modes are low frequency. As with propane and butane, there should be more state-mixing because of the increasing rovibrational density of states for both pentane and the PC and hence better phonon-PC coupling. In addition, the τ_D for pentane on Pt(111), calculated using Equation 7.1, is ~40 ns which is much longer than butane (~1.5 ns). The increased phonon-PC coupling and long τ_D are responsible for pentane undergoing full thermalization on Pt(111). Since it was determined that pentane fully thermalizes to the surface temperature, no $S_n(T_g, T_s)$ measurements were conducted for hexane, octane, or nonane on Pt(111), and it was instead assumed that $S_{bkg}(T_g, T_s) = S(T_s) = S(T)$.

As the alkane size is increased from methane to nonane, there is a collapse of the non-equilibrium DSCs, $S_n(T_g \neq T_s)$ towards the equilibrium DSCs, $S_n(T_g = T_s)$. By pentane, there is sufficient collapse that the approximation, $S_n(T_g, T_s) = S(T_s) = S(T)$ can be made. However, the cause of this phenomenon is slightly convoluted. As the alkane size increases, the gas-surface energy transfer increases at the same time that the activation energy decreases. With enough gas-surface energy transfer, the energy of the PC is equilibrated to that of the surface such that, there is no apparent gas temperature dependence (i.e., $S_n(T_g, T_s) = S(T_s) = S(T)$ for all (T_s, T_g) combinations). On the other hand, as the activation energy decreases, the reaction becomes insensitive to variations in either the surface or gas temperature because such little energy is required to overcome the barrier. By calculating differential energy uptakes for the various alkanes, it is possible to discern whether or not the increasing gas-surface energy transfer is responsible for the apparent thermalization of impinging alkanes sans theory; however, this, in effect, confirms gas-surface energy transfer in the MURT and PMMT models. When an alkane successfully dissociates, both surface energy and molecular energy were used to overcome the barrier for dissociation, and the fraction of energy from either degree of freedom is the differential energy uptake, d_j. Within the confines of the PMMT model, the energy uptake is defined as,[4]

$$d_j = \frac{\langle E_j(T_j)\rangle_R - \langle E_j(T_j)\rangle}{\langle E^*(T)\rangle_R - \langle E^*(T)\rangle} = \frac{E_a(T_j)}{E_a(T)} \qquad \text{Equation 7.2}$$

where $\langle E_j(T_j)\rangle$ is the mean energy derived from the *j*th degree of freedom of the molecules or the surface that form all PCs, and $\langle E_j(T_j)\rangle_R$ is the mean energy derived from the *j*th degree of freedom of the molecules or the surface that form reactive PCs. $\langle E^*(T_j)\rangle$ is the mean total energy of all PCs formed, $\langle E^*(T_j)\rangle_R$ is the mean total energy of the reactive PCs, and $E_a(T)$ is

the thermal activation energy. Experimentally $\langle E_j(T_j)\rangle_R$-$\langle E_j(T_j)\rangle$ is given by the effective activation energy of the surface or gas, $E_a(T_j)$, by a non-equilibrium Tolman relation,[5]

$$E_a(T_i) = \langle E_i(T_i)\rangle_R - \langle E_i(T_i)\rangle \qquad \text{Equation 7.3}$$

where $\langle E_i(T_i)\rangle_R$ is the mean surface or gas energy of PCs reacting and $\langle E_i(T_i)\rangle$ is the mean surface or gas energy of all PCs formed at the given (T_g, T_s) combination. The effective activation energy of either the gas or surface, $E_a(T_i)$, can be easily calculated from experimental measurements via,[32]

$$E_a(T_i) = -R\,\frac{\partial(\ln[S(T_i)])}{\partial(\frac{1}{T_i})} \qquad \text{Equation 7.4}$$

where R is the ideal gas constant. Combining Equations 7.2, 7.3, and 7.4 yields the experimentally derived differential energy uptake, d_j,

$$d_j = \frac{\langle E_j(T_j)\rangle_R - \langle E_j(T_j)\rangle}{\langle E^*(T)\rangle_R - \langle E^*(T)\rangle} = \frac{\langle E_j(T_j)\rangle_R - \langle E_j(T_j)\rangle}{E_a(T)} =$$

$$\frac{E_a(T_j)}{E_a(T)} = -R\,\frac{\partial(\ln[S(T_j)])}{\partial(\frac{1}{T_j})}\Big/E_a(T) \qquad \text{Equation 7.5}$$

Ideally $d_s + d_g$ should equal 1; however, because of experimental errors in measuring DSCs which results in errors in calculated $E_a(T_j)$ and $E_a(T)$, this was not always the case. According to Bukoski et al.,[5] the T_g and T_s dependent effective activation energies, $E_a(T_j)$, should sum to the true thermal activation energy, $E_a(T)$, such that,

$$E_a(T) = \sum_j E_a(T_j) \qquad \text{Equation 7.6}$$

$E_a(T_g)$ is defined as the T_g dependent effective activation energy of a random gas distribution impinging on a surface; however, our effusive molecular beam source emits directed flux, and so

we make the approximation, $E_a(T_g;\ T_s,\ \vartheta = 0°) \approx E_a(T_g)$ which holds well in modeling. From Equation 7.5, $d_j = E_a(T_j)/E_a(T)$, and the sum rule should work,

$$1 = \sum_j d_j \qquad \text{Equation 7.7}$$

Because of the approximation that $E_a(T_g)$ can be defined using the effusive molecular beam source, and the error inherent in measuring $E_a(T_j)$ and $E_a(T)$, we instead define operationally that,

$$d_j^* = \frac{E_a(T_j)}{\sum_i E(T_i)} \qquad \text{Equation 7.8}$$

which avoids error from $E_a(T)$ and $E_a(T_j)$ and also insures that the sum rule holds such that,

$$\sum_{j\,=\,s,g} d_j^* = 1 \qquad \text{Equation 7.9}$$

The differential energy uptake is the fraction of energy from either the surface or the gas that was consumed to overcome the barrier for dissociation. If the sole source of exchangeable energy to surmount the barrier was derived from the surface, then d_s^* would approach 1 and d_g^* would approach 0. Such a scenario would occur if the gas-surface energy transfer was sufficient enough to cause the impinging molecule to thermalize to the surface temperature before reaction or the total exchangeable energy from the gas is low (i.e., low T_g). Conversely, if the gas is the sole source of exchangeable energy for surmounting the barrier, then d_g^* would approach 1 and d_s^* would approach 0. In this case, either the total exchangeable energy from the surface is low (i.e., low T_s) or the desorption lifetime at reactive energies is so short that there is negligible energy transfer between the PC and the surface. However, the limiting case where one d_j^* approaches 0 and the other d_j^* approaches 1 is not too informative about the relative importance of exchangeable energy in promoting dissociation. Varying T_s and T_g varies the total available energy for reaction but d_j^* defines the exchangeable energy consumed and in a sense measures the effectiveness of the surface and gas exchangeable energies to promote reaction. Therefore, by comparing d_j^* at different T_s and T_g for a given alkane, it should then be possible to determine

how effectively the surface and gas promote reactivity. In order to calculate d_j^* from Equation 7.5 for the various alkanes, $\partial \ln[S(T_i)]/\partial(1/T_i)$ was calculated by first plotting $\ln[S(T_i)]$ against $(1/T_i)$. The plots were then fit using a polynomial function and the slope of the function was extracted at each T_i. By definition, this slope is equal to $\partial \ln[S(T_i)]/\partial(1/T_i)$. Figures 7.7 and 7.8 show $\ln[S(T_i)]$ versus $1/T_i$ with polynomial fits and d_s^* *(*T_s*)* and d_g^* *(*T_s*)* calculated for methane and ethane on Pt(111) respectively along with spline fits of the d_j^* to guide the eye. As shown in Figures 7.7(c) and 7.7(d) for methane, at $T_s \geq 600$ K and $T_g = 295$ K, the surface supplies the majority of energy as indicated by d_s^* approaching 1 and d_g^* approaching 0 with increasing T_s. However, for elevated gas temperatures ($T_g = 600$ K and $T_g = 800$ K), $d_s^* < 0.6$ over the entire T_s range of measurements. Additionally, d_s^* decreases with increasing T_g. In order to overcome the barrier for dissociation, energy is required from either the gas, the surface, or both. If one degree of freedom is energy rich (i.e., higher temperature) compared to the other, then there is more energy available for reaction from the energy rich degree of freedom. Whereas, the energy poor degree of freedom (i.e., lower temperature) contributes significantly less energy to overcome the barrier and so does not affect reactivity as much. Hence, for $T_s >> T_g$, d_s^* tends towards 1 and d_g^* tends towards 0 and for $T_s << T_g$ the opposite is true.

The behavior of differential energy uptakes for ethane on Pt(111) is similar to that of methane with subtle variations. Figures 7.8(c) and (d) show that as T_s increases, d_s^* increases with a corresponding decrease in d_g^*; as T_g increases, the converse is true. As with methane on Pt(111), as the energy is increased in one degree of freedom, more energy is available for reaction and so, the contribution of energy to promote reaction is increased as well. However, unlike methane, ethane achieves the limiting case where d_s^* tends towards 1 and d_g^* tends towards 0 at ($T_g = 300$ K, $T_s = 600$ K) whereas, methane achieves this limiting case at ($T_g = 300$ K, $T_s = 800$ K). Additionally, for ethane, each $d_s^*(T_g, T_s)$ value is greater than the corresponding value for methane, excepting cases where $d_s^* \sim 1$. Therefore, over the measured

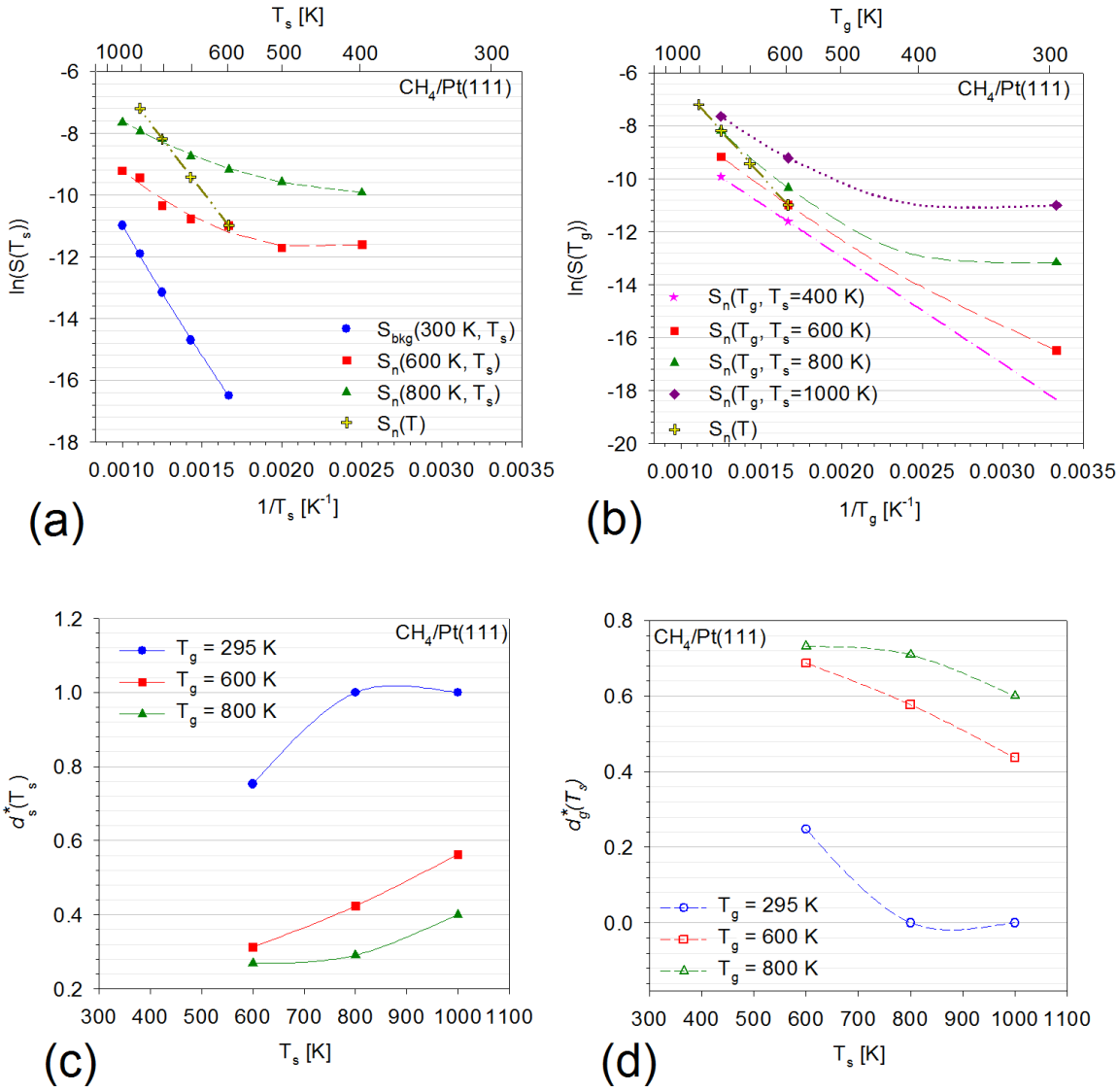

Figure 7.7: Plots of ln[S(T_i)] versus $1/T_i$ with polynomial fits and experimentally derived differential energy uptakes for the surface, d_s^*, and gas, d_g^*, for methane dissociative chemisorption on Pt(111): ln[S(T_s)] (a), ln[S(T_g)] (b), $d_s^*(T_s)$ (c), and $d_g^*(T_s)$ (d). Curves in (c) and (d) are spline fits to guide the eye. As T_s or T_g is increased, there is a corresponding increase in d_s^* and d_g^* respectively. As more energy is available from a degree of freedom, more energy is contributed to the reaction from that degree of freedom.

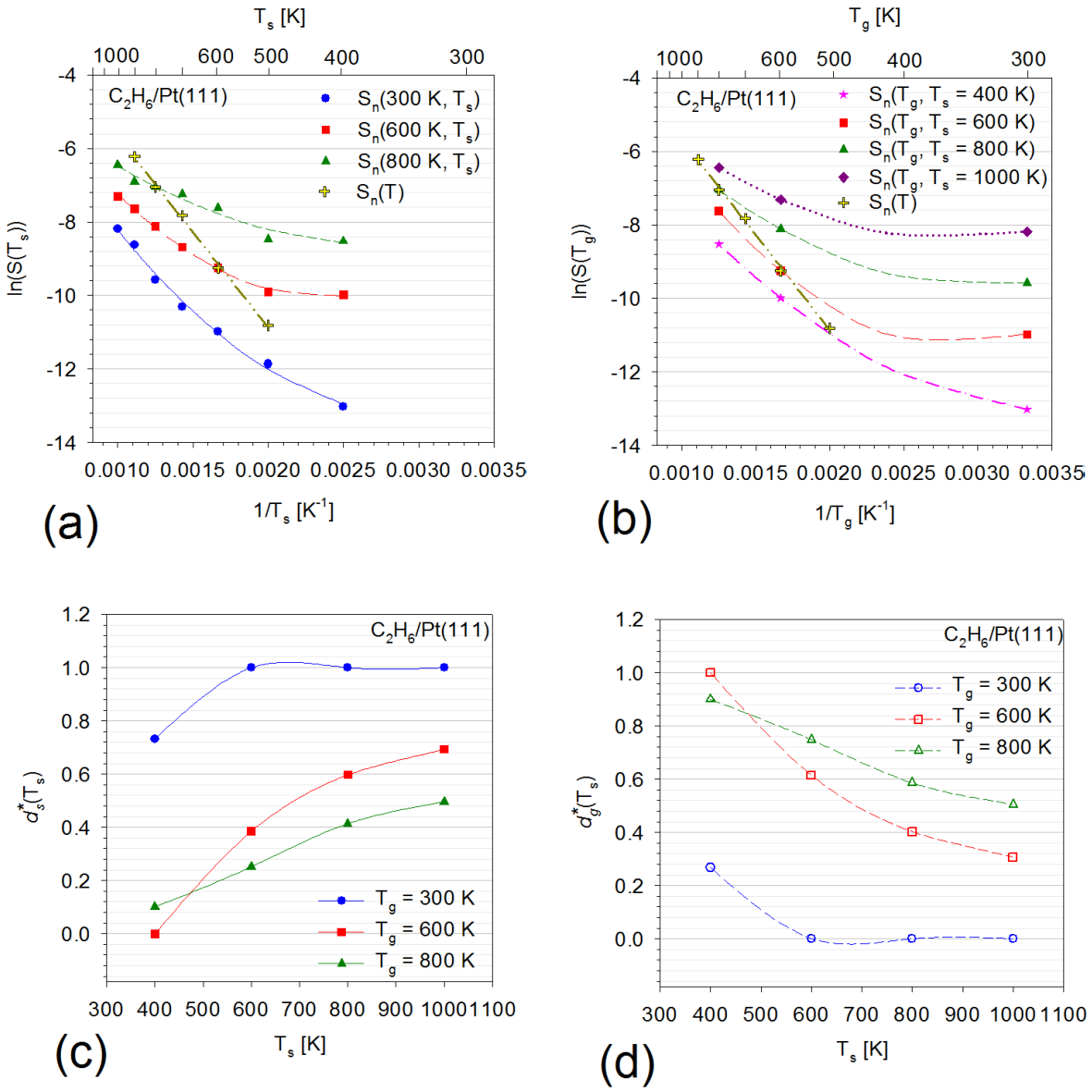

Figure 7.8: Plots of $\ln[S(T_i)]$ versus $1/T_i$ with polynomial fits and experimentally derived differential energy uptakes for the surface, d_s^*, and gas, d_g^*, for ethane dissociative chemisorption on Pt(111): $\ln[S(T_s)]$ (a), $\ln[S(T_g)]$ (b), $d_s^*(T_s)$ (c), and $d_g^*(T_s)$ (d). Curves in (c) and (d) are spline fits to guide the eye. As T_s or T_g is increased, there is a corresponding increase in d_s^* and d_g^* respectively. As more energy is available from a degree of freedom, more energy is contributed to the reaction from that degree of freedom.

temperature range, it appears that surface energy plays an enhanced role for ethane dissociation on Pt(111) compared to methane dissociation.

As previously shown in Figure 7.4, MURT and PMMT modeling shows that propane undergoes significant gas-surface energy transfer on Pt(111). Experimentally, this can be seen as a collapse of non-equilibrium DSCs, $S_n(T_g \neq T_s)$, towards equilibrium DSC values, $S_n(T_g = T_s = T)$. Because of the increased gas-surface energy transfer, d_j^* should exhibit some interesting behavior. Figure 7.9 shows $\ln[S(T_i)]$ versus $1/T_i$ with polynomial fits and calculated $d_s^*(T_s)$ and $d_g^*(T_s)$ for propane on Pt(111) along with spline fits of the d_j^* to guide the eye. The same limiting behavior that d_s^* approaches 1 when $T_s >> T_g$ is true for propane as it is for methane and ethane. In addition, as T_j increases or decreases there is an identical response for d_j^*. However, unlike methane and ethane, for all T_g, $d_s^* > 0.8$ when $T_s = 1000$ K; this was not the case for methane nor ethane where $d_s^* < 0.8$ for $T_g = 600$ and 800 K at $T_s = 1000$ K.

Although no PMMT modeling was conducted for butane dissociative chemisorption on Pt(111), differential energy uptakes can determine the efficiency of gas-surface energy transfer for butane on Pt(111). Figure 7.10 shows $\ln[S(T_i)]$ versus $1/T_i$ with polynomial fits and $d_s^*(T_s)$ and $d_g^*(T_s)$ calculated for butane on Pt(111) along with spline fits of the d_j^* to guide the eye. Abnormal $d_i(T_s)$ in Figures 7.10(c) and 7.10(d) are caused by errors in DSC measurements due to high reactivity at high T_s and T_g and short dosing times. As shown in Figure 7.10(c) and 7.10(d), butane shows the same limiting behavior for d_j^* as methane, ethane, and propane exhibit. However, $d_s^* > 0.8$ for all T_g at $T_s = 800$ K which, was achieved for propane only at an elevated surface temperature of 1000 K and was not achieved for methane nor ethane. Additionally, $d_s^*(T_s) > 0.3$ for all T_g which indicates the increasing importance of surface energy for butane reactivity on Pt(111) compared to methane, ethane, and propane which had a lower d_s^* boundary.

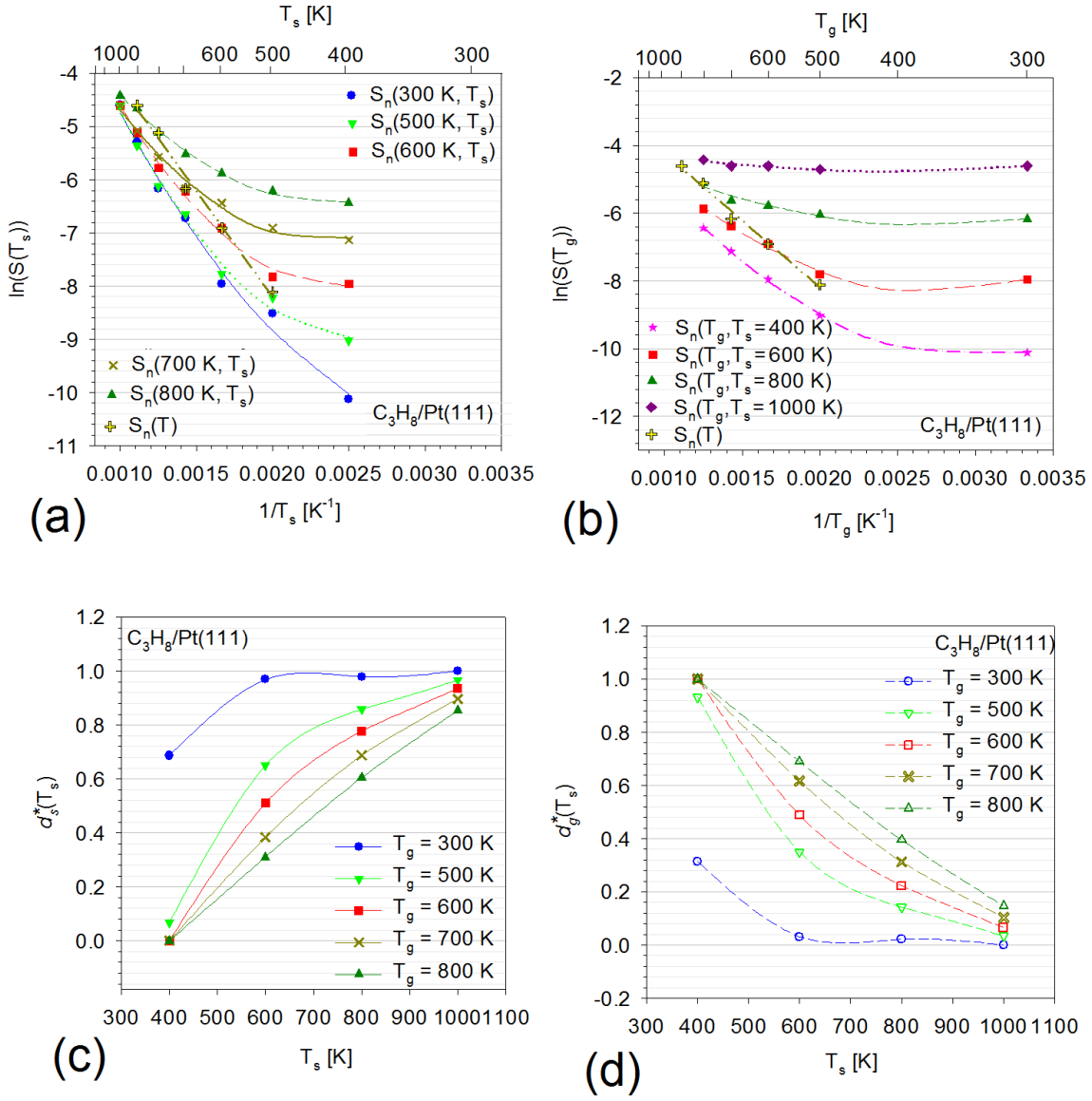

Figure 7.9: Plots of ln[S(T_i)] versus 1/T_i with polynomial fits and experimentally derived differential energy uptakes for the surface, d_s^*, and gas, d_g^*, for propane dissociative chemisorption on Pt(111): ln[S(T_s)] (a), ln[S(T_g)] (b), d_s^*(T_s) (c), and d_g^*(T_s) (d). Curves in (c) and (d) are spline fits to guide the eye. As T_s or T_g is increased, there is a corresponding increase in d_s^* and d_g^* respectively. As more energy is available from a degree of freedom, more energy is contributed to the reaction from that degree of freedom. Note that the d_s^* curve becomes less curved as T_g increases and would most likely invert for higher T_g.

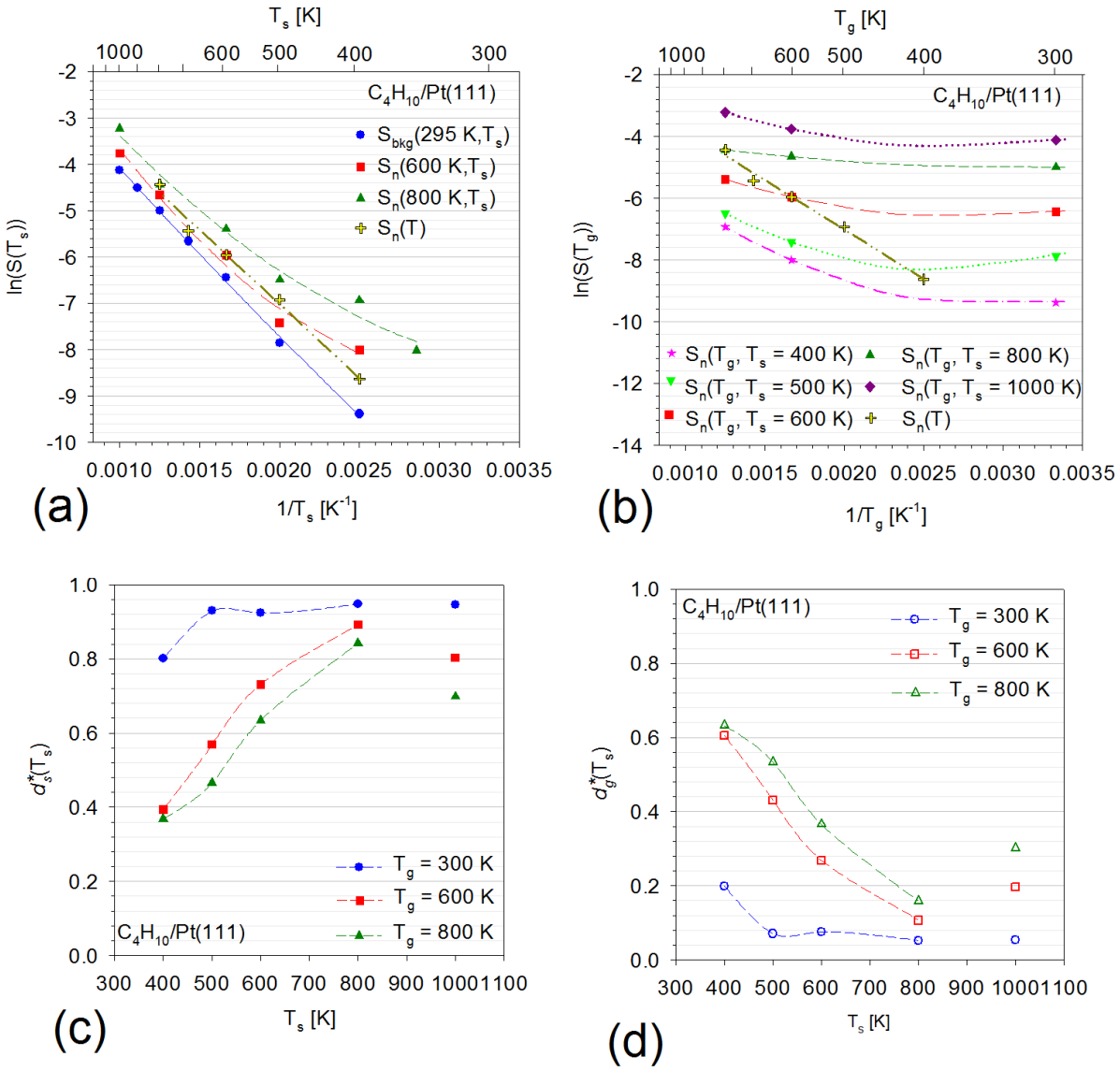

Figure 7.10: Plots of ln[S(T_i)] versus 1/T_i with polynomial fits and experimentally derived differential energy uptakes for the surface, d_s^*, and gas, d_g^*, for butane dissociative chemisorption on Pt(111): ln[S(T_s)] (a), ln[S(T_g)] (b), d_s^*(T_s) (c), and d_g^*(T_s) (d). Curves in (c) and (d) are spline fits to guide the eye. Abnormal d_i(T_s) in (c) and (d) are caused by errors in DSC measurements due to high reactivity at high T_s and T_g and short dosing times. As T_i is increased, there is a corresponding increase in d_i^*; more energy in a degree of freedom can be contributed to the reaction. d_s^* and d_g^* approach 1 and 0 respectively, as T_s is increased much faster than for methane, ethane, or propane.

In general, we find some interesting trends when comparing differential energy uptakes amongst the various alkanes. For all four gases, as T_s is increased, $d_s^*(T_s)$ increases and $d_g^*(T_s)$ decreases. Conversely, as T_g is increased, there is a corresponding decrease in $d_s^*(T_s)$ and an increase in $d_g^*(T_s)$. Increases in temperature correspond to increases in internal energy content and as the energy content of a particular degree of freedom, either the surface or gas, is increased, there is more exchangeable energy available for reaction. Therefore, a larger fraction of the energy consumed in a reaction should come from that degree of freedom which has an increase in energy content. However, the variation of the differential energy uptake varies depending on the (T_g, T_s) combination as well as the gas. When the energy content of the gas is relatively low (~300 K), the $d_s^*(T_s)$ approach an asymptote of 1 over the measured temperature range as T_s is increased. As the temperature of the gas increases, this limiting behavior shifts to higher T_s. For methane, this change is quite apparent; at T_s = 1000 K, $d_s^*(T_s)$ drops from 1 at T_g = 295 K to 0.56 at T_g = 600 K (Figure 7.7(c)). When the internal energy content of the gas is relatively high (~800 K) the $d_g^*(T_s)$ approach an asymptote of 1 as T_s is decreased (Figure 7.7(d)). Additionally, the d_j^* spline curves, which are intended merely to guide the eye, do reveal some interesting behavior. For methane (Figure 7.7), as T_g is increased from 295 K to 800 K, the curvature of the $d_s^*(T_s)$ spline fits invert from opening downward to opening upward. In addition, for propane (Figure 7.9), as T_g increases, the $d_s^*(T_s)$ spline curves, which open downwards, become less curved and straighten out and would most likely begin to curve upwards in the opposite direction for even higher T_g. This change in curvature of the $d_s^*(T_s)$ and $d_g^*(T_s)$ spline fits as well as the limiting behavior when the energy of one degree of freedom is much higher than the other, indicates that $d_s^*(T_s)$ and $d_g^*(T_s)$ could be fit to an "S" shaped curve that is pinned at the ends to d_j^* = 0 and d_j^* = 1 with the inflection point of the curve shifting depending on T_g. A schematic of a theoretical "S" shaped curve for $d_s^*(T_s)$ is shown in Figure

7.11. For $d_s^*(T_s)$, as T_g is increased, the inflection point shifts to higher T_s, and for $d_g^*(T_s)$, the opposite is true. This is somewhat expected; however, when one temperature is significantly higher than the other, then d_j^* goes to 1 for the high temperature degree of freedom and 0 for the low temperature degree of freedom. When the exchangeable energies of both degrees of freedom are near each other in value, then both d_s^* and d_g^* will be more sensitive to variations in T_s and T_g and will be near in value as well. Thus comparisons of d_s^* and d_g^*, reveal the relative importance of exchangeable gas and surface energy in overcoming the barrier for dissociation for a particular alkane. However, in order to determine if gas-surface energy transfer is responsible for the increase in apparent thermalization, direct comparisons of d_s^* and d_g^* must be made over the range of alkanes at constant (T_g, T_s) conditions so that there is no convolution with temperature effects.

Figures 7.12 and 7.13 show $d_s^*(T_s)$ and $d_g^*(T_s)$ calculated for methane, ethane, propane, and butane as a function of T_s for several different T_g with spline fits to the d_j^* to guide the eye. As with Figures 7.7 through 7.10, if either T_s or T_g is increased, there is a corresponding increase in $d_s^*(T_s)$ and $d_g^*(T_s)$ respectively. Additionally, the Figures 7.12 and 7.13 show similar "S" shape characteristics like those in Figures 7.7 through 7.10. However, what is interesting is that as the alkane size is increased, there is an increase in d_s^* for any and all given (T_g, T_s) combinations (excepting $d_s^*(T_s) \approx 1$). Clearly, there is a link between d_s^*, d_g^*, and alkane size. Figure 7.14 shows d_s^* and d_g^* at constant (T_g, T_s) conditions as a function of the alkane size for low T_g (~300 K) and high T_g (800 K). The anomalies at d_i(800 K, 1000 K), N = 4 for Figures 7.14(c) and 7.14(d) are caused by errors in DSC measurements due to high reactivity and short dosing times for butane on Pt(111) when both T_s and T_g are at relatively high values. Figure 7.15 shows equilibrium temperature d_s^* and d_g^* as a function of alkane size. Figures 7.14 and 7.15 both have spline fits to d_j^* to guide the eye.

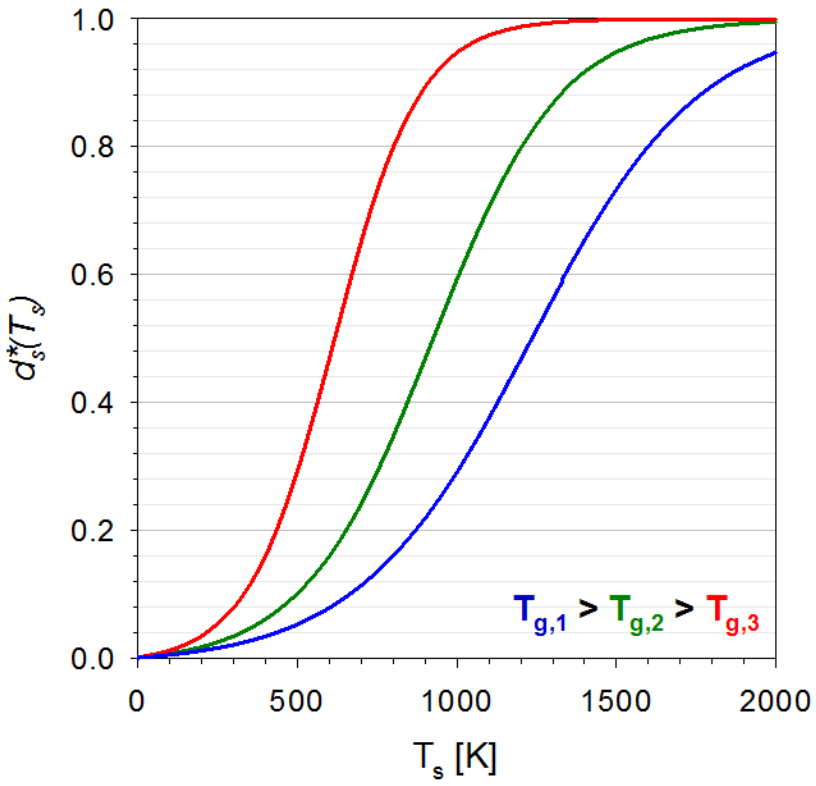

Figure 7.11: Theoretical "S" plot of $d_s^*(T_s)$ for three different gas temperatures, $T_{g,i}$. The inflection point of the curve moves to higher T_s as T_g increases; if more energy is available from the gas, then the fraction of energy available for reaction, coming from the surface, decreases. When the energy content of the surface is low ($T_s \approx 0$ K), there is little surface energy available for reaction and so, $d_s^* = 0$. When the energy content of the surface is much greater than that of the gas ($T_s >> T_g$) then $d_s^* = 1$.

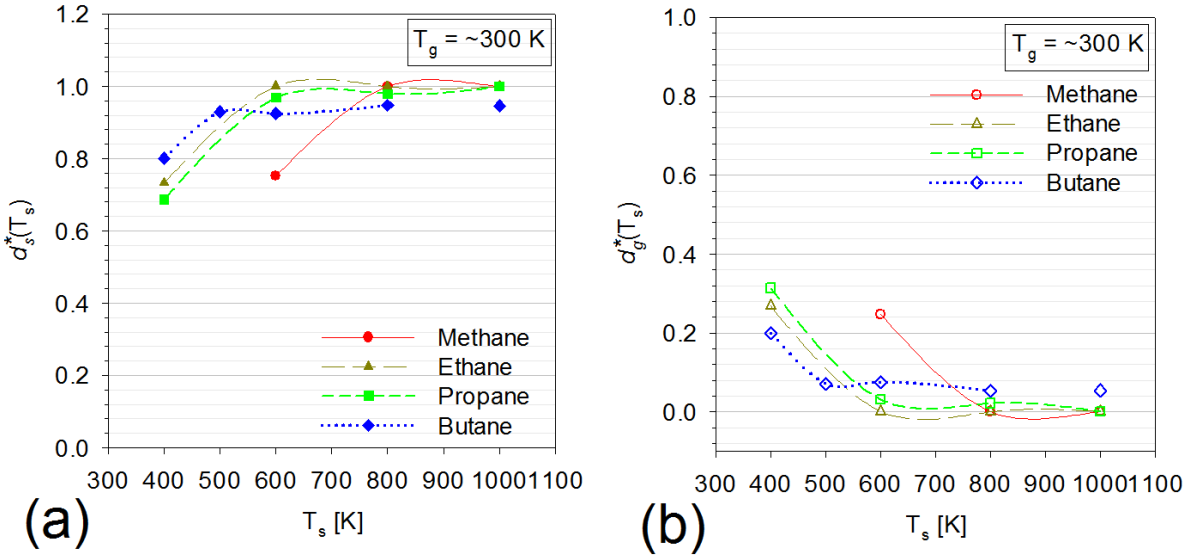

Figure 7.12: Plots of experimentally derived differential energy uptakes for the surface, d_s^*, and gas, d_g^*, for methane, ethane, propane, and butane dissociative chemisorption on Pt(111) with spline fits to guide the eye: $d_s^*(T_s)$ at T_g = ~300 K (a) and $d_g^*(T_s)$ at T_g = ~300 K (b). As T_s increases, d_s^* increases and d_g^* decreases; since the energy of the gas is relatively low with respect to the surface, d_s^* approaches 1 and d_g^* approaches 0 with increasing T_s for all gases.

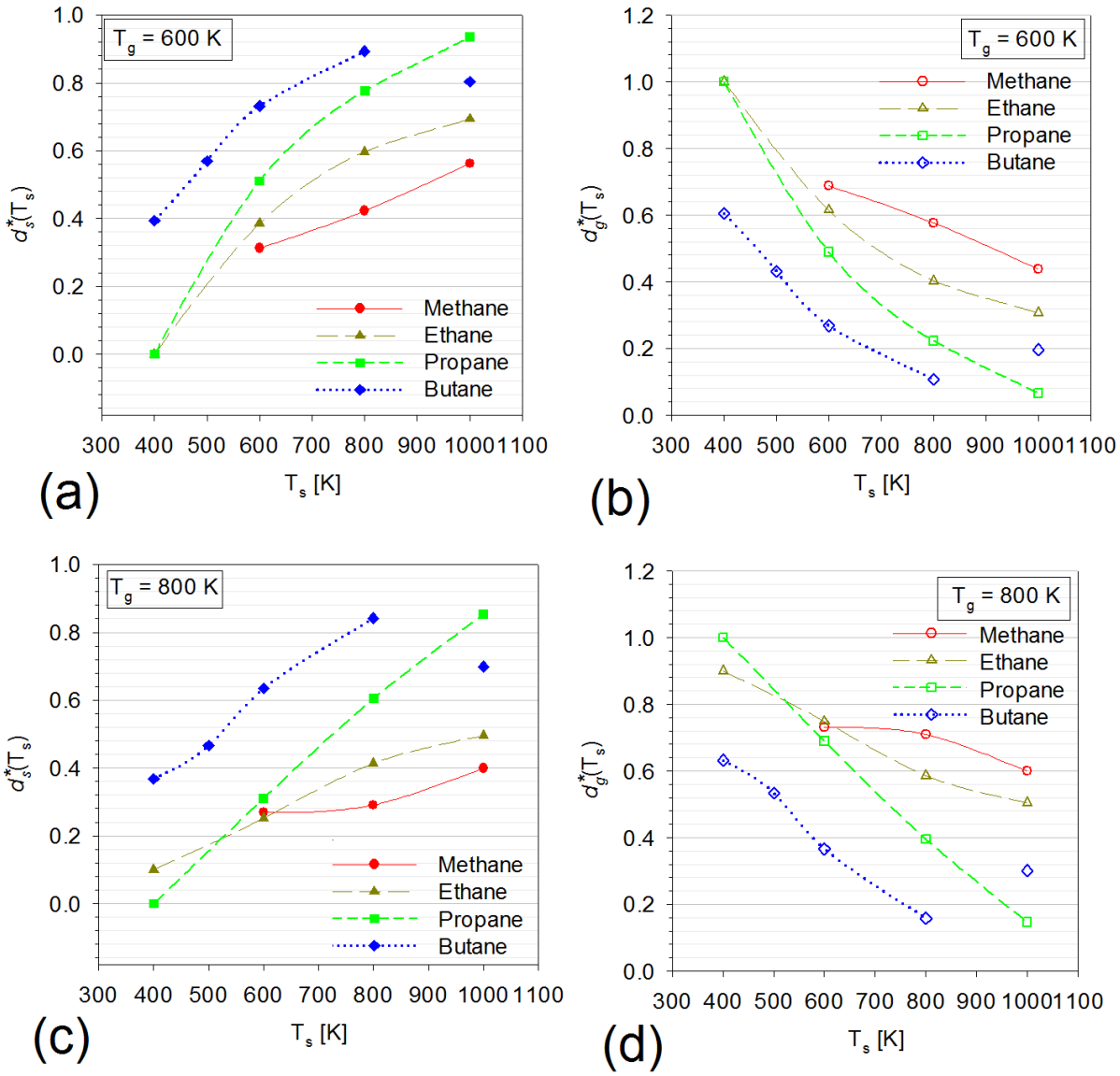

Figure 7.13: Plots of experimentally derived differential energy uptakes for the surface, d_s^*, and gas, d_g^*, for methane, ethane, propane, and butane dissociative chemisorption on Pt(111) with spline fits to guide the eye: $d_s^*(T_s)$ at T_g = 600 K (a), $d_g^*(T_s)$ at T_g = 600 K (b), $d_s^*(T_s)$ at T_g = 800 K (c), and $d_g^*(T_s)$ at T_g = 800 K (d). As T_s increases, d_s^* increases and d_g^* decreases; d_s^* trends towards 1 and d_g^* trends towards 0 with increasing T_s. Since the energies of the gas and surface are comparable, d_s^* approaches 1 only for propane and butane at T_s = 1000 K. Additionally, for a given T_s, d_s^* tends to increase with alkane size.

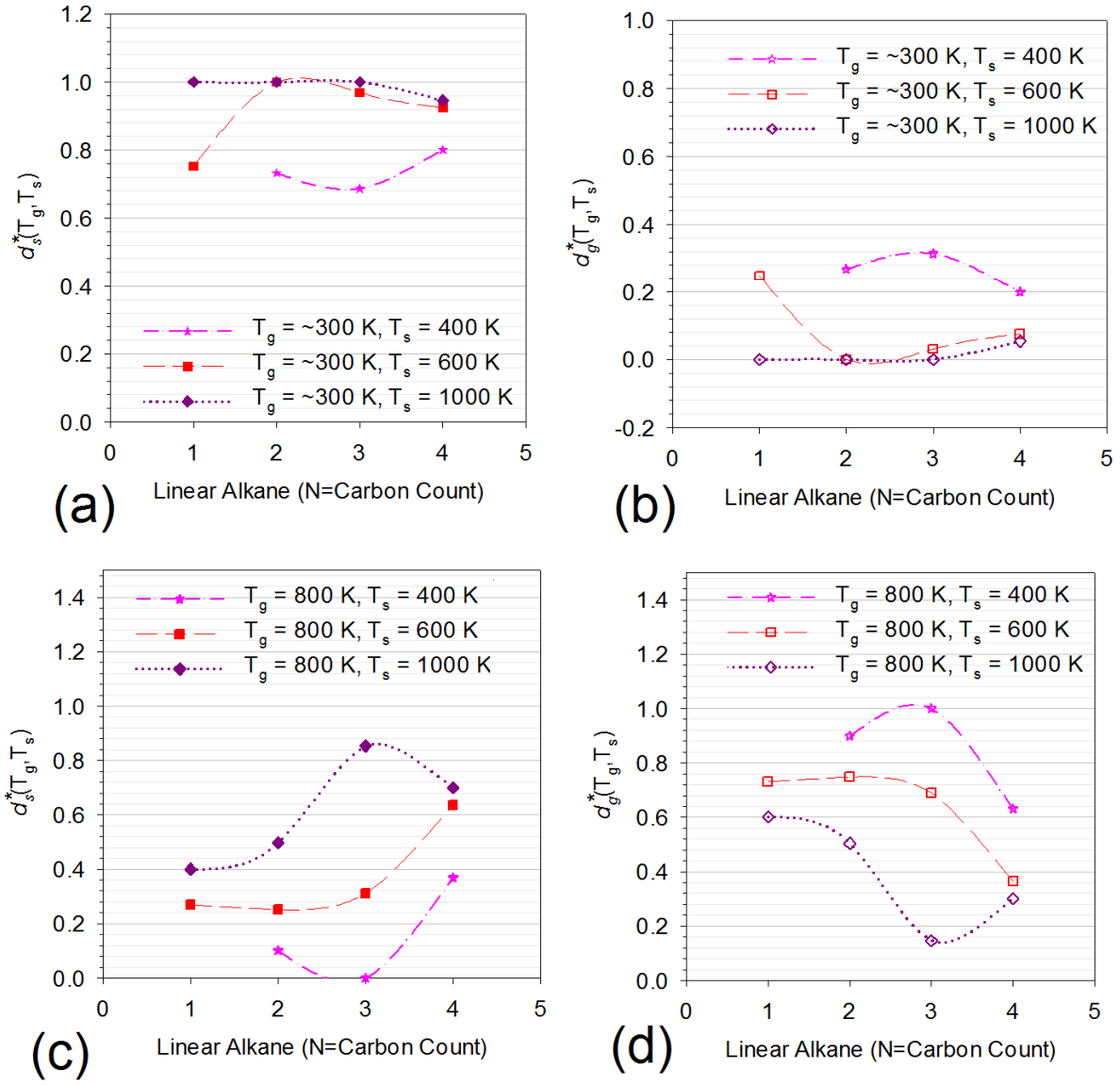

Figure 7.14: Plots of experimentally derived differential energy uptakes for the surface, d_s^*, and gas, d_g^*, as a function of alkane size for alkane dissociative chemisorption on Pt(111) with spline fits to guide the eye: d_s^*(~300 K, T_s) (a), d_g^*(~300 K, T_s) (b), d_s^*(800 K, T_s) (c), and d_g^*(800 K, T_s) (d). The anomalies at d_i(800 K, 1000 K), N = 4 for (c) and (d) are caused by errors in DSC measurements due to high reactivity and short dosing times for butane on Pt(111) when both T_s and T_g are at relatively high values. For any given (T_g, T_s) combination, d_s^* increases with increasing alkane size and d_g^* decreases; this indicates that increasingly efficient gas-surface energy transfer with increasing alkane size is responsible for the apparent thermalization of the gas to the surface temperature.

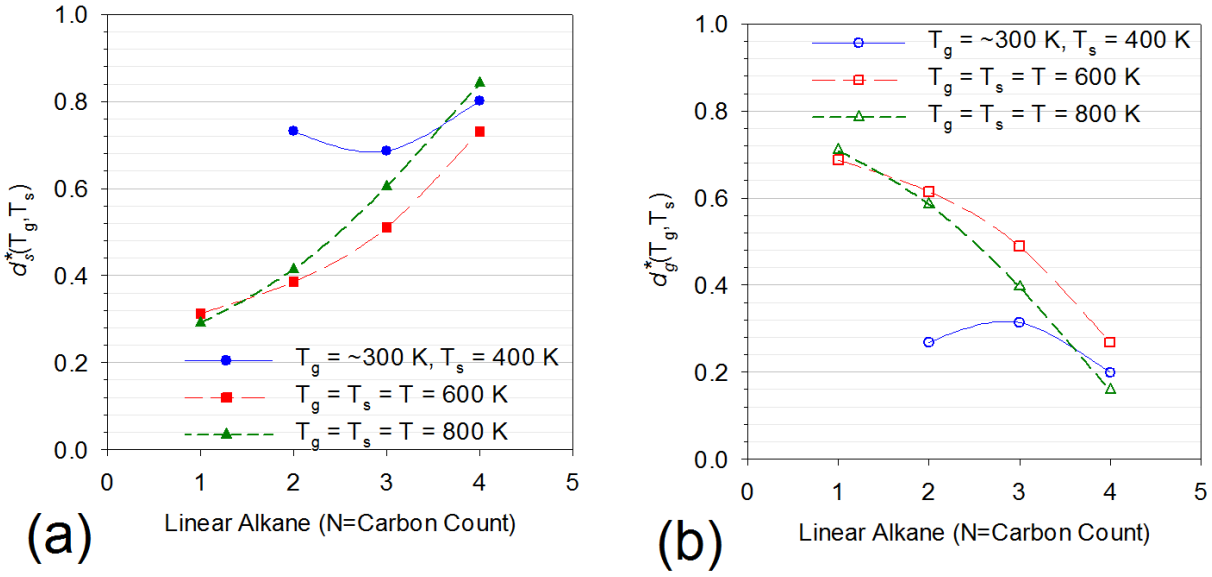

Figure 7.15: Plots of experimentally derived differential energy uptakes for the surface, d_s^*, and gas, d_g^*, as a function of alkane size for dissociative chemisorption on Pt(111) with spline fits to guide the eye: $d_s^*(T_g = T_s)$ (a) and $d_g^*(T_g = T_s)$ (b). Since S(T_g = 300 K, T_s = 300 K) and S(T_g = 400 K, T_s = 400 K) were not measured, comparisons were made for (T_g = 300 K, T_s = 400 K) instead. For any given (T_g, T_s) combination, d_s^* increases with increasing alkane size and d_g^* decreases; this indicates that increasingly efficient gas-surface energy transfer with increasing alkane size is responsible for the apparent thermalization of the gas to the surface temperature.

Overall, Figures 7.12 through 7.15 reveal that as the alkane size is increased from methane to butane, there is a substantial increase in d_s^* and a corresponding decrease in d_g^* for all (T_g, T_s) combinations. Therefore, the collapse of the non-equilibrium DSCs towards the equilibrium DSC values is caused not by the reduction of E_a as alkane size increases, but by the increase in gas-surface energy transfer.

The increasing gas-surface energy transfer with alkane size is caused by two factors: the increasing rovibrational density of states and the increase of the desorption lifetime of the PC at reactive energies. The increasing rovibrational density of states of the alkane molecule should also increase the density of states of the PC which should allow better coupling of surface phonons to the PC vibrational modes and increase IVR rates within the PC. Surface phonons should more efficiently transfer energy to the PC if the PC vibrational modes can be in near resonance with the low frequency phonon modes or their combinations (i.e., multiquanta energy transfer events may occur).[5] As alkane size increases, the number of vibrational modes increases as well as the number of low frequency vibrational modes. For methane, the vibrational modes are stiff and have high vibrational frequencies. Conversely, for a large alkane, such as nonane, there are many low frequency vibrational modes which should theoretically couple more efficiently to the low frequency phonons. The density of rovibrational states increases drastically with the number of vibrations in a molecule, and so the increased density of states should theoretically help with PC-phonon coupling at reactive energies.[28,29] Table 7.2 shows vibrational frequency ranges and the number of modes in each range for a series of gas phase alkanes.[33] The total number of vibrational modes as well as the number of low frequency vibrational modes increases with increasing alkane size.

Alkane	Vibrational Modes ($<500cm^{-1}$)	Vibrational Modes ($500\text{-}1000cm^{-1}$)	Vibrational Modes ($1000\text{-}2000cm^{-1}$)	Vibrational Modes ($2000\text{-}3500cm^{-1}$)	Total
Methane	0	0	5	4	9
Ethane	1	3	8	6	18
Propane	3	4	12	8	27
Butane	5	5	16	10	36
Pentane	7	6	20	12	45
Hexane	9	7	24	14	54

Table 7.2: Vibrational modes for select gas-phase linear alkanes.

The desorption lifetime at reactive energies, τ_D, should be sufficiently long so that multiple surface phonons can strike the PC consecutively thus increasing the overall energy transfer with the PC that tends towards thermalization to the surface temperature. For the small alkanes methane, ethane, and propane, τ_D is relatively short at ~100 fs, ~2 ps, and ~60 ps respectively.[7,8] Since τ_D scales exponentially with alkane size, for larger alkanes such as butane and pentane, τ_D is much longer at ~1.5 ns and ~40 ns respectively. Therefore, increasingly large alkanes interact with the surface for a longer amount of time allowing for more phonon collisions to occur thus allowing more efficient thermalization of the PC to the surface temperature.

7.3 Summary

In conclusion, there is a drastic increase in the efficiency of gas-surface energy transfer as the size of the alkane is increased from methane to nonane on Pt(111). Experimentally, this can be seen as a collapse of non-equilibrium DSC values, $S_n(T_g \neq T_s)$, towards equilibrium DSC values, $S_n(T_g = T_s)$. The PMMT model properly reproduces the experimental DSCs and also indicates that gas-surface energy transfer increases with alkane size. However, the trend of increasingly efficient gas-surface energy transfer is convoluted with the decreasing E_a for alkane dissociative chemisorption on Pt(111). By calculating differential energy uptakes it was clearly determined that the surface supplies more exchangeable energy for dissociation than the gas as the alkane size is increased; this is evidenced by the increasing insignificance of the initial state of the impinging gas molecule. Therefore, the differential energy uptakes enforce that the inclusion of a gas-surface energy transfer parameter in the PMMT model is justified. The increasingly efficient gas-surface energy transfer has several causes. As the alkane size is increased, the number of vibrational modes, the population of low frequency vibrational modes, and also the overall density of states increase as well. These new modes allow greater coupling to low frequency surface phonons and their combination modes. In addition, as the alkane size is increased, there is an exponential rise in the desorption lifetime at reactive energies that allows for more phonon collisions to occur allowing the PC to thermalize towards the surface temperature.

References

(1) Hellberg, L.; Stromquist, J.; Kasemo, B.; Lundqvist, B. I. Electron-Transfer Pathways in Dynamic Processes: Cl_2 on K. *Phys. Rev. Lett.* **1995**, *74*, 4742.

(2) Rahinov, I.; Cooper, R.; Matsiev, D.; Bartels, C.; Auerbach, D. J.; Wodtke, A. M. Quantifying the Breakdown of the Born-Oppenheimer Approximation in Surface Chemistry. *PCCP* **2011**, *13*, 12680.

(3) Weaver, J. F.; Carlsson, A. F.; Madix, R. J. The Adsorption and Reaction of Low Molecular Weight Alkanes on Metallic Single Crystal Surfaces. *Surf. Sci. Rep.* **2003**, *50*, 107.

(4) Bukoski, A.; Abbott, H. L.; Harrison, I. Microcanonical Unimolecular Rate Theory at Surfaces. III. Thermal Dissociative Chemisorption of Methane on Pt(111) and Detailed Balance. *J. Chem. Phys.* **2005**, *123*, 094707.

(5) Bukoski, A.; Blumling, D.; Harrison, I. Microcanonical Unimolecular Rate Theory at Surfaces. I. Dissociative Chemisorption of Methane on Pt(111). *J. Chem. Phys.* **2003**, *118*, 843.

(6) Donald, S. B.; Navin, J. K.; Harrison, I. Methane Dissociative Chemisorption and Detailed Balance on Pt(111): Dynamical Constraints and the Modest Influence of Tunneling. *J. Chem. Phys.* **2013**, *139*.

(7) Cushing, G. W.; Navin, J. K.; Donald, S. B.; Valadez, L.; Johanek, V.; Harrison, I. C-H Bond Activation of Light Alkanes on Pt(111): Dissociative Sticking Coefficients, Evans-Polanyi Relation, and Gas-Surface Energy Transfer. *J. Phys. Chem. C* **2010**, *114*, 17222.

(8) Cushing, G. W.; Navin, J. K.; Donald, S. B.; Valadez, L.; Johánek, V.; Harrison, I. Addition/Correction to: C-H Bond Activation of Light Alkanes on Pt(111): Dissociative Sticking Coefficients, Evans-Polanyi Relation, and Gas-Surface Energy Transfer (vol 114, pg 17222, 2010). *J. Phys. Chem. C* **2010**, *114*, 22790.

(9) Cushing, G. W. "Hydrocarbon Reactivity on Pt(111): Dissociative Sticking Coefficients and Evans-Polanyi Relation", Ph.D. Thesis, University of Virginia, Charlottesville, VA, (2011).

(10) Cushing, G. W.; Navin, J. K.; Valadez, L.; Johanek, V.; Harrison, I. An Effusive Molecular Beam Technique for Studies of Polyatomic Gas-Surface Reactivity and Energy Transfer. *Rev. Sci. Instrum.* **2011**, *82*, 11.

(11) Donald, S. B.; Harrison, I. Dynamically Biased RRKM Model of Activated Gas-Surface Reactivity: Vibrational Efficacy and Rotation as a Spectator in the Dissociative Chemisorption of CH_4 on Pt(111). *PCCP* **2012**, *14*, 1784.

(12) Navin, J. K.; Donald, S. B.; Harrison, I. Angle-Resolved Thermal Dissociative Sticking of Light Alkanes on Pt(111): Transitioning from Dynamical to Statistical Behavior. *J. Phys. Chem. C* **2014**, *Currently under review*.

(13) Navin, J. K.; Donald, S. B.; Tinney, D. G.; Cushing, G. W.; Harrison, I. Communication: Angle-Resolved Thermal Dissociative Sticking of CH_4 on Pt(111): Further Indication that Rotation is a Spectator to the Gas-Surface Reaction Dynamics. *J. Chem. Phys.* **2012**, *136*, 4.

(14) Beck, R. D.; Maroni, P.; Papageorgopoulos, D. C.; Dang, T. T.; Schmid, M. P.; Rizzo, T. R. Vibrational Mode-Specific Reaction of Methane on a Nickel Surface. *Science* **2003**, *302*, 98.

(15) Bisson, R.; Sacchi, M.; Dang, T. T.; Yoder, B.; Maroni, P.; Beck, R. D. State-Resolved Reactivity of $CH_4(2\nu_3)$ on Pt(111) and Ni(111): Effects of Barrier Height and Transition State Location. *J. Phys. Chem. A* **2007**, *111*, 12679.

(16) Brass, S. G.; Reed, D. A.; Ehrlich, G. Vibrational Excitation and Surface Reactivity: An Examination of n_3 and $2n_3$ Modes of CH_4. *J. Chem. Phys.* **1979**, *70*, 5244.

(17) Higgins, J.; Conjusteau, A.; Scoles, G.; Bernasek, S. L. State Selective Vibrational ($2n_3$) Activation of the Chemisorption of Methane on Pt (111). *J. Chem. Phys.* **2001**, *114*, 5277.

(18) Juurlink, L. B. F.; Killelea, D. R.; Utz, A. L. State-Resolved Probes of Methane Dissociation Dynamics. *Prog. Surf. Sci.* **2009**, *84*, 69.

(19) Juurlink, L. B. F.; McCabe, P. R.; Smith, R. R.; DiCologero, C. L.; Utz, A. L. Eigenstate-Resolved Studies of Gas-Surface Reactivity: CH_4 (n_3)Dissociation on Ni(100). *Phys. Rev. Lett.* **1999**, *83*, 868.

(20) Juurlink, L. B. F.; Smith, R. R.; Killelea, D. R.; Utz, A. L. Comparative Study of C-H Stretch and Bend Vibrations in Methane Activation on Ni(100) and Ni(111). *Phys. Rev. Lett.* **2005**, *94*, 4.

(21) Lee, M. B.; Yang, Q. Y.; Ceyer, S. T. Dynamics of the Activated Dissociative Chemisorption of CH_4 and Implication for the Pressure Gap in Catalysis: A Molecular Beam-High Resolution Electron Energy Loss Study. *J. Chem. Phys.* **1987**, *87*, 2724.

(22) Maroni, P.; Papageorgopoulos, D. C.; Sacchi, M.; Dang, T. T.; Beck, R. D.; Rizzo, T. R. State-Resolved Gas-Surface Reactivity of Methane in the Symmetric C-H Stretch Vibration on Ni(100). *Phys. Rev. Lett.* **2005**, *94*, 4.

(23) Smith, R. R.; Killelea, D. R.; DelSesto, D. F.; Utz, A. L. Preference for Vibrational over Translational Energy in a Gas-Surface Reaction. *Science* **2004**, *304*, 992.

(24) Utz, A. L. Mode Selective Chemistry at Surfaces. *Curr. Opin. Solid State Mater. Sci.* **2009**, *13*, 4.

(25) Walker, A. V.; King, D. A. Dynamics of the Dissociative Adsorption of Methane on Pt{110} (1x2). *Phys. Rev. Lett.* **1999**, *82*, 5156.

(26) Yates, J. T.; Zinck, J. J.; Sheard, S.; Weinberg, W. H. Search for Vibrational Activation in the Chemisorption of Methane. *J. Chem. Phys.* **1979**, *70*, 2266.

(27) Stewart, G. M.; McDonald, J. D. Intramolecular Vibrational Relaxation from C–H Stretch Fundamentals. *J. Chem. Phys.* **1983**, *78*, 3907.

(28) Boyall, D.; Reid, K. L. Modern Studies of Intramolecular Vibrational Energy Redistribution. *Chem. Soc. Rev.* **1997**, *26*, 223.

(29) Uzer, T.; Miller, W. H. Theories of Intramolecular Vibrational-Energy Transfer. *Phys. Rep.* **1991**, *199*, 73.

(30) Frey, F.; Hepp, H. Thermal Decomposition of Simple Paraffins. *Ind. Eng. Chem.* **1933**, *25*, 441.

(31) Andersen, W. C.; Bruno, T. J. Rapid Screening of Fluids for Chemical Stability in Organic Rankine Cycle Applications. *Ind. Eng. Chem. Res.* **2005**, *44*, 5560.

(32) Abbott, H. L.; Harrison, I. Dissociative Chemisorption and Energy Transfer for Methane on Ir(111). *J. Phys. Chem. B* **2005**, *109*, 10371.

(33) Shimanouchi, T.; Matsuura, H.; Ogawa, Y.; Harada, I. Tables of Molecular Vibrational Frequencies. *J. Phys. Chem. Ref. Data* **1978**, *7*, 1323.

Appendix Section A - Introduction

As discussed in Section 1, many industrial reactions involve gases reacting on supported metal nanocatalysts at high pressures and temperatures. Many of these reactions are studied by varying the pressure, temperature, and initial concentrations of reactants. However, in order to truly understand the mechanisms and kinetics of the overall reaction, experiments must be conducted that directly probe the individual steps at the gas-surface interface. In order to qualitatively, as well as quantitatively, study the chemistry at the gas-surface interface, two prerequisites are required: the gas-surface interface must be free of unwanted species and the surface properties must be constant from reaction to reaction.

When gas strikes a surface, there is a probability that the impinging molecule with adsorb to the surface. Over time, the entire surface will be covered in a single layer of molecules, known as a "monolayer." At this point, the surface is quite different from the original "clean" surface that had no adsorbates present. However, the rate at which the surface becomes covered in molecules is dependent on the pressure of the impinging gas. Assuming that each molecule striking the surface adsorbs to the surface (unitary sticking), the surface will be covered in a monolayer in one second at a gas pressure of 10^{-6} Torr. A useful unit of exposure is the Langmuir, defined as 10^{-6} Torr of pressure impinging on a surface for one second; this exposure will cover the surface in one monolayer of molecules. For example, if a surface is subjected to a gas pressure of 10^{-5} Torr, and assuming unitary sticking, the surface will be covered in one monolayer in 0.1 seconds and after one second, will be subjected to 10 Langmuirs of exposure. At a pressure of 10^{-9} Torr, the surface is fully covered in a monolayer after 1,000 seconds assuming unitary sticking. Generally, however, the probability that a gas will adsorb to the surface is not unity and at elevated temperatures, the majority of gases have no probability of

adsorption (e.g. CO has a unitary sticking probability at surface temperatures less than 300 K but has a sticking probability of ~0 at surface temperatures above 500 K). Nonetheless, gas-surface reactivity is studied in ultra-high vacuum (UHV) conditions ($< 10^{-9}$ Torr) in order to limit the adsorption of undesirable gas species.

In addition to having UHV conditions, it is important to ensure that the surface is free of impurities and its properties are reproducible over the course of experimentation in order to study gas-surface chemistry. Species that react on the surface decompose leaving molecular fragments or lone atoms (adatoms). In addition, surface reactions can affect the surface morphology, which leads to defects in the surface. In order to ensure that the surface is clean of contaminants and defects, chemical and physical cleaning of the surface is paramount to ensuring reproducible results. Chemical cleaning involves the removal of surface species through reaction (e.g. $C + O_2 \rightarrow CO_2$). Physical cleaning involves processes that remove impurities through physical means or reordering of the surface structure (e.g. removing impurities through atomic bombardment or heating the crystal to a high temperature).

Overall, in order to properly study gas-surface reactivity, experiments must be conducted under UHV conditions, the surface being studied must be clean, and the surface structure must be reproducible from reaction to reaction. However, a reasonable amount of technical knowledge is required to maintain a UHV chamber, prepare UHV components, and operate instrumentation. To those ends, the purpose of these appendices is to help the reader in operation of the UHV chamber and to explain some commonplace techniques in vacuum science.

Appendix Section B - UHV Chamber Preparation

B.1 Introduction

The main structure of a UHV chamber is generally a large stainless steel container that is outfitted with various ports connected to the main structure via large diameter stainless steel tubes as shown in Figure B.1. Various analytical instrumentation and vacuum pumps are then attached to the chamber at these ports. A gasket is first placed between an individual UHV component and the chamber port and then the chamber and component are bolted together. This combination of airtight gaskets and vacuum pumps maintain UHV conditions within the chamber. Additionally, most UHV chambers are outfitted with a gas manifold that stores gases used in research. Because UHV chambers are maintained at such low pressures ($< 10^{-9}$ Torr), it is paramount to reduce the contamination of vacuum components and to avoid the use of materials which have a high vapor pressure.

B.2 Lab Preparation

B.2.1 Introduction

All materials exhibit a partial pressure that increases with increasing temperature. Certain materials, especially bodily fluids, have vapor pressures which are higher than 10^{-8} Torr and so should not come in contact with any component or surface that will be present in the UHV chamber. In addition, if organic material, such as oils present on the skin, come in contact with a filament, the filament may break when heated. Therefore, it is important to practice techniques that minimize or remove the possibility of contamination.

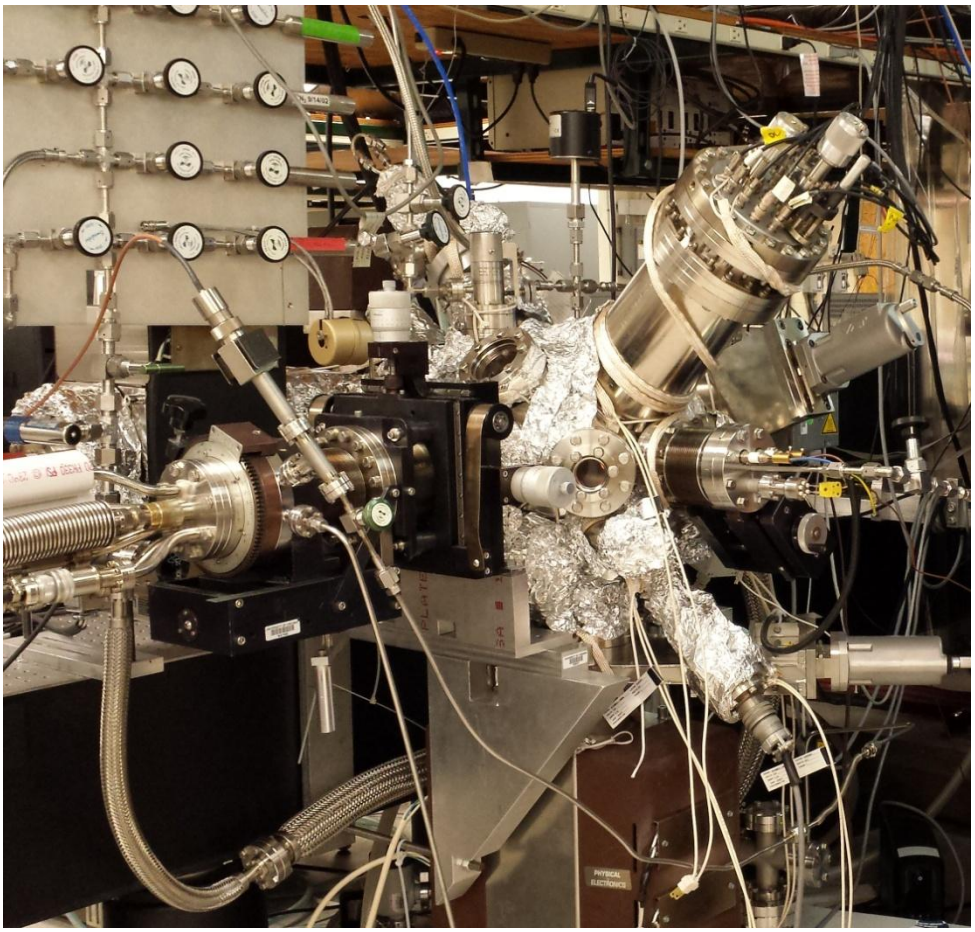

Figure B.1: Image of a UHV chamber of the Harrison research group at the University of Virginia.

B.2.2 Maintaining Clean Conditions

The most important means to limit contamination of UHV components is to wear gloves (latex or nitrile) in order to limit skin contact. In addition, do not cough, sneeze, or blow air onto any UHV component or surface. All work performed on UHV components outside of the chamber should be conducted in a clean hood that has a constant flow of air filtered by a HEPA filter. No tool or material should touch a UHV component unless it is cleaned for use in UHV and is UHV compatible (e.g. not plastic or wood) or is first covered in fresh aluminum foil. In addition, all surfaces that will come into contact with UHV components (e.g. tables and carts) should be covered in fresh aluminum foil. Lastly, UHV components that are to be stored, should be covered in fresh aluminum foil. Aluminum foil is an ideal candidate because it does not undergo rapid oxidation, does not easily form alloys, is malleable, and is inexpensive.

All tools used in UHV work should be wiped clean using acetone and delicate task wipes and then sonicated for ~30 minutes in each of the three following fresh solvents: acetone, methanol, and acetone. After sonication, the tools should be allowed to air dry. If the tools contain plastic parts, then only the metal portion should be sonicated. Tools that have already been cleaned, but have not been used recently, should be sprayed down with acetone and allowed to dry. As an important note, do not allow metals that are easily alloyed to come in to contact with each other, (e.g. zinc and copper).

The particular cleaning procedures for UHV parts vary depending on the materials present in the component as well as the actual type of component. In addition, if the UHV component was never contaminated, no cleaning should be required and any dust should be removed by flowing dry N_2 over the component. As a side note, do not sonicate UHV parts that contain sensitive components; also, do not sonicate UHV compatible materials with non-UHV

compatible materials or with contaminated UHV materials. Never sonicate or use solvents to clean components that contain any type of fluoropolymer (e.g. PTFE ("Teflon")), nor edge-welded bellows. Solvents dissolved in fluoropolymers and solvents trapped in edge-welds can never be fully removed, which results in poor minimum pressure in the UHV chamber. Lastly, do not scratch any sealing surface, such as knife-edges in ConFlat flanges or rounded edges in VCR fittings, and do not attempt to wipe down or clean UHV windows as scratches can damage the window.

For simple metal UHV parts like flanges, tubing, and fittings, the cleaning procedure is fairly straight forward. The parts are to be wiped down with delicate task wipes and acetone, taking care not to damage any sealing surfaces. Afterwards, remove any lost fibers using clean stainless steel tweezers. The component can then be sonicated for ~30 minutes in each of the three following fresh solvents: acetone, methanol, and acetone. The components are then allowed to dry in air. Stock metals such as, stainless steel, aluminum, and refractory metals (e.g. tantalum, chromium, tungsten, etc.) can also be clean using the same methodology. If the materials are already cleaned but lie unused, dust should be removed using flowing dry N_2.

For materials which are UHV compatible, but have high surface area and are porous (alumina and silica), the cleaning method is somewhat more challenging. For alumina, first sonicate the pieces for ~30 minutes in each of the three following fresh solvents: acetone, methanol, and acetone. After sonicating, rinse the pieces with distilled water. Next, place the pieces in a steaming solution composed of one part concentrated nitric acid (HNO_3) and 2 parts distilled water for 1 hour. Remove the piece and rinse it thoroughly with deionized water. Next, create a solution of 5% H_2O_2 using 30% H_2O_2 stock solution. Add enough ammonium hydroxide (NH_4OH) to the 5% H_2O_2 solution to attain a pH of 11. Add additional distilled

water to bring the final H_2O_2 concentration to 1.5% and additional NH_4OH if necessary. Bring the solution of NH_4OH and H_2O_2 to a boil and immerse the alumina pieces in the solution for 1 hour. Afterwards, rinse the pieces thoroughly with deionized water. After the acid and base treatments, sonicate the alumina pieces for ~30 minutes in each of the following three fresh solvents: acetone, methanol, and acetone. Lastly, place the alumina pieces in a clean, dry beaker covered with a clean, dry watch glass. Heat the alumina in the covered beaker for at least 8 hours at ~80^{o}C using a hot plate. The alumina is now ready for use in a UHV chamber.

For complex UHV parts, no sonication or solvents should be used for cleaning as sensitive components are easily damaged by sonication; additionally alumina and silica components can easily absorb solvents. No cleaning should be needed for complex UHV parts, but if cleaning is required, first remove any components that are composed of one type of material, and then clean the individual components using the methods described in the previous paragraphs. After the individual components are cleaned, the part can be reassembled. As a side note, when a UHV component is removed from the chamber, cover the open port with aluminum foil.

B.3 UHV Materials

When constructing custom UHV components it is important to remember that many materials are incompatible with a UHV environment. Materials that have a relatively high partial pressure not only raise the minimum attainable chamber pressure, but also can be deposited on other surfaces within the chamber. Two requirements are needed in order for a material to be UHV compatible: extremely low vapor pressure ($< 10^{-16}$ Torr) and resistance to thermal degradation. As a side note, the vapor pressure of a material can increase substantially

with only a moderate increase in temperature; in addition, materials that resist degradation at low temperatures can rapidly degrade at elevated temperatures. Therefore, some materials are only UHV compatible at low temperatures. Also, note that some parts, in particular components such as screws, washers, and electrical components, are coated in metals which are not UHV compatible.

Stainless steel (Types 316 and 304), tantalum, tungsten, copper, gold, silver, titanium, alumina, and silica are common examples of UHV compatible materials. Sulfur, lead, zinc, cadmium, and phosphorus are some examples of non-UHV compatible materials that should never be used in a UHV system. Although many of the non-UHV compatible materials are not used to build components, they are present in many alloys and can be used as plating (e.g. cadmium). Lastly, there are materials which are UHV compatible at low temperature but degrade quickly at higher temperatures; two examples are PTFE and Macor.

B.4 Installing UHV Components and Connections

B.4.1 Common Connection Types

When connecting components directly to the UHV chamber or when connecting two vacuum components, there are several different types of connections which are nearly omnipresent on all vacuum systems. In order from the lowest leak rate, the series of connections are: ConFlat, KF, VCR, compression tube fittings, CGA, and NPT.

Conflat flanges are the most common flange type that is directly connected to the UHV chamber. Figure B.2 shows an example of a ConFlat flange. The mating side of the flange is recessed in order to hold a gasket composed of oxygen-free high conductivity (OFHC) copper; there is also a knife-edge within the recess used to "bite" into the gasket for sealing. In addition,

a series of holes are drilled in the outer portion of the flange to accept bolts. Two ConFlat flanges are connected together by first seating a metal gasket in the recess of one flange and aligning the second flange on top of the gasket. The two flanges are then bolted together, and the knife-edges of both flanges dig into the gasket making an airtight seal. Because of the destructive nature of the sealing design, ConFlat gaskets cannot be reused.

Another common connection type is the Klein Flansche (KF) flange. Figure B.3 (a) shows an image of a KF port. The mating edge of a KF flange is flat and is designed to mesh with a Viton o-ring. Two KF flanges are connected via a Viton o-ring that is positioned on a steel centering ring. The o-ring and centering ring are placed into a groove on the first KF flange and the second KF flange is placed on top. The two flanges are then held in place by a clamp as shown in Figure B.3 (b). Generally, KF flanges are not directly connected to the UHV chamber, but are instead used for roughing pumps. Viton gaskets can be reused until the gasket begins to degrade.

The VCR connection is used on both the UHV chamber as well as for normal vacuum line connections. Like the ConFlat flange design, VCR connections use a metal gasket to seal the surfaces together. Figure B.4 shows a male VCR connection. In order to connect two VCR connections together, an OFHC copper, nickel, or 316 stainless steel gasket is first placed between the two rounded VCR sealing faces and then the female threaded cap is tightened over the male threaded cap. The two VCR pieces are then tightened, which pulls the two faces together thus crushing the metal gasket and sealing the connection. Much like the ConFlat flange, the gaskets used in VCR fittings cannot be reused. In addition, some VCR fittings are non-rotatable and so, after ~10 uses, the copper begins to grind into the VCR sealing face and the VCR fitting must be replaced.

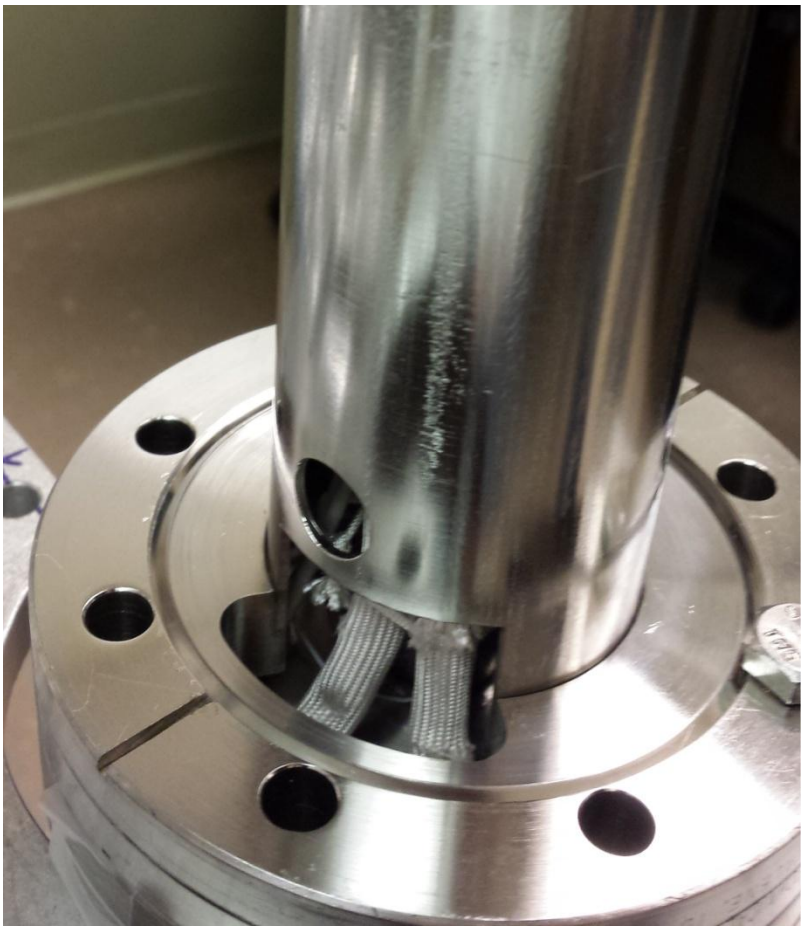

Figure B.2: Close-up image of a ConFlat flange showing bolt holes and a recessed knife-edge.

(a)

(b)

Figure B.3: Close-up image of a KF port (a) and KF clamps (b). The KF clamps are used to tighten two KF flanges together.

Figure B.4: Close-up view of a male VCR fitting that shows the VCR sealing face and threaded male cap.

Compression tube fittings are almost exclusively used for rough pumping and are generally not directly connected to UHV components. Figure B.5 (a) shows the components for a compression tube fitting. In a compression tube fitting, a nut, a disk shaped back ferrule, and a cone-shaped front ferrule are all placed onto a piece of tubing. The tubing and both ferrules are placed into a fitting body and the nut is screwed down in order to mate the two pieces together. The seal is made through a concerted effort by all of the pieces involved. The nut applies force to the back of the back ferrule which in turn, applies pressure to the front ferrule. The inner portion of the front ferrule is thus forced into the tubing and into the body of the fitting which makes a seal on the top and bottom of the front ferrule (Figure B.5 (b)). Because the front and rear ferrules flex each time the compression tube fitting is tightened, compression tube fittings should only be reused 10 to 15 times.

The Compressed Gas Association (CGA) fittings as well as the National Pipe Thread (NPT) fittings are very similar in design except that most CGA fittings use a PTFE gasket. CGA fittings are used to connect gas cylinders to regulators and NPT fittings are the standard fittings for gas and water lines.

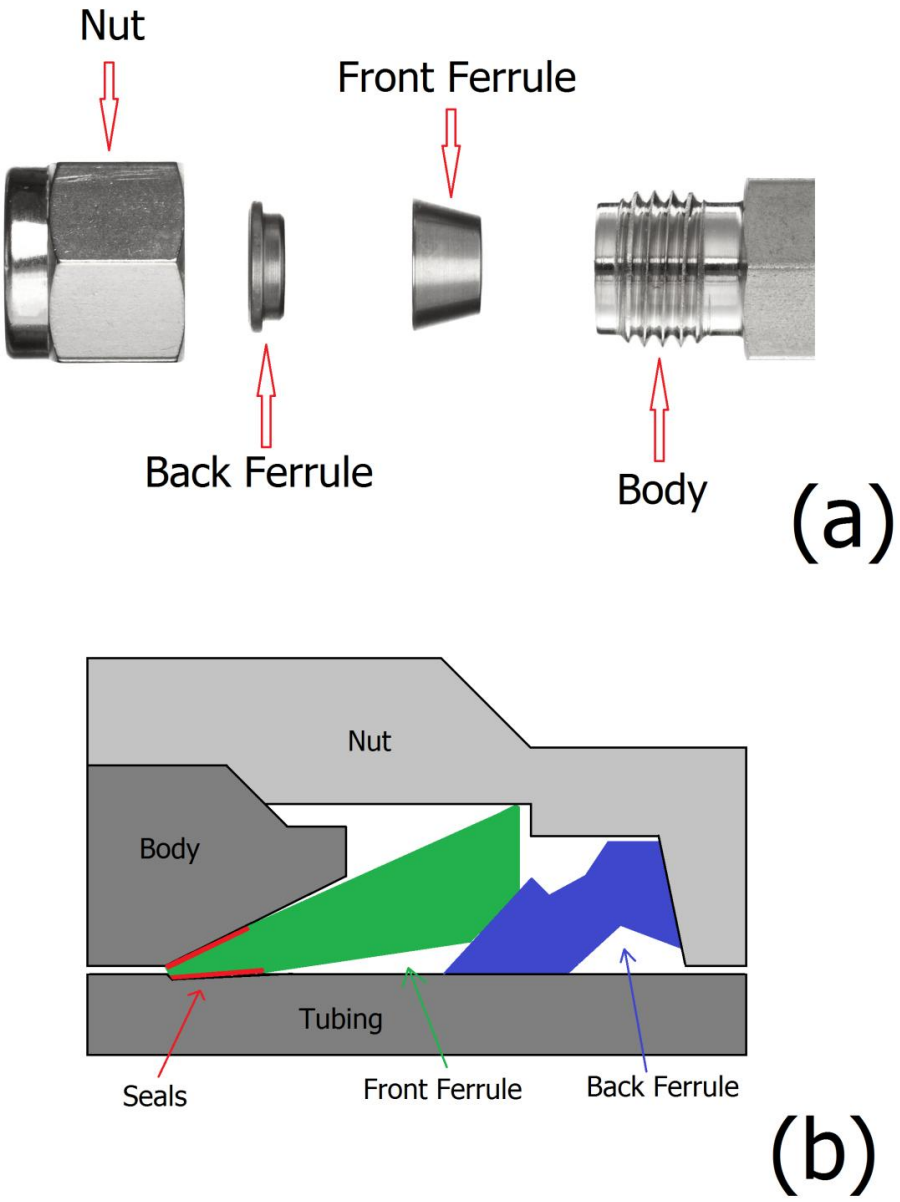

Figure B.5: The components of a compression tube fitting (a) and the schematic of making a seal using a compression tube fitting (b). The nut, back ferrule, and front ferrule are slipped onto a tube and the tube and components are placed into a fitting. When the nut is tightened, the back ferrule is crushed into the front ferrule; this pushes the front ferrule into the tube and body thus, making the seal.

B.4.2 Procedure

Although it should go without saying, UHV components cannot be connected to the chamber if the chamber is currently being operated. Before connecting any components to the UHV chamber, ensure that all connections are cleaned and cleared of debris. For ConFlat flanges and VCR fittings, ensure that the sealing surfaces are not damaged in any way. For KF flanges and compression fittings, ensure that all sealing surfaces are smooth and have no defects. Lastly, for CGA and NPT fittings, make sure to remove all residue PTFE tape from the threads. Systems that use metal gaskets (e.g. ConFlat and VCR) should use gaskets that are new from the package or having been thoroughly cleaned and sonicated (Appendix Section B.2.2). The Viton gaskets used for KF flanges need only be replaced if the gasket is significantly degraded. For CGA fittings, the gaskets should be newly purchased when used.

Generally, UHV components that are directly connected to the chamber are connected via ConFlat flanges. Before attempting to connect a ConFlat flange, first be sure that the bolts and nuts (or backing plates) are nearby. Set the OFHC copper gasket into the recess of the ConFlat port. If the gasket can easily fall off of the port, then the gasket can be taped in place; however, do not allow the tape to go past the knife-edge of the flange, otherwise, the tape will be in the UHV chamber. After the gasket is situated, insert the UHV component into the chamber ensuring that no debris falls into the chamber, that the component does not hit the sides of the chamber or the knife-edge, and also that the orientation is correct. Once fully inserted, ensure that the gasket is situated properly by gently rocking or rotating the flange while holding the flange against the chamber. Once the gasket is situated, apply pressure to the flange to hold it in place and insert four bolts positioned 90 degrees from each other on the flange; tighten the nuts until they are hand-tight; pressure can now be released. Check the spacing between the two

flanges; the gap should be uniform around the entire flange. Now, all of the bolts can be put in place and tightened until they are hand-tight. As a side note, not all of the bolts will have the same torque because gravity is pulling down on the component.

Before fully tightening the flange, be sure to check the resistance on any electrical feedthroughs to be sure that none of the electrical components were damaged. Two different methods can be used to fully tighten the flange: the star pattern and the sequential pattern. Figure B.6 (a) shows the star pattern for tightening flanges. For this method, first begin by gently tightening one bolt. Then tighten the bolt that is directly on the other side of the flange. After this second bolt is tightened, tighten the bolt that is situated next to it (clockwise). After the third bolt is tightened, tighten the bolt directly on the other side of the flange, and so forth. Basically, bolts are tightened on alternating sides of the flange in a clockwise pattern and for each cycle around the flange, the bolts should all be tightened to a similar pressure. As a side note, do not increase the pressure too drastically between cycles; otherwise, the flange will be tightened asymmetrically and the flange may leak. In addition, our group has determined that each bolt should be tightened to ~180 in*lbs of torque in order to limit leaks for 2 3/4 inch diameter flanges and larger. The sequential pattern for tightening flanges is fairly straight forward and is shown in Figure B.6 (b). First, gently tighten one bolt. Then, tighten the next adjacent bolt (clockwise) to roughly the same tightness and so on. This process is repeated until the proper torque is achieved. The sequential pattern is much easier for very large flanges; however, much less force can be applied per cycle because this tightening method is asymmetrical.

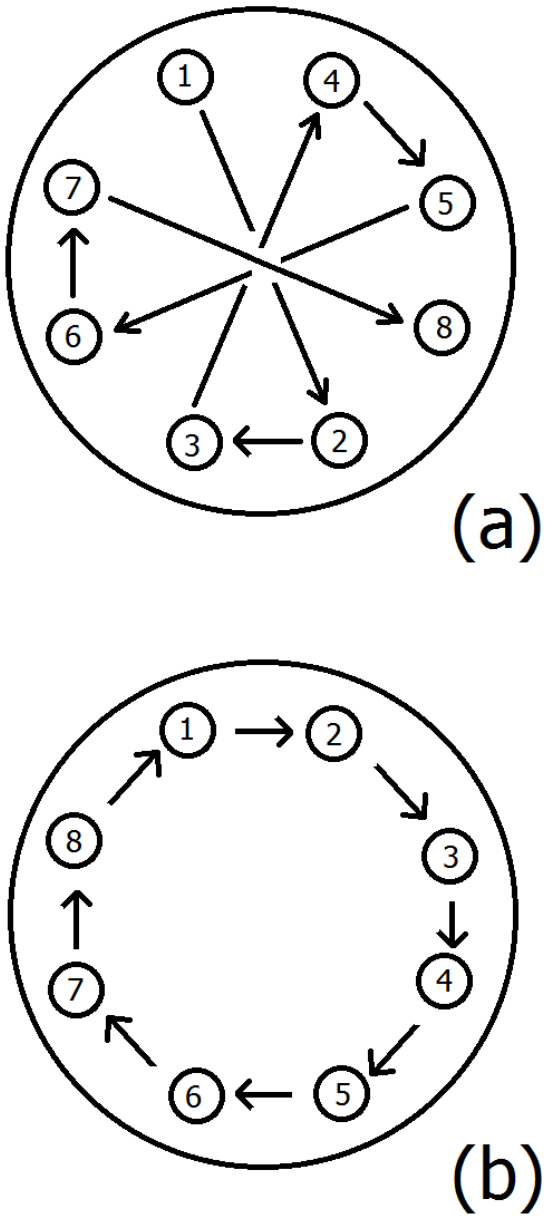

Figure B.6: Two methods for tightening bolts on a ConFlat flange: the star pattern (a) and the sequential pattern (b). The small circles are bolts and the numbers indicate the order.

KF flanges are never connected to a UHV system except as connections to roughing pumps. Therefore, cleanliness is less of an issue since almost all roughing pumps contain oil. In order to connect KF flanges, first place the centering ring and gasket onto the port and ensure that it fits properly. Next, place the component onto the KF fitting and make sure that the centering ring meshes properly with both flanges. Lastly, take the clamp and place it onto both KF flanges and tighten the butterfly nut until it is hand-tight.

VCR fittings have the ability to hold vacuum to almost the same levels that ConFlat flanges are able to hold vacuum. Generally, VCR fittings are used for both gas manifolds as well as for UHV components connected directly to the chamber. In order to connect two VCR fittings together, first pull back the nut on the female fitting to reveal the inner gland. Then place a gasket between the female and male glands and hold the two together. While applying pressure on the gasket, tighten the nut onto the male threads until it is hand-tight. The gasket should appear perpendicular to the tubing through the side hole. If this is not so, the gasket might not be flush with the glands, and the procedure should be repeated. For an OFHC copper gasket, tighten the nut 90 degrees from the original hand-tight position; if the gasket is stainless steel or nickel, tighten the nut 45 degrees.

Compression fittings are found almost solely on gas manifolds, although there are exceptions. If a compression fitting is already made, simply tighten the fitting to the port until the connection is relatively tight. However, making a compression connection is slightly more difficult. First, take the tubing and place the components on the tube in the following order: nut, back ferrule, and then front ferrule. Insert the tube all of the way to the base of the port and gently push the front and back ferrules into the port. Begin tightening the nut, and stop tightening the nut once there is slight resistance when pulling on the tube. At this point, push the

tubing to the base of the port and then pull it out 2 mm. This is to ensure that the tubing does not hit the base of the port while tightening and to prevent the ferrules from slipping off of the end of the tube. At this point, fully tighten the compression fitting.

CGA and NPT connections are used to connect gas tanks to regulators and gas/water lines respectively. In order to connect these fittings, first, ensure that no debris is on the connections. Next, wrap PTFE tape around the male threads ~1.5 full rotations. As a side note, the first thread should be free of PTFE tape and the tape should be wrapped such that tightening the connection does not unravel the tape. For an NPT fitting, simply insert the wrapped male connector into the female connector and tighten. For a CGA fitting, first put the PTFE gasket between the male and female connectors and then tighten the two together. CGA gaskets deform upon use and cannot be reused.

Concerning all fittings and flanges on the chamber, do not overly tighten the connections. Overly tightening the connections can potentially damage components as well as cause leaks. If an operator believes that a flange or connection might be too tight, then leave the connection alone. After the chamber is restarted, the operator can then leak check the connection and determine if the connection needs to be tightened more.

B.5. Starting the Vacuum System

The exhaust port on the main chamber turbo molecular pump (TMP) is connected to a mechanical pump by means of a KF hose and a valve; behind that valve, the mechanical pump has a secondary valve that is connected to the outer differentially pumped region of the rotary flange. Also, the main TMP and the mechanical pump are connected via an interlock which allows the simultaneous starting of both the main TMP and the mechanical pump. When the

main TMP is started, the mechanical pump starts as well; when the main TMP is turned off, the mechanical pump turns off too. In addition to the interlock and mechanical pump, the main TMP is also connected to a vent valve which is connected to dry N_2 for venting. When a TMP is turned off, it slowly spins down and when the rotational speed reaches a certain value, the vent valve opens, allowing air to rush into the chamber (venting). When a chamber is vented, the chamber pressure is increased to atmospheric pressures in a controlled manner. It's essential to always keep in mind that if a TMP rotates below half speed under molecular flow conditions (e.g., ~1 Torr or lower) then backstreaming of oil from the mechanical pump into the main UHV chamber could occur. To avoid this catastrophe, the system must always be able to vent the chamber with dry N_2 to atmospheric pressure or better through the TMP vent valve and to simultaneously turn off all vacuum pumps and chamber electronics (which may control ion gauge and electron gun filaments, etc.). The short molecular diffusion length at the high vented pressure prevents any oil backstreaming possibilities. Lastly, the main TMP is controlled via a display control unit (DCU) on the control tower.

The manifold pumping station consists of a turbo molecular pump and mechanical pump combined into one individual unit; therefore, the two are interlocked. The manifold pumping station is connected to the manifold by a series of ConFlat and VCR tubes and two valves. In addition, the manifold pumping station is also connected to the inner differentially pumped region of the manipulator by a stainless steel tube and valve. Like the main TMP, the manifold pumping station TMP is connected to dry N_2 to allow for venting. As a side note, the dry N_2 lines for the main TMP and the manifold pumping station TMP share a common connection that is separated from the main N_2 tank by a green valve which controls N_2 flow to the TMPs.

Before starting the main chamber and manifold pumping station, ensure that there are no connections to the chamber or manifold that are open to atmosphere and also that the dry N_2 vent lines are connected to the main chamber TMP as well as the manifold pumping station TMP; do not pressurize the lines yet. Make sure that the interlock is connected between the main TMP and the mechanical pump that pumps on the main TMP. Additionally, the two valves on the mechanical pump that connect to the main TMP and the outer differentially pumped region should be closed. The valves between the pumping station and the inner differentially pumped region and the manifold should already be closed; if the manifold is already vented, then leave the two valves on the base of the manifold open.

To start the chamber, first turn on the TMP by means of the DCU on the control tower; the mechanical pump should start simultaneously. Once the TMP and mechanical pump are running, fully open the valve that separates the mechanical pump from the TMP exhaust port and also open the red valve that separates the mechanical pump from the outer differential pumping region on the manipulator. At this point, the mechanical pump should be running and the TMP rotational speed should be increasing. Next, start the manifold pumping station from the front panel (TMP and mechanical pump start simultaneously). After confirming that the manifold pumping station, the main chamber TMP, and the mechanical pump are operating, open the valve between the main dry N_2 tank and the vent lines (~5 psi) to ensure that N_2 can flow to the vent valves in the event of emergency venting.

After the main TMP achieves a rotational speed of 1000 Hz, the ion gauge can be turned on. In order to turn on the ion gauge, ensure that the ion gauge is set to high pressure mode on the internal control panel (lower operating current) and then turn on the gauge. Initially, the gauge will turn on and then immediately turn off; however, on the second or third try, the gauge

should remain on. After venting a chamber, the ion gauge is covered in adsorbed molecules. When the ion gauge first starts, it degasses and creates an artificially high pressure reading which causes the ion gauge to turn off. After the gauge stays on, the chamber pressure should be at 10^{-5} Torr or less and decreasing, and the manifold pumping station TMP should indicate that the maximum rotational speed has been achieved (via the front panel light). When the maximum rotational speed of the pumping station TMP has been attained, open the two valves that separate the manifold from the pumping station and also open the valve at the inner differentially pumped region. At this point, the main TMP and the manifold pumping station TMP should have reached their maximum operating rotational speeds. Additionally, the chamber pressure should be less than 10^{-5} Torr and decreasing. At this time, check again that the dry N_2 vent lines are connected to the main chamber TMP and manifold pumping station TMP and pressurized to ~5 psi.

Sometimes the manifold pumping station must be vented independently of the main chamber. In order to restart the manifold pumping station, while the chamber is operating, simply turn on the pumping station via the front panel. After initially starting the pump, ensure that the dry N_2 vent line is connected to the station and that the line is pressurized to ~5 psi. After the pump has achieved the maximum rotational speed, open the valves to the manifold.

B.6 Helium Leak Checking

Once the main chamber pressure has achieved a value of less than 10^{-7} Torr, it is possible to begin leak checking the chamber. Connect the residual gas analyzer (RGA) head to the chamber and attach the power and control cables. Turn on the filament from the computer control software and then degas the filament. If the degassing stops abruptly, restart the RGA

and wait ~1 hour before attempting to degas the filament again. After the filament has been degassed, turn on the electron multiplier, and start a continuous helium leak check scan from the control software. Before leak checking, ensure that the actually RGA electronics indicate that both the filament and electron multiplier are active.

Leak checking the main chamber is relatively straight forward. Begin by flowing helium at a moderate flow rate over all of the newly added chamber components as well as all of the locations with junctions: flanges, feedthroughs, windows, edge-welded bellows, etc. Conflat flanges are relatively reliable in terms of leaking, so most leaks occur at newly added components and not at components already installed on the chamber. If a leak is present, then the partial pressure of helium will increase and a peak will show up on the mass spectrum as shown in Figure B.7.

In order to determine the exact location of the leak, reduce the helium pressure and move slowly over the entire flange or component. When there is an increase in the helium signal, remove the helium flow from the flange and allow the partial pressure to return to the original value. Afterwards, place the helium near the leak again, for a split second, and remove. The type and severity of leak is dependent on the relative signal intensity, the broadness of the peak, the peak shape, and the rate of signal decrease. To find small leaks, insert a plastic pipette tip into the rubber hose from the helium regulator and reduce the helium flow such that the flow from the tip can be just barely felt on wetted lips; use this low flow to pinpoint leaks. Table B.1 shows the relative relationship between the helium signal characteristics and the type of leak. It is important to note that the values in Table B.1 are for rough analysis only and are dependent on the actual size and type of the leak as well as the flow rate of helium. In addition, the table represents leaks generally found on ConFlat flanges, VCR fittings, and UHV components.

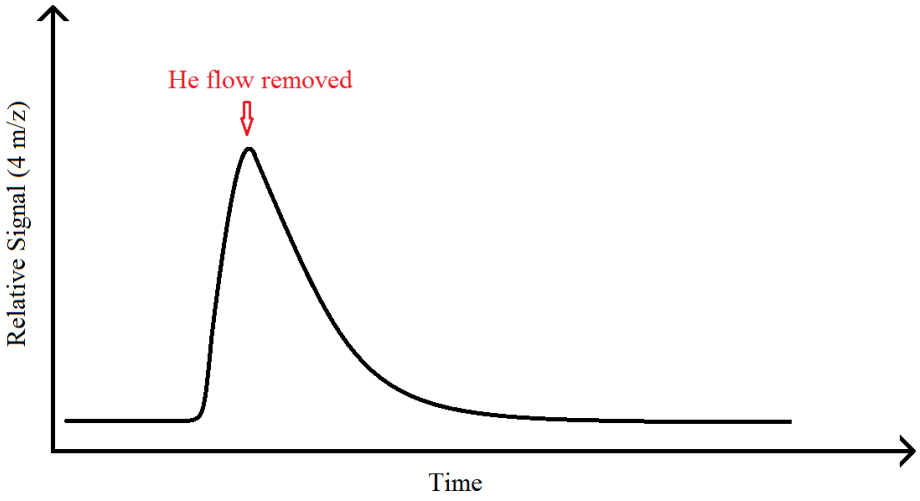

Figure B.7: Graphical representation of helium signal during helium leak checking. When the helium flow is removed from the leak, the helium signal decays slowly over time.

Relative Signal Intensity	**Broadness**	**Shape**	**Rate of Signal Decrease**	**Likely Cause**
Strong	Small Width	Sharp	Fast Decay	Metal Seal, Damaged Component
Moderate	Small Width	Sharp	Fast Decay	Metal Seal, Damaged Component
Moderate	Slightly Broad	Sharp	Moderate Decay	Metal Seal, Damaged Component
Moderate	Moderately Broad	Not Sharp	Moderate Decay	Damaged Component, Rotary Flange, Leak Elsewhere on Chamber
Weak	Small Width	Sharp	Fast Decay	Metal Seal
Weak	Very Broad	Not Sharp	Slow Decay	Rotary Flange, Ceramic Feedthroughs, Leak Elsewhere on Chamber

Table B.1: Relative relationship between helium leak peak characteristics and the likely cause of the leak. Note: the table does not encompass all possibilities.

Sometimes, the cause of certain leaks is difficult to determine. If the cause of a leak is difficult to pinpoint, try narrowing down the cause by first placing tape over all of the junctions near the apparent leak point; instead of taping UHV components, cover the components in plastic and tape the plastic to the chamber. Now, uncover and leak check each component, one at a time, until the cause it found. Once the cause of a leak has been determined, tighten the bolts around the problem area. As a side note, when one bolt is tightened, the other bolts around it loosen slightly; when this occurs, tighten the adjacent bolts to a slightly lesser degree, and then tighten the next set of adjacent bolts to a even lesser degree. If the leak is near the TMP, it is safer to first vent the chamber and then tighten the area around the leak; this will prevent damage to the TMP. Once all of the leaks have been found, the RGA can be shut down by first turning off the electron multiplier, and then the filament, and finally the power.

B.7 Bakeout Procedures

B.7.1 Introduction

As discussed in Appendix A, in order to study reactions at the gas-surface interface, the chamber pressure must be sufficiently low so that the surface is contaminant free. When a chamber is initially pumped down from atmospheric pressure, unreactive gases that do not readily adsorb to surfaces, such as nitrogen and argon, are quickly removed. However, many residual gases, such as water vapor and carbon monoxide, adsorb with relative ease to surfaces. At any given instant, the gases adsorbed to the chamber walls are in constant equilibrium with those in gas phase. In order to achieve UHV pressures, these adsorbed gases must be removed from the chamber walls so that the overall chamber pressure decreases. Given enough time (ca., years) the gas desorbing from the chamber walls would eventually be removed by the TMP or ion pumps. However, gas can be easily removed from a surface by heating. The purpose of the bakeout is to increase the temperature of the entire chamber in order to more efficiently desorb gas from the internal UHV components as well as the chamber walls.

B.7.2 Precautions

Although baking out a chamber seems like a straight forward process, there are several precautions one must take before undergoing a bakeout. Metals such as stainless steel, Kovar, nickel, and aluminum are strong and highly resistant to fluctuations in temperature and temperature gradients as well. Therefore, there is relatively little concern for metals during a bakeout. However, care should taken with materials that are sensitive to thermal shock and temperature gradients such as alumina, silica, borosilicate glass, and magnesium fluoride. In addition, many UHV components are a composition of multiple materials with different

coefficients of thermal expansion and heat conductivities: electrical feedthroughs, windows, and optical feedthroughs. During a bakeout, care should be taken with all of the aforementioned materials by reducing the chances of thermal shock and temperature gradients. Additionally, avoid concentrating heat in small areas on the chamber, as many UHV components have maximum bakeout temperatures. Windows, electrical feedthroughs, and Viton gaskets should not be heated above 150 ^{o}C, and one should check with the manufacturer in order to find out the maximum bakeout temperature for components. Lastly, while a bakeout is ongoing, do not open valves that contain fluoropolymers or Viton components since these materials become easily deformed and damaged at higher temperatures.

B.7.3 Preparation

A proper bakeout involves heating the chamber in a uniform manner, to a relatively high temperature ($\geq$ 115 ^{o}C), and holding the chamber at that temperature for at least 3 days. Although every vacuum chamber is different, the steps for baking out a chamber are relatively the same for all of them.

Assuming that the pressure is low enough for the ion pumps to operate ($< 10^{-7}$ Torr), first disconnect all electrical connections from the chamber that are not required to operate the chamber, including the RGA and lines connecting to the TSP (titanium sublimation pump) filaments. Do not remove the cabling from the TMP, ion pumps, ion gauge, or doser. In addition, position the crystal straight up, and move the crystal out of the chamber so that the bellows are expanded. Next, all of the components that are not resistant to thermal shock should be protected; all windows, electrical feedthroughs, and ceramic components should be covered in aluminum foil (before wrapping the chamber in heating tapes) and care should be taken not to

scratch the windows. Any components that are sensitive to thermal degradation should not be covered in too much aluminum foil. The following components are sensitive to thermal degradation: gate valves, rotary flanges, and any other components that contain Viton or fluoropolymer seals. Additionally, never wrap the TMP in aluminum foil; most TMPs can only handle temperatures of 60^{o}C before being damaged.

In the next step, the chamber is wrapped uniformly with heating tapes. When placing heating tapes on the chamber, do not allow the strips to overlap. Overlapped heating tapes greatly increase local heating and can damaged components, the heating strip, or both. Take care not to place the wraps across windows, electrical feedthroughs, or ceramic components in order to avoid damaging them. Additionally, do not wrap the ion pumps, TMP, ion gauge, front face of the doser, nor any portions of the chamber that are already equipped with heaters. As a side note, try to place the heating tapes so that the electrical plugs are near one another; this makes connecting the plugs to power strips much easier later on.

Once the chamber is uniformly wrapped with heating tapes, wrap sheets of aluminum foil around the chamber. For areas that have no components, such as blank flanges and the actual chamber, large sheets of aluminum foil should be used. Flanges that have multiple electrical feedthroughs should be tented with aluminum foil. To tent a component, first wrap the foil around the base of the flange, forming a hollow cylinder of foil and then crimp the sides closed; do not allow the foil to touch the inner components. Add an additional layer of foil over the windows, electrical feedthroughs, and ceramic components. At this point, the majority of the chamber and components should be covered in aluminum foil, and there are most likely gaps between the various sheets of aluminum foil. The most efficient method of filling the gaps is to gently crumple foil and then shove the foil into the gaps; take care not to damage sensitive

components. Repeat this process until all of the areas of the chamber are covered in foil excepting the TMP, ion pumps, ion gauge, doser face, components with built-in heaters, and any components that should not be over heated (e.g. rotary flanges). Lastly, connect the water lines to the heat exchanger attached to the TMP, and begin flowing water through the XPS water chiller.

Now that the chamber is wrapped in heating tapes and is well insulated with aluminum foil, connect the heating tapes to power strips and ensure that there are no more than three heating tapes per power strip. Each power strip is then connected to a heater box or variac. Before starting the bakeout, begin monitoring the pressure using a program such as LabView and ensure that the TMP is cooled by the water chiller as well as a fan.

B.7.4 Procedure

In order to start the bakeout, plug the heater boxes into wall sockets such that they are placed uniformly on two or three separate circuits and make sure that the heater boxes are set to 0. As a side note, a given circuit is rated to ~40 Amps, so it is safe to put two heater boxes or ion pump heaters on one circuit. Now, plug all of the ion pump heaters into wall sockets that are on separate circuits; separate circuits ensure that the individual circuits do not trip. After powering up the ion pump heaters, these devices will become very hot quite quickly (~150^{o}C in 30 minutes). While the ion pump heaters are warming up, set all of the heater boxes to 5% of the full scale, turn on the sleeve heating for the TMP via the DCU control unit, and also set the doser to 4.5% heating power. At this point, all of the various heating elements should be getting hotter and the TMP should be both water and air cooled. Wait approximately two hours before changing any heater settings.

After ~2 hours, the chamber pressure should be steadily increasing and the chamber should have achieved a relatively steady state temperature; in addition, the doser should be at ~400 K. At this point, the operator should begin increasing the heating power of the heating tapes; however, there are some notes to point out first. As the chamber becomes hotter, the amount of power required to increase the temperature increases as well. For example, increasing the power of a heater box from 0% to 5% might increase the temperature from 20^{o}C to 45^{o}C; however, if the power is then increased to 10%, the temperature might only increase an additional 15^{o}C. In addition, when the heating power is increased, some time is required in order to achieve a steady state temperature (~1 hour per 5% power increase). Before increasing the heating power, take a thermocouple and check the temperature at various locations on the chamber, do not hit windows or feedthroughs, and make a note of the temperature readings as well as the temperature of the crystal. The crystal temperature is a good indication of the average temperature of the chamber. Also note that the actual metal under the aluminum foil can be ~10^{o}C - 15^{o}C hotter than the temperature reading; additionally, the temperatures that are measured are highly dependent on the placement of aluminum foil and heating tapes, so the method of increasing the temperature of the chamber varies.

After measuring the temperature at various locations on the chamber, make sure that none of the readings are above 150^{o}C or 120^{o}C near Viton seals (at 5% heating power, these values are unlikely to be attained). In addition, make a note of how much the temperature increased from the original value. At this point, increase the heating power of the heater boxes to 10% and wait one hour before increasing the heating power again. After an hour, once again measure the temperature at various locations around the chamber and be sure that the temperatures are under the limits stated above. If the measured temperatures are acceptable, increase the power of the

heater boxes to 15% and wait another hour before increasing the heating power. When the chamber temperature becomes asymmetric, increase or decrease the heating power on the heater boxes corresponding to the areas that are too cool or too hot. This cycle is repeated until the chamber temperature is at 115^{o}C - 145^{o}C (the values on the heater boxers are probably not the same). As a side note, before leaving the building at the end of the day, be sure that the chamber has reached a steady state, equilibrium temperature; this is to limit the possibility of overheating the chamber. Once the chamber has achieved the desired temperature, the chamber is held at that temperature for at least three days. Throughout the beginning phase of the bakeout, the chamber pressure will increase readily. As the chamber reaches a steady-state temperature, the pressure should plateau and then decrease over time. Through the course of a bakeout, the chamber pressure should vary as shown in Figure B.8.

B.7.5 Ending

The bakeout is complete once the chamber pressure is lower than $3*10^{-8}$ Torr while the chamber temperature is at 115^{o}C - 145^{o}C. In addition, the chamber pressure should be reaching an asymptotic value as indicated in Figure B.8. Once the bakeout is deemed complete, the chamber can then be cooled. Unplug the ion pump heaters, set the heater boxes to 0%, and unplug the heater boxes from the outlets. Additionally, turn off the TMP sleeve heating from the DCU control unit but leave the doser heating on. As a side note, every two or three bakeouts, the lead screws on the DPRF 450 should be coated with new PTFE grease.

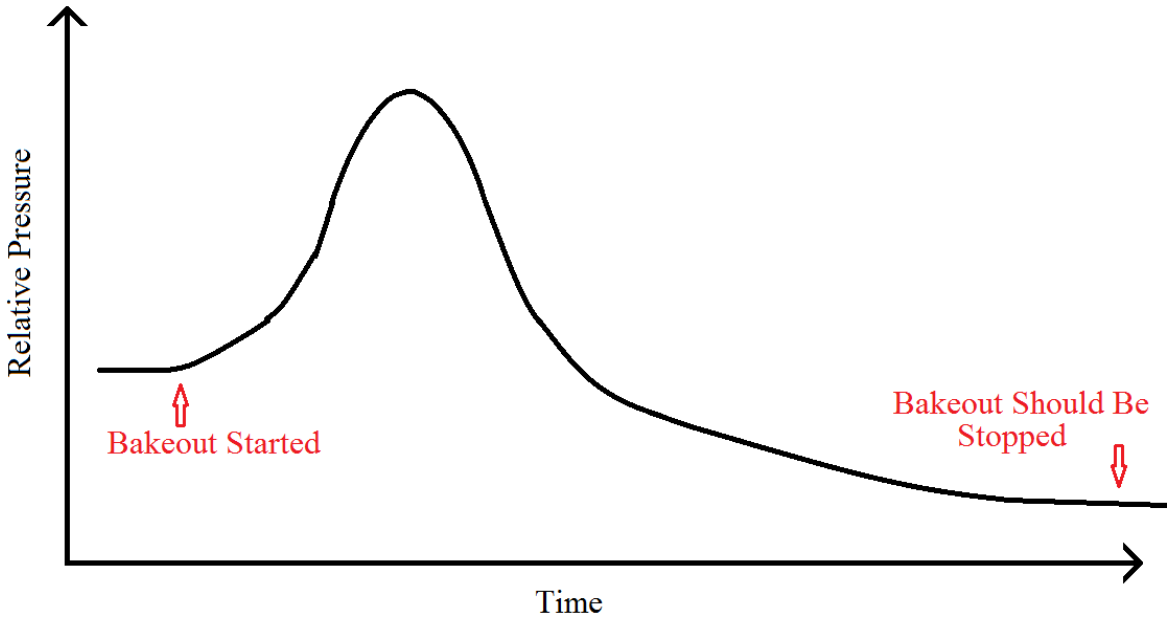

Figure B.8: Pressure variation as a function of time for a bakeout. As the chamber is heated, gas desorbs at a faster rate, causing an increase in pressure. Once the desorbing gas is depleted, the pressure drops. After a majority of the adsorbed gas is removed, the pressure approaches an asymptotic value.

As the chamber cools, the chamber pressure will begin to drop as the outgassing rate decreases. At this time, the doser heating power should be slowly increased (0.5% / 30 minutes) as the chamber cools; however, the doser temperature should not reach above 700 K while the chamber temperature is still hot. In addition, some components that normally operate at higher temperatures, such as filaments, require an additional degassing step. In order to prevent trap to trap distillation, where gas desorbing from a hot surface is deposited onto a cold surface, degassing these components must be accomplished while the chamber is relatively warm (~50^{o}C - 60^{o}C). In order to degas a UHV component, the temperature of the component flange must first be less than 60^{o}C. When this temperature is achieved, gently removed the aluminum foil to allow the component to cool. Reattach the electrical connections to the flange when the flange is cool enough to touch.

For filaments (excepting TSP filaments and instrumentation filaments (e.g. mass spectrometer filament)), slowly increase the current until the chamber pressure begins to increase and then hold the current constant. When the chamber pressure begins to recover or holds constant, continue to slowly increase the filament current. This process is repeated until the maximum operating current is achieved. When degassing filaments, the pressure will behave similar to Figure B.8, except that the peak will be much sharper. Once the pressure stops decreasing while the filament is at the maximum operating current, slowly decrease the filament current. TSP filaments are very large, have a relatively high surface area, and operate with substantial amounts of current. In order to degas the TSP filaments, the operating current should first be set to 15 Amps on the control unit. The filaments are then sequentially degassed for ~60 seconds each. The operating current is then increased to 25 Amps and the filaments are sequentially heated again. This process is repeated until all of the filaments have been degassed

at 45 Amps. Generally filaments in instrumentation (e.g. mass spectrometers and electron guns) are thin and relatively brittle. Therefore, great care should be taken when outgassing these types of filaments. To outgas these filaments, the current is first set to a relatively low value (~0.1 mA) and held at that value for ~4 hours. After four hours, the current is then increased in 0.1 mA increments every 30 minutes until the maximum operating current is achieved. Once the pressure stops decreasing, and the filament is at the maximum operating current, the current should be slowly decreased. In order to outgas the RGA, simply turn the filament on, wait 5 minutes, and then degas it using the control software; afterwards, turn off the RGA. For the vacuum system discussed in this dissertation, the following components should be outgassed: RGA, ion gun, electron gun, TSP filaments, and differentially pumped mass spectrometer. Although not included in the list, the doser must also be outgassed; however, the alumina on the doser is so porous that the doser is degassed during the actual bakeout as well as after the chamber begins to cool.

At this point, the chamber should be cooling, all of the filaments should have been degassed, the ion pumps should be working properly, and the doser should be heated to ~500 K - 700 K. However, the doser should be baked to a temperature at least 200 K higher than the desired operational temperature. For example, if the desired operational gas temperature is 600 K, then the doser must be heated to at least 800 K for a day or two. If the temperature of the doser must be increased at this point, increase the power by 1% and wait until the temperature equilibrates. Continue to increase the doser heating power in this manner until the desired temperature is achieved; then, hold the doser at this temperature for one or two days depending on the absolute background pressure. As a side note, any time the doser temperature is above

700 K, leave foil on the window between the TMP and the doser in order to prevent the TMP fan air from cracking the window.

After the bakeout has stopped, the chamber will still require a day to fully cool down. In addition, for the next day or so, the TSP filaments should be run three times a day until the chamber pressure is less than $5*10^{-10}$ Torr; in the normal course, run the TSP in the mass spectrometer chamber and the main chamber once per day at the end of the day. Lastly, the chamber should be fully helium leak checked again since heating and cooling can warp gaskets. If the leak is severe, the chamber may need to be baked out again; however, if the leak is small, a bakeout is most likely not required.

B.8 Chamber Contaminant Removal

B.8.1 Introduction

Most compounds that are present in a UHV chamber can be removed by simply baking out the chamber. However, sometimes a chamber becomes contaminated with oil or some other compound that cannot be easily removed. In these instances, extreme measures must be taken in order to deal with contamination. Oils and organic substances readily degrade into smaller molecules when subjected to high temperatures (> 600 K) and these smaller compounds can be removed through pumping. However, these temperatures are impossible to achieve throughout the entirety of the chamber. Therefore, it makes more sense to remove these compounds through chemical reactions whose products are small molecules that are easily pumped from the chamber.

B.8.2 Titanium Sublimation Pump (TSP)

A titanium sublimation pump (TSP) works on the principle that highly reactive surfaces can easily chemisorb and breakdown compounds which are difficult to remove through means of a TMP. TSP filaments are generally surrounded by a stainless steel shroud situated within an ion pump that aids in pumping gas. The actual operating principles of a TSP are fairly straight forward. A current is first passed through a large coiled piece of titanium which, is in turn heated to a substantial temperature (> 1500 K). At these temperatures, titanium atoms sublimate from the filament and deposit onto the walls of the shroud that surrounds the filament. After heating for some time, the shroud becomes covered in a thin film of titanium atoms. This freshly laid layer of titanium is very reactive towards a variety of molecular species and almost all molecules that strike the surface react (except for noble gases). The TSP is a very effective method of pumping contaminants from the chamber; however, for molecules with a high sticking coefficient (e.g. oil), the amount of gas phase molecules is much lower than the species adsorbed on the chamber walls. Therefore the TSP is not ideal for removing these types of contaminants.

B.8.3 NO Cleaning

For contaminants which cannot be easily removed by traditional means (TSP, TMP, and ion pumps), chemical reactions are required in order to remove the contaminants at the source. Although O_2 seems like a likely choice to remove contaminants, it is too weak of an oxidizer at mild temperatures (~80^{o}C - 120^{o}C); additionally, ozone is by far too unstable to be used. However, nitric oxide, NO, is a relatively stable compound that is an excellent oxidizer even at mild temperatures. Therefore, NO is the proper choice for cleaning an extremely contaminated UHV chamber.

The procedure for NO cleaning a UHV chamber is quite similar to the procedure for baking out a chamber. First, the NO gas cylinder is connected to the gas manifold. Next, the chamber is heated to ~100^{o}C, the doser is heated to ~400 K, the gas manifold is pressurized to ~1 Torr of NO, and all of the extraneous filaments and ion pumps in the chamber are turned off. In addition, the gate valve between the chamber and TMP should be most of the way closed. The variable leak valve is then opened to the chamber and the chamber is filled with ~10^{-5} Torr of NO. The chamber is baked with the NO flowing for ~2 days. Afterwards, the residual NO is pumped away from the manifold and the NO tank is removed. The chamber is then baked using standard bakeout procedures (Appendix Section B.7). Figure B.9 (a) and B.9 (b) show mass spectra of a chamber with oil contamination and a chamber after NO cleaning respectively.

B.8.4 Doser Cleaning

If the doser has been previously cleaned, only a bakeout is required; and this is true even if the chamber has been vented multiple times. Because the doser design incorporates two large pieces of alumina, machined using oil as a lubricant, the initial cleaning of the doser should be conducted in a separate preparation chamber. After the doser is constructed (Appendix Section F.1) it is outfitted onto the preparation chamber. The chamber is first baked out (Appendix Section B.7) with the doser being heated to 1000 K by the end of the bakeout. The doser is then NO cleaned (Appendix Section B.8.3) with one variation. The doser is first cooled to 400 K before dosing NO, and after the NO dosing is complete, the doser is heated to 1000 K for two days in order to remove any NO and trapped gasses from the bulk of the alumina. The doser is now ready to be loaded onto a UHV chamber.

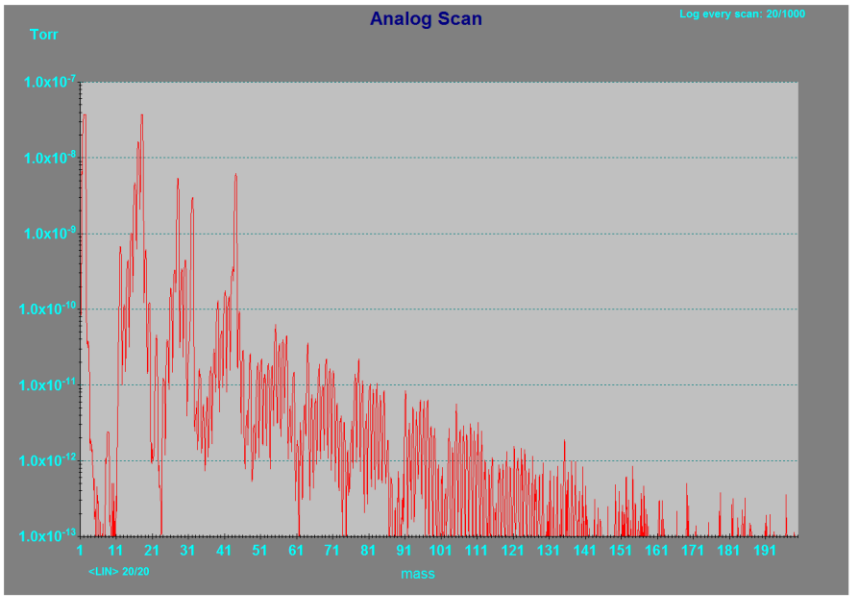

(a)

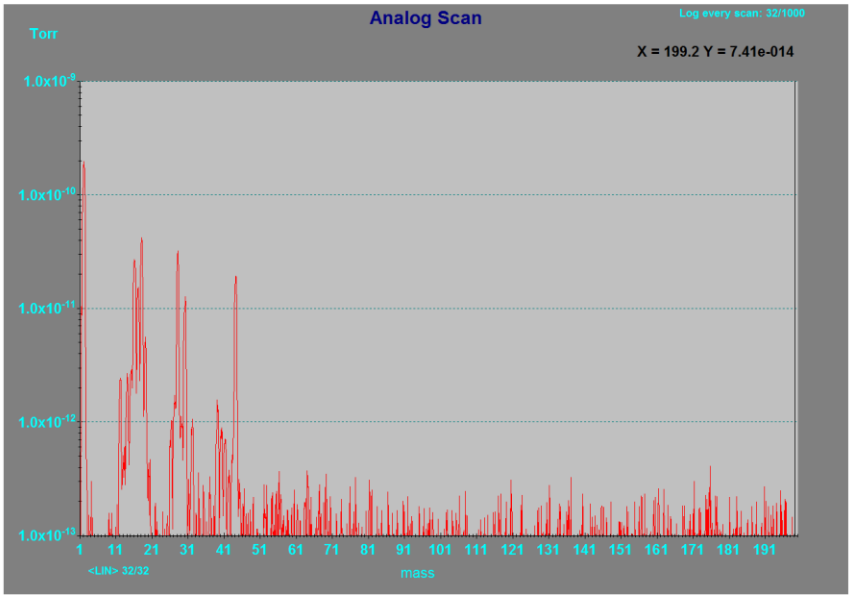

(b)

Figure B.9: Mass spectra of a chamber contaminated with oil before NO cleaning (a) and after NO cleaning (b). The mass spectra come from an SRS RGA 200.

B.9 Venting

B.9.1 Main Chamber

In order to repair any component on the chamber or to switch samples, the chamber must be vented. When all of the heated elements are cooled to room temperature, turn off all of the components of the chamber except for the ion gauge and TMP. In addition, ensure that the vent lines are pressurized (~5 psi) and connected to the TMP and the pumping station.

First, close the red valve that separates the mechanical pump from the outer differentially pumped region on the manipulator and also close the valve that separates the mechanical pump from the TMP. Once both of those valves are shut, turn off the TMP from the DCU control unit; the mechanical pump will turn off as well. The ion gauge can be left on to monitor the chamber pressure until the TMP rotational speed is ~650 Hz. Unless the settings are changed, the TMP should begin venting at 600 Hz, at which point air will flow into the chamber. Once venting has begun, the TMP rotational speed will drop quickly; ensure that air is flowing to the chamber by listening for a hissing sound at the dry N_2 regulator. After ~ 2 minutes, the TMP rotational speed should be less than 10 Hz, and the air should not be flowing as quickly; at this point, the operator can begin to remove the desired flange. If there is suction between the flange and the chamber, increase the flow of dry N_2. Once the flange is removed, shut off the flow of N_2. The chamber is now fully vented. As a side note, if the manifold pumping station is still operating, disconnect the vent line from the chamber TMP and cap it; after capping the vent line, open the valve between the dry N_2 tank and the vent lines so that they are pressurized once again.

B.9.2 Manifold Pumping Station

In order to repair components on the gas manifold, the manifold pumping station does not generally need to be vented because two valves separate the gas manifold from the station. However, the pump station must be vented in order to change the oil. First, ensure that the vent lines are pressurized (~5 psi) and connected to the TMP and the pumping station. Next, close the two valves beneath the gas manifold separating the gas manifold from the pumping station. In addition, ensure that the valve between the inner differentially pumped region on the manipulator and the pumping station is closed. The station is now isolated from the chamber and manifold and is ready to be vented. Turn off the pumping station from the front panel and after a few minutes, the pump station will begin venting. Unlike the main chamber, the manifold pumping station vents quite quickly and can easily become over pressurized. When the pumping station TMP stops spinning after venting (indicated by a lack of sound after spinning down), remove a flange to relieve the pressure. Once the flange is removed, place aluminum foil over the port and turn off the N_2 flow. Then, replace the flange using a new gasket and now the pumping station is fully vented. As a side note, the dry N_2 vent lines for the main chamber TMP and the pump station share a common tank. Therefore, after the pumping station is vented, remove the vent line from the rear of the station and cap the line with a blank. After the line is capped, pressurize the line again so that the main chamber TMP can be vented if needed.

Appendix Section C - UHV Chamber Maintenance

C.1 Changing Oil

C.1.1 Mechanical Pump Oil

Although it might not seem that important, changing mechanical pump oil is actually integral to obtaining UHV conditions. Over time, oil begins to degrade and produces an increasingly high partial pressure of hydrogen gas. The average velocity of hydrogen is high enough at room temperature that a relatively large fraction of molecules (1 in 10^5) can escape back into the UHV chamber from behind the TMP blades. In addition, failure to change mechanical pump oil can damage the pump over time because of increased friction. Generally, mechanical pump oil should be changed every 6 months. However, if the chamber was cleaned using NO, then the pump oil should be changed immediately afterwards. Large mechanical pumps use medium viscosity oil from Kurt J. Lesker (Model: KJLSS19) and smaller Pfeiffer mechanical pumps use model P3 oil from Pfeiffer.

In general, when changing oil in mechanical pumps that are attached to a vacuum system, the system should be first vented. If the mechanical pump is part of a unit (pumping station), do not remove the mechanical pump when changing the oil. In the case of NO cleaning, the mechanical pump oil should be changed immediately, but venting the vacuum system would require another full bakeout. Therefore, the pump oil must be changed while the TMP is running. First, place a jack under the valve that separates the mechanical pump from the TMP and then close this valve and also close the red valve separating the outer differentially pumped region on the manipulator from the mechanical pump. Next, close the gate valve separating the TMP from the chamber. At this point, disconnect the electrical connection from the TMP that connects to the interlock and then turn off the mechanical pump. The partial pressure behind the

TMP will slowly rise, so the operator has ~30 minutes to change the pump oil and to change the oil trap beads (Appendix Section C.1.2). Remove the KF fitting from the valve and take off the mechanical pump with the oil trap attached. Change the pump oil and oil trap beads and reconnect the mechanical pump. Once the pump is attached to the valve, plug the power cord back into the interlock and turn the mechanical pump switch to the on position. Next, reinsert the interlock cable to the TMP and the mechanical pump should start. As a side note, it is imperative that the mechanical pump switch is set to "on", if not, then the interlock will sense that the mechanical pump is off and the TMP will start to spin down.

In the case where mechanical pump oil has not been changed for a year or the oil has become discolored, then the mechanical pump must be flushed. In order to flush a mechanical pump, first drain the oil from pump. After the oil is drained, pour additional fresh oil through the pump for about 10 seconds to remove any viscous used oil. Next, fill the pump with fresh oil and cap the KF intake port with a blank flange. Run the mechanical pump for ~30 minutes and then drain the oil. Repeat this process once more, and then refill the mechanical pump with fresh oil. If the oil is still discolored, repeat this process an addition one or two times, depending on the cleanliness of the oil. The pump is now ready for use.

C.1.2 Oil Trap

Because most mechanical pumps contain oil, oil traps are required in order to prevent oil from back streaming into TMPs. Oil traps contain extremely porous, high surface area alumina beads that can readily trap oil. The oil traps in Harrison group contain activated alumina from Edwards (Model: H02600050). The beads in the oil traps should be changed every 3 months;

however, oil is generally changed every 6 months. Therefore, the alumina beads should be changed every 6 months or whenever the oil is changed.

C.1.3 Turbo Molecular Pump Oil Wicks

While the blades in a turbo molecular pump are spinning, an oil wick at the base of the TMP provides lubricant to ensure that the TMP does not seize. Therefore, changing oil wicks is a very important part of chamber upkeep. For newer turbo molecular pumps, the frequency of oil changes varies depending on the pump. However, the older designs (2010 or older) need to have oil wicks exchanged every 6 months. Ideally, the oil wicks should be changed after NO cleaning, but this is not feasible given the fact that the TMP must be stopped in order to change the oil wick. The oil wick used for the TSU 065D pumping station is a model PM 103 593-AT Pfeiffer oil wick (the oil wick model on the station is obsolete) and the oil wick for the main chamber TMP is a Pfeiffer oil wick (Model: PM 063 265-T).

In order to install the oil wick on the chamber TMP, first remove the outer cap from the rear of the TMP. As a side note, never tip a TMP past the point where it is perpendicular with the floor (the TMP can face straight up though), as oil from the wick can contaminate the TMP blades. After the cap is removed, use a small screwdriver to pry out the oil wick taking care not to strike or scratch the inside of the TMP. After the oil wick is removed, push the new oil wick into the recess behind the TMP until the gasket on the oil wick clicks past the opening. Replace the gasket on the cap and then screw the cap back onto the TMP; be careful not to overly tightening the cap. For the pumping station, the new oil wick fits very tightly into the recess and does not easily click into the slot. In order to more easily replace the oil wick, first gently slide the new oil wick into the recess behind the TMP, without attempting to click the gasket into

place (hold it with your hand). In one smooth motion, remove your hand from the oil wick and replace it with the new cap and gasket. Screw the cap into place taking care not to cross-thread the cap. While tightening, the cap will at first tighten easily and then, will become slightly more difficult to tighten; the cap will then become easier to tighten again and finally, the cap will become very difficult to tighten. The first difficulty in tightening comes from the resistance of the oil wick. Stop tightening the cap once it becomes difficult to tighten it further. Be careful not to over tighten the cap.

C.2 Changing Titanium Sublimation Pump (TSP) Filaments

Over time, TSP filaments become brittle and break because of the intense temperatures that they are subjected to. Although the lifetimes of TSP filaments vary based on the actual filament and the amount of use, TSP filaments generally break after 3 years. If a TSP filament measures infinite resistance, then the TSP filament is most likely broken. Most TSPs contain three or four filaments, and only one filament is required to operate the TSP. Therefore, TSP filaments should only be replaced when the chamber is being vented for other reasons.

When the chamber is vented, remove all of the wires that are attached to the TSP and then remove the TSP; be careful not to damage the knife-edge on the ConFlat flange when removing the TSP. Once the TSP is fully removed, remove all of the filaments, even if the filaments are not broken. Before the filaments are replaced, use a clean stainless steel brush to remove any films or carbon that has built up on the TSP. Lastly, replace the filaments and reinsert the TSP into the chamber.

C.3 Refilling Liquid Nitrogen Dewar/Cryostat Operation

In order to control the temperature of the crystal, liquid nitrogen is flowed to the crystal mount using the setup described in Sections 2.2.1 and 2.3. Although refilling the liquid N_2 dewar is not necessarily maintenance, liquid N_2 is nevertheless a consumable. First and foremost, do attempt to remove the cryostat arm from the chamber unless both the cryostat and crystal temperatures are above 280 K and below 350 K. If the temperature is too high, move the crystal mount away from the heated doser and allow the mount to cool. When working with liquid N_2, be sure to wear insulated gloves to avoid frostbite and wear goggles to avoid liquid N_2 that splashes. Figure C.1 shows images of the cryostat arm and dewar.

After the mount is within the proper temperature range, remove the pumping line from the back of the cryostat arm and slowly open the yellow vent valve on the side of the dewar. After the tank is depressurized, loosen the nut holding the cryostat arm at the top of the dewar and then unscrew the cap connecting the cryostat arm to the chamber. When the cap is loose, slide the cryostat arm out from the chamber by gently pulling on the cap with one hand, and pushing the dewar backwards with the other hand. Be sure to hold the cryostat arm straight when it is removed from the chamber so that the internals of the flange are not damaged. When the arm is free of the chamber, push the dewar and cryostat arm away from the chamber. Then, lift the cryostat arm out of the dewar, while holding the bellowed part of the cryostat arm relatively level, and hang the cryostat arm on hooks. As a side note, be sure to wear a glove on your hand when removing the arm from the dewar as to avoid frostbite. After the cryostat arm is removed from the dewar, close the valve at the top of the dewar and remove the locking cap and gasket from the top valve and set aside.

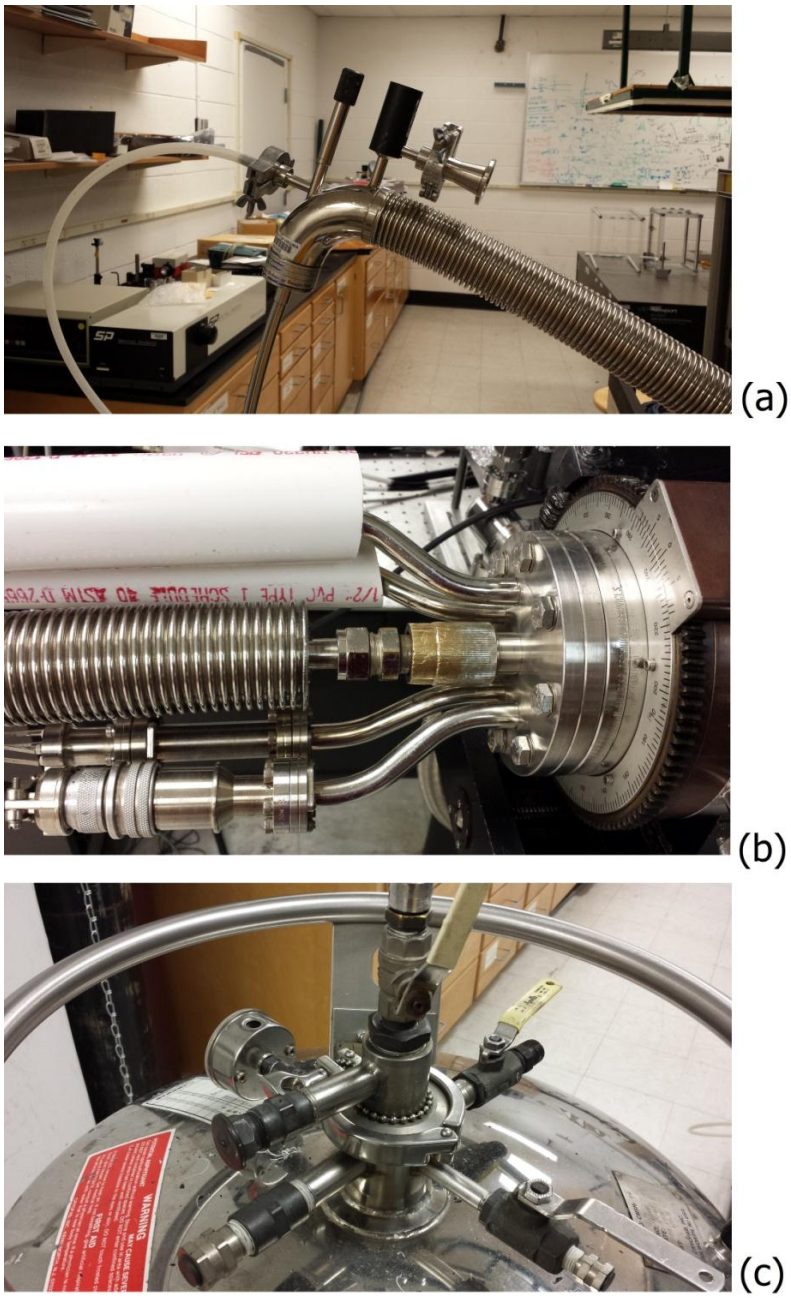

Figure C.1: Close-up images of the cryostat arm (a), the cryostat arm connection to the chamber (b), and the liquid N_2 dewar (c). On the arm, the small black cap is used for liquid N_2 flow control, the large cap and KF port are used for pumping out the cryostat arm, and the white hose connects to the flow control unit. The arm is inserted into the top port of the dewar. The valves on the dewar that are perpendicular to the floor are for venting built up pressure.

After the cryostat arm and dewar are separated, wrap PTFE tape around the threads of the top port on the dewar and connect it to the liquid N_2 hose from the refilling tank. Before filling the dewar, aim the exhaust port (yellow handle) of the dewar away from people and the chamber. Now, open the valve on the top port and the valve on the exhaust port (yellow handle) of the dewar to allow liquid N_2 to flow into the dewar and allow N_2 gas to escape respectively. Next, slowly open the valve on the refilling tank and allow liquid nitrogen to flow. As the liquid N_2 flows, gas will intermittently be pushed out of the dewar in bursts; this is normal. However, if a great deal of air is pushed out continuously, reduce the flow of liquid N_2; this is especially true if the dewar was completely empty (liquid N_2 vaporizes when in contact with warm surfaces). Once the N_2 gently flows out of the exhaust port on the dewar, the valve on the refilling tank can be opened fully. Depending on the original volume of liquid N_2 in the dewar, the filling time can vary from 2 to 10 minutes; the tank is almost full when air being pushed out of the exhaust port looks like fog (water condensing). When this happens, reduce the flow of liquid nitrogen until the fog subsides; if the dewar starts spraying liquid N_2, decrease the flow rate severely. The tank is full when liquid nitrogen drips out of the exhaust port on the dewar. At that point, fully close the valve on the refilling tank and close the top port valve on the dewar; then, remove the refilling tank hose from the dewar.

After filling the dewar, the entire top of the it will be very cold and will need to be heated to room temperature. To warm the top of the dewar, first remove the PTFE tape from the threads on the top port using tweezers. Afterwards, take a heat gun and gently warm the port body and the ports on the dewar. Do not place the heat gun very close to the ports and do not overheat any component that contains PTFE tape or Viton gaskets. Once all of the ice has been melted,

remove any excess water with a paper towel and then continue heating the components until they are slightly warm to the touch.

While the dewar is being filled, the cryostat arm is warming to room temperature. However, there will still be water present on the length of the cryostat arm. This water must be removed so that it does not block the flow of liquid N_2 to the crystal mount. As a side note, do not wipe the water from the cryostat arm; the water is a good indicator of whether or not water is present on the inside of the cryostat arm. As with the dewar, gently heat the entire portion of the cryostat arm that was immersed in the liquid N_2 until the water has evaporated and the arm is warm to the touch.

After the water has been removed from the dewar and the cryostat arm, place the locking cap and gasket back onto the top port of the dewar (do not tighten) and open the valve; also, ensure that the exhaust port valve is open as well. Before placing the cryostat arm into the dewar, first open the flow control knob at the top of the cryostat arm a full six turns which will allow moist air to flow out of the cryostat arm when placed in the dewar. Now, slowly lower the cryostat arm into the dewar until the arm reaches the bottom of the tank. Next, while holding the end of the cryostat arm level, slowly insert the arm into the chamber until it reaches the locking nut. Once the arm is fully inserted into the chamber, tighten the nut until it is hand-tight. Next, align the dewar so that the cryostat arm is relatively straight and is not exerting significant force on the chamber. Then, using a pair of locking pliers, tighten the locking cap on the top port of the dewar and be careful not to overly tighten it. Finally, close the exhaust port valve (yellow handle) on the dewar and reattach the pumping line to the back of the cryostat arm. Now the cryostat is ready for operation. As a side note, the secondary exhaust port valve (bare metal

handle) on the dewar should always be left open; this ensures that the dewar is not overly pressurized.

To operate the cryostat, first start the pump that pumps on the liquid N_2 flow control unit. After 10 seconds, open the flow knob on the control unit a quarter turn counterclockwise and the needle should indicate that a vacuum is being pulled. After 30 seconds, the cryostat temperature should start decreasing. At this point, the liquid N_2 flow should be controlled via the control unit. However, if the cryostat cools too quickly, the liquid N_2 flow can be further restricted by closing the flow control at the top of the cryostat arm. While the cryostat is operating, place water on the locking cap to see if the gasket is leaking (bubbles will form); this only needs to be performed when the dewar is refilled. If there is a leak, tighten the locking cap further, and then remove the water. In order to shut down the liquid nitrogen flow, first close the flow control at the top of the cryostat arm. Next, turn the flow control knob on the control unit clockwise until it stops. Lastly, turn off the pump that pumps on the flow control unit.

Every couple of weeks, the volume inside of the cyrostat arm must be pumped out in order to maintain a reasonable vacuum in the arm (poor vacuum results in poor cooling). While the cryostat arm is connected to the chamber, connect a mechanical pump to the KF flange on the cryostat arm, and then turn the pump on. After the mechanical pump is turned on, open the large black cap above the KF port until it has moved a quarter inch above its original position. Allow the mechanical pump to pump on this volume for ~30 minutes. After the pumping is complete, fully tighten the black cap above the KF port and then turn off the mechanical pump and remove it from the cryostat arm.

Appendix Section D - Crystal Preparation

D.1 Introduction

In order to accurately measure reactivity at the gas-surface interface, the surface must be free of unwanted elements (i.e. "clean"). There are two ways to clean single crystal surfaces: chemical and physical. Chemical cleaning involves the conversion of strongly bound contaminates into products that can easily desorb from the surface. Physical cleaning involves the bombardment of a surface with atoms in order to dislodge strongly bound impurities that are either unreactive or whose products of reaction do not easily desorb. However, the niceties of cleaning can be quite different depending on the surface as well as the identity of the impurity. For chemical cleaning, after the surface species have reacted, the crystal is then heated to an elevated temperature to desorb any volatile products; this process is known as flashing the crystal. After physical cleaning, the crystal surface is then chemically cleaned to remove additional impurities and is then annealed by holding the surface at an elevated temperature for a period of time; annealing is used to remove defects from the surface. This appendix section discusses the removal of certain surface impurities from a Pt(111) single crystal. An Auger spectrum of a clean Pt(111) crystal is shown in Figure D.1.

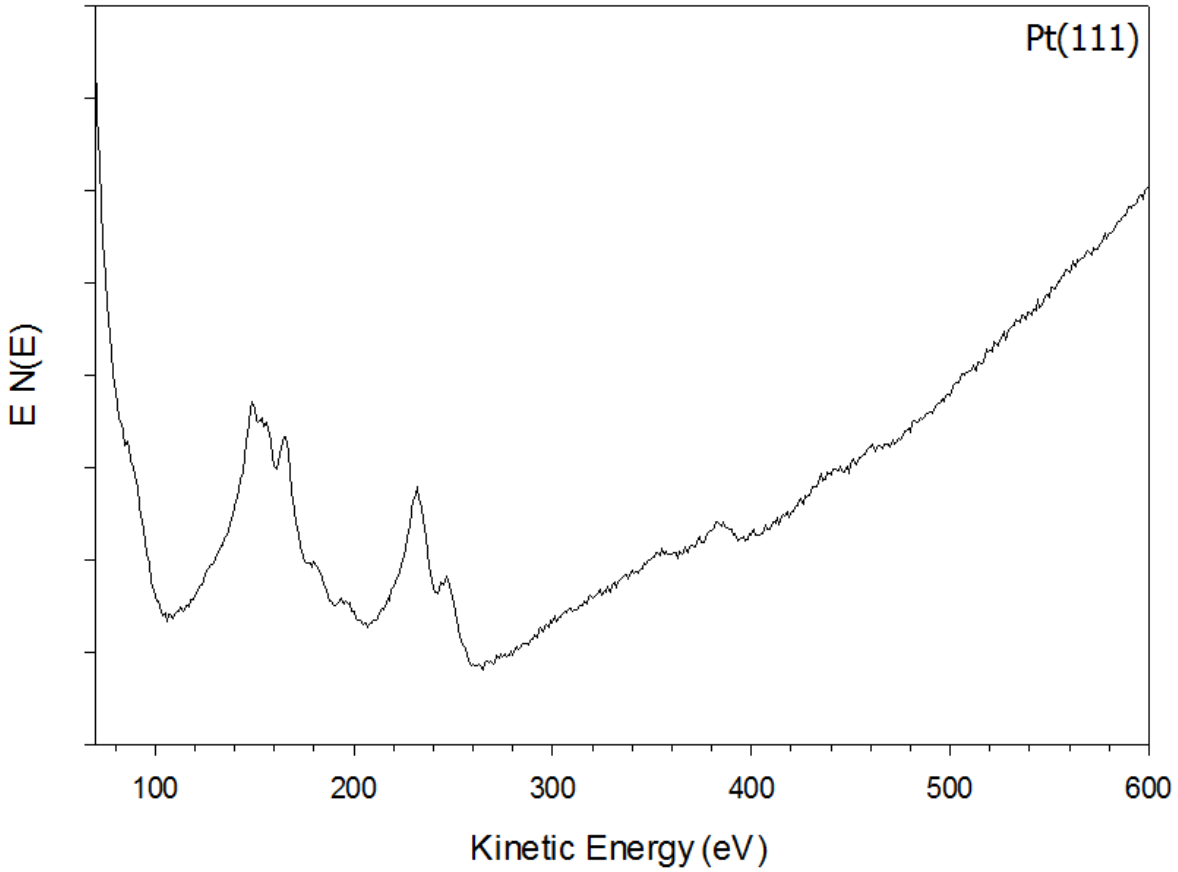

Figure D.1: Auger spectrum of a clean Pt(111) crystal acquired using a 15-255 GAR double-pass CMA.

D.2 Cleaning by Oxidation

The most common form of chemical cleaning is the reaction of surface impurities with oxygen. Most surface reactions involving oxygen occur via a Langmuir-Hinshelwood mechanism. For this mechanism, oxygen first dissociates into adatoms on the surface. Next, the oxygen adatoms react with surface species forming products that then desorb from the surface.

$$O_{2,g} \rightarrow 2O_c$$

$$nO_c + mX_c \rightarrow O_n X_{m_g}$$

Although this reaction is straight forward, there are several issues that need to be addressed. The probability that O_2 will dissociate onto the surface and the kinetics of reaction are both temperature dependent. In addition, the surface impurity can dissolve into the bulk at certain temperatures. Therefore, oxygen cleaning must be conducted at a temperature that generates a reasonable steady-state coverage of oxygen adatoms, limits the diffusion of the impurity into the crystal bulk, and maximizes the rate of impurity removal.

For oxygen cleaning of a Pt(111) crystal, the crystal is first heated to the desired temperature of reaction. The crystal is then directed at an capillary array doser, and oxygen is flowed over the crystal for a period of time. After the reaction, the Pt(111) crystal is then flashed to 1200 K and the surface cleanliness is checked using Auger electron spectroscopy (AES). The oxygen pressure, dosing time, and crystal temperature are dependent on the impurity being removed. However, the reaction is always conducted at crystal temperatures lower than 900 K for Pt(111); at a surface temperature of 900 K, the dissociative sticking coefficient of O_2 on Pt(111) is negligible. As a side note, for oxygen pressures above $5*10^{-8}$ Torr, the gate valve that separates the main chamber from the ion pump should be shut.

D.3 Argon Ion Sputtering

Certain surface impurities are difficult to remove through chemical reaction; either the impurities do not readily react or the products of reaction do not easily desorb from the surface. For these types of impurities, the surface must be cleaned via argon ion sputtering. Ion sputtering involves directing high energy ions at the crystal surface which strike with enough force to dislodge atoms from the surface. Although any atom or molecule can be converted into an ion, generally argon is used for ion sputtering because it is a noble gas that does react with any surface, does not decompose, and is more easily ionized than helium.

For argon ion sputtering, argon ions are first formed via electron bombardment. As argon ions are formed, they are accelerated towards the surface by a series of negatively charged focusing elements. The argon ions then strike the surface, dislodging and removing impurities (as well as atoms of the crystal). After argon ion sputtering is complete, the surface is cleaned with oxygen and is then annealed at a high temperature to remove defects from the surface.

In order to perform argon ion sputtering on Pt(111), the filament on the ion gun is slowly increased to 2 mA and allowed to degas. After degassing the filament, turn off all of the ion pumps, except the ion pump on the rotary flange, and close the TMP gate valve so that 90% of the TMP is covered. The chamber is then back-filled with argon to a pressure of $5*10^{-5}$ Torr (refilled as needed) and the crystal is heated to 600 K. After heating the crystal, the crystal face is then positioned in front of the ion gun. The desired ion energy and the ion focusing elements are set at the control unit and the system is then started. After sufficient ion bombardment, the ion gun is turned off and the TMP gate valve is fully opened. The crystal is then cleaned in oxygen to remove carbon deposited from ionization of background gases. Once oxygen cleaning is completed, and the chamber pressure is lower than 10^{-8} Torr, the ion pumps are restarted and the surface is annealed at 1200 K for 5 minutes. Lastly, surface cleanliness is checked using AES.

D.4 Removing Surface Impurities from Pt(111)

D.4.1 Carbon

Carbon is one of the most common impurities found in Pt(111). Carbon deposition occurs from any organic compound that decomposes on the surface; for example, hydrocarbons, excluding methane, readily react on platinum at temperatures above 300 K. On platinum, at surface temperatures above 1100 K, carbon begins to dissolve into the bulk metal lattice. Figure D.2 shows an Auger spectrum of carbon on Pt(111); carbon is easily identified by an Auger peak at 275 eV.

When removing carbon from the platinum surface, the surface temperature should be set to 800 K in order to facilitate fast reaction and desorption kinetics, and at this temperature the dissociative sticking coefficient (DSC) for oxygen is relatively high. In addition, the rate of carbon oxidation scales with oxygen pressure, such that, 10^{-8} Torr of oxygen impinging on a surface for 100 seconds removes the same amount of carbon as flowing 10^{-7} Torr of oxygen for 10 seconds.

If the carbon coverage is less than 1 monolayer (ML), with respect to platinum, and there is no carbon dissolved in the bulk, then carbon is easy to remove from the surface. An oxygen pressure of ~10^{-7} Torr will remove approximately 1 ML of carbon in ~15 minutes at a surface temperature of 800 K. However, if a large amount of carbon is present in the bulk, then the oxygen cleaning procedure varies slightly.

When the carbon concentration in the platinum bulk is high, carbon segregates to the surface. However, the surface carbon is in equilibrium with the bulk carbon, and only a fraction of the bulk carbon segregates to the surface. As carbon is removed from the surface through reaction, more carbon then segregates to the surface from the bulk. If carbon is not removed from the surface, then no more carbon segregates to the surface from the bulk. Therefore,

removing all surface carbon is limited by carbon segregating to the surface. In order to remove carbon from this type of platinum surface, oxygen cleaning must be conducted with moderate pressures for an extended period of time. If the bulk concentration of carbon is high, then standard oxygen cleaning will only yield a small reduction in the carbon coverage; carbon segregates to the surface as surface carbon is removed. For this type of surface, oxygen cleaning should be conducted at a pressure of ~10^{-8} Torr for ~2 hours and repeated until all surface carbon is removed.

Lastly, if the surface is extremely contaminated with carbon ($\geq$ 2 ML), then sputtering is required. For this type of surface, the concentration of carbon is so high that there are few open surface sites for oxygen adatoms to form. In order to remove the carbon, the surface should first be sputtered for 30 minutes with 1000 eV argon ions at a temperature of 600 K. Afterwards, oxygen cleaning should be conducted with an oxygen pressure of 10^{-7} Torr for an hour. After oxygen cleaning is completed, the surface should be checked for cleanliness, and if the carbon concentration has been noticeably reduced, then oxygen cleaning should be conducted again. However, if the carbon concentration has not been reduced, then cycles of argon sputtering followed with oxygen cleaning should be conducted.

D.4.2 Hydrogen

Hydrogen is by far the most abundant gas in a well baked out chamber and hydrogen can only be detected on the surface via temperature programmed desorption (TPD). In order to remove hydrogen, simply heat the surface above 400 K and the hydrogen adatoms will recombine and desorb from the surface.

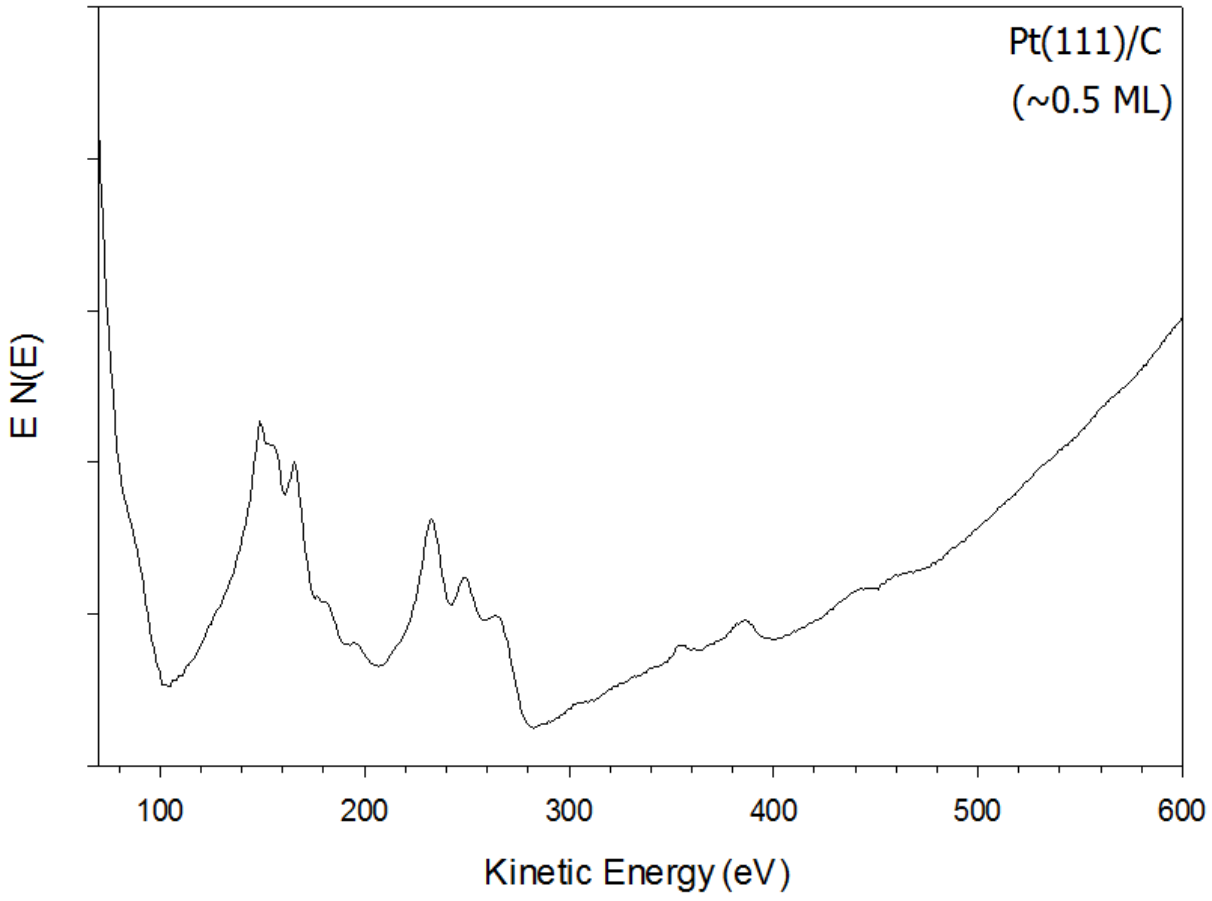

Figure D.2: Auger spectrum of carbon on Pt(111) acquired using a 15-255 GAR double-pass CMA. The Auger peak at 275 eV is indicative of carbon.

D.4.3 Argon

Generally, argon contamination results from argon ion sputtering. While sputtering, many of the high energy argon ions become lodged in the first few layers of the platinum surface. By flashing the crystal to 1200 K, all of the argon should be removed. Figure D.3 shows an Auger spectrum of argon on Pt(111). Argon generally appears as a small peak or shoulder at 219 eV in Auger spectra.

D.4.4 Oxygen

Oxygen contamination results from organic compounds decomposing onto the platinum surface and also from oxygen cleaning. Oxygen adatoms recombine and desorb from the platinum surface above a temperature of 900 K. Therefore, if oxygen is present on surface, flashing the crystal to 1200 K should remove all of the oxygen. Because platinum oxide is a very unstable compound and is not known to exist on platinum surfaces, no oxygen should be present on the surface after flashing the crystal. However, if oxygen remains after flashing, then the oxygen is most likely present as an oxide. If no other impurity peaks are present in the Auger spectra, then the oxygen is most likely caused by silicon dioxide; this is because the main Auger peak for silicon (96 eV) overlaps with a platinum Auger peak (97 eV). Figure D.4 shows an Auger spectrum of Pt(111) contaminated with oxygen. Although slightly difficult to detect, oxygen is recognizable from the Auger peak at 510 eV.

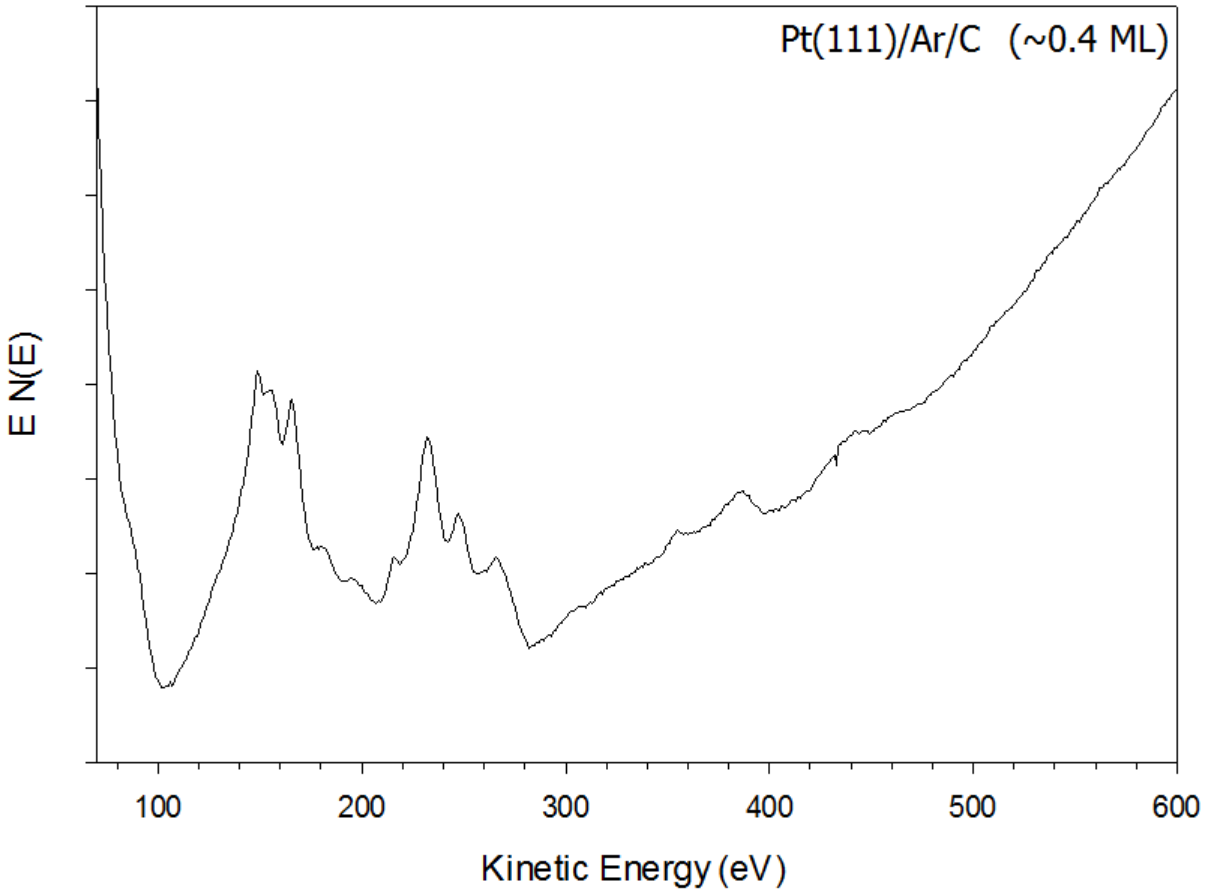

Figure D.3: Auger spectrum of argon and carbon on Pt(111) acquired using a 15-255 GAR double-pass CMA. The Auger peak at 275 eV is indicative of carbon and the peak at 219 eV is indicative of argon.

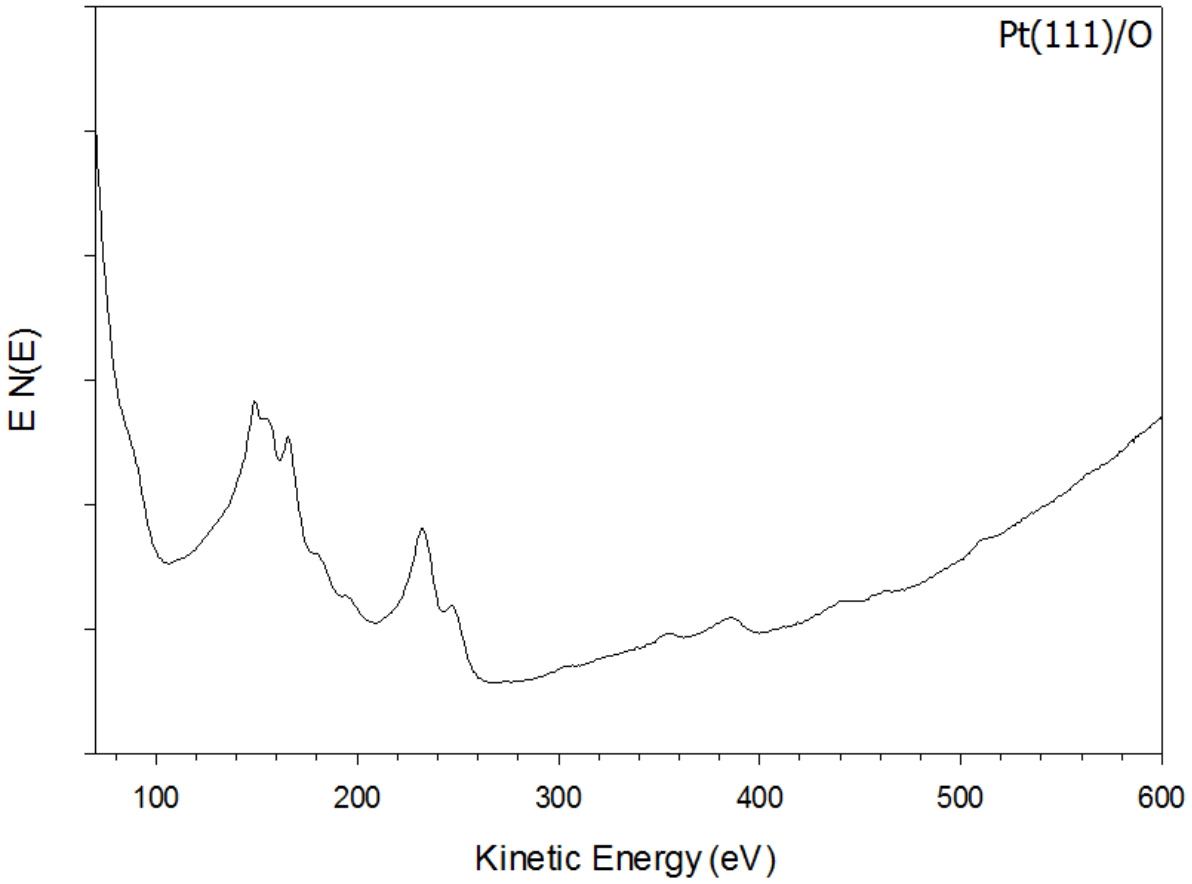

Figure D.4: Auger spectrum of oxygen on Pt(111) acquired using a 15-255 GAR double-pass CMA. The Auger peak at 510 eV is indicative of oxygen.

D.4.5 Sulfur

Many elements inhibit the reactivity of catalysts and sulfur is perhaps one of the worst. Sulfur binds quite strongly to platinum and is slightly more difficult to remove from the surface than carbon; sulfur contamination is also much more difficult to recognize from Auger spectra. The main Auger peak for sulfur (153 eV) overlaps with two platinum Auger peaks (155 eV and 163 eV); fortunately, the main sulfur Auger peak has a much greater intensity than the surrounding platinum Auger peaks. Therefore, sulfur contamination is easily identified as a significant distortion of the platinum Auger spectrum at 153 eV. Figure D.5 shows an Auger spectrum of Pt(111) contaminated with sulfur. In order to remove sulfur, elevated pressures of oxygen and extended dosing times are required. For example, for a surface temperature of 800 K, an oxygen pressure of $2*10^{-7}$ Torr and a dosing time of 30 minutes did not change the sulfur coverage at all; however, an oxygen pressure of $5*10^{-7}$ Torr and a dosing time of 2 hours completed removed the sulfur contamination.

D.4.6 Potassium

Generally, metal surface contaminants are a result of the manufacturing process of single crystals; although, potassium is not generally found as an impurity in platinum. However, at elevated temperatures, certain materials can deposit potassium, as well as other alkali atoms, onto surfaces. Potassium, like sulfur, is difficult to detect in platinum Auger spectra because one Auger peak of potassium (252 eV) overlaps with a platinum Auger peak (256 eV), and the other potassium Auger peak (276 eV) overlaps with that of carbon (275 eV). Figure D.6 shows an Auger spectrum of Pt(111) contaminated with potassium. In general, alkali atoms do not alloy

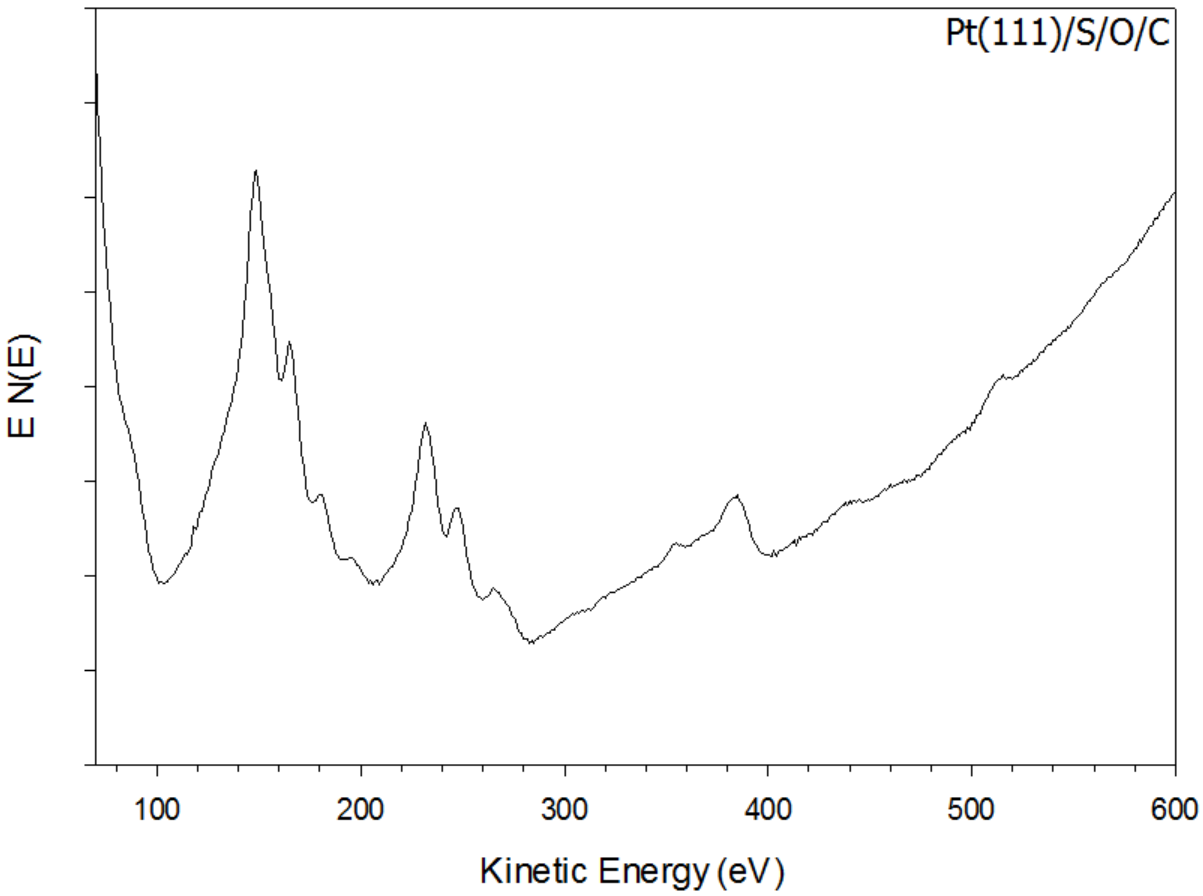

Figure D.5: Auger spectrum of sulfur, oxygen, and carbon on Pt(111) acquired using a 15-255 GAR double-pass CMA. The large Auger peak at 153 eV, that distorts the platinum peaks, is indicative of sulfur. The Auger peak at 275 eV is indicative of carbon and the Auger peak at 510 eV is indicative of oxygen.

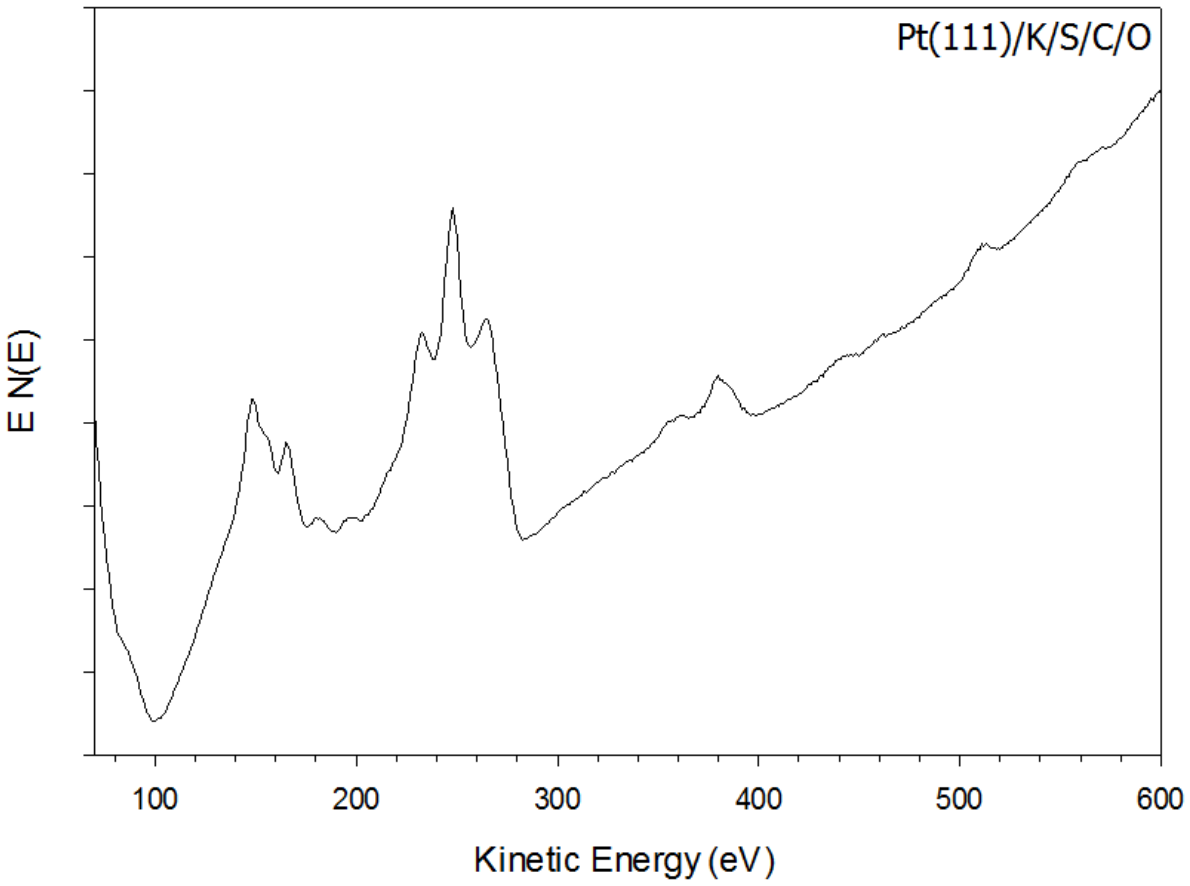

Figure D.6: Auger spectrum of potassium, sulfur, oxygen, and carbon on Pt(111) acquired using a 15-255 GAR double-pass CMA. The distortion of the platinum peak at 153 eV is indicative of sulfur. The large peak at 252 eV and the distortion of the platinum peak at 204 eV is indicative of potassium. The large peak at 275 eV is caused by both potassium and carbon. Lastly, the Auger peak at 510 eV is indicative of oxygen.

well with platinum and so, readily segregate to the surface. In addition, alkali atoms desorb from platinum at very high temperatures. Therefore, potassium can be removed from platinum by annealing the crystal at 1100 K for 5 minutes. If the potassium coverage is reduced, repeat the annealing process until the potassium is removed. If the potassium coverage has not decreased by much, sputter the surface (1000 eV, 30 minutes, T_s = 600 K) and then oxygen clean using the procedure for carbon; repeat as necessary until the potassium is removed.

D.4.7 Silicon

Silicon is a common impurity found in platinum single crystals. Silicon contamination is derived from the manufacturing process of platinum single crystals as well as silica sources that come into contact with the platinum surface. Silicon is very difficult to detect on the platinum surface because the Auger peak for silicon (96 eV) matches well with one of the Auger peaks for platinum (97 eV). However, silicon readily reacts with oxygen to produce SiO_2 on the platinum surface. Therefore, silicon contamination is indicated by the presence of an oxygen Auger peak (Figures D.4, D.5, and D.6) that remains after the crystal is flashed to 1000 K when no other impurities are present. Silicon can be removed from the surface by cycling between oxygen cleaning (10^{-7} Torr, 30 minutes, T_s = 800 K) and argon ion sputtering (1000 eV, 30 minutes, T_s = 600 K) until the silicon is removed.

Appendix Section E - Adding Gases to the Manifold

E.1 Overview

Over the course of conducting experiments, gases present on the gas manifold will be consumed and must be replenished. In addition, new gases must be added to the manifold as research progresses. Although each gas is chemically different, most gases are added to the manifold following similar procedures. The following paragraphs explain how to add gases to the manifold in a safe and efficient manner.

E.2 Precautions

Although compressed gases are relatively safe to handle, there are certain precautions that should be taken. First and foremost, compressed gas cylinders are generally at high pressure (> 1000 psi), so take care not to damage the cylinders in any way; damaged gas cylinders can potentially rupture. Additionally, before connecting gas regulators, ensure that all of the valves are closed or set to zero. This is to prevent the gases from over pressurizing the regulator or gas lines when opening the valve on the cylinder. As a side note, although most valves are right-hand threaded, generally the central control valve on a regulator is inverse; rotating the regulator valve clockwise increases gas flow.

When purchased, most gas cylinders will have an NPT plug with or without a PTFE gasket inserted into the port to act as a dust barrier as well as to prevent gas from leaking out of the tank. Before attaching the tank to a regulator, the NPT plug should be "vented" in a fume hood (this is especially important for strong oxidizers (e.g. NO) and CO). First, ensure that the valve is completely closed. Next, aim the port towards the rear of the fume hood and unscrew the NPT plug with PTFE gasket and set the plug and gasket aside on fresh aluminum foil.

Lastly, place the tank on fresh aluminum foil with the port facing to the rear of the fume hood (to prevent dust from getting into the valve). Wait 30 minutes and then retighten the NPT fitting with PTFE gasket on the tank. Now the tank can be brought to the chamber and attached to the regulator.

When choosing a regulator for a gas cylinder, ensure that the regulator is undamaged and is compatible with the gas as well as the gas cylinder. For caustic gases, ensure that the regulator is designed to handle them (generally, all steel components). In addition, do not use regulators for dissimilar types of gases; this will contaminate the incoming gas stream. In general, regulators can be used for multiple gases, provided that the gases do not easily decompose or react. For example, a regulator that is used for argon or helium can be used for other gases; a regulator used for methane can be used for ethane. However, one should not use a regulator that regulates caustic gases or oxidizers for any other type of gas. For example, a regulator that regulates the flow of NO, F_2, or Cl_2, should not be used for any other gas; a regulator used for ethylene should not be used for methane, because ethylene easily adsorbs to surfaces and is not easily removed from the regulator.

After the gas cylinder and regulator are connected to the gas manifold, but before opening the gas cylinder valve, leak check all of the connections between the gas tank, regulator, vacuum connections, and the gas manifold. This step is important for two reasons: to ensure that the gas purity remains high and to ensure that no gas leaks into the atmosphere. Although methane is relatively harmless, NO and CO are very toxic, so ensuring that the seals are airtight is extremely important. In addition, remember that all gases can displace O_2 and at high concentrations can cause asphyxiation.

E.3 Attaching a Reagent Gas Cylinder to the Manifold

Figure E.1 shows schematic of the front and back of the gas manifold. Before attaching a gas cylinder to a regulator, be sure to clear foreign contaminants from the threads of the regulator and gas cylinder. In addition, use flowing dry N_2 to clear out any dust from the regulator, gas cylinder ports, and PTFE gasket. After removing all contaminants, wrap PTFE tape around the gas cylinder threads ~1.5 times; avoid covering the first thread and ensure that the PTFE tape is wrapped in the proper direction. Next, place the PTFE gasket between the gas cylinder and the regulator ports and tighten the two together until the connection is hand-tight; do not fully tighten the regulator to the gas cylinder until the regulator is attached to the manifold. Place the gas cylinder and regulator near the connection port on the rear of the manifold, just behind the reagent variable leak valve. Secure the gas cylinder and regulator to the table such that the regulator is parallel with the table and the gas cylinder is placed upright. Now, connect the outlet of the regulator to the vacuum connection behind the reagent variable leak valve. After all of the connections have been made to the manifold, fully tighten the regulator to the gas cylinder. At this point, all of the connections between the gas cylinder, regulator, and manifold should be tightened.

After connecting the gas cylinder, close the valve at the top of the manifold that separates the manifold from the doser and close the valves that connect to the gas filter on the rear of the manifold. Now, open the valves on the regulator, but not the actual gas cylinder valve. Slowly open the reagent variable leak valve that separates the gas cylinder from the manifold and evacuate the gas, taking care to keep the manifold pressure less than 1 Torr. As the gas is evacuated, the pressure in the manifold will begin to drop; when this occurs, increase the flow rate at the reagent variable leak valve.

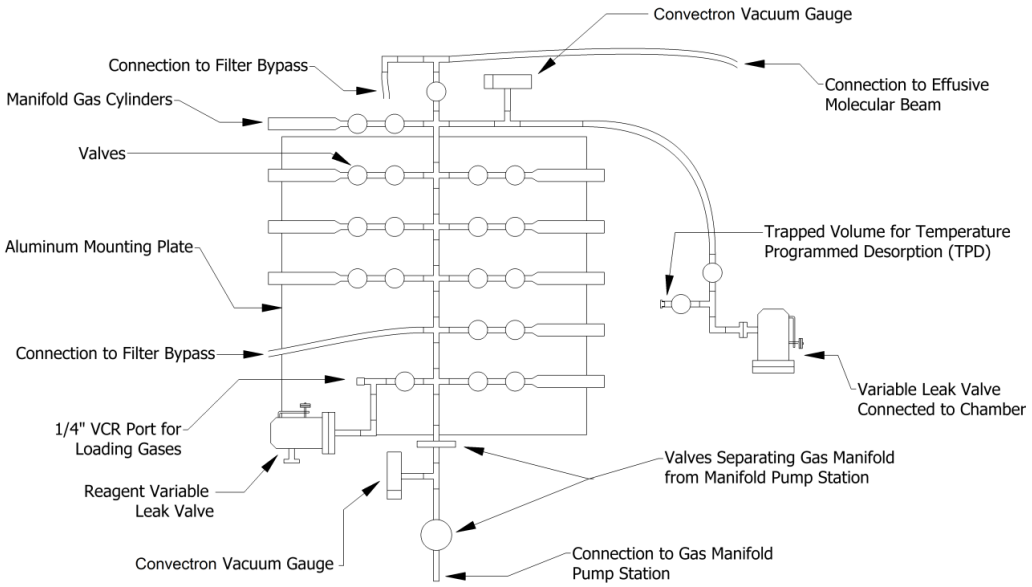

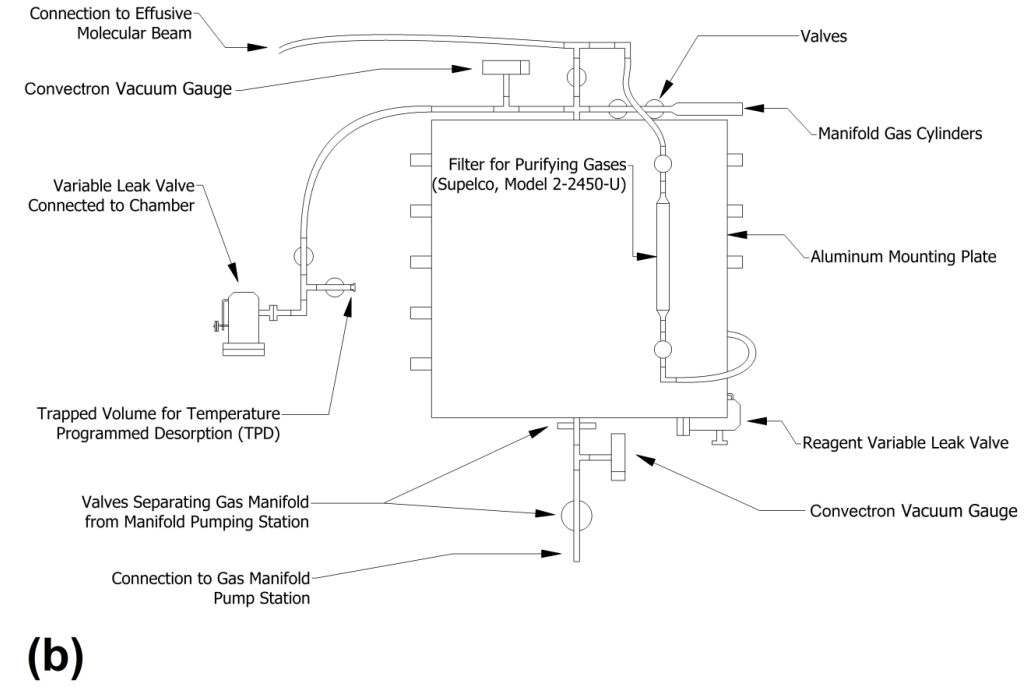

Figure E.1: Schematic representation of gas manifold front (a) and back (b).

As a side note, it should take ~30 minutes to fully evacuate the gas line and manifold. Once the volume between the gas cylinder and the manifold is fully evacuated ("0" Torr when the variable leak valve is fully opened), perform helium leak checking by closing the valve at the bottom of the manifold and slightly opening the variable leak valve on the chamber. If the pressure in the manifold holds at an elevated value, slightly tighten the connection between the gas cylinder and the regulator and then first perform a helium leak check with the manifold open to the pumping station. Tighten any connections where leaks are detected. After all connections are determined to be leak free, the reagent variable leak valve should remain open and the volume between the gas cylinder and the manifold should be evacuated overnight. As a side note, even when the gas cylinder is fully closed, gas can escape into the vacuum connections from the gas cylinder; therefore, the pressure reading of the manifold might not be a leak, but may actually be caused from the gas in the actual cylinder.

After the gas line has been fully evacuated, it can be purged with the reagent gas. First, the flow rate valve on the regulator and the reagent variable leak valve should be fully closed. The valve on the regulator positioned after the flow rate valve (if there is one), should be left open. After ensuring that no gas will flow through the regulator, slowly open the gas cylinder valve until the pressure reaches a maximum value on the inlet side of the regulator. When the inlet of the regulator is fully pressurized, close the gas cylinder valve thus leaving a portion of gas in the regulator. Slowly increase the pressure on the outlet side of the regulator until a value of 15 psi is achieved. Now, slowly open the reagent variable leak valve and evacuate the gas as previously performed.

After the trapped volume at the gas cylinder is evacuated, close the flow rate valve on the regulator and close the reagent variable leak valve. Next, slowly open the gas cylinder valve

until the maximum pressure is achieved on the inlet side of the regulator; leave the gas cylinder valve open after pressurization. Next, slowly increase the pressure on the outlet side of the regulator until a value of 15 psi is achieved. Once this pressure is attained, close the flow rate valve so that no more gas can flow, and then fully evacuate the gas on the outlet side of the regulator as previously performed. After the trapped volume is evacuated, refill the outlet side of the regulator with 15 psi (while the reagent variable leak valve is closed) and evacuate again; perform this procedure once more. After the outlet side of the regulator has been flushed three times, the gas line can be pressurized to the desired value. At this point, the valve on the gas cylinder should be open, the inlet pressure of the regulator should be identical to the cylinder pressure, the outlet pressure should be set to the desired pressure, and the reagent variable leak valve should be closed. For experiments, the gas pressure should be varied using the reagent variable leak valve. For NO cleaning, the line does not need to be flushed before flowing NO and the pressure on the outlet side of the regulator should be maintained beneath atmospheric pressure in order to limit the possibility of NO exposure.

E.4 Refilling a Manifold Gas Cylinder

When refilling a gas cylinder on the manifold, the procedures for flushing the regulator gas cylinder are the same as outlined in Appendix Section E.3; however, the regulator and gas cylinder should be connected to the VCR loading port located directly above the reagent variable leak valve on the front of the gas manifold. The valve between the VCR loading port and the manifold is first closed, and then the VCR cap is removed; the gas cylinder and regulator are connected to the manifold via the VCR loading port. The volume between the manifold and the gas cylinder is then evacuated and helium leak checked. Once no leaks are detected, the valve

between the VCR port and the manifold is closed and the manifold gas cylinder is evacuated. Afterwards, the valve between the VCR port and the manifold, and the manifold gas cylinder valves are left open and are evacuated overnight. The following day, close the flow rate valve on the regulator and close the two valves on the manifold gas cylinder. Proceed to flush the regulator as outlined in Appendix Section E.3 and then evacuate the remaining gas on the outlet side of the regulator. Once evacuated, open the two valves on the manifold gas cylinder and close all of the other valves that do not separate the manifold gas cylinder from the regulator (the regulator and gas cylinder stand alone in a closed system). Then, adjust the flow rate valve on the regulator until the desired pressure is achieved on the outlet side. At this point, the gauge on the outlet side of the regulator is equal to the pressure in the manifold gas cylinder (because the two are connected). After the manifold gas cylinder is pressurized, close the two valves on the manifold gas cylinder and close the valve on the gas cylinder connected to the regulator.

The remaining pressure in the regulator and manifold should be relatively high ($\geq$ 10 psi for the outlet side, and potentially greater than 2000 psi on the inlet side) and therefore, care should be taken when removing this residual gas. In order to remove the residual gas, first move the convectron cable from the top convectron gauge to the convectron gauge at the bottom of the manifold. If the pressure reading is less than 1 Torr (between the two bottom valves), slowly open the valve at the very bottom of the manifold and then slowly open the valve directly above it; if the reading is above 1 Torr, then partially open the bottom valve and wait until the pressure drops; then fully open the valve. As gas is evacuated from the manifold, be sure that the convectron pressure is held beneath 10^{-1} Torr. After all of the residual gas is removed (which might take upwards of a day), close the valves on the regulator and close the valve between the VCR loading port and the manifold. The regulator is then removed from the manifold and the

VCR cap is replaced. After replacing the cap, slowly open the valve between the VCR loading port and the manifold to evacuate the trapped air; allow the pumping station to pump on the manifold for at least a day before performing experiments after loading a gas. Lastly, label the manifold gas cylinder with the gas identity, gas purity, manufacturer, absolute pressure, and the fill date.

E.5 Argon

Argon is relatively safe to work with since it is non-reactive. Zero grade argon (purity 99.998%, Praxair) was added to the gas manifold following the procedure in Appendix Section E.4. However, when argon ion sputtering, argon is flowed through the Supelco filter located on the rear of the manifold.

E.6 Oxygen

Although oxygen naturally exists in the atmosphere and is relatively innocuous, at high oxygen concentrations, flammable compounds can spontaneously ignite; mixing pure oxygen and flammable compounds in a closed environment can cause an explosion. For that reason, the inlet and outlet port on the regulator and the port on the oxygen gas cylinder should be cleared of any debris or organics before using. In addition, avoid open flames near the oxygen gas cylinder (true for all cylinders). Ultra-high purity oxygen (purity 99.993%, Praxair) was added to the gas manifold following the procedure in Appendix Section E.4.

E.7 Methane, Ethane, Propane, Butane, and Pentane

The linear alkanes methane through pentane are highly combustible and so their gas cylinders should avoid open flame. Methane, ethane, propane, and butane are gases at room temperature; however, propane and butane are liquefied when present in compressed gas cylinders. Pentane is a liquid at room temperature but can be purchased in a compressed gas cylinder. At high vapor concentrations, all five of these alkanes can cause asphyxiation and all but methane can cause anesthetic-like effects (dizziness, tingling sensations, etc.). However, the concentrations required to induce such effects are quite high, and thus the biggest potential hazard is fire. Methane (purity 99.999%), ethane (purity 99.999%), propane (purity 99.999%), butane (purity 99.99%), and pentane (purity 99%) were obtained from Matheson Tri-Gas and were added to the manifold following the procedure in Appendix Section E.3. Alternatively, if purchased as a liquid, pentane can be added to the manifold via freeze-pump-thaw (FPT) as in Appendix Section E.8. Additionally, during experiments, methane was filtered using the Supelco filter (model: 2-2450-U) on the rear of the manifold. However, this filter cannot be used with the other alkanes; they will react within the filter.

E.8 Hexane

Hexane is a highly combustible liquid with a relatively high vapor pressure (~130 Torr at 20^{o}C) and can cause asphyxiation and anesthetic-like effects. In addition, hexane can be absorbed through the skin and potentially affect the nervous system. Hexane can only be purchased as a liquid in a glass vessel and not in a gas cylinder; therefore, the method of adding hexane to the gas manifold is different from all of the other gases discussed. Hexane (purity 99.7%) was purchased from Sigma-Aldrich and was purified using the freeze-pump-thaw (FPT) method. The apparatus which contains the hexane is composed of a UHV valve that has a male VCR fitting on one end, and a Pyrex tube welded to a Kovar sleeve on the other end. A depiction of the apparatus is shown in Figure E.2.

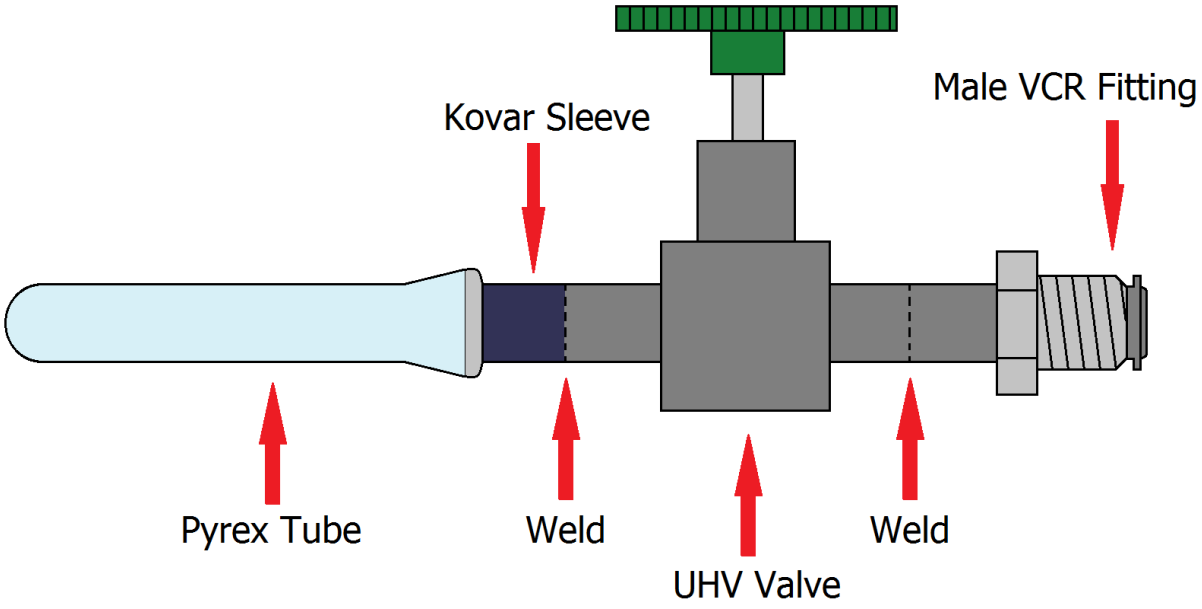

Figure E.2: Apparatus used to perform freeze-pump-thaw on liquids and also used to store liquids for use in UHV systems.

The process for loading hexane onto the manifold is as follows. First, a valve is added to the end of the vacuum connections behind the reagent variable leak valve. The apparatus is then connected to this valve and is evacuated and helium leak checked. After no leaks are detected, the apparatus is evacuated overnight. The following day, the valve on the apparatus, the secondary valve, and the reagent variable leak valve are all closed and then the apparatus is removed from the manifold. Next, the apparatus valve is opened in a clean hood and then the hexane is added to the Pyrex tube through the valve. As a side note, make sure that the volume of hexane added is less than half of the volume of the Pyrex tube; this prevents the Pyrex tube from exploding during FPT procedures. After adding the hexane, the valve is closed and then the apparatus is reattached to the manifold at the same location as before. Since the Pyrex tube is welded to the valve, only the secondary valve is opened and helium leak checked. The hexane is then purified using the FPT method with liquid nitrogen as a cooling agent.

Because oxygen can condense at liquid nitrogen temperatures, it is important to remove large quantities of oxygen from the hexane before performing FPT; mixing pure liquid oxygen and organic compounds in a closed vessel is a potentially explosive combination. To remove the majority of residual oxygen from the hexane, first open the two valves between the hexane and the variable leak valve. After opening the valves, slowly open the reagent variable leak valve until the manifold pressure is ~1 Torr (while the manifold is open to the pumping station). Over time, the pressure in the manifold will decrease as volatile atmospheric gases are removed (open the variable leak valve to maintain ~1 Torr, as necessary). Once the pressure has stabilized at ~1 Torr, the majority of volatile gases have been removed; at this point, close all three valves.

To perform FPT, first submerse the Pyrex tube and Kovar sleeve into liquid nitrogen and wait for five minutes; ensure that the liquid N_2 covers the weld between the Pyrex tube and the

Kovar sleeve. As a side note, liquid N_2 quickly evaporates, so add liquid N_2 as necessary to keep the volume constant. After five minutes, slowly open the two valves on the apparatus and then slowly open the reagent variable leak valve. The gas is then evacuated and the manifold pumping station is allowed to pump on the frozen hexane for approximately 30 minutes. While pumping on the hexane, prepare a separate container that contains tepid water. After 30 minutes have passed, close all three valves and then thaw the hexane. In order to thaw the hexane, first remove the liquid N_2 container from the Pyrex tube and then immediately replace it with the tepid water container; ensure that the water covers the weld between the Pyrex tube and the Kovar sleeve. When the hexane has completely thawed, remove the water container and wipe off the water and ensure that the Pyrex is dry (do not scratch the Pyrex). At this point, one cycle of FPT was performed. FPT is then repeated an additional three times to ensure adequate removal of all dissolved gases. During experiments, both valves on the hexane apparatus are left open and the pressure is varied using the reagent variable leak valve. After a given experiment is completed, both of the valves on the hexane apparatus are closed in addition to closing the reagent variable leak valve.

E.9 Nitric Oxide

Nitric oxide (NO) is a very toxic gas and is a much stronger oxidizing agent than oxygen. Gas concentrations above 25 ppm are considered hazardous to one's health; fortunately, the odor threshold is about 1.0 ppm. NO can severely burn the skin, lungs, and any other mucous membranes; in addition, the chronic effects of NO exposure may not be apparent until days later (burning is instant however). Therefore, great care should be taken when working with NO. NO was added to the manifold following the procedure in Appendix Section E.3.

Appendix Section F - Instrumentation Repairs

F.1 Effusive Molecular Beam Doser

As discussed in Section 2.4, the effusive molecular beam doser was completely redesigned. This section discusses the procedures for constructing the actual effusive beam nozzle. Schematics of the effusive beam flange and the effusive molecular beam nozzle are shown in Figures F.1 and F.2 respectively. As a side note, although it is possible to construct the doser with one person, it is much easier with two people.

Before attempting to construct the doser, have UHV cleaned tools (Appendix Section B.2.2) and a spot-welder with UHV cleaned welding tips (Appendix Section B.2.2) prepared. In addition, have the following on hand: UHV cleaned alumina (Appendix Section B.2.2), tungsten wire, paraffin film, latex gloves, a 316 stainless steel gasket (1/4" VCR), Be/Cu inline barrel connectors, OFHC copper rods (~0.250" in diameter), 316 stainless steel barrel connectors (for 0.250" rods), and alumel and chromel thermocouple wire.

Mount the flange near a clean hood with the UHV side pointing straight up. Attach the stainless steel doser to the effusive beam flange using a 316 stainless steel gasket and attach a thermocouple feedthrough flange on the 1.33" port as well. Connect OFHC copper rods to the electrical feedthroughs using the Be/Cu connectors; the OFHC copper rods should be long enough so that they terminate at the ends of the alumina doser pieces. Once the rods are installed, place a 316 stainless steel barrel connector on the end of each of the OFHC copper rods at the rough location of the alumina pieces' ends. Lastly, spot-weld a small piece of tungsten wire on the doser that is roughly 6.1 inches from the front of the doser (the alumina is ~6 inches long). The doser assembly can now be constructed.

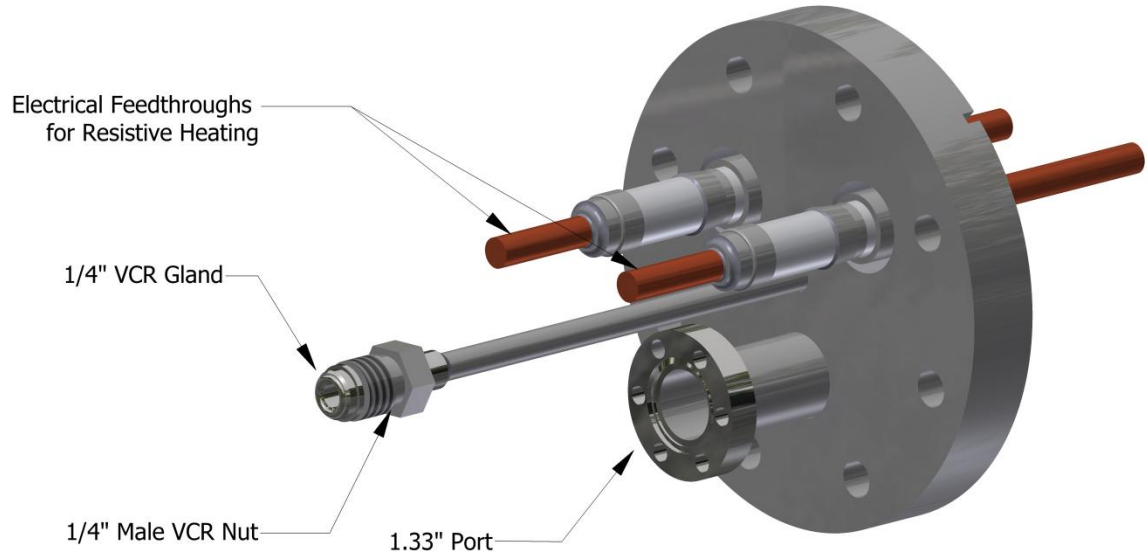

(a)

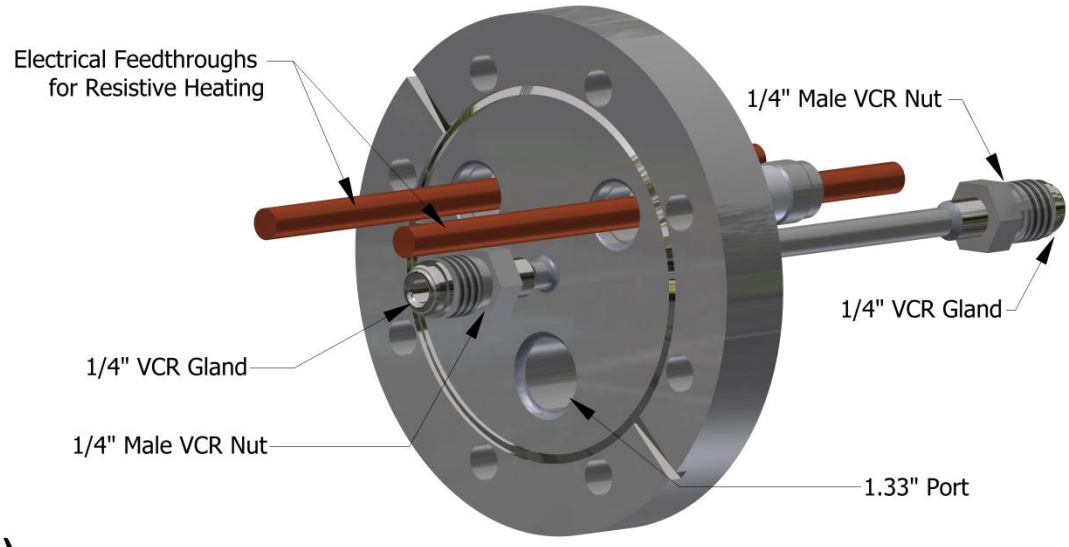

(b)

Figure F.1: Schematic representation of effusive beam flange from the atmosphere side (a), and the UHV side (b).

Figure F.2: Schematic representation of the effusive molecular beam nozzle. From top to bottom: nozzle, with inner alumina tube, with tungsten filament, with outer alumina tube.

Inset: Close-up of doser front.

First, wrap tungsten wire around the threaded alumina piece, taking care to place the wire within the grooves and leaving ~5 inches of free wire at both ends of the alumina. As a side note, tungsten wire is very stiff and has spring-like characteristics; therefore, hold the wire tightly when wrapping the alumina. In addition, do not kink the wire; otherwise, the wire could potentially snap when heated. If wrapping the wire becomes difficult, tightly wrap paraffin film over the already wrapped threads, and continue wrapping. When the wire has reached the top of the alumina piece, wrap the end tightly in paraffin film, ensuring that the last few threads are not covered.

Once the alumina is fully wrapped in tungsten wire, slip the alumina sleeve over the stainless steel nozzle down to the small piece of spot-welded tungsten wire. Take the wire at the top of the alumina, and rewrap any wire that has slipped off of the end; then, hold the last coil of wire in place on the top of the alumina. Pull the piece of wire, that is hanging off of the alumina, over to the stainless steel connector. Ensure that the wire between the alumina and steel connector is relatively taut, and then spot-weld the wire to the connector. Once the top wire is secured, remove the paraffin film from the base of the doser while making sure that the wire does not unravel. Make the bottom wire taut and then spot-weld it to the bottom steel connector. At this point, both the top and bottom of the ceramic should be wrapped relatively tightly in tungsten wire that is spotted to steel connecters on the copper rods. Now, remove the paraffin film from the entirety of the alumina and then spot-weld a alumel/chromel thermocouple to front of the doser. As a side note, weld the thermocouple onto the tube edge as to not damage the front face of the doser.

The purpose of the next procedure is to anneal the tungsten filament allowing it to hold its coiled shape. Take the completed doser (sans outer ceramic) and place it on a preparation

chamber. Start the chamber and ensure that the chamber pressure is less than 10^{-7} Torr, and that there are no leaks present. Connect a temperature controller to the thermocouple feedthrough and also connect a variable transformer (standard 120 VAC) to the electrical feedthroughs. Heat the doser to 5% of the total voltage and wait two hours. After two hours, increase the voltage by 5% and wait an additional hour. Continue increasing the voltage is this manner until the doser filament is orange in color. When the doser filament is at this point, stop increasing the voltage; maintain this voltage for one day. After one day has passed, slowly cool the filament by decreasing the voltage by 5% every 30 minutes. After the filament has cooled to room temperature, vent the chamber and then remove the doser and place it back in the clean hood.

Once in the clean hood, gently remove the top filament wire from the stainless steel connector and remove the thermocouple as well; if the filament wire breaks at the connector, that is fine. At the top of the doser, gently and slowly bend the tungsten wire such that ~ 2 inches of the wire points vertically. As a side note, if there is not enough wire at the top of the alumina, simply break the bottom weld and slowly rotate the wire towards the top and then carefully unwind the wire so it does not break (it is somewhat brittle). Adjust the ceramic so that the ends of the ceramic and nozzle are even; if need be, break off the small piece of tungsten at the base of the doser. After adjusting the threaded alumina, spot-weld the bottom tungsten filament back onto the steel connector. Next, slide the outer alumina piece onto the doser and ensure that the top portion of the filament can go through the center and out the top of the outer alumina piece. If the outer alumina piece is longer than the front of the doser, use a rotary tool to cut the alumina to the proper length. Once the outer alumina sleeve has been placed on the doser, gently bend the top portion of the filament towards the steel connector and spot-weld it.

Lastly, place a thermocouple wire on the front of the doser and one at the rear of the doser (near the ceramic).

At this point, the entirety of the doser should be fully assembled. However, the effusive beam doser is not yet ready to be loaded onto a UHV chamber. Take the fully assembled doser and load it back onto the preparation chamber; start the chamber and ensure that the pressure is less than 10^{-7} Torr and that no leaks are present. Bake out the chamber as outlined in Appendix Section B.7. After the chamber is cooled, but still wrapped in foil, connect a temperature controller to the doser thermocouple and connect a variable transformer (standard 120 VAC) to the electrical feedthroughs. Heat the doser to 5% of the total voltage and wait two hours. After two hours, increase the voltage by 5% every hour until the doser is at a temperature of 1100 K. When the doser temperature is 1100 K, stop increasing the voltage and hold the doser at this temperature for two days. After two days, reduce the voltage in 5% increments every 30 minutes until the doser temperature is 400 K. Once at 400 K, clean the doser using NO (Appendix Section B.8.4). After the NO cleaning is complete, heat the doser to 1000 K (5%/hr) and hold the doser at this temperature for two days; this process removes residual NO and trapped gases from the alumina bulk. After two days, reduce the voltage in 5% increments every 30 minutes until the doser and chamber are at room temperature; once cooled, vent the chamber. The doser is now ready to be loaded onto a UHV chamber.

F.2 15-255 GAR Double-Pass Cylindrical Mirror Analyzer Repair

F.2.1 Introduction

The 15-255 GAR double-pass cylindrical mirror analyzer (CMA), is generally used for Auger electron spectroscopy. During the course of our work, the Auger system failed at one time and would no longer produce Auger spectra. Although this section does not explain how to fix all issues with the analyzer, it does explain the steps required to disassemble and shim the analyzer.

The analyzer is composed of several different components as depicted in Figure F.3. The outermost layer of the analyzer is a stainless steel magnetic shield. When the magnetic shield is removed, there is conical shield, supported by four posts, that sits at the top of the analyzer. Underneath of the conical shield is a series of ceramic resistors and OFHC copper cylinders. There are two copper cylinders within the analyzer, and each cylinder is composed of two shorter sections that mate with each other. The outer cylinder (OC) and the inner cylinder (IC) are separated by a series of three ceramic resistors. There is one conical ceramic resistor at the very top of the analyzer, one disk-shaped resistor in the middle, and one disk-shaped resistor at the base. When a potential is applied to the OC and IC , the cylinders and the ceramic resistors work in unison to create an electric field that guides electrons to the electron multiplier. Underneath of the cylinders and ceramics are the electron gun, the electron multiplier, and the rotary motion controls. The electron gun has a filament used to generate an electron beam, and the electron beam can be biased in order to raster the beam.

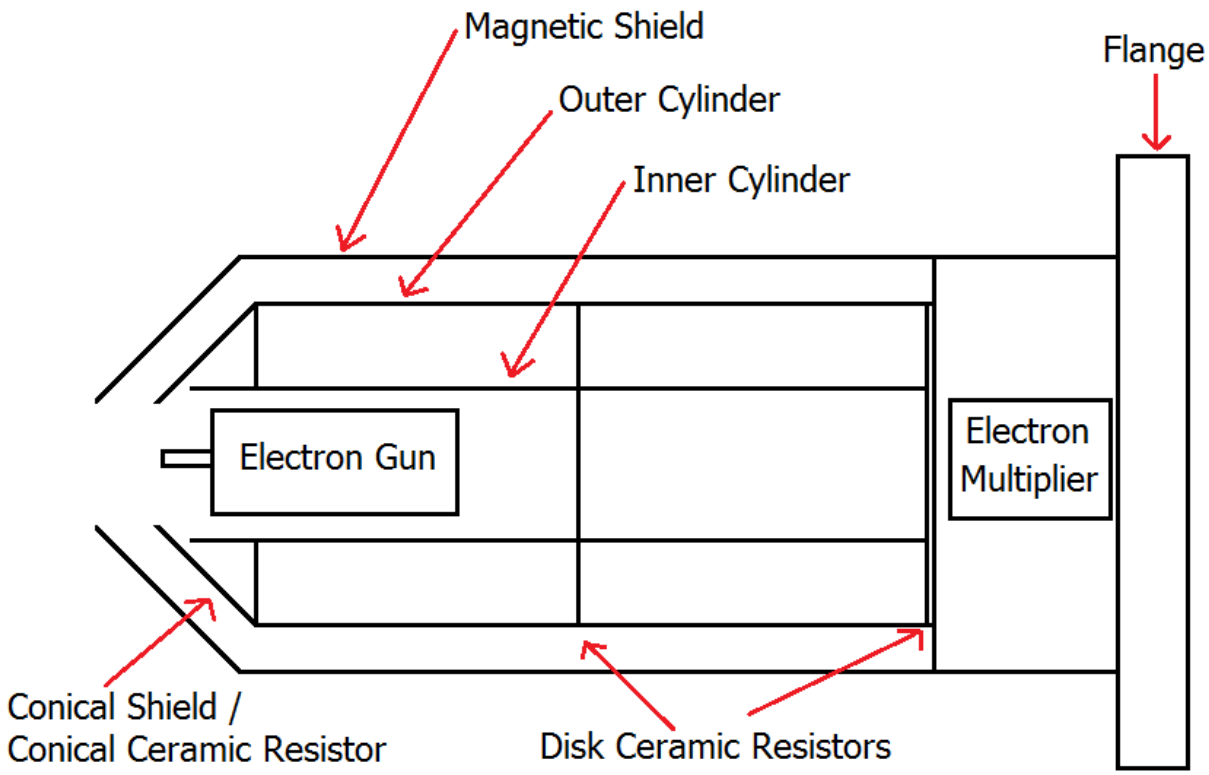

Figure F.3: Schematic representation of the 15-255 GAR double-pass CMA.

F.2.2 Troubleshooting

When the Auger system fails, first turn off the entire Auger system and then remove all of the cables that are connected to the 15-255 GAR flange. Take a voltmeter and measure the resistance on all of the connections and check the values against Table F.1. If any of the connections are measuring a resistance and should actually be open, then the components are touching each other. If the resistance measured between the OC and IC is larger than 800 kΩ then the internal ceramic resistors are most likely not making proper contact with the either the OC, the IC, or both and must be shimmed (Appendix Section F.2.4). If the resistance between the OC and IC is lower than 600 kΩ, then there is a short between the IC and OC. For the multiplier, if the resistance is low, then the multiplier is shorted out. However, if the multiplier resistance is much larger than 200 MΩ, call the manufacturer. V1 and V2 are used to raster the beam and should not interfere with producing Auger spectra. Lastly, if the filament resistance is much higher than 1Ω or if the circuit is open, then the filament most likely burned out.

Connection	(IC)	(OC)	(+)	(-)	(V1)	(V2)	(F1)	(F2)	(GND)
Inner Cylinder (IC)	-----	600 kΩ -800 kΩ	Open	Open	Open	Open	Open	Open	Open
Outer Cylinder (OC)	-----	-----	Open	Open	Open	Open	Open	Open	Open
+ Electron Multiplier (+)	-----	-----	-----	> 100 MΩ	Open	Open	Open	Open	Open
- Electron Multiplier (-)	-----	-----	-----	-----	Open	Open	Open	Open	Open
Beam Bias 1 (V1)	-----	-----	-----	-----	-----	Open	Open	Open	Open
Beam Bias 2 (V2)	-----	-----	-----	-----	-----	-----	Open	Open	Open
Filament (+) (F1)	-----	-----	-----	-----	-----	-----	-----	~1 Ω	Open
Filament (-) (F2)	-----	-----	-----	-----	-----	-----	-----	-----	Open
Ground (GND)	-----	-----	-----	-----	-----	-----	-----	-----	-----

Table F.1: List of nominal resistances across connections on the 15-255 GAR flange.

F.2.3 Dismantling

In order to repair the 15-255 GAR double-pass CMA, first vent the chamber and then remove the analyzer and mount it in the clean hood (this will most likely require two or more people). As a side note, the ceramic resistors are delicate and the gold leaf on the inner and outer edges can be damaged easily; in addition, the resistors and inner and outer cylinders are all machined to extremely tight tolerances so do not force them together or apart. To dismantle the 15-255 GAR double-pass CMA, first remove the magnetic shield from the analyzer and then remove the conical shield and the four support rods. Next, remove the conical ceramic from the top of the analyzer. Afterwards, remove the top portion of the outer cylinder and make sure that the ceramic resistor in the middle does not move. After removing the first half of the outer cylinder, remove the lower half of the outer cylinder.

Now that the outer cylinder has been completely removed, the inner cylinders can be removed next. Remove the top inner cylinder and be sure that the middle ceramic disk is left behind. As a side note, the electron gun is housed in this section so tolerances are very tight. Therefore, lift the cylinder with even pressure; if the cylinder becomes lodged, push the cylinder back down slightly, readjust, and then try lifting again. Also, do not damage the screens on the inner cylinders. At this point, electron gun maintenance can be completed. To continue dismantling the analyzer, gently remove the middle ceramic resistor. At this point, the analyzer can be shimmed (Appendix Section F.2.4). Finish dismantling the analyzer by removing the bottom inner cylinder, and then removing the final ceramic resistor.

The analyzer is reassembled by following the reverse procedure with one extra step; the analyzer must first be de-gaussed, in order to remove any stray magnetic field, before replacing the magnetic shield on the analyzer. In order to de-gauss the analyzer, first take the de-gaussing

ring and turn it on at least 5 feet away from the analyzer. Next, move the ring back and forth over the analyzer several times (be careful not to touch the analyzer) and then remove the ring. Lastly, move the ring at least 5 feet away from the analyzer, and then turn the ring off.

F.2.4 Shimming

If the resistances are not correct for the IC and OC, then the electric field will be distorted and electrons will not reach the electron multiplier. The increased resistance is caused by poor electrical contact between the ceramic resistors and the OC or IC, or both. In order to increase contact between the cylinders and the resistors, small pieces of copper foil (0.002" to 0.020"), known as shims, are placed between the cylinders and resistors. As a side note, if the pieces of the analyzer fit together much more tightly while shimming, reduce the thickness of the shims or the number of shims.

Once the analyzer has been dismantled to the point where only the bottom inner cylinder and ceramic resistor remain (Figure F.4), the analyzer can be shimmed; when shimming, be sure that the pieces of copper foil are flush and not hanging out in the open. First, lift the bottom inner cylinder high enough to clear the bottom ceramic resistor. Place two to four thin pieces of copper foil between the base of the inner cylinder and the resistor as indicated in Figure F.4; be sure that pieces are evenly distributed around the base. Next, gently push the inner cylinder back into place. Now, evenly distribute two to four copper shims on top of the outer ring of the bottom ceramic resistor and place two to four partially folded copper shims evenly around the top edge of the bottom inner cylinder (Figure F.4). After the shims are placed, set the lower half of the outer cylinder onto the bottom ceramic resistor.

In order to shim the middle ceramic resistor, place two to four partially folded copper shims evenly around the top edge of the bottom outer cylinder and then replace the middle ceramic resistor (the inner cylinder was shimmed in the previous paragraph). Next, slide the top inner cylinder back onto the analyzer into the middle ceramic resistor. Finally, replace the top outer cylinder.

The last location that requires shimming is the top conical ceramic. First, evenly distribute two to four copper shims around the top of the top inner cylinder as indicated in Figure F.5. Then, evenly place two to four partially folded copper shims around the top of the top outer cylinder as indicated in Figure F.6. Next, slip the conical ceramic resistor over the tops of both the inner cylinder and the outer cylinder. Be sure that the copper shims around the inner cylinder are pushed against the ceramic and inner cylinder so that the copper does not touch the conical shield. The analyzer is now fully shimmed. Check the resistance across the OC and IC to be sure that the shims have been installed correctly.

F.3 Dismantling the Manipulator

In order to remove the manipulator from the chamber, first remove all of the connections to the manipulator and remove the z-axis control handle as well. In addition, change the crystal position so that the crystal is facing straight up and ensure that it will not strike the chamber when the manipulator is removed. Set up two jacks on a cart and place the manipulator holder on top of the jacks; then, place this setup beneath the manipulator as shown in Figure F.7. Unbolt the manipulator from the UHV chamber and move the cart away from chamber; adjust the jacks as the cart is being removed so that neither the bolts nor the crystal strike the chamber. Figure F.8 is an image of the crystal mount on the manipulator.

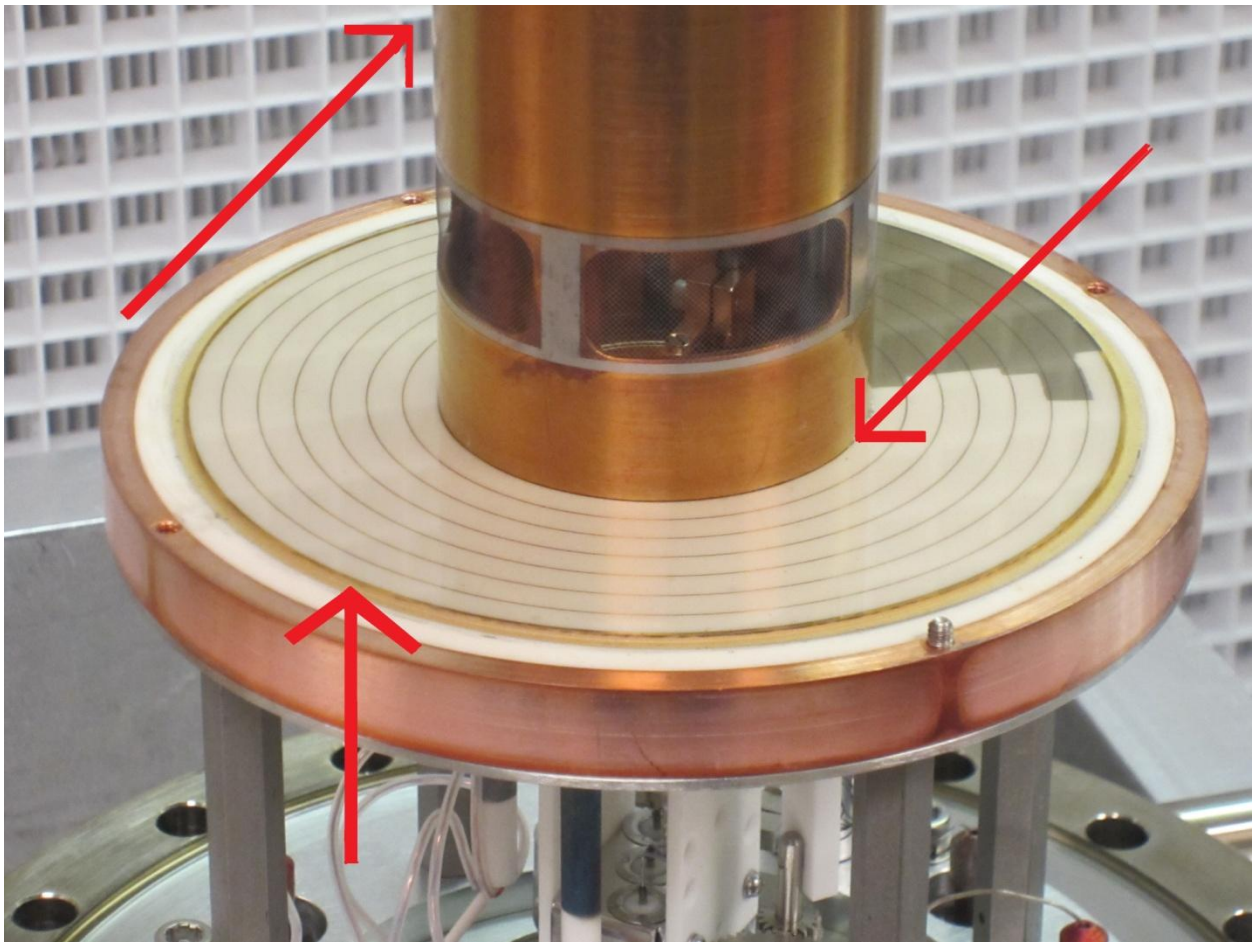

Figure F.4: Close-up view of the base of the 15-255 GAR double-pass CMA that shows the bottom ceramic disk resistor and bottom inner cylinder. The red arrows indicate the locations where copper foil should be placed for proper shimming.

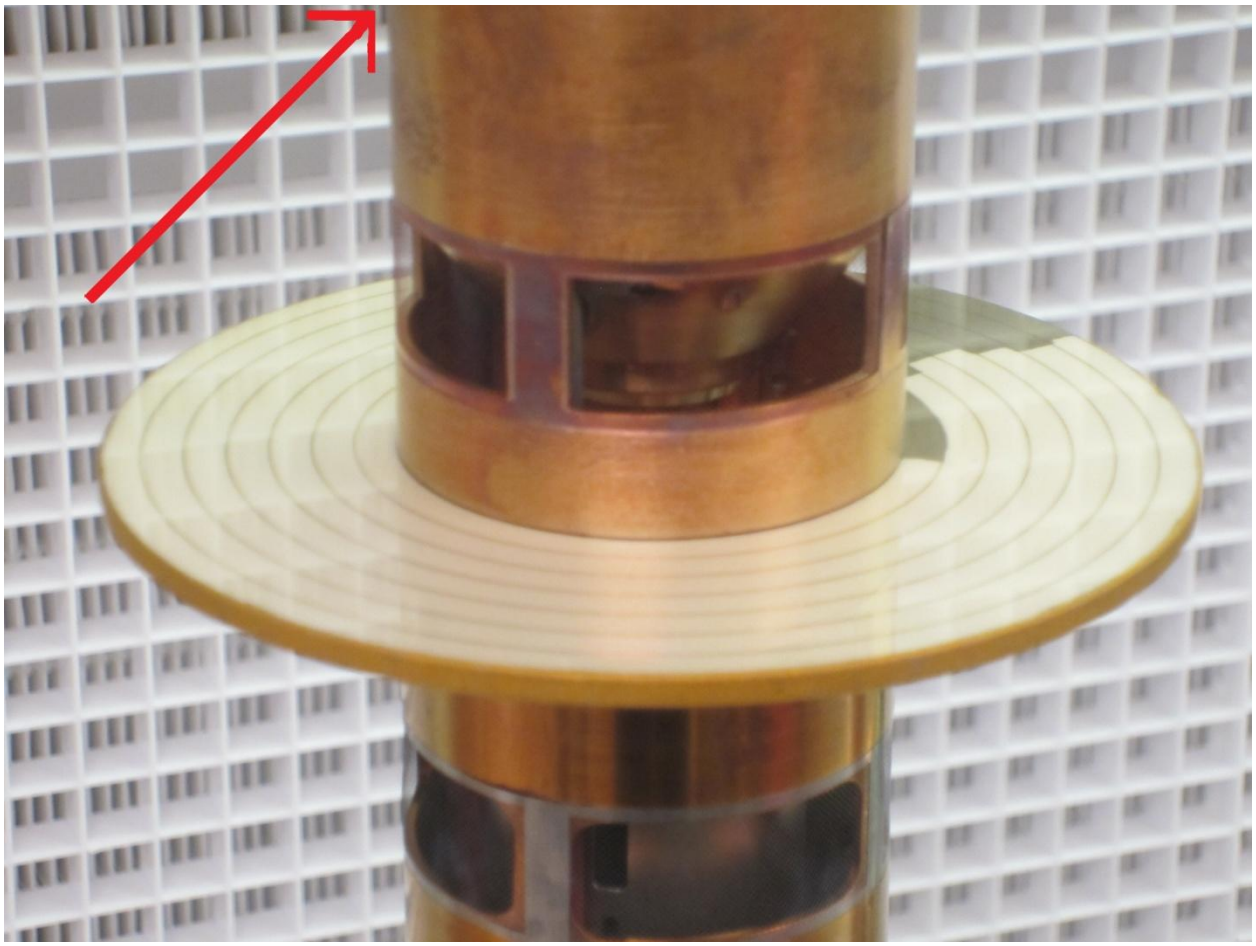

Figure F.5: Close-up view of the middle section of the 15-255 GAR double-pass CMA that shows the middle ceramic disk resistor and both inner cylinders. The red arrow indicates the location where copper foil should be placed for proper shimming.

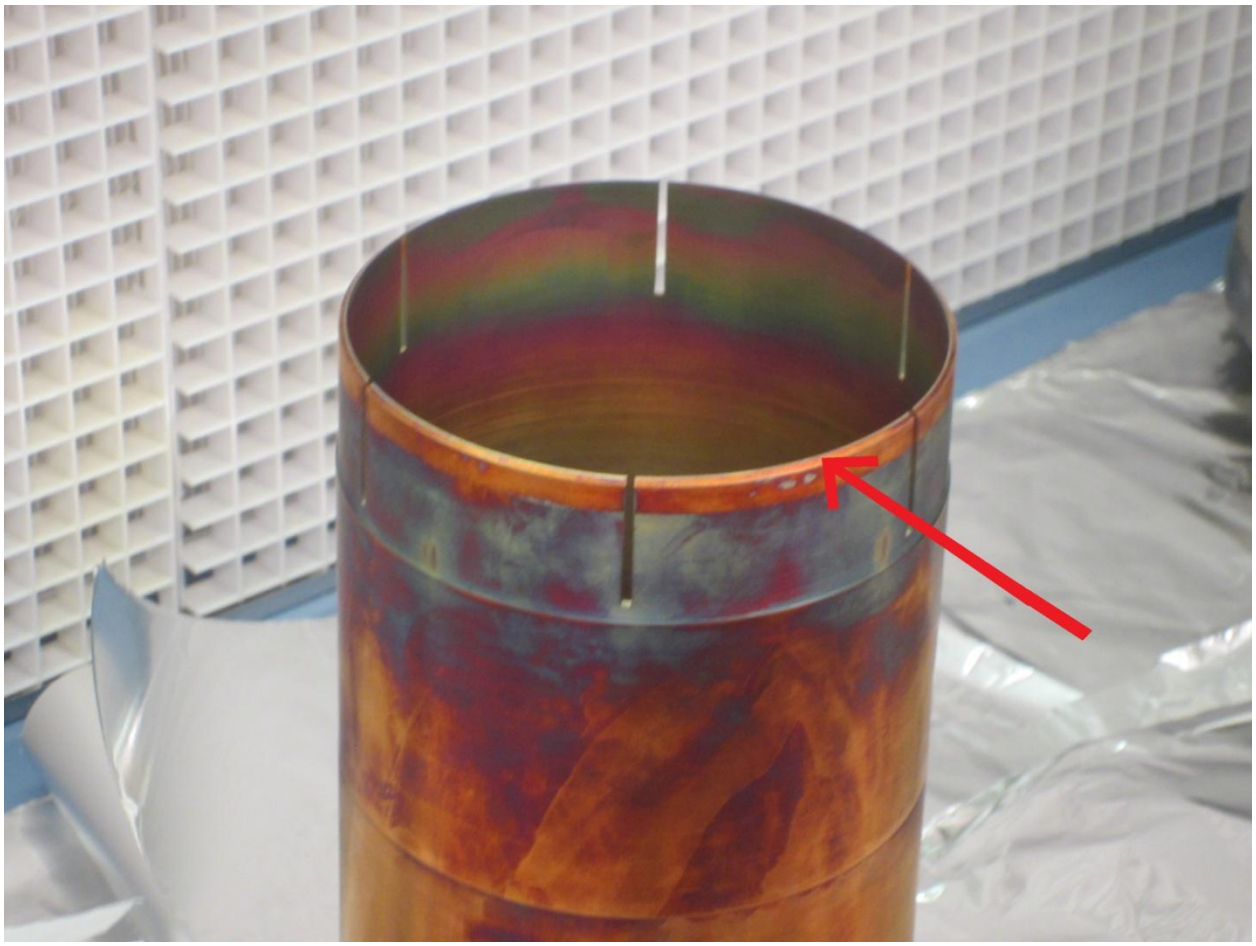

Figure F.6: Close-up view of the outer cylinder of the 15-255 GAR double-pass CMA. The red arrow indicates the location where copper foil should be placed for proper shimming.

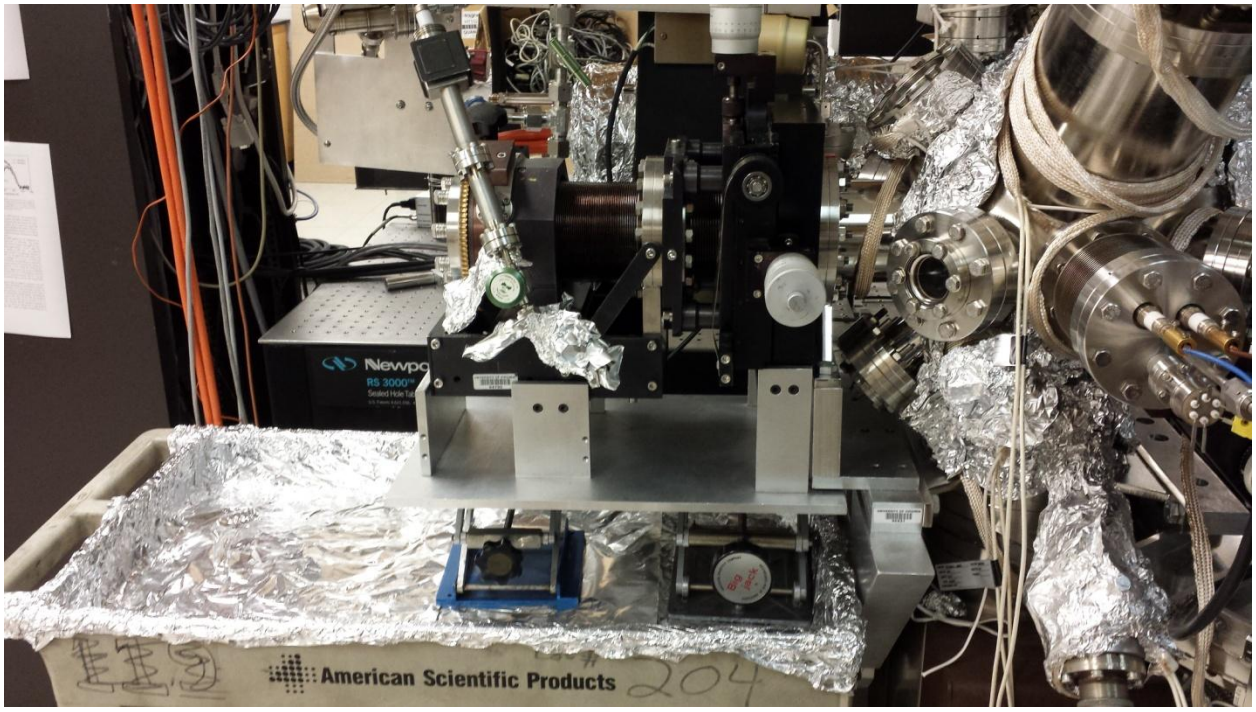

Figure F.7: Front chamber view that shows the proper orientation of the jacks, manipulator mount, and cart for removal of the manipulator.

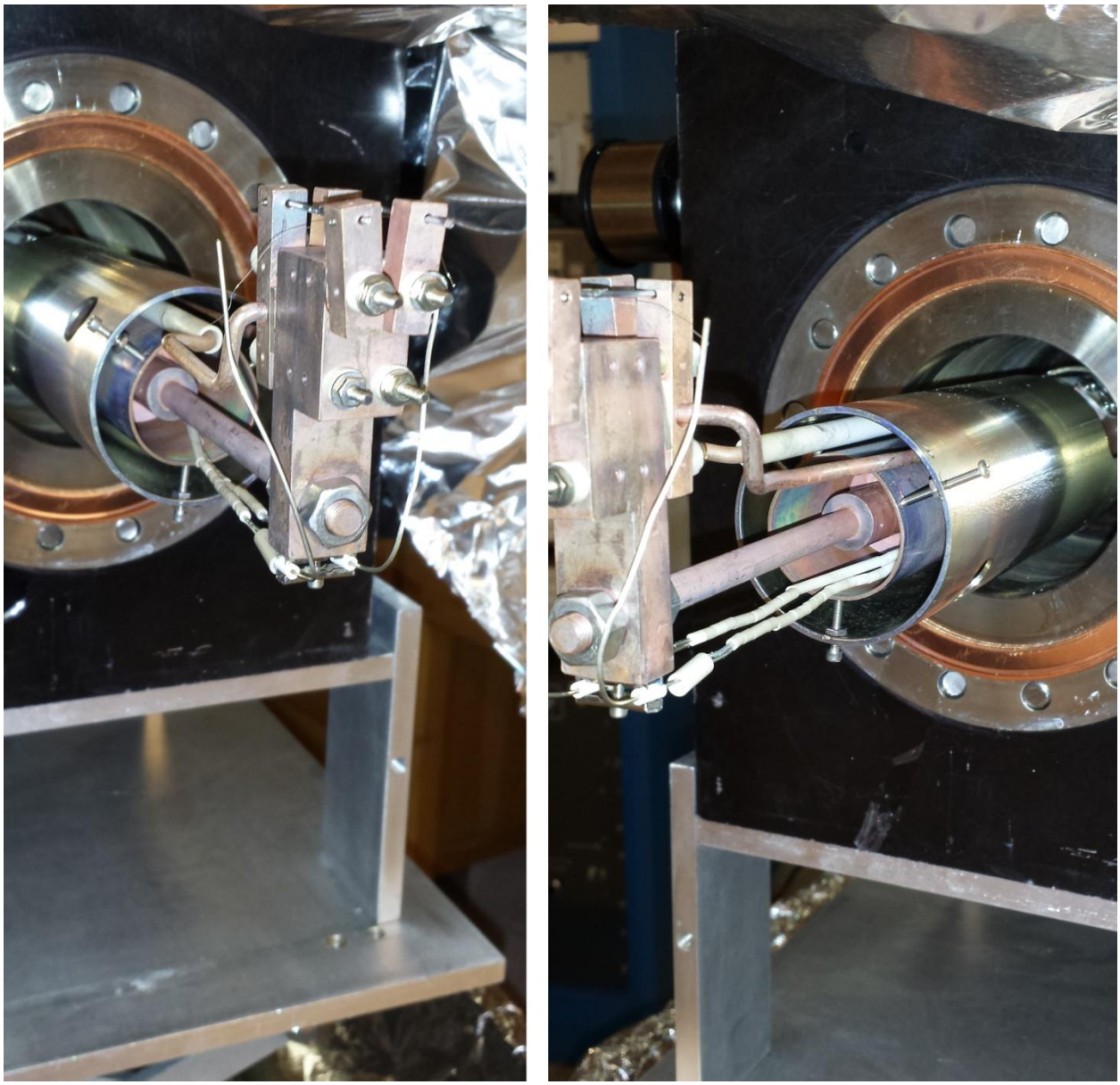

Figure F.8: Close-up side views of the crystal mount attached to the manipulator. The stainless steel shroud helps support the mount.

Once the manipulator is removed from the chamber, tent the mount as shown in Figure F.9 and move the manipulator to a clean hood. As an important note, it is imperative that nothing touches the crystal.

In order to remove the crystal mount, first break the thin thermocouple wires off of the thick thermocouple wires and also remove the stainless steel piece from the bottom of the crystal mount. Next, disconnect the copper heating leads from the crystal. After the heating and thermocouples leads are disconnected, bend all of the leads away from the crystal mount taking care not to break any material inside of the manipulator (Figure F.10). Make sure to bend the leads far enough away from the mount so that it can spin freely. Lastly, remove the nut from the central copper rod and unscrew the entire mount and set the mount aside (Figure F.11); do not allow anything to touch the crystal face.

Continue dismantling the manipulator by first bending the heating and thermocouple leads straight (after removing the crystal mount). Next, tape the feedthrough and shroud flanges together at the rear of the manipulator and then unbolt and remove both pieces as one unit. Then, place the two flanges in a clean hood as shown in Figure F.12. Remove the three screws from the shroud flange that support the heat exchanger at the end of the manipulator. With the help of another person, remove the tape from the two flanges and separate the feedthrough flange from the shroud flange as shown in Figure F.13. At this point, any repairs can be made to the rotary flange or to the components on the feedthrough flange.

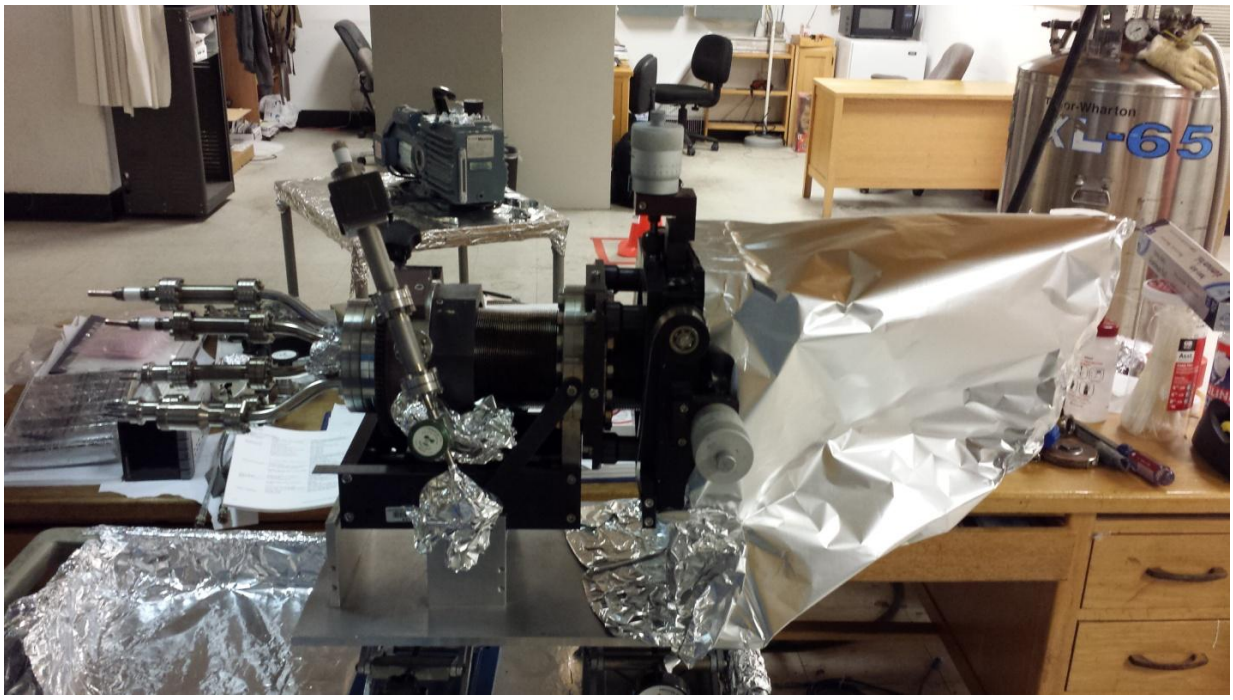

Figure F.9: Proper tenting of the crystal mount and manipulator. The foil does not touch any UHV component, and all edges of the foil are crimped and sealed.

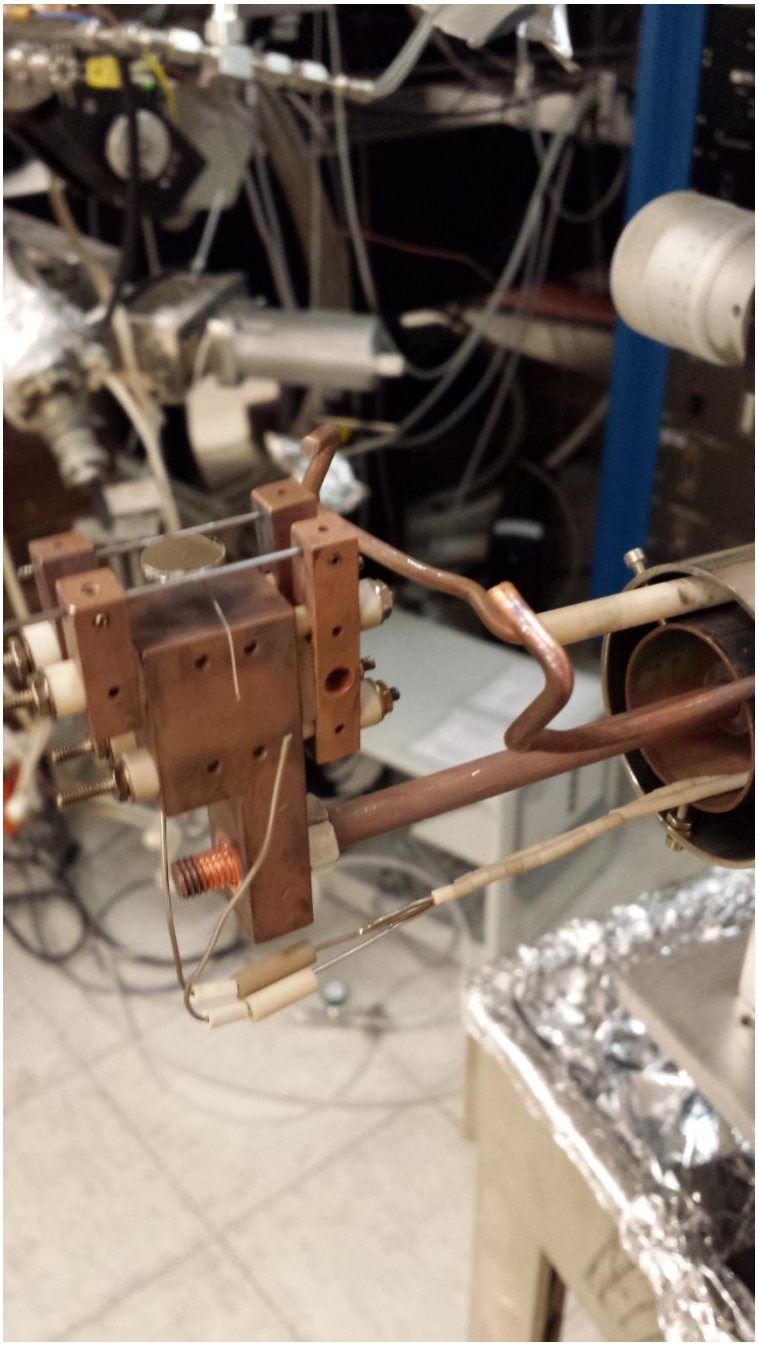

Figure F.10: Close-up view of the crystal mount attached to the manipulator. The power leads (copper) and thick thermocouple leads (near the base) are bent away from the crystal mount to aid in removing the mount from the manipulator. Additionally, the front nut has been removed from the central copper rod so that the mount can be unscrewed.

Figure F.11: Close-up view of the end of the manipulator. The crystal mount has been removed from the central copper rod. The power leads (copper) and thick thermocouple leads are bent away from the central copper rod to aid in removing and replacing the mount.

Figure F.12: Image of manipulator flange and shroud flange in a clean hood. The two are taped together at the base to allow for ease of removal from the manipulator.

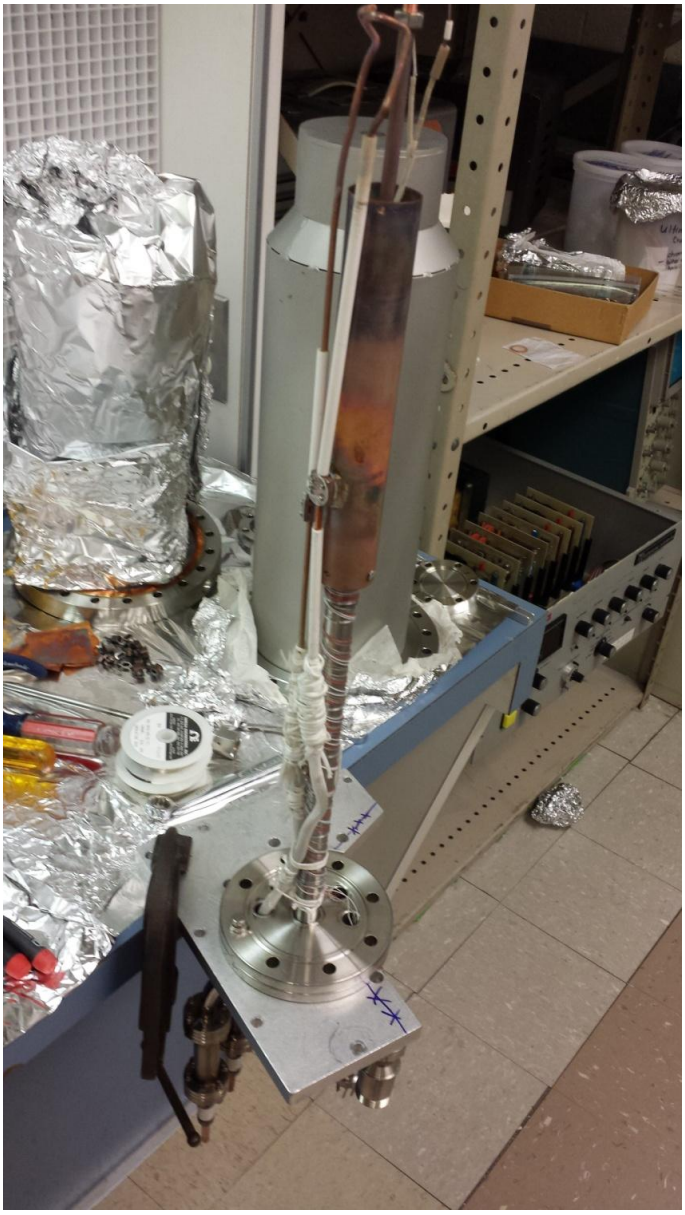

Figure F.13: Image of the manipulator flange (sans shroud flange) placed in the clean hood.

F.4 DPRF 450 Rotary Flange Repair

F.4.1 Introduction

The DPRF 450 is a twice differentially pumped rotary flange produced by McAllister Technical Services and is designed to maintain UHV conditions while rotating a sample or instrument. The DPRF 450 maintains these conditions by using a series of Viton gaskets and ports to allow for differential pumping. Over time, the seals wear down and need to be replaced; this appendix section discusses how to change the gaskets and how to clean the DPRF 450. During the repair of the DPRF 450, do not allow any material (fibers, dust, MoS_2 grease, etc.) to fall into the manipulator or bellows. In addition, make a note of the orientation of the components so that the DPRF 450 can be properly reassembled; when reassembling the DPRF 450, do not overly tighten the bolts. Lastly, the DPRF 450 is machined to extremely tight tolerances, so make sure that even pressure is applied when removing or replacing components.

F.4.2 Disassembly

After removing the manipulator (Appendix Section F.3) place a 4.5" ConFlat flange on the DPRF 450 port, remove the handle and worm drive, and remove the angle indicator as indicated in Figure F.14. Afterwards, place the manipulator on fresh aluminum foil in the clean hood with the DPRF 450 oriented straight up. In order to dissemble the DPRF 450, first remove the dial face (Figure F.15), and then remove the brass gear (Figure F.16); do not allow the gear to touch other components, because the gear is coated with MoS_2 grease. After the gear is removed, remove the gear support ring as shown in Figure F.17; again, do not allow the MoS_2 grease to touch other components. After removing the gear support ring, remove the cover ring that is above the bearing retainer ring (Figure F.18); note that there is a gasket inside of the cover

ring. This gasket is used to prevent dust from entering the rotary flange components. At this point, the bearing and bearing retainer ring can be removed as one piece (Figure F.19); both components are covered in MoS_2 grease, so do not allow the components to touch anything else. As a side note, after the bearing and retainer ring are removed, the outer rotary flange can slide freely. However, do not move the flange around because doing so could potentially contaminate the differentially pumped regions that are separated by the Viton o-rings. After the bearing retainer and bearing have been removed, the outer Viton o-ring should be clearly visible as shown in Figure F.20. Remove the outer rotary flange by lifting it directly upwards while leaving the o-rings behind on the DPRF. The Viton o-rings and o-ring retainer rings should be visible after removing the flange as shown in Figure F.21. Remove the o-rings and retainer rings one by one starting from the outer most ring; do not scratch the bottom face of the DPRF and do not allow the o-rings or retainer rings to touch the UHV portion of the DPRF. As a side note, the outermost o-ring is the most contaminated component amongst the o-rings and retainer rings; the innermost o-ring retainer is the cleanest. Therefore, clean the tools used to remove the o-rings and retainers before removing the innermost o-ring retainer. The base of the DPRF has several small holes to hold the retainer rings and two large holes for differential pumping (Figure F.22)

F.4.3 Cleaning and Preparation

Cleaning the DPRF 450 requires many steps to complete. First, wipe down the base of the DPRF (Figure F.22) using delicate task wipes and acetone; do not scrub the surface and do not allow fibers to fall into the flange or into the differential pumping ports. In addition, use different delicate task wipes to clean the outer, middle, and inner regions of the base. Thoroughly scrub the o-ring retainer rings using methanol and a soft bristle tooth brush and then sonicate the retainers (Appendix Section B.2.2). As a side note, do not sonicate the retainer rings in the same

vessel; otherwise, the retainer rings may contaminate each other (the rings have different levels of cleanliness). To clean the outer rotary flange, flip the flange over and clean it following the same procedure used to clean the base of the DPRF 450 (Figure F.23). Additionally, the outer faces of the base and outer rotary flange can be wiped down using acetone and delicate task wipes (Figure F.24).

In order to clean the bearing and bearing retainer, first remove the bearing by evenly tapping it out of the bearing retainer as depicted in Figure F.25; make a note of the bearing orientation. After the bearing and retainer are separated, clean the entire bearing retainer using delicate task wipes and acetone. In order to clean and prepare the bearing (Figure F.26), first rotate the bearing back forth and wipe away any dried MoS_2 grease while wearing a glove. After the dried grease is removed, use delicate task wipes and acetone to wipe away MoS_2 grease that is on the inner and outer stainless steel rings; do not wipe the top nor the bottom of the bearing nor pour solvents on the bearing. Set the bearing aside after wiping it down.

Now, clean the cover ring by first removing the Viton gasket and then wiping out the groove using delicate task wipes and acetone (Figure F.27). Clean the gear support ring by using acetone and delicate task wipes to remove grease from the face. Remove excess grease from the gear using delicate tasks wipe but do not use solvents. If the gear teeth are excessively worn, replace the gear or rotate the gear when reassembling the rotary flange. The front dial should be wiped down with acetone and delicate task wipes. For the handle and worm gear, wipe all of the grease off of the worm gear using delicate task wipes (do not use solvents) and clean the handle and frame with methanol and delicate task wipes; make sure that no grease from the worm gear touches other components. Lastly, the indicator can be cleaned using acetone and delicate task wipes.

After all of the components are thoroughly cleaned, the bearing needs to be greased with MoS_2 grease. Add MoS_2 grease evenly around the bearing (Figure F.28). After placing the

grease, smear the grease into the bearing while wearing a glove and then rotate the bearing back and forth to coat the internals. Repeat this procedure once more for the top of the bearing and then grease the underside of the bearing twice. After fully greasing the bearing, remove the excess MoS_2 grease from the top and bottom (while wearing gloves) and clean off any excess MoS_2 grease from the inner and outer steel rings using delicate task wipes. Next, push the bearing back into the bearing retainer ring by applying uniform pressure around the bearing (Figure F.29); then, wipe the excess grease off of the bearing retainer ring using delicate task wipes.

F.4.4 Reassembly

When reassembling the DPRF 450, do not excessively tighten the bolts. In order to reassemble the DPRF 450, first place the cleaned o-ring retainer rings into the base of the DPRF 450 (Figure F.30). Next, place three new o-rings (McAllister Technical Services) in between the retainer rings (Figure F.31). After replacing the o-rings and retainers, place the outer rotary flange on top of the o-rings (Figure F.20). Next, slip the bearing and bearing retainer ring over the rotary flange and place them on top of the DPRF base (Figure F.32); make sure that the bolt holes are properly aligned. Place a new o-ring (McAllister Technical Services) inside of the bearing cover ring (Figure F.27) and then bolt the cover ring into place on top of the bearing retainer ring (Figure F.33). Next, place the gear support ring on the DPRF and bolt it into place (Figure F.34). Now, place the brass gear and then the dial onto the flange and bolt them into place (Figure F.35). Lastly, bolt the handle and worm gear and the indicator to the DPRF and apply a fresh layer of PTFE grease to the worm gear. Before reinserting the manipulator and shroud flanges, first reattach the newly assembled manipulator to the chamber and leak check the DPRF.

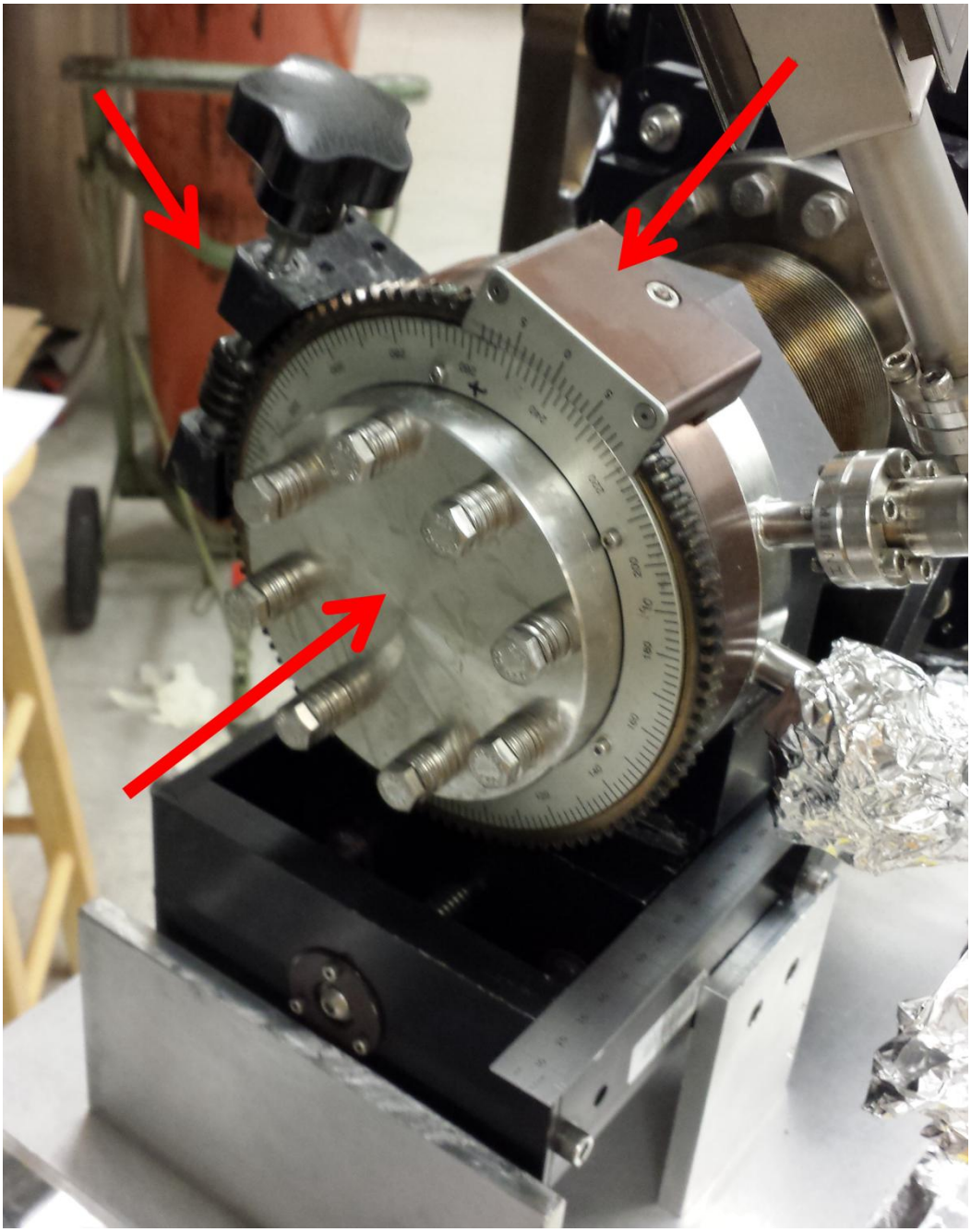

Figure F.14: Image of the manipulator that shows the front face of the DPRF 450. The arrows indicate the handle and worm gear, the indicator, and the blank flange.

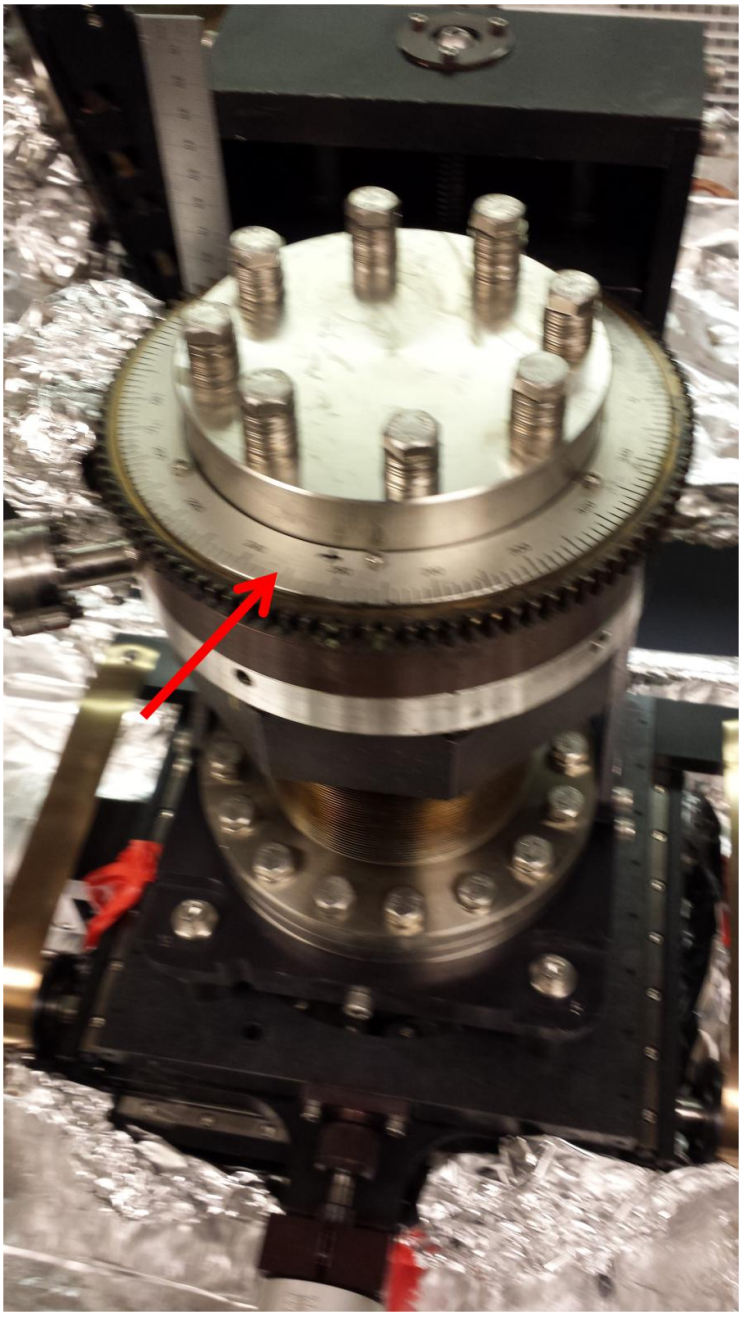

Figure F.15: Image of the manipulator that shows the front face of the DPRF 450. The arrow indicates the dial.

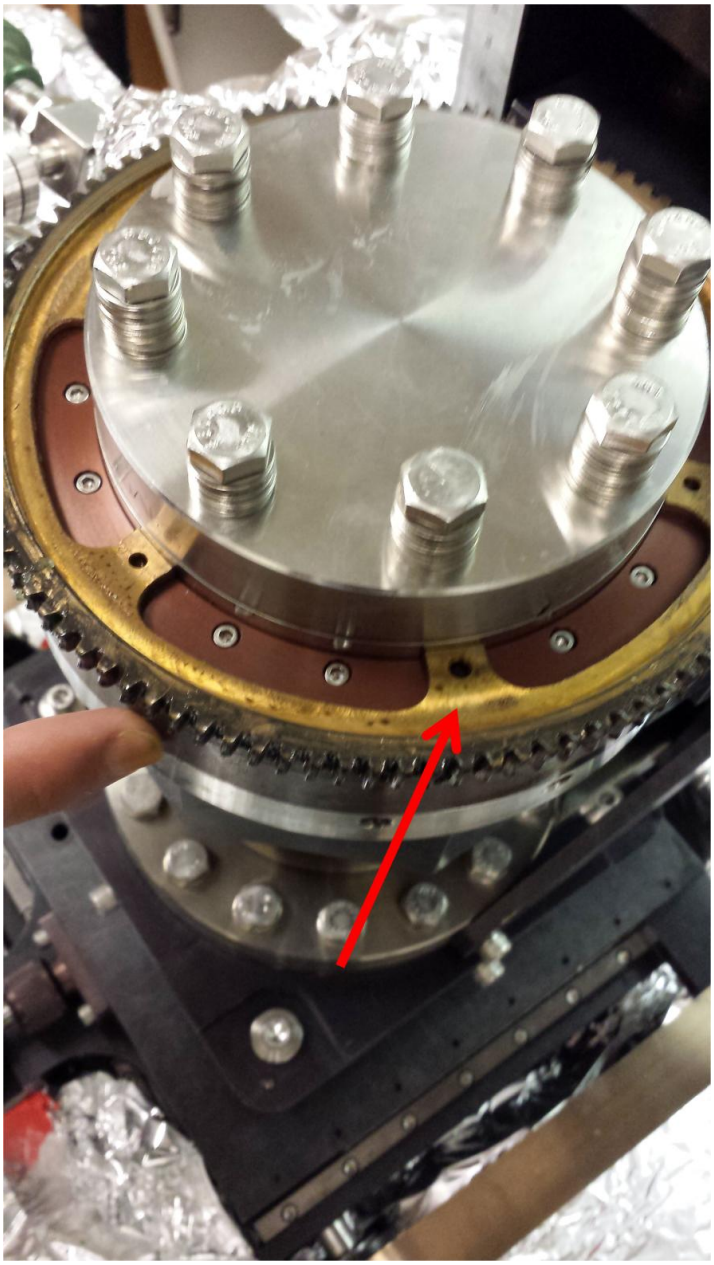

Figure F.16: Image of the manipulator that shows the front face of the DPRF 450. The arrow indicates the brass gear.

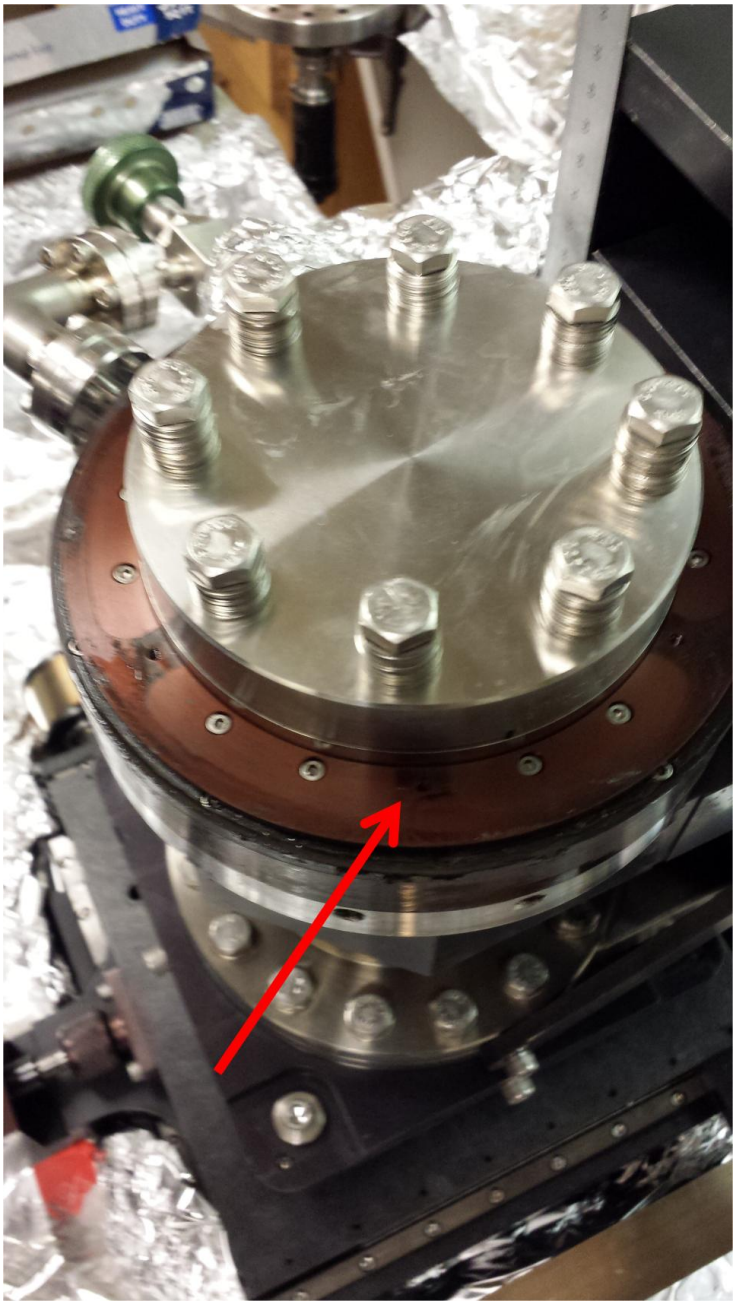

Figure F.17: Image of the manipulator that shows the front face of the DPRF 450. The arrow indicates the gear support ring.

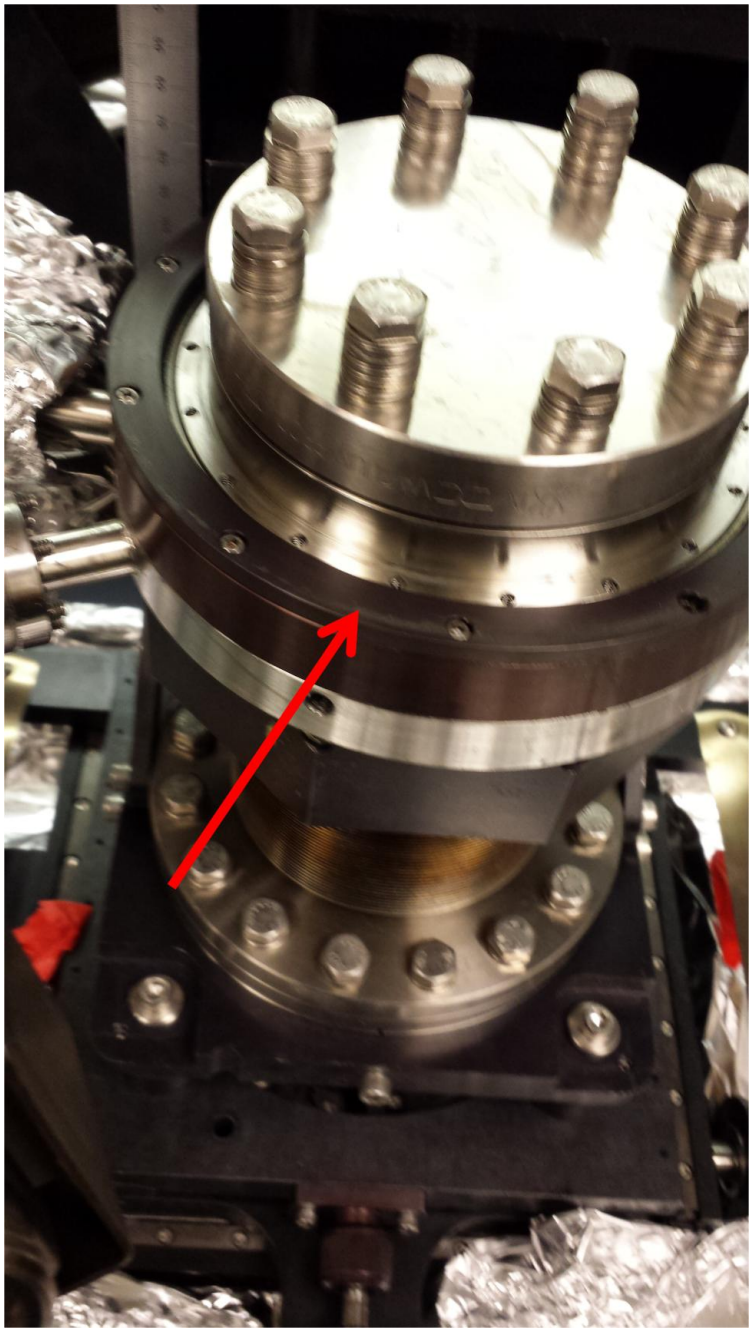

Figure F.18: Image of the manipulator that shows the front face of the DPRF 450. The arrow indicates the cover ring.

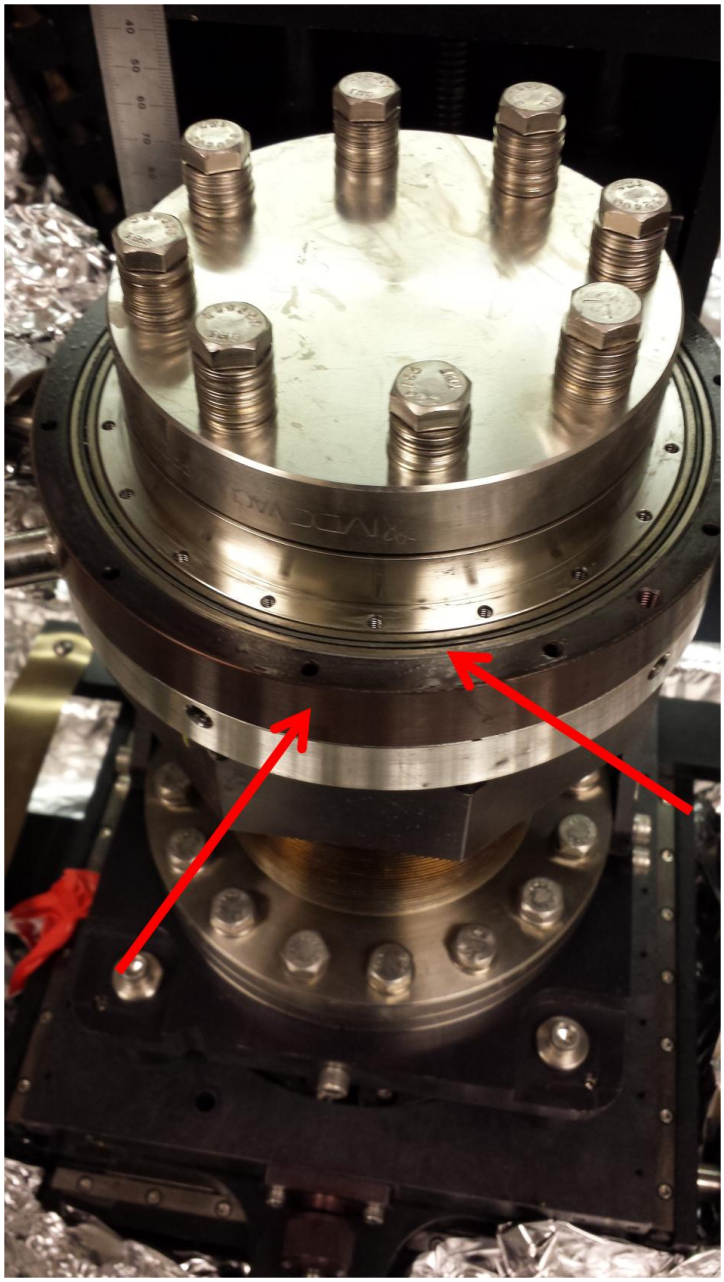

Figure F.19: Image of the manipulator that shows the front face of the DPRF 450. The arrows indicates the bearing (top arrow) and the outer bearing retainer ring.

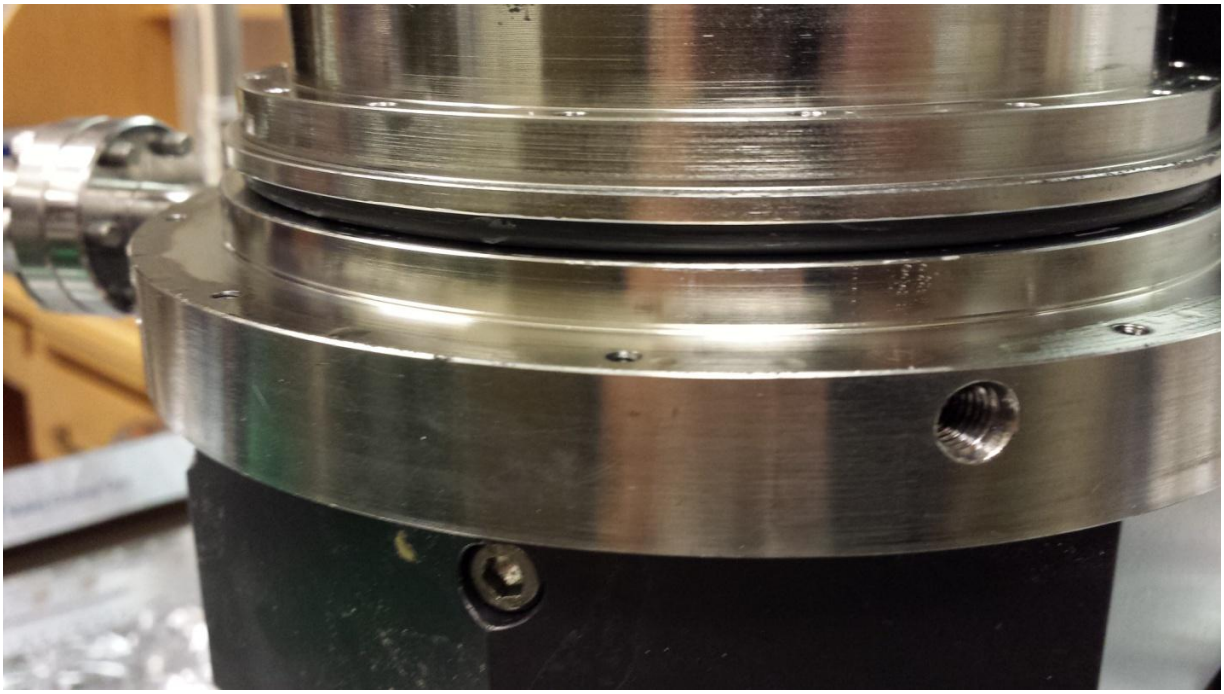

Figure F.20: Close-up, side image of the DPRF 450. The outer rotary flange and the base of the DPRF 450 are separated by three Viton o-rings.

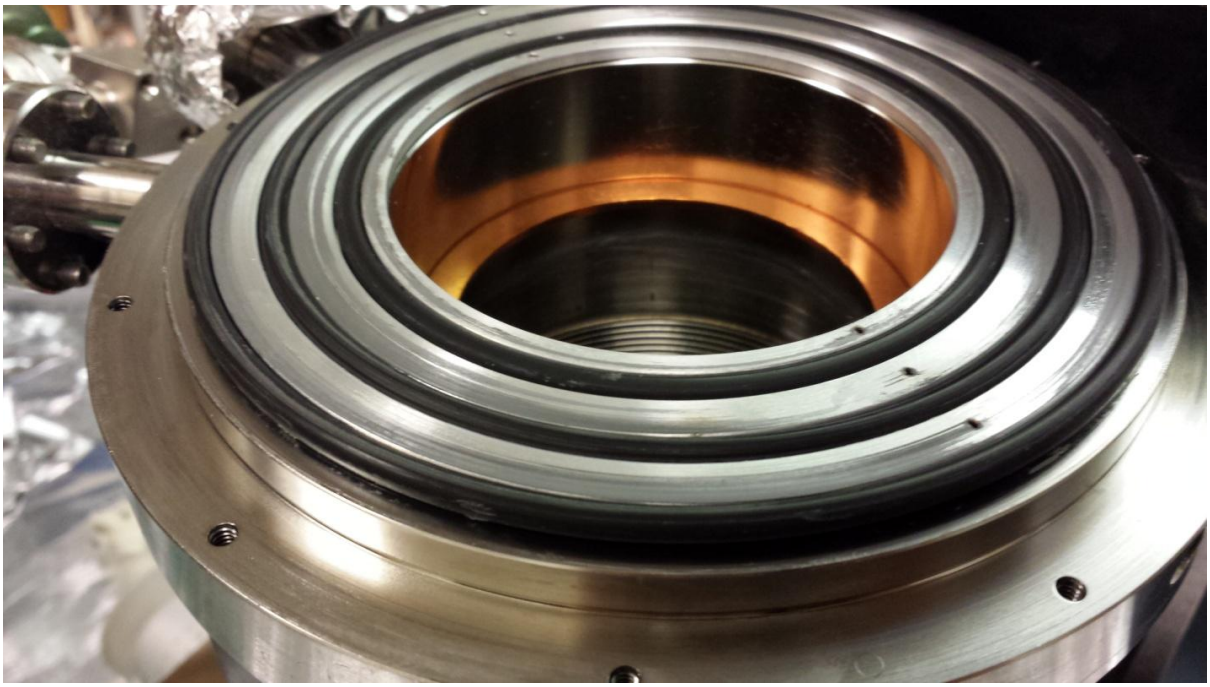

Figure F.21: Close-up image of the base of the DPRF 450. Three Viton o-rings separate the UHV side of the chamber from the atmosphere side. The Viton o-rings are held in place using three retainer rings. Note that the retainer rings are covered in grey material; this indicates that the gaskets are deteriorating.

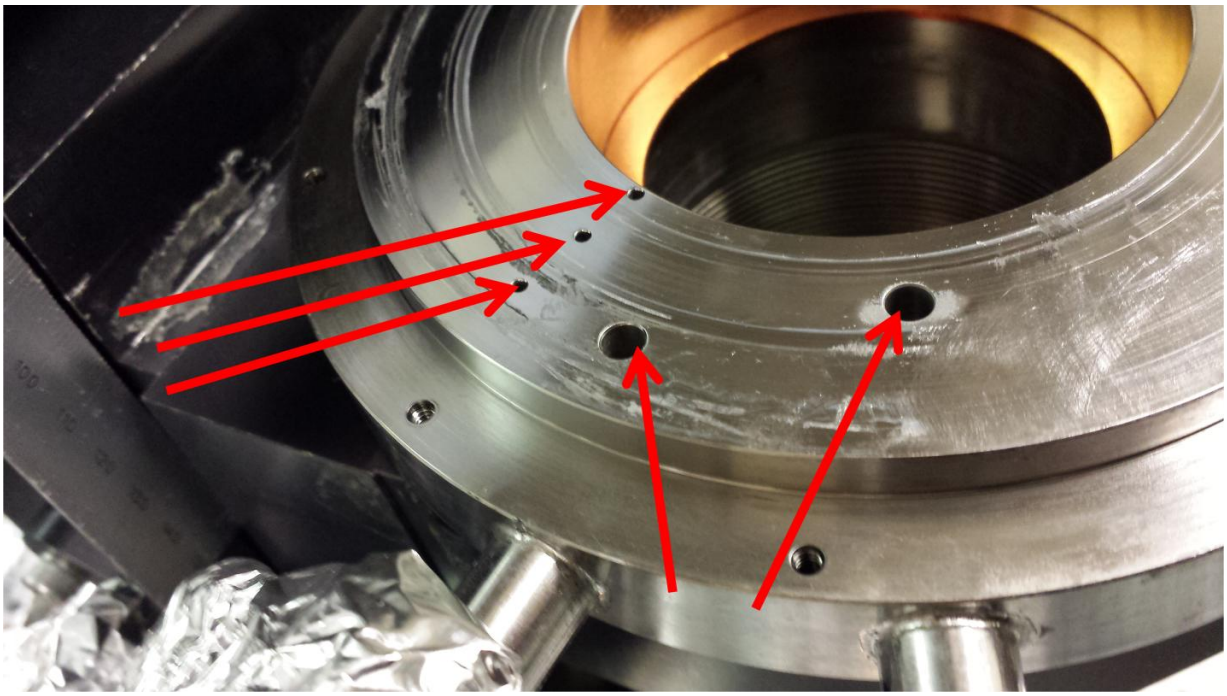

Figure F.22: Close-up image of the base of the DPRF 450. The three small holes, indicated by arrows, are designed to hold the o-ring retainer rings in place. The two larger holes, indicated by the arrows, connect to the inner and outer differential pumping. Note that the base is covered in grey material; this indicates that the gaskets are deteriorating; this buildup must be removed.

Figure F.23: Close-up image of the rear of the outer rotary flange. Note that the mating surface is covered in grey material. The material indicates that the gaskets are deteriorating; this buildup must be removed.

Figure F.24: Close-up image of the side of the DPRF 450. The outer rotary flange and the base of the DPRF 450 are separated by three Viton o-rings. The arrows indicate surfaces that can be cleaned; these areas do not come into contact with the UHV side of the flange.

Figure F.25: Image that shows the proper procedure to remove the bearing from the bearing retainer ring. The ring is first placed upside down on wood to prevent marring. Then, place a piece of wood against the bearing and gently tap the wood using a hammer. Repeat this procedure evenly around the bearing.

Figure F.26: Image of the DPRF 450 rotational bearing.

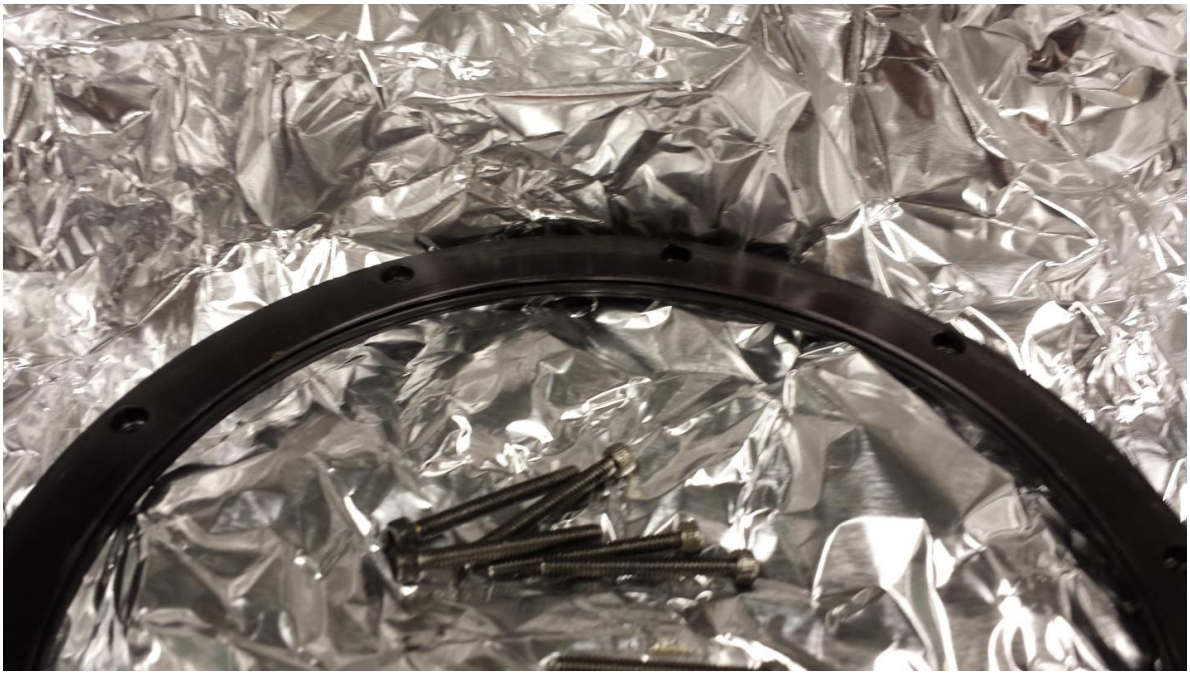

Figure F.27: Close-up image of the DPRF 450 cover ring that shows the internal gasket.

Figure F.28: Close-up image of the DPRF 450 rotational bearing that shows the proper placement of MoS_2 grease (grey drops).

Figure F.29: Close-up image of the DPRF 450 rotational bearing and bearing retainer ring.

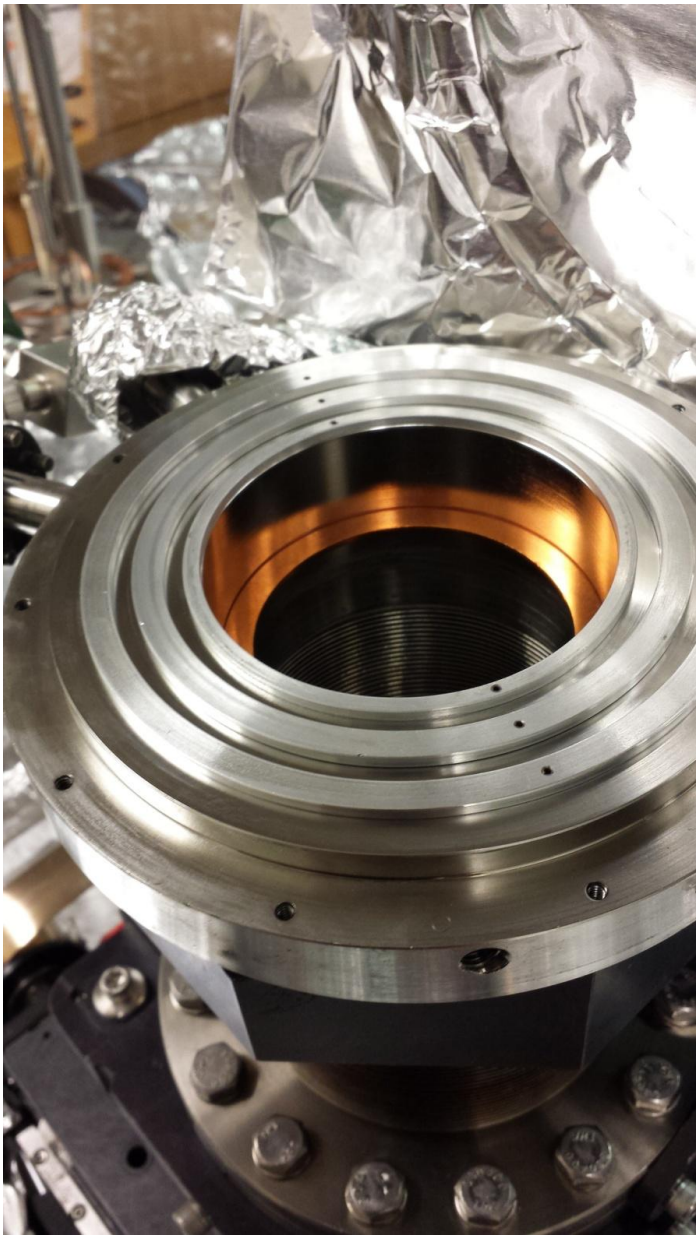

Figure F.30: Close-up image of the base of the DPRF 450 that shows three cleaned retainer rings inserted into the base.

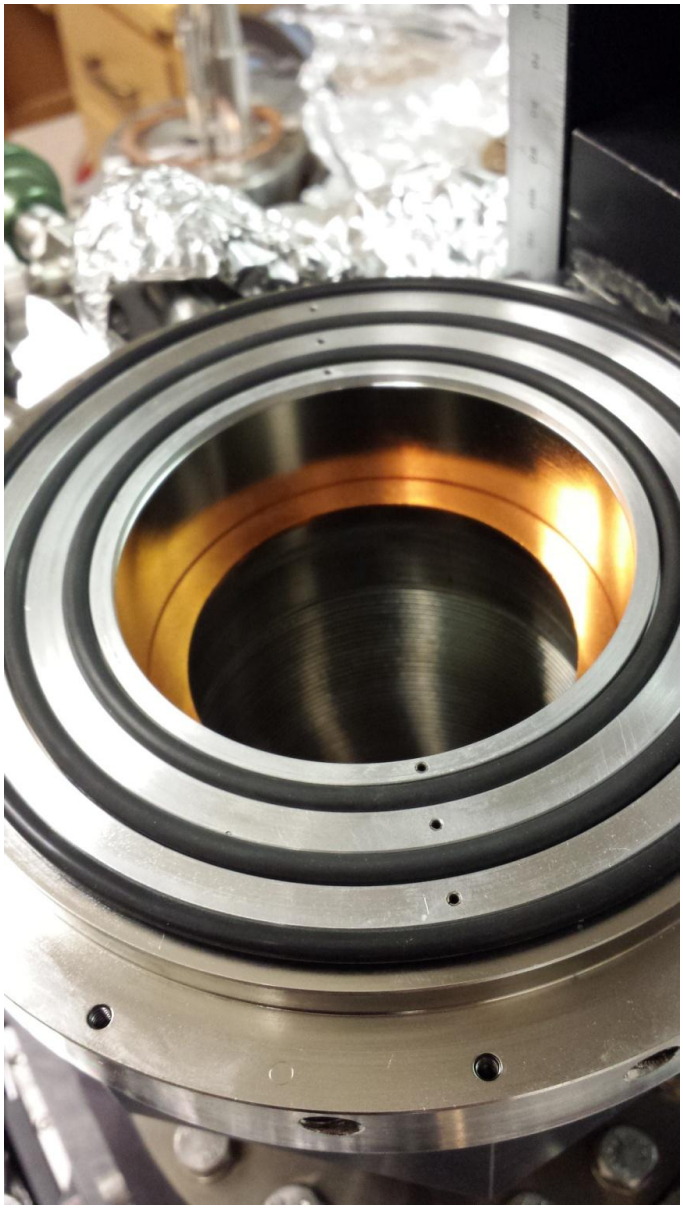

Figure F.31: Close-up image of the base of the DPRF 450. The image shows three new Viton o-rings separated using three clean retainer rings.

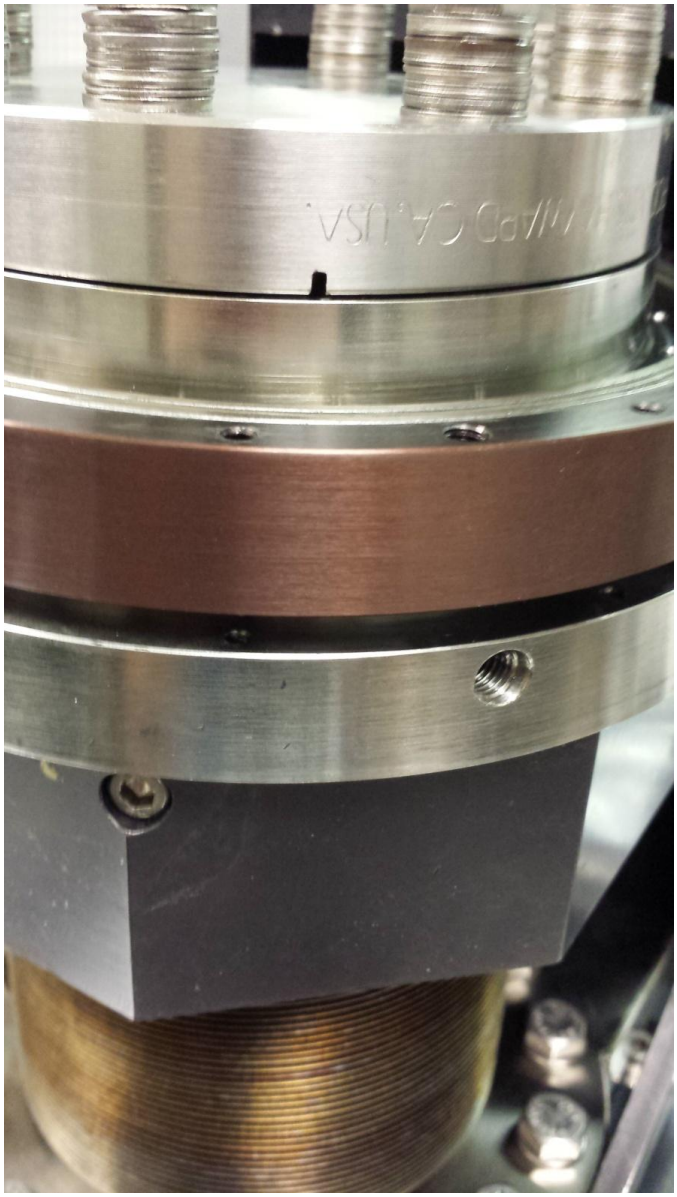

Figure F.32: Close-up image of the side of the DPRF 450 that shows the bearing and bearing retainer ring being replaced. The bearing and bearing retainer ring should be replaced by exerting uniform pressure around the ring and the bolts holes should be aligned as well.

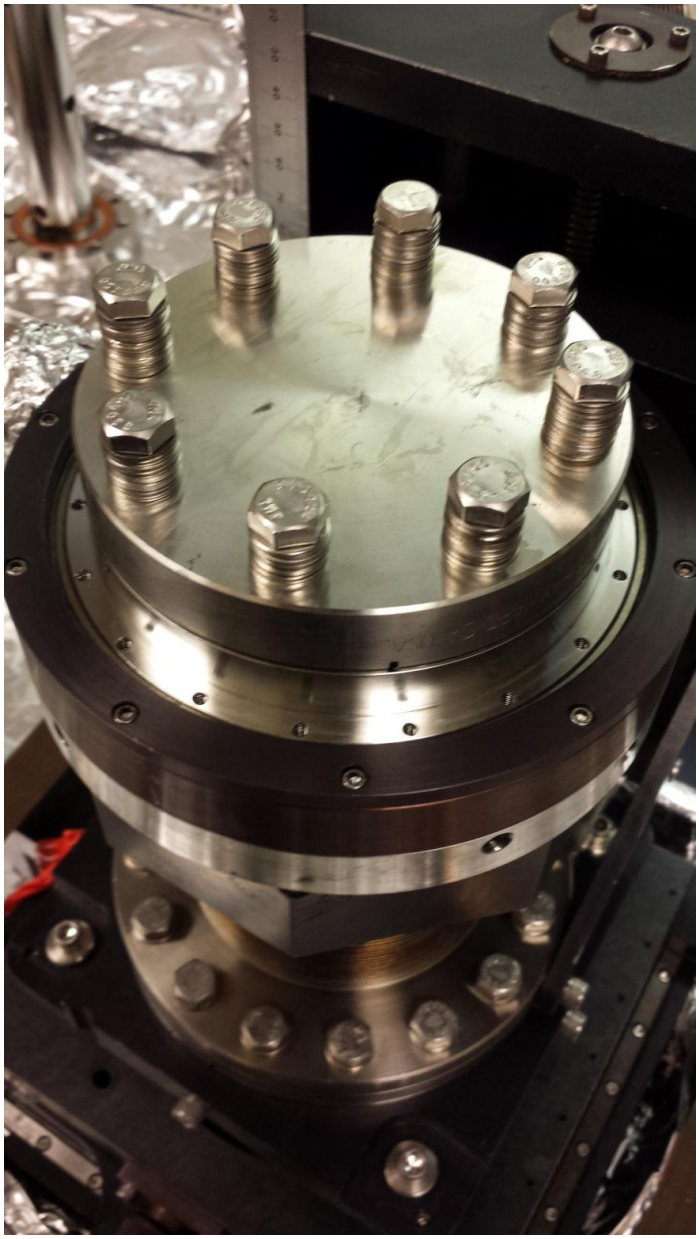

Figure F.33: Image of the manipulator that shows the front face of the DPRF 450 being reassembled. The bearing cover ring was cleaned and installed using a new Viton gasket.

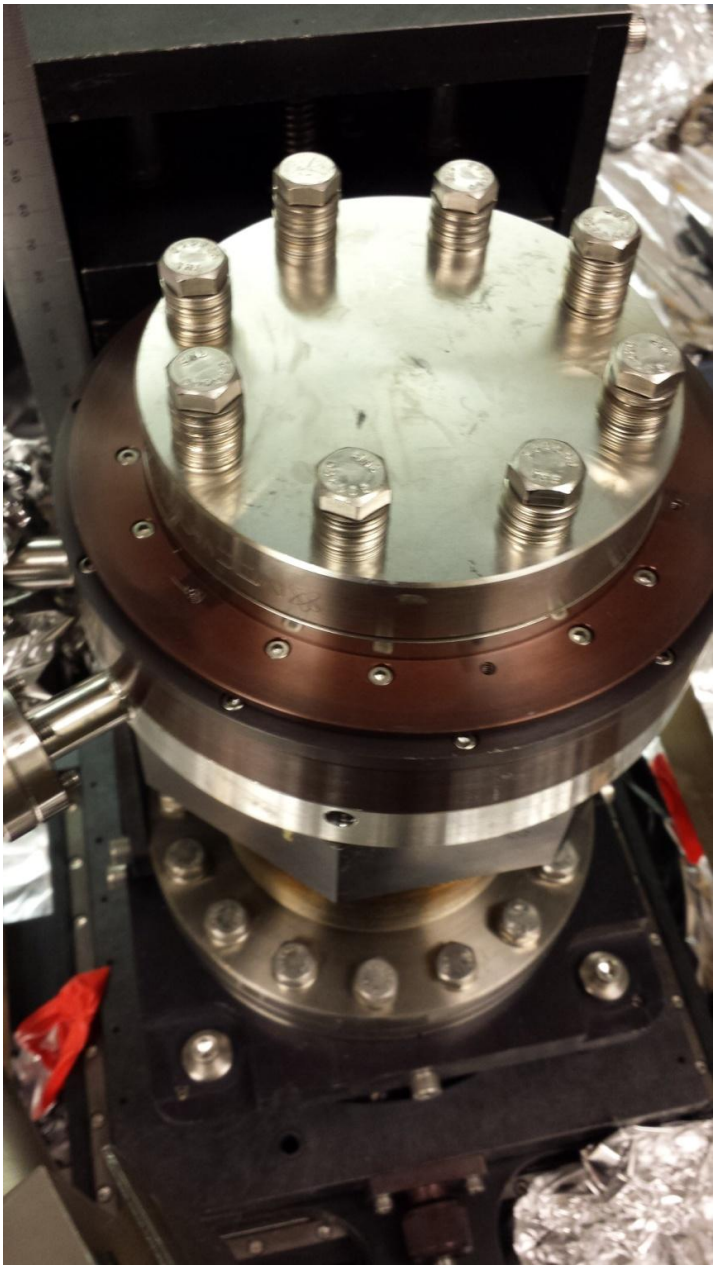

Figure F.34: Image of the manipulator that shows the front face of the DPRF 450 being reassembled. The gear support ring was cleaned and then reinstalled.

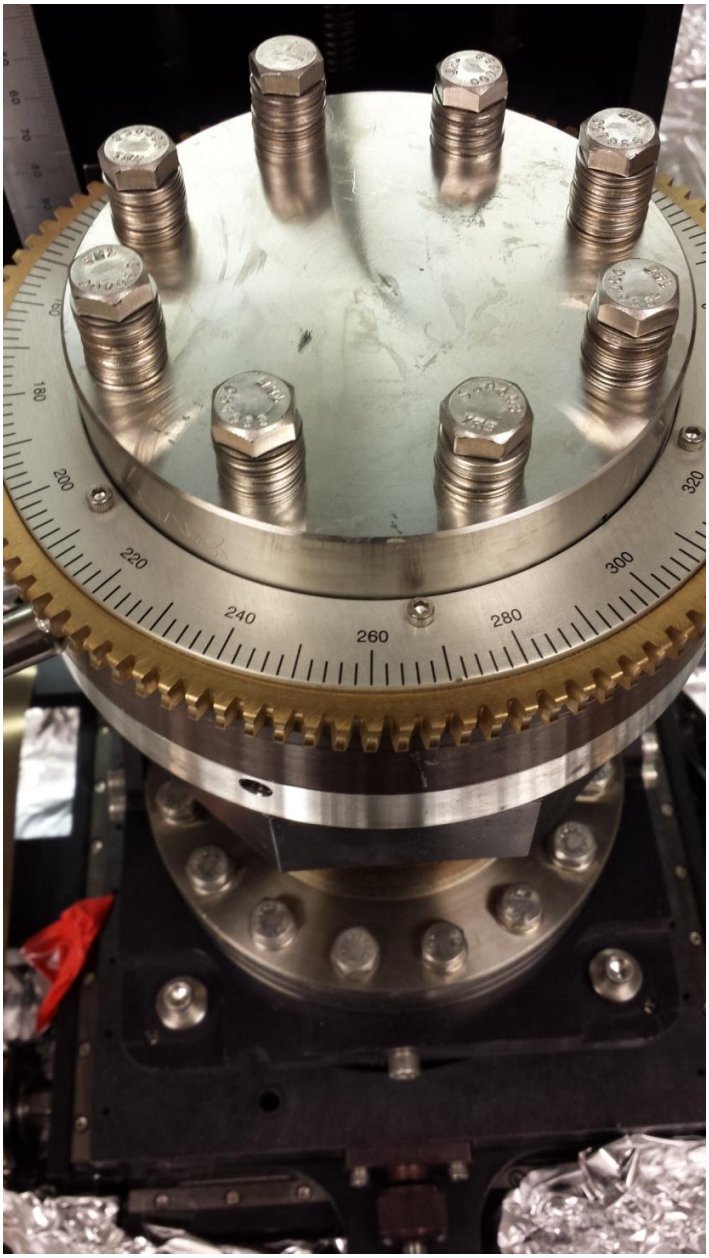

Figure F.35: Image of the manipulator that shows the front face of the DPRF 450 being reassembled. A new brass gear and the cleaned dial were installed.